

Ballistic transport in graphene nanostructures

Von der Fakultät für
Mathematik, Informatik und Naturwissenschaften
der RWTH Aachen University
zur Erlangung des akademischen Grades
eines Doktors der Naturwissenschaften
genehmigte Dissertation

vorgelegt von

Dipl.-Ing.
Bernat Terrés
aus Barcelona (ES)

Berichter: Universitätsprofessor Dr. Christoph Stampfer
Universitätsprofessor Dr. Markus Morgenstern

Tag der mündlichen Prüfung: 16. August 2016

Diese Dissertation ist auf den Internetseiten
der Hochschulbibliothek online verfügbar.

Abstract

This work aims to contribute to the progress and understanding of the sources of disorder in nano-structured graphene devices. The first part of the thesis starts with the introduction of disordered two-terminal graphene nanoribbons of different aspect ratio, in order to unveil and characterize the amount of potential fluctuations on silicon dioxide (SiO_2) substrates. The experimental results reveal the diffusive nature of the transport behavior and a Coulomb blockade dominated transport regime close to the charge neutrality point. Besides its disordered nature, results appoint very short graphene constrictions, with levels of conductance close to $\sim 0.1 e^2/h$, as prime candidates for exploring Fano resonances in graphene nano-structures.

In an attempt to reduce the contributions of the potential fluctuations to transport, we initially identify the different sources of disorder, with bulk and edges arising as the major contributors in nano-structured devices. The strong influence from the bulk is characterized via the tunneling processes through magnetically confined quantum dots arising from the aforementioned bulk disorder.

First evidences of an edge induced disorder are treated in the following section, where we investigate the crystal structure of the nanoribbon's edges by means of Raman spectroscopy experiments. Results on lithography-free graphene nanoribbons, shaped by the exfoliation process itself, are compared to traditional plasma etched graphene ribbons. In these pristine ribbons, the correlation length ξ , figure of merit to characterize the edges, is one order of magnitude higher than on plasma etched structures. Results highlight the strong edge-induced disorder present in traditionally plasma-etched graphene devices.

With the edge-induced disorder identified via Raman spectroscopy measurements, we implement in the next section an electrostatic approach to reduce its effects. Short and relatively narrow graphene constrictions are side-gated by graphene gate electrodes. We demonstrate the reduction in disorder by transport and bias spectroscopy measurements. Results are further supported by the formation of a quasi-1D channel upon application of a lateral electrostatic potential. The 1D-like nature of the electronic path

is justified by its Fano-like interference with a 0D-like charged puddle located at the interface with the leads. Results represent the very first reported indications of Fano interference phenomena in graphene.

To reduce bulk disorder, we implement a dry transfer technique for the fabrication of encapsulated graphene devices in between a top- and a bottom-layer of hexagonal boron nitride (hBN). Mobility values approaching $200\,000\text{ cm}^2/(V\text{ s})$ confirm the high quality achieved with our fabrication technique. The residual disorder is characterized via the temperature dependence of the symmetry broken states in the quantum Hall regime, in a hBN/graphene/hBN Hall bar device. The values of localization length found in the variable-range-hopping (VRH) regime exceed $1\mu\text{m}$, one order of magnitude higher than the reported values for graphene on SiO_2 substrates.

In the second part of the thesis, we demonstrate ballistic transport and quantized conductance of size-confined Dirac fermions in lithographically-defined graphene quantum point contacts (QPCs). Close to the charge neutrality point, bias voltage spectroscopy measurements reveal a renormalized Fermi velocity ($v_F \approx 1.5 \times 10^6\text{ m/s}$) in our graphene constrictions. Moreover, at low carrier densities, transport measurements allow probing the density of localized states at the edges, thus offering a unique handle on edge physics in graphene devices.

Direct comparison between successive cool-downs of a same QPC device reveal the lifting of the four-fold degenerate subbands. Results are supported by bias voltage and magnetic field dependent measurements. The amount of dopands/contaminants collected by the edges during the successive cool-downs is appointed as the source of this degeneracy breaking process. Quantum Hall measurements are used to spatially resolve the change in capacitance profile, supporting this change in dopands/contaminants at the edges.

Zusammenfassung

Zielsetzung ist es, einen Beitrag zum Fortschritt und dem Verständnis des unklaren Ursprungs von Unordnung in nanostrukturierten Graphen Proben zu leisten. Der erste Teil der Arbeit beginnt mit der Untersuchung von Transporteigenschaften durch Unordnung dominierten Graphen Nanoribbons mit zwei Kontakten und verschiedenen Aspektverhältnissen, um den Einfluss der vom Siliziumdioxid SiO_2 Substrat induzierten Potentialfluktuationen zu charakterisieren. Die Messdaten zeigen, dass die Proben durch diffusiven Ladungsträgertransport charakterisiert sind und bei niedrigen Energien statistische Coulomb-Blockade aufweisen. Trotz des diffusiven Charakters, zeigen die kurzen Graphen Nanoribbons seine Leitfähigkeit von ungefähr $\sim 0.1 e^2/h$, und sind daher ein vielversprechender Kandidat um Fano-Resonanzen zu studieren.

Um den Einfluss der Potentialvariationen in den Graphen Nanostrukturen zu reduzieren werden zunächst Ursachen und Auswirkungen von die Potentialfluktuationen die sowohl von Randeffecten als auch vom inneren der Probe herrühren identifiziert. Die Präsenz von angeregten Zuständen in den Bias-Spektroskopiemessungen und die Analyse ihrer Energien zeigt, dass Elektron-Phonon Wechselwirkung eine wichtige Rolle für das Energiespektrum von quasi nulldimensionalen Graphenstrukturen auf Siliziumdioxid spielen könnten.

Erste Anzeichen von Randeffecten werden im nächsten Kapitel behandelt, wo die Kristallstruktur der Ränder der Nanoribbons mit Raman-Spektroskopie untersucht wird. Die Ergebnisse von "Lithographie-frei" hergestellten Graphen Nanoribbons, die durch einen neu entwickelten Fabrikationsprozess bei der Exfolierung hergestellt wurden, zeigen eine hohe Korrelationslänge ξ im Vergleich mit durch Plasmaprozesse geätzte Nanoribbons. Die Ergebnisse bestätigen ein höheres Mass an Unordnung in den Rändern der durch Plasmaätzen hergestellten Graphen Strukturen.

Im nächsten Kapitel wird eine elektrostatische Methode entwickelt um die Effekte von ungeordnete Rändern zu reduzieren. Wir bauen kurze und schmale Graphen Nanoribbons mit seitlich angeordneten Graphen Elektroden. Eine Reduktion der in den Transportdaten sichtbaren Unordnung wird insbesondere durch Bias Spektroskopie Mes-

sungen gezeigt.

Weiterhin zeige ich die Entstehung von quasi-eindimensionalen Kanälen bei symmetrisch angelegten Potentialen an den seitlich angeordneten Elektroden. Der eindimensionale Charakter des Ladungstransportes wird durch Fano-Interferenzen zwischen dem 1D-Kanal mit Punktartigen Ladungswolken an den Kontaktbereichen gezeigt. Diese Ergebnisse stellen die erstmalige Beobachtung von Fano-Interferenzen in Graphen dar.

Um die Unordnung in den Proben weiter zu reduzieren wird eine trockene Transfermethode genutzt um Graphen geschützt von zwei Lagen hexagonalem Bornitrid herzustellen. Die Ladungsträgermobilitäten erreichen Werte von bis zu $200.000 \text{ cm}^2/(\text{Vs})$ in diesen Proben und unterstreichen die hohe Probenqualität die bei dieser Herstellungsmethode erreicht wird. Die verbleibende Unordnung wird durch die Temperaturabhängigkeit von symmetriegebrochenen Quanten Hall Zuständen in einem Hallbarren untersucht. Eine Lokalisierungslänge von über $1 \mu\text{m}$ wurde im variable-range-hopping (VRH) Regime bestimmt. Dieser Wert ist mehr als eine Größenordnung grösser als für ähnliche Proben auf Siliziumdioxid.

Im zweiten Teil der Dissertation zeige ich ballistischen Transport und quantisierte Leitfähigkeit von eingeengten Dirac-Fermionen in durch Lithographie hergestellten Quantenpunktkontakten (QPC). Nahe am Ladungsneutralitätspunkt zeigen Bias Spektroskopie Messungen eine Fermigeschwindigkeit von $v_F \approx 1.5 \times 10^6 \text{ m/s}$ in unseren Graphen QPCs. Bei niedrigen Ladungsträgerdichten kann die Zustandsdichte direkt durch transportmessungen untersucht werden, was einen direkten Zugang zu lokalisierten Randzuständen ermöglicht. Der direkte Vergleich zwischen den Daten der selben Probe, die mehrfach abgekühlt und vermessen wurde zeigt zweifelsfrei eine Brechung der vierfach entarteten Subbänder. Die Ergebnisse werden durch Bias Spektroskopie Messungen und Magnetfeldabhängige Messungen untermauert. Die bei verschiedenen Abkühlvorgängen angehäuften Kontaminationen an den Rändern werden als Ursache für die Symmetriebrechung angenommen. Dies wird mit Messungen zum Quanten Hall Effekt weiter untersucht, indem ein veränderliches Dotierprofil und eine Kapazitätsänderung am Rand analysiert wird.

Contents

Contents	i
1 Introduction	1
1.1 The slowing of Moore's law	1
1.2 Graphene as a host material for electronics	2
2 Theory of graphene	7
2.1 Description of graphene	7
2.2 Graphene in strong magnetic fields	17
2.3 Description of graphene ribbons	21
3 Fabrication methods	29
3.1 Graphene on SiO ₂	29
3.2 Graphene on hBN	33
3.3 Encapsulated hBN-graphene-hBN	36
4 Disordered graphene nano-structures	41
4.1 Experimental evidences of a diffusive transport behavior	41
4.1.1 Transport characteristics close to the charge neutrality point: Disorder-induced Coulomb gaps in graphene constrictions	44
4.2 Evidences of a bulk-induced disorder	53
4.2.1 Magnetically confined quantum dots	53
4.3 Evidences of an edge-induced disorder	70
4.3.1 Raman spectroscopy on mechanically exfoliated pristine graphene ribbons	70
4.4 Reduction of edge-disorder via electrostatic gating	80
4.4.1 Electrical transport indications of a reduced disorder	80
4.4.2 Observation of Fabry-Pérot oscillations as a proof of disorder reduction	91
4.4.3 Fano resonances as a proof of disorder reduction	95
4.5 Applications: in-plane electronic interconnects	112

5	High-mobility graphene	121
5.1	Characterization of the residual disorder	121
6	Ballistic graphene nano-structures	135
6.1	Ballistic transport in graphene quantum Point Contacts	135
6.2	Effect of edge localized states in the transport behavior	153
6.3	Breaking of the four-fold degeneracy in ballistic graphene nano-structures	161
7	Conclusion and outlook	173
7.1	Conclusion	173
7.2	Outlook	174
8	Appendices	175
8.1	Magnetically confined QDs	175
8.2	Temperature dependence of symmetry broken states.	176
8.3	Process parameters	180
8.4	List of samples	183
	Publications	187
	List of Figures	189
	Acknowledgements	194
	Curriculum Vitae	195

1.1 The slowing of Moore's law

Communication has been an important cornerstone of civilization. The way we interact with the environment and with each other has evolved over the last centuries. Owing to the rapid development of the information technology (IT) many of the fundamental aspects of our society, e.g. family, personal and professional relationships, entertainment etc., have adapted to the new technological trends (cloud computing, portable electronics, internet, etc...). To make it possible, tremendous efforts have been undertaken in the development of faster, smaller and cheaper electronics. The market of consumer electronics is nowadays so eager to the latest developments and technology breakthroughs that its revenue is expected to reach 9.2 billion U.S. dollars by 2019 just in the USA (forecast issued from [1]).

Although the huge electronics market has been mainly motivated by the cadence in which technological innovations have progressed, we are recently facing a noticeable slowdown in technology's pace. Instead of doubling the amount of transistors on a given area every 24 months, known as Moore's law (estimated in 1965 by Gordon E. Moore [2]), the rhythm has dropped to roughly 30 months, approximately a 25% increase, by the end of 2015 and beginning of 2016 [3]. All these changes are even confirmed by Intel, the biggest player in chip-making technology, in its latest road-map [4]. Technology industry is therefore facing the first retraction in its amazing 50-year run.

The slowdown though does not come as a surprise, given the challenges of manufacturing transistors and circuits at an increasingly tiny scale. Actually, the scaling down progress has to be attributed to manufacturing technology rather than the host material itself: silicon (Si). However, with transistors' latest chips already as small as 14 nanometers, it is becoming very hard to produce them cost effectively. Technology must then look for different routes to keep increasing raw computing power. Substitute materials with increased electron mobilities allowing for higher clock rate, i.e. the number of operations per second, or fundamentally new technologies like spintronics or tunneling transistors are right now investigated. Intel's chief of manufacturing himself said in February 2016 that the company needs to swap over from Si-based transistors

in about four years: "The new technology will be fundamentally different" [5].

Understandably, the urge for suitable next generation materials has had an influence in most levels of science and fundamental research. During the last two decades, we have seen an explosion in solid state physics and material research with the development of new layered materials, like graphene, Molybdenum disulfide (MoS_2) [6] and other two-dimensional transition metal dichalcogenides [7]. Moreover, conceptually different trends in computation have also been explored, like spintronics [8, 9] or majorana fermions-based electronics [10, 11].

1.2 Graphene as a host material for electronics

Back in 2004, K. Novoselov and A. Geim were aiming to study the electronic properties of layered graphite when they first encountered graphene [12]. The discovery came as a big surprise since the single layer configuration of graphite, i.e. graphene, was believed to be thermodynamically unstable [13, 14] and thus non-feasible experimentally. This one atom-thick allotrope of carbon was quickly identified as a substitute for Silicon. Indeed, publication volumes have been growing at exponential rates since then [15], encouraged by the outstanding electronic and mechanical properties that theoretical studies predicted [16]. Particularly appealing was the high electron mobility envisaged for graphene, with values over $10^5 \text{ cm}^2(\text{Vs})^{-1}$ at room temperature [17]. This has been one of the main reasons graphene has been considered as a suitable material for the post-silicon revolution even at his earlier stages [18].

As usually for scientific advances, the improvements in graphene-related fabrication techniques and the experimental findings have been following behind the pace of the theoretical predictions. In fact, the first observation of graphene came way after the first calculations of graphene's band structure [19], which at that time was rather considered a calculation exercise.

Aside from its fundamental interest, the first experimental graphene-based devices were far behind the expectations in carrier mobility [20, 21]. Graphene was initially developed on Silicon dioxide (SiO_2) chips, a substrate later on identified to induce fair amounts of disorder in graphene [22, 23]. Although suspending the graphene above the substrate brought significant improvements in device quality [23, 24] this fabrication method has some fundamental limitations. The back-gate sweeping rate and maximum voltage loads are heavily compromised, structures are prone to bend under temperature and electrostatic loads and the suspended devices tend to be extremely fragile and non-reproducible [25]. Furthermore, within this fabrication method, the graphene structures remain unprotected from the processing or ambient contaminants.

The first quality breakthrough in graphene's short history came with the emergence of hexagonal boron nitride (hBN) as a suitable substrate [26]. Hexagonal boron nitride has an atomically smooth surface and it is relatively free of charge traps and dangling bonds compared to SiO_2 . Moreover, hBN has a small lattice mismatch of around 1.7% with graphene [27]. The properties of this insulating 2D system [28] triggered the

theoretical investigation of 2D hBN-graphene heterostructures [27], even before having been realized experimentally [26].

The second and latest breakthrough in graphene technology came with the full encapsulation of graphene between a top and a bottom layer of hBN [29]. The resulting stack showed once again an outstanding jump in quality [30] compared to graphene on hBN substrate [26]. The extracted mobility values even surpass the theoretical prediction for mobility of $10^5 \text{ cm}^2(\text{Vs})^{-1}$ at room temperature [17]. These findings revealed how sensitive graphene is to ambient impurities and processing contaminations.

Aside from the advances in fabrication, finding ways to implement graphene in semi-conducting technology has been a major concern in graphene research. For graphene to become a viable channel material for transistor applications, it is mandatory to open an energy gap. A valid approach is to brake the A-B sublattice symmetry to obtain an energy gap, owing to the same reasons hexagonal boron nitride is an insulating material of about 7 eV [28]. Another possibility is to confine the wave-like charge carriers across a size constrained path, also known as graphene nanoribbons or constrictions. This second method relies on the amount of discrete states across the constrictions to control the conductance flowing along. Although the opening of a transport gap also depends on the specific crystallographic orientation at the edges (see Section 2.3) this is the route considered throughout the thesis.

The first section reviews the fundamentals of bulk graphene (see Section 2.1) and the theoretical description of graphene nanoribbons (Section 2.3). We follow by introducing the three main fabrication methods available nowadays for the fabrication of graphene devices, e.g. graphene on SiO_2 substrates (Section 3.1), on hBN flakes (Section 3.2) and encapsulated in between a top- and bottom-layer of hBN (Section 3.3). The thesis follows the same chronological timing as graphene research, starting with the analysis of graphene on SiO_2 substrates (Section 4.1) to end up with devices based on hBN-graphene-hBN stacks (Section 5.1 and Section 6.1). Throughout the sections, we identify the main sources of disorder, e.g. bulk (Section 4.2.1) and edge (Section 4.3) disorder.

Phase coherent transport measurements have been used to characterize disorder in metals and semiconductors [31–34]. Within this Thesis, we keep on this tradition with the detailed study of coherent localization (Section 4.2.1) and coherent conductance fluctuations (Section 4.4.2). These studies reveal important information on the nature of disorder and allow us to propose an electrostatic mechanism (Section 4.4) and a newly developed fabrication method (Section 4.3.1) to control and reduce the sources of disorder in graphene nanostructures.

This thesis ends up with the experimental observation, for the very first time, of robust and reproduceable quantized conductance in hBN-graphene-hBN quantum point contacts (Section 6.1). Special mention receives Section 6.3 in which we underline how disorder/scattering couples to the special symmetries of electrons in graphene, i.e. the ‘valley’ degree of freedom (also known as pseudospin). Section 7.2 gives an outlook on prospects for future research along these lines.

References

1. Statista. *Revenue of consumer electronics and appliance rental (NAICS 53221)* <http://www.statista.com/forecasts/409739/united-states-consumer-electronics-and-appliance-rental-revenue-forecast-naics-53221>. [Online]. 2013.
2. Moore, G. Cramming more components onto integrated circuits. *Electronics Magazine* **38**, 8 (1965).
3. Technology review, M. *Move over and silicon* <https://www.technologyreview.com/s/600716/intel-chips-will-have-to-sacrifice-speed-gains-for-energy-savings/>. [Online]. 2016.
4. Corp., I. (*Annual Report for the Period Ending 12/26/15* <http://files.shareholder.com/downloads/INTC/867590276x0xS50863-16-105/50863/filing.pdf>). [Online]. 2016.
5. Simonite, T. & technology review, M. *Intel Puts the Brakes on Moore Law* <https://www.technologyreview.com/s/601102/intel-puts-the-brakes-on-moores-law/>. [Online]. 2016.
6. Kobayashi, K. *et al.* Electronic structure and scanning-tunneling-microscopy image of molybdenum dichalcogenide surfaces. *Physical Review B* **51**, 17085 (1995).
7. Wang, Q. *et al.* Electronics and optoelectronics of two-dimensional transition metal dichalcogenides. *Nature Nanotechnology* **7**, 699–712 (2011).
8. Wolf, S. A. *et al.* Spintronics: A Spin-Based Electronics Vision for the Future. *Science* **294**, 1488–1495 (2001).
9. Wolf, S. A. *et al.* Spintronics and a retrospective and perspective. *IBM Journal of Research and Development* **50**, 101–110 (2006).
10. Nayak, C., Simon, S. H., Stern, A., Freedman, M. & Sarma, S. D. Non-Abelian anyons and topological quantum computation. *Rev. Mod. Phys.* **80**, 1083 (2008).
11. Wilczek, F. *et al.* Majorana returns. *Nature Physics* **5**, 614–618 (2009).
12. Novoselov, K. S. *et al.* Electric Field Effect in Atomically Thin Carbon Films. *Science* **306**, 666–669 (2004).
13. Peierls, R. E. Quelques proprietes typiques des corps solides. *Ann. I. H. Poincare* **5**, 177–222 (1935).
14. Landau, L. D. Zur Theorie der phasenumwandlungen II. *Phys. Z. Sowjetunion* **11**, 26–35 (1937).
15. editorial, N. The rise and rise of graphene. *Nature Nanotechnology* **5**, 755 (2010).
16. Geim, A. K. *et al.* The rise of graphene. *Nature Materials* **6**, 183–191 (2007).
17. Hwang, E. H. *et al.* Acoustic phonon scattering limited carrier mobility in two-dimensional extrinsic graphene. *Phys. Rev. B* **77**, 115449 (2008).
18. Eisberg, N. Electronics graphene set to replace silicon. *Chem Ind*, **11** (2008).
19. Wallace, P. R. The band theory of graphite. *Phys. Rev.* **71**, 622 (1947).

20. Novoselov, K. S. *et al.* Two-dimensional gas of massless Dirac fermions in graphene. *Nature* **438**, 197–200 (2005).
21. Zhang, Y. *et al.* Experimental observation of the quantum Hall effect and Berry’s phase in graphene. *Nature* **438**, 201–204 (2005).
22. J.H.Chen *et al.* Intrinsic and extrinsic performance limits of graphene devices on SiO₂. *Nature Nanotechnology* **3**, 206–209 (2008).
23. Martin, J. *et al.* Observation of electron hole puddles in graphene using a scanning single-electron transistor. *Nature Physics* **4**, 144–148 (2008).
24. Bolotin, K. I. *et al.* Temperature dependent transport in suspended graphene. *Phys. Rev. Lett.* **101**, 096802 (2008).
25. Tombros, N. *et al.* Quantized conductance of a suspended graphene nanoconstriction. *Nature Physics* **7**, 697–700 (2011).
26. Dean, C. R. *et al.* Boron nitride substrates for high-quality graphene electronics. *Nature Nanotechnology* **5**, 722–722 (2010).
27. Giovannetti, G. *et al.* Substrate-induced band gap in graphene on hexagonal boron nitride: Ab initio density functional calculations. *Phys. Rev. B* **76**, 073103 (2007).
28. Watanabe, K. *et al.* Direct-bandgap properties and evidence for ultraviolet lasing of hexagonal boron nitride single crystal. *Nature Materials* **3**, 404–409 (2004).
29. Wang, L. *et al.* One-dimensional electrical contact to a two-dimensional material. *Science* **342**, 614–617 (2013).
30. Mayorov, A. S. *et al.* Micrometer-Scale Ballistic Transport in Encapsulated Graphene at Room Temperature. *Nano Lett.* **11**, 2396–2399 (2011).
31. Hikami, S. *et al.* Micrometer-Scale Ballistic Transport in Encapsulated Graphene at Room Temperature. *Prog. Theor. Phys.* **63**, 707 (1980).
32. Beenakker, C. W. J. *et al.* Quantum Transport in Semiconductor Nanostructures. *Solid State Phys.* **44**, 1–228 (1991).
33. Mathur, H. *et al.* Random Berry phase magnetoresistance as a probe of interface roughness in Si MOSFETs. *Phys. Rev. B* **64**, 235325 (2001).
34. Pierre, F. *et al.* Dephasing of electrons in mesoscopic metal wires. *Phys. Rev. B* **68**, 085413 (2003).

2.1 Description of graphene

This section serves as an introduction to the electronic transport properties of graphene. All analytical expressions are presented such that a neophyte of graphene can follow through the development of the analysis. The purpose of every development is motivated by an brief introduction and we comment the experimental implications of the end-results. It is important to note that none of the expressions here presented has been developed by the author, being this section a basic review on the many theoretical efforts on the topic [1–13]. We plot the relevant mathematical expressions in Matlab for an self-explanatory visualization of the phenomenon under discussion.

To understand to basic principles of graphene it is useful to review the bonding structure of its carbon atoms. A single carbon atom is formed by six electrons configured as $1s^2 2s^2 2p^2$ in its ground state. Hence, two electrons occupy the inner shell $1s$ and four electrons fill the outer $2s$ and $2p$ shells. It is important to mention that the $2p$ orbitals are roughly $4 eV$ higher in energy than its $2s$ counterpart, making it energetically favorable to occupy completely the $2s$ shell (2 electrons) and leave the $2p$ orbitals ($2p_x$, $2p_y$ and $2p_z$) filled with the two remaining electrons. However, in the presence of other atoms, such as Hydrogen H, Oxygen O, or other Carbon C atoms, it is energetically favorable to excite one electron from the $2s$ shell up to the $2p$ orbitals in order to form covalent bonds with the neighboring atoms. The four equivalent quantum mechanical states $|2s\rangle$, $|2p_x\rangle$, $|2p_y\rangle$ and $|2p_z\rangle$ from the excited state, can therefore hybridize. A sp^n hybridization refers to the quantum-mechanical superposition of the $|2s\rangle$ state with n $|2p_j\rangle$ states. The planar sp^2 hybridization is common to all graphitic allotropes (graphite, carbon nanotubes and graphene), although other form of hybridization, e.g sp^1 or sp^3 , are possible in organic chemistry or in a three-dimensional 3D diamond structure, respectively. The sp^2 hybridized orbitals [14, 15] are oriented in 120° angles within the $x-y$ plane (Fig. 2.1a) and are responsible for the so called σ -bonds between carbon atoms. The remaining unhybridized $2p_z$ orbitals (π -bonds) point perpendicular to the $x-y$ plane and allow the π -electron to stand delocalized over the whole crystal lattice.

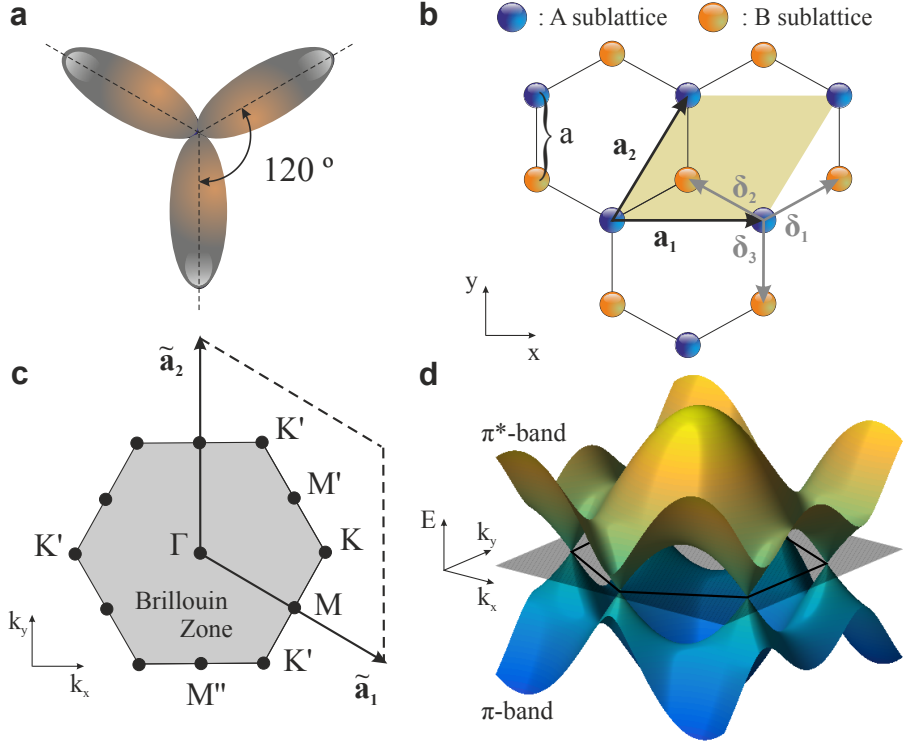


Figure 2.1: **Crystallographic description of graphene.** **a**, Schematic representation of the sp^2 hybridized orbitals. **b**, Honeycomb lattice structure with the vectors δ_1 , δ_2 and δ_3 connecting the nearest-neighbor (NN) carbon atoms, separated by a distance $a = 1.42 \text{ \AA}$. Vectors \mathbf{a}_1 and \mathbf{a}_2 are the basis vectors of a triangular Bravais sublattice (sublattice B in that case) in real space. **c**, Spatial representation of the first Brillouin zone (BZ) (shaded gray region) in reciprocal space ($\mathbf{k}_x, \mathbf{k}_y$). The reciprocal lattice vectors $\tilde{\mathbf{a}}_1, \tilde{\mathbf{a}}_2$ and the nonequivalent symmetry points Γ, M, M', M'', K and K' are also shown. **d**, Graphene's energy dispersion obtained within the tight-binding approximation. The valence band (π -band) touches the conduction band (π^* -band) at the Fermi level (gray shaded plane).

In graphene, two adjacent carbon sites are not equivalent from a crystallographic point of view. Indeed, the nearest-neighbors (NNs) of an A-sublattice site (blue circles in Fig. 2.1b) are found in different directions, defined by the δ_1, δ_2 and δ_3 vectors, as the NNs of a B-sublattice site (yellow circles in Fig. 2.1b). The three NNs vectors defined in real space basis (\mathbf{x}, \mathbf{y}) are given by:

$$\delta_1 = \frac{a}{2}(\sqrt{3}, 1) \quad , \quad \delta_2 = \frac{a}{2}(-\sqrt{3}, 1) \quad \text{and} \quad \delta_3 = -a(0, 1), \quad (2.1)$$

where $a = 0.142 \text{ nm}$ is the Carbon-to-Carbon bond-length, also noted a_{C-C} , and \mathbf{a}_1 and \mathbf{a}_2 the basis vectors in real space of one sublattice (refer to Fig. 2.1b). Thus, the honeycomb structure does not classify as a Bravais lattice but rather a combination of two triangular Bravais lattices (sublattice A and B in Fig. 2.1b). Although one may

consider the graphene lattice as a triangular Bravais lattice with a 2-atoms (A and B) unit cell (yellow shaded rhombus in Fig. 2.1b), it is convenient to describe it as a combination of two triangular sublattices in order to intuitively understand the concept of A-B sublattice symmetry, inversion symmetry, pseudospin and chirality.

As shown in Fig. 2.1b, the triangular Bravais lattice can be defined as a linear combination of:

$$\mathbf{a}_1 = \sqrt{3}a \hat{\mathbf{x}} \quad \text{and} \quad \mathbf{a}_2 = \frac{\sqrt{3}a}{2} (\hat{\mathbf{x}} + \sqrt{3} \hat{\mathbf{y}}). \quad (2.2)$$

Both basis vectors \mathbf{a}_1 and \mathbf{a}_2 have the same length $|\mathbf{a}_1| = |\mathbf{a}_2| = \sqrt{3}a = 0.24 \text{ nm}$. In reciprocal space (Fig. 2.1c), the resulting lattice is defined by the basis vectors:

$$\tilde{\mathbf{a}}_1 = \frac{2\pi}{\sqrt{3}a} (\hat{\mathbf{k}}_x - \frac{\hat{\mathbf{k}}_y}{\sqrt{3}}) \quad \text{and} \quad \tilde{\mathbf{a}}_2 = \frac{4\pi}{3a} \hat{\mathbf{k}}_y. \quad (2.3)$$

The first Brillouin zone (BZ) is the gray shaded hexagonal region in Fig. 2.1c and the Γ -point, placed at the center of the first BZ, represents the location of the long wavelength excitations. Sitting at the corners of the BZ, we find the two inequivalent \mathbf{K} and \mathbf{K}' points, expressed in reciprocal space $(\mathbf{k}_x, \mathbf{k}_y)$ as:

$$\mathbf{K} = \frac{4\pi}{3\sqrt{3}a}(1, 0) \quad \text{and} \quad \mathbf{K}' = -\mathbf{K} = -\frac{4\pi}{3\sqrt{3}a}(1, 0). \quad (2.4)$$

The four remaining corners are equivalent to these \mathbf{K} and \mathbf{K}' points, i.e. they can be defined by translational symmetry of the reciprocal basis vectors. The \mathbf{K} and \mathbf{K}' points play an important role defining the electronic properties of graphene, since the low-energy excitations probed in transport measurements are centered around them. For completeness, we also show the three inequivalent \mathbf{M} , \mathbf{M}' and \mathbf{M}'' points sitting at the middle of the BZ's edges (Fig. 2.1c).

Electronic band structure

As mentioned previously, the hybridization of the $2s$ and $2p$ orbitals into molecular sp^2 orbitals form strong covalent σ -bonds between NNs carbon atoms. On the other hand, the so-called π -bonds are weakly bounded to the neighboring carbon atoms and are thus responsible for the electronic properties at low energies [7]. This section aims to describe these π - and π^* -energy bands within a tight-binding approximation. The dispersion relation of graphene has been originally calculated by R. Wallace [4], we will review in this section most of his major findings.

According to the Bloch wave ansatz, we may write a wave-function for the charge carriers in the graphene lattice as follows:

$$\psi_{\mathbf{k}}(\mathbf{r}) = a_{\mathbf{k}} \psi_{\mathbf{k}}^A(\mathbf{r}) + b_{\mathbf{k}} \psi_{\mathbf{k}}^B(\mathbf{r}), \quad (2.5)$$

where $a_{\mathbf{k}}$ and $b_{\mathbf{k}}$ are complex functions of momentum \mathbf{k} and [16]:

$$\psi_{\mathbf{k}}^i(\mathbf{r}) = \frac{1}{\sqrt{N}} \sum_{\mathbf{R}_j}^N e^{i\mathbf{k} \cdot \mathbf{R}_j} \Phi(\mathbf{r} - \mathbf{R}_j^i), \quad (2.6)$$

where $i = A, B$ depending on the sublattice, N is the number of unit cells considered, \mathbf{k} is the wave-vector in reciprocal space and $\Phi(\mathbf{r})$ are the wave functions of the $2p_z$ orbitals of the carbon atoms. $\mathbf{R}_j = n\mathbf{a}_1 + m\mathbf{a}_2$ specifies the position of the j^{th} unit cell with coordinates $j = (n, m)$ in the real space basis (\mathbf{x}, \mathbf{y}) and \mathbf{R}_j^i the position of the j^{th} $i = A, B$ carbon atoms. For simplicity, we center the unit cell at the location of an A atom (see Fig. 2.1):

$$\mathbf{R}_j^A = \mathbf{R}_j \quad \text{and} \quad \mathbf{R}_j^B = \mathbf{R}_j + \boldsymbol{\delta}_3. \quad (2.7)$$

The wave-function is then expressed as:

$$\psi_{\mathbf{k}}(\mathbf{r}) = \frac{1}{\sqrt{N}} \sum_{\mathbf{R}_j}^N e^{i\mathbf{k}\cdot\mathbf{R}_j} [a_{\mathbf{k}}\Phi(\mathbf{r} - \mathbf{R}_j) + b_{\mathbf{k}}\Phi(\mathbf{r} - \mathbf{R}_j - \boldsymbol{\delta}_3)]. \quad (2.8)$$

It is important to note that the complex functions $a_{\mathbf{k}}$ and $b_{\mathbf{k}}$ denote the amplitude of the ψ wave-function of the π -orbital on the lattice sites A and B, respectively (illustrated by the blue and yellow spheres in Fig. 2.1b). Assuming no orbital overlap between adjacent π -states, the eigenvalue problem in the sublattice subspace reads:

$$\begin{pmatrix} \epsilon & -tf^*(\mathbf{k}) \\ -tf(\mathbf{k}) & \epsilon \end{pmatrix} \begin{pmatrix} a_{\mathbf{k}} \\ b_{\mathbf{k}} \end{pmatrix} = E \begin{pmatrix} a_{\mathbf{k}} \\ b_{\mathbf{k}} \end{pmatrix} \quad \text{with} \quad f(\mathbf{k}) = \sum_{j=1}^3 e^{i\mathbf{k}\cdot\boldsymbol{\delta}_j} \quad (2.9)$$

where just the NNs contributions have been considered and the NN hopping amplitude (hopping between different sublattices) can be defined as [10]:

$$t \equiv \int d^2\mathbf{r} \Phi^*(\mathbf{r}) \Delta V \Phi(\mathbf{r} + \boldsymbol{\delta}_3). \quad (2.10)$$

The "perturbative" term ΔV considers all the potential contributions other than the atomic orbitals. The on-site energies ϵ (diagonal terms of the Hamiltonian) are, as expected, equal $\epsilon_A = \epsilon_B = \epsilon$, since the atoms forming the unit cell are two equivalent carbon atoms. In the reduced sublattice subspace, hopping is just possible from A to B sites or vice-versa (off-diagonal terms in the Hamiltonian from Eq. 2.9). The system has therefore a sublattice symmetry, i.e. chiral symmetry, which allows to calculate the energy spectrum as follows $\varepsilon_{\pm}(\mathbf{k}) = \epsilon \pm |f(\mathbf{k})|$, where the \pm sign represents the positive/negative energy band, i.e. the π - or π^* -band. The function $f(\mathbf{k}) = e^{i\mathbf{k}\cdot\boldsymbol{\delta}_1} + e^{i\mathbf{k}\cdot\boldsymbol{\delta}_2} + e^{i\mathbf{k}\cdot\boldsymbol{\delta}_3}$ is a complex function collecting the sum of the phase factors, where $\boldsymbol{\delta}_1$, $\boldsymbol{\delta}_2$ and $\boldsymbol{\delta}_3$ are the vector position of the three NNs carbon atoms B, relative to an A atom (Fig. 2.1b). Using the (x, y) coordinates defined in Fig. 2.1b, the solution to the Eigenvalue problem leads to the following dispersion relation:

$$\varepsilon_{\pm}(\mathbf{k}) = \pm t \sqrt{1 + 4 \cos\left(\frac{\sqrt{3}k_y a}{2}\right) \cos\left(\frac{k_y a}{2}\right) + 4 \cos^2(k_x a/2)}, \quad (2.11)$$

where, again, the \pm sign defines the bonding and anti-bonding π energy bands. The on-site energies (diagonal terms of the Hamiltonian) are set to zero $\epsilon=0$ and the transfer/hopping integral is valued $t = -3.033 \text{ eV}$ in order to represent this dispersion relation throughout the first Brillouin zone (Fig. 2.1d). As can be observed, the two π - and π^* -bands are degenerate at the K -points, confirming graphene as a zero-gap material. It

is important to note that the lack of a band gap requires the two atoms sitting at the A and B sites to be equivalent. The highest energy separation between valence and conductance bands happens at the Γ -point, with an energy band gap of $6t \approx 18 eV$. Similarly, the band gap at the M -points is $2t \approx 6 eV$. This is an important value, since it limits the maximum theoretical band gap that could be achieved by slicing graphene into one-dimensional (1D) armchair ribbons, i.e. taking a "finite size" route in order to open a band gap (see Section 2.3).

In this section we uncovered the semi-metallic nature and the peculiar band structure of graphene. The linear dispersion relation close the low energy K -points is already visible from the numerical representation of the energy bands (Fig. 2.1). However, in order to mathematically demonstrate the linear $\varepsilon(\mathbf{k})$ relation for the the low-energy excitations, we will need to "expand" the dispersion relation Eq. 2.11 around the K -points. This approximation method, also known as $\mathbf{k}\cdot\mathbf{p}$ perturbation theory [9], will be developed in the next section.

Low-energy electronic structure

It is general to semiconductors that, the low-energy excitations are the ones probed by transport measurements. The relevant part of the band-structure is therefore close to Fermi energy. The so-called $\mathbf{k}\cdot\mathbf{p}$ perturbation theory [9] allows us to conveniently calculate the eigenvalues problem in such a low energy range and thus extract an approximate but meaningful $\varepsilon(\mathbf{k})$ dispersion relation. More importantly, this "expansion around K " method yields a linear mathematical expression of the \mathbf{k} vs. ε relation.

In the following part, we will restrict the analysis to the quantum states in the vicinity of the K -points (see Eq. 2.4). Thereafter, we decompose the wave-vector in momentum space as $\mathbf{k} = \pm\mathbf{K} + \mathbf{q}$, where \mathbf{q} can be understood as a perturbative contribution to \mathbf{K} [4]. Under this approximation, $\mathbf{q} \ll \mathbf{K} \sim 1/a$, i.e. $\mathbf{q}a \ll 1$. For the Taylor series expansion of $f(\mathbf{k})$, we will consider an approximation of $f(\mathbf{k})$ up the second order term, in other words $e^x \approx 1 + x/1! + x^2/2!$. The resulting function reads:

$$\begin{aligned}
f(\mathbf{q})^\pm &\equiv f(\mathbf{k})|_{\mathbf{k}=\pm\mathbf{K}+\mathbf{q}} = \sum_{j=1}^3 e^{\pm i\mathbf{K}\cdot\delta_j} e^{i\mathbf{q}\cdot\delta_j} \\
&\approx e^{\pm i2\pi/3} \left[1 + i\mathbf{q}\cdot\delta_1 - \frac{1}{2}(\mathbf{q}\cdot\delta_1)^2 \right] \\
&\quad + e^{\mp i2\pi/3} \left[1 + i\mathbf{q}\cdot\delta_2 - \frac{1}{2}(\mathbf{q}\cdot\delta_2)^2 \right] \\
&\quad + \left[1 + i\mathbf{q}\cdot\delta_3 - \frac{1}{2}(\mathbf{q}\cdot\delta_3)^2 \right] \\
&= f(\mathbf{q})_{(0)}^\pm + f(\mathbf{q})_{(1)}^\pm + f(\mathbf{q})_{(2)}^\pm,
\end{aligned} \tag{2.12}$$

where $f(\mathbf{q})_{(0)}^\pm$, $f(\mathbf{q})_{(1)}^\pm$ and $f(\mathbf{q})_{(2)}^\pm$ are the zero, first and second order expansion terms. From the position of the K -points in reciprocal space we have $f(\mathbf{q})_{(0)}^\pm = f(\pm\mathbf{K})^\pm = 0$.

The first order term will contribute as:

$$\begin{aligned} f(\mathbf{q})_{(1)}^{\pm} &= i\frac{a}{2} \left[(\sqrt{3}q_x + q_y) e^{\pm i2\pi/3} - (\sqrt{3}q_x - q_y) e^{\mp i2\pi/3} \right] - iq_y a \\ &= \mp \frac{3a}{2} (q_x \pm iq_y). \end{aligned} \quad (2.13)$$

To a first order approximation, we will neglect the second-order term of the Taylor expansion since the first term is already sufficient to obtain a linear expression for the dispersion relation. The effective subspace Hamiltonian up to the first-order term is now centered at the K-points and, with the calculated off-diagonal terms $f(\mathbf{q})^{\pm}$, leads to:

$$h_K(\mathbf{q}) = \frac{3at}{2} \begin{pmatrix} 0 & q_x - iq_y \\ q_x + iq_y & 0 \end{pmatrix}, \quad h_{K'}(\mathbf{q}) = \frac{3at}{2} \begin{pmatrix} 0 & -q_x - iq_y \\ -q_x + iq_y & 0 \end{pmatrix} \quad (2.14)$$

where the Eigenvalues solution is as follows:

$$\varepsilon_{\pm}(\mathbf{q}) = \pm \frac{3a|t|}{2} |\mathbf{q}|. \quad (2.15)$$

The group velocity is usually defined as $\mathbf{v} = \hbar^{-1} \partial \varepsilon / \partial \mathbf{k}$. We can then re-write the obtained dispersion relation:

$$, \varepsilon_{\pm}(\mathbf{q}) = \pm \hbar v_F |\mathbf{q}|, \quad (2.16)$$

where $v_F = 3a|t|/2\hbar$. After replacing the t and a parameters by $|t| = 2.9 \text{ eV}$ and $a = 1.42 \text{ \AA}$, we obtain an analytical expression for the Fermi velocity $v_F \approx 10^6 \text{ m/s}$, which is roughly 300 times lower than the speed of light $c = 3.10^8 \text{ m/s}$. As observed, both subspace hamiltonians $h_K(\mathbf{q})$ and $h_{K'}(\mathbf{q})$ yield the same eigenvalues. From an energy point of view the bands at the K - and K' -points are indistinguishable, i.e. degenerate.

In this section, we mathematically demonstrate the linear dependence of ε_{\pm} as a function of momentum $|\mathbf{q}|$. This linear energy dispersion relation in the vicinity of the K -points plays an important role in defining the electronic properties of graphene.

Density of states

The density of states (DOS) of an electronic system is the number of available states per energy interval dE , per unit volume (or unit area for 2D materials) [17]. To understand the derivation of the DOS, we first consider the area of a single state in reciprocal space $(2\pi)^2/A$, with A being the area in real space. The number of states dN inside the gray-shaded ring of radius k_F and width dk (Fig. 2.2) can be estimated as $dN = (2\pi k_F A)/(4\pi^2) dk$. Through the definition of DOS [17] and the linear energy dispersion of graphene (see Eq. 2.16), we reach the following expression:

$$DOS = g_s g_v \frac{1}{A} \frac{\partial N}{\partial E} = \frac{2E}{\pi \hbar^2 v_F^2}, \quad (2.17)$$

where the $g_s = 2$ and $g_v = 2$ factors account for the spin and valley degeneracies.

The DOS of graphene appears to be linear as a function of energy (Fig. 2.2b), as apposed to most of the 2DEGs for which the DOS is constant [17]. This result is directly observed in transport measurements [18] and it represents one of the characteristic traits of graphene.

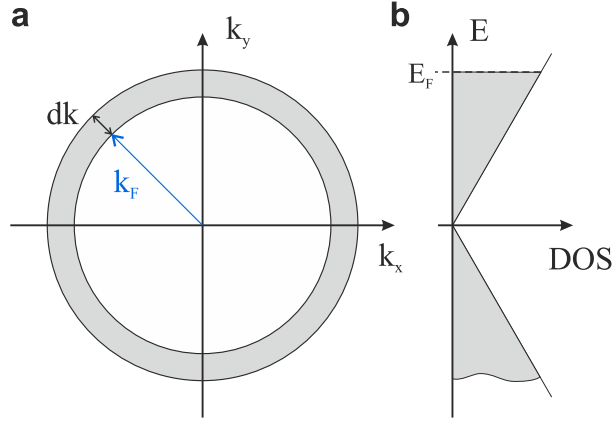


Figure 2.2: **Density of states and transport characteristics.** **a**, Reciprocal space representation of the ring of radius k_F and width dk that includes dN number of states. **b**, Linear density of state characteristic of graphene.

High-energy electronic structure

Although the fundamental principles of graphene have been already exposed within the first-order approximation (Eq. 2.14), it is useful to review the influence of the next nearest-neighbor (NNNs) contributions and the second-order terms of the expanded dispersion relation (Eq. 2.12). As expected, the higher order corrections of the electronic bands (Eq. 2.12) will become relevant at higher energies. In fact, in electronic transport measurements, where energies are usually below $\sim 0.2 eV$, the linear expression of the dispersion relation (Eq. 2.16) already describes the experimental observations [18] pretty accurately.

The corrections within this section will include the second order contributions of the expanded $f(\mathbf{k})$, noted $f(\mathbf{q})_{(2)}^{\pm}$ in Eq. 2.12 and the NNNs hopping term t' . The spectrum around the K -points is then defined as [19]:

$$\varepsilon_{\pm}(\mathbf{q}) \approx 3t' \pm v_F|\mathbf{q}| - \left(\frac{9t'a^2}{4} \pm \frac{3ta^2}{8} \sin(3\theta_q) \right) |\mathbf{q}|^2, \quad (2.18)$$

where $\theta_q = \arctan(q_x/q_y)$ is the angle between the x - and y -component of the vector momentum \mathbf{q} in reciprocal space. As can be deduced from the analytical expression in Eq. 2.18, the NNNs term t' breaks the electron-hole symmetry of the electronic bands (refer to Fig.3 from [19]). Another important aspect of this energy dispersion relation happens at higher energies ($\gtrsim 1 eV$), where the contribution of $f(\mathbf{q})_{(2)}^{\pm}$ (Eq. 2.13) forms the so-called trigonal warping effect [1]. This Trigonal warping phenomenon is recognized by an anisotropy in the energy dispersion around the K -points (Fig. 2.3). This anisotropy stems from the $\sin(3\theta_q)$ term in Eq. 2.18 and reflects the underlying symmetry of the graphene lattice. In Fig. 2.3 can be seen the dispersion relation (panel a) as well as the contour maps (panel b) in order to visualize this effect.

Up to this section, we accurately described the band structure of graphene and highlight the differences between the K - and K' -points. Nevertheless, to understand some

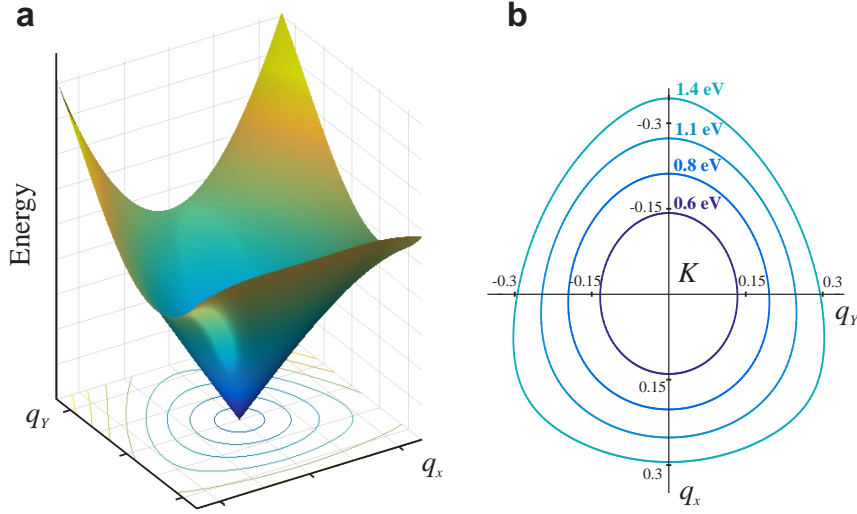


Figure 2.3: **Trigonal warping of the electronic spectrum.** **a**, Representation of the upper π^* -band from the dispersion relation in Eq. 2.18. The band touches the Fermi energy $E_F = 0$ at the K -points. **b**, Countour plot of the π^* -band from panel a at energies $\varepsilon = 0.6, 0.8, 1.1$ and 1.4 eV . The color code is shared with panel a.

of the peculiar transport characteristics of graphene, e.g. the lack of backscattering, it is helpful to introduce the Dirac Hamiltonian notation.

Dirac notation

Eventhough the charge carriers in graphene travel at velocities 300 times lower than the speed of light, their behavior mimics the one of relativistic particles (see Eq. 2.16). Hence, it appeared natural to adopt the Dirac notation to describe the graphene Hamiltonian [20]:

$$\begin{aligned}
 h_\xi(\mathbf{q}) &= \hbar v_F \begin{pmatrix} 0 & \xi q_x - i q_y \\ \xi q_x + i q_y & 0 \end{pmatrix} = \hbar v_F (q_x \xi \sigma_x + q_y \sigma_y) \\
 &= \xi \hbar v_F (q_x \sigma_x + q_y \xi \sigma_y),
 \end{aligned} \tag{2.19}$$

where σ_x and σ_y are the Pauli matrices:

$$\sigma_x = \begin{pmatrix} 0 & 1 \\ 1 & 0 \end{pmatrix} \quad \text{and} \quad \sigma_y = \begin{pmatrix} 0 & -i \\ i & 0 \end{pmatrix}. \tag{2.20}$$

In Eq. 2.19, the effective subspace Hamiltonians at the K and K' -points (Eq. 2.14) are now described by a single expression $h_\xi(\mathbf{q})$ (Eq. 2.19) where we introduced the *valley isospin* $\xi = \pm$ term. The K' - and K -points are now indicated by $\xi = +$ and $\xi = -$, respectively. The subspace eigenfunctions at the K and K' -point are called Spinors within the Dirac notation and can be described by a single expression [19]:

$$\psi_{\mathbf{q}, \xi} = \begin{pmatrix} a_{\mathbf{q}, \xi}^A \\ b_{\mathbf{q}, \xi}^B \end{pmatrix} = \frac{1}{\sqrt{2}} \begin{pmatrix} \lambda e^{-i\xi\theta_{\mathbf{q}}/2} \\ e^{i\xi\theta_{\mathbf{q}}/2} \end{pmatrix}. \tag{2.21}$$

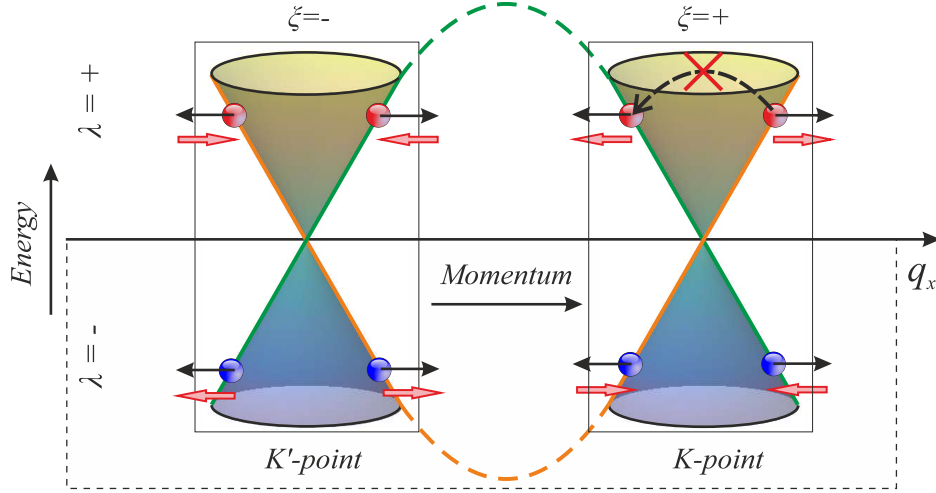


Figure 2.4: **Pseudospin and back-scattering in graphene.** The *pseudospin* states $|\uparrow\rangle+|\downarrow\rangle$ (bonding-symmetric) and $|\uparrow\rangle+|\uparrow\rangle$ (antibonding-antisymmetric) are represented in orange and green colors. The *pseudospin* degree of freedom protects the carriers from flipping their momentum (back-scattering) within a Dirac cone. The quasi-particle index λ and the valley isospin ξ are also shown. The charge carriers wave-vector and the projection of the pseudo-spin vector on the q_x -axis are denoted by solid black and red arrows, respectively.

Here $\lambda = \pm$ is the quasi-particle index and it represents the π and π^* bands, and θ_q is the angle between the wave-vector \mathbf{q} and the q_x -axis (Fig. 2.4). In other words, $\theta_q = \arctan(q_y/q_x)$. A very important implication of this eigenfunction expression is its dependence with the direction of the momentum. For a chosen direction of propagation, e.g. along the q_x -axis direction, the wave-function components $(a_{q,\xi}^A, a_{q,\xi}^B)$ depend on the direction of propagation ($\theta_q = 0$ or $\theta_q = \pi$, for the forward and backward directions, respectively). This situation is depicted in Fig. 2.3, where the *pseudo-spin* vector $(a_{q,\xi}^A, a_{q,\xi}^B)$ can be described by $(1,1)$ or $(-1,1)$, after substituting λ, ξ and $\theta_q = 0, \pi$ in Eq. 2.21. In analogy with the real spin degree of freedom of a relativistic particle, where the spin-up $|\uparrow\rangle$ and spin-down $|\downarrow\rangle$ states are noted $(1,0)$ and $(0,1)$, we can understand the combination $(1,1)$ as a *pseudo-spin* up $|\uparrow\rangle +$ down $|\downarrow\rangle$ combination or vice-versa, and $(-1,1)$ as $|\uparrow\rangle + |\uparrow\rangle$ or $|\downarrow\rangle + |\downarrow\rangle$ of the two electrons per unit cells.

These results have strong implications on transport, since the charge carriers cannot back-scatter (flip their momentum wave-vector \mathbf{q}) within a Dirac cone (Fig. 2.3). Charge carriers are therefore not affected by long-range scattering processes, which is the main reason for having higher electron/hole mobilities compared to bi-layer graphene. Short-range scatterers though, can result in back-scattering by giving charge carriers enough momentum to shift from the K to the K' cone, or vice versa.

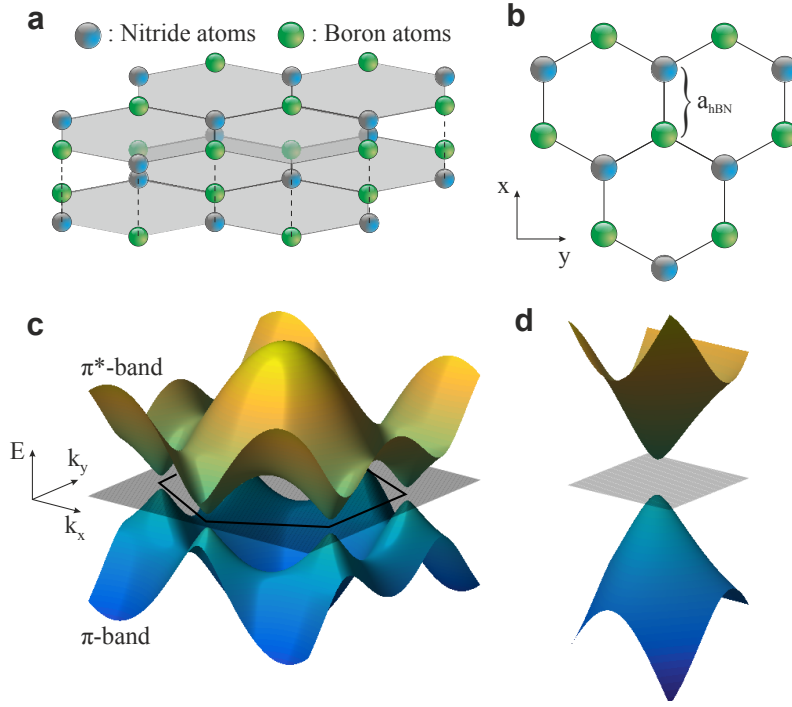


Figure 2.5: **Crystallographic description of hBN.** **a**, Stacking structure of a multi-layer hBN. The boron (B) and nitride (N) atoms are represented by green and blue circles, respectively. **b**, The crystal structure of a single layer hBN is equivalent to the one of graphene, with the B and N atoms sitting at the A and B sublattices sites (Fig. 2.1b). **c**, Band structure of a single layer hBN (also called 'gapped graphene') under a tight-binding approximation. The energy ε is represented as a function of momentum (k_x, k_y) in the first Brillouin zone. The energy gap 2Δ was set to $0.15t$. **d**, Zoom in of the low energy massive Dirac cones from panel c.

Hexagonal boron nitride as a suitable substrate for graphene

Hexagonal boron nitride (hBN) is conceptually very similar to graphene. Its multi-layered crystal structure (Fig. 2.5a) also shows an hexagonal arrangement of its boron (B) and nitride (N) elements. As shown in Fig. 2.5b for the single layer configuration, every B and N atom occupy a sublattice site A and B, respectively. For the 3D allotrope (Fig. 2.5a), every element of a hBN layer sits perfectly on top/bottom of the element of the upper/lower layer. The B and N atoms are located such that every B atom sits on top of a N element, and vice-versa (Fig. 2.5a). The bond length between two NNs elements is $a_{hBN} = 1.44\text{\AA}$ [21, 22], this value is only 1.7% larger than the carbon spacing a_{C-C} in graphene.

To calculate the band structure of hBN we can start from the tight-binding graphene Hamiltonian of Eq. 2.9. We should take into account that the unit cell is now defined by a boron and a nitride atom instead of two identical carbon atoms. The on-site energies are therefore not equal $\varepsilon_A \neq \varepsilon_B \neq 0$ [11]. The diagonal ε_B and ε_A terms are thus added

to the Hamiltonian Eq. 2.9. Assuming symmetry conditions $\varepsilon_A = -\varepsilon_B = \Delta > 0$, the eigenvalues become $\varepsilon(\mathbf{k}) = \sqrt{\Delta^2 + |f(\mathbf{k})|^2}$ and the low energy Hamiltonian:

$$H_\xi = v_F p_x \xi \sigma_x + v_F p_y \sigma_y + m v_F^2, \quad (2.22)$$

with $m v_F^2 \equiv \Delta$. The energy spectrum reads $\varepsilon(\mathbf{k}) = \sqrt{(m v_F^2)^2 + (v_F k)^2}$. It is then clear, that the σ_z term induces the Dirac fermions to acquire a mass $m \equiv \Delta/v_F^2$ and the hBN an energy band gap. As a side note, hBN appears as a perfect example of A-B sublattice breaking phenomenon that, in graphene, would induce an energy gap [2, 3, 12]. As stated, hBN is a semiconducting material with a band gap of 5.97 eV [23]. The thin hBN flakes are therefore not visible in the visible spectra although the hBN flakes used to support graphene are usually ~ 20 to 80 nm thick, making them perfectly visible in the optical microscope (see Fig. 2.5a).

The highly insulating behavior together with an atomically flat surface, free of dangling bonds, make hBN a perfect insulating material for graphene [13, 24, 25]. In the following section we will demonstrate the impact on the electronic transport characteristics of graphene samples encapsulated in between a top- and a bottom-layer of hBN (see Section 5.1 and Section 6.1).

2.2 Graphene in strong magnetic fields

Landau level formation

Under a perpendicular and uniform magnetic field B , the cone-like band structure of graphene (Fig. 2.1) condense into an arrangement of Landau levels (Fig. 2.6). The Landau level spectrum can be derived by replacing the momentum \mathbf{q} by $\mathbf{q}' = \mathbf{q} + e\mathbf{A}(\mathbf{r})$ in Eq. 2.19, where $\mathbf{A}(\mathbf{r})$ is the vector potential that generates the magnetic field $\mathbf{B} = \nabla \times \mathbf{A}(\mathbf{r})$. The resulting Hamiltonian reads [19]:

$$h(\mathbf{q}) = \hbar v_F \boldsymbol{\sigma}(\mathbf{q} + e\mathbf{A}(\mathbf{r})), \quad (2.23)$$

where the matrix notation $\boldsymbol{\sigma} = (\sigma_x; \sigma_y)$ [19] has been introduced in Eq. 2.19. Solving the energy eigenvalues [19, 26] we obtain:

$$\varepsilon_\pm(N) = \pm \hbar \omega_c = \pm v_F \sqrt{2e\hbar B|N|} \quad \text{with } N \in \mathbb{N}, \quad (2.24)$$

where $\omega_c = \sqrt{2N} v_F / l_B$ is the cyclotron frequency and $l_B = \sqrt{\hbar / eB}$ the magnetic length. The \sqrt{B} dependence of the Landau Levels' energy $\varepsilon(N)$ is shown in Fig. 2.6c and the complete DOS appear in Fig. 2.6a and b. The fact that l_B , and therefore $\varepsilon(N)$, scales like \sqrt{B} is specific to graphene and it clearly diverges from non-relativistic 2DEGs, where l_B scales linearly as a function of magnetic field. These results have strong experimental implications since, for the same value of magnetic field, e.g $B = 10$ T, the energy difference $\varepsilon(1) - \varepsilon(0)$ between the two first LLs is in graphene two orders of magnitude higher than for 2DEGs [27]. The most remarkable feature of graphene dispersion relation at finite B -fields is the existence of a zero-energy Landau level (LL_0), which is related to the parity anomaly of the 2D Dirac equation [11]. This zero Landau

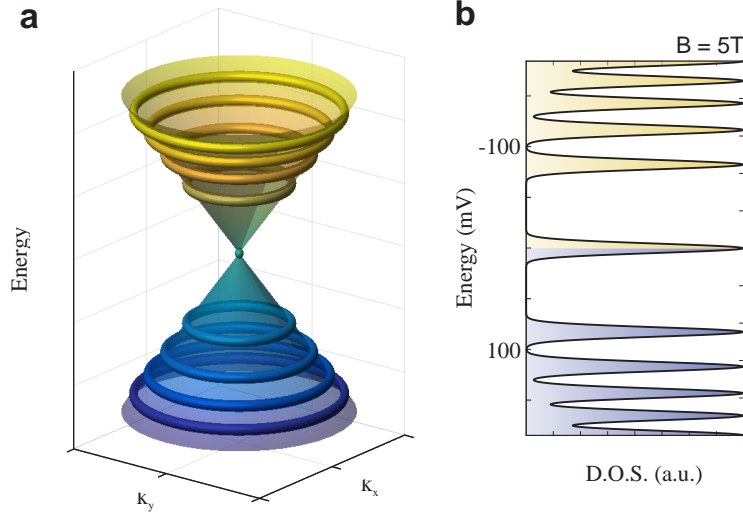


Figure 2.6: **Band structure of massless Dirac fermions at finite B -fields.** **a**, The linear dispersion relation of graphene (shaded cône) condense into relativistic Landau levels (colored torus) of energy $E_\lambda(N) = \lambda v_F \sqrt{2e\hbar B |N|}$. **b**, The corresponding density of states (disorder broadened) shows the \sqrt{B} -dependence of the Landau levels (LLs).

level LL_0 separates the electron from the hole states (Fig. 2.4). We further note that, every landau level in graphene is four-fold degenerate owing to the contribution of the K and K' valleys.

Quantum Hall effect

Under finite magnetic fields, the magneto-transport fingerprints of any 2D system evolves from the classical Hall effect to the so-called quantum Hall effect [28]. At relatively high values of magnetic field and low temperatures, the Hall resistance develops into well defined plateaus at specific values of resistance $R_{XY} = nh/(e^2)$, with $n \in \mathbb{N}$ (Fig. 2.7). Simultaneously, the longitudinal resistance drops to zero, showing an oscillating behavior as a function of B -field, known as Shubnikov–de Haas oscillations (Fig. 2.7). Magneto-transport measurements have been traditionally carried on Hall bar devices (inset of Fig. 2.7). A constant current I_x is applied between contacts 1 and 4 while a longitudinal V_{xx} and a transversal V_{xy} voltages are measured across and along the samples, respectively. The essential longitudinal and transversal voltages are often given as resistivities and/or conductivities:

$$\rho_{xx} = R_{xx} \frac{W}{L} = \frac{V_{xx} W}{I_c L} \quad \text{and} \quad \rho_{xy} = -R_{xy} = \frac{V_{xy}}{I_c}, \quad (2.25)$$

where L and W are the length and width of the Hall bar devices (inset of Fig. 2.7). The inversion from resistivity (ρ) to conductivity (σ) is given by [29]:

$$\begin{pmatrix} \sigma_{xx} & \sigma_{xy} \\ -\sigma_{xy} & \sigma_{xx} \end{pmatrix} = \frac{1}{\rho_{xx}^2 + \rho_{xy}^2} \begin{pmatrix} \rho_{xx} & \rho_{xy} \\ -\rho_{xy} & \rho_{xx} \end{pmatrix}, \quad (2.26)$$

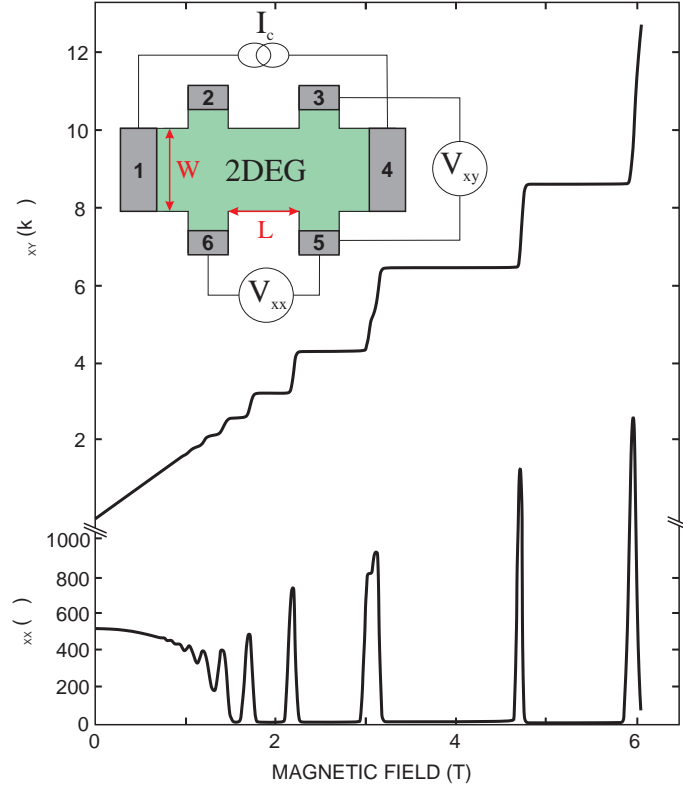


Figure 2.7: **Transition from Hall to quantum Hall effect.** The classical magneto-resistance trace at low magnetic fields develops into quantum Hall effect at high values of B -field ($B > 1 T$) (Figure re-plotted from [28]). The inset shows the typical Hall bar geometry and connections to measure the Hall resistance $R_{xy} = V_{xy}/I_c$ and the longitudinal resistance $R_{xx} = V_{xx}/I_c$.

or vice-versa, from conductivity (σ) to resistivity (ρ) [29]:

$$\begin{pmatrix} \rho_{xx} & \rho_{xy} \\ -\rho_{xy} & \rho_{xx} \end{pmatrix} = \frac{1}{\sigma_{xx}^2 + \sigma_{xy}^2} \begin{pmatrix} \sigma_{xx} & \sigma_{xy} \\ -\sigma_{xy} & \sigma_{xx} \end{pmatrix}. \quad (2.27)$$

With the calculated values of resistivity, we can define the ohm's law (for a 2DDEG) by the resistivity tensor ρ :

$$\vec{E} = \rho \vec{j} \Leftrightarrow \begin{pmatrix} E_x \\ E_y \end{pmatrix} = \begin{pmatrix} \rho_{xx} & \rho_{xy} \\ \rho_{yx} & \rho_{xx} \end{pmatrix} \begin{pmatrix} j_x \\ j_y \end{pmatrix} \Leftrightarrow \begin{cases} E_x = \rho_{xx} j_x + \rho_{xy} j_y \\ E_y = \rho_{yx} j_x + \rho_{xx} j_y \end{cases} \quad (2.28)$$

Alternatively, the current density \vec{j} can be expressed by the conductivity vector σ as follows:

$$\vec{j} = \sigma \vec{E} \Leftrightarrow \begin{pmatrix} j_x \\ j_y \end{pmatrix} = \begin{pmatrix} \sigma_{xx} & \sigma_{xy} \\ \sigma_{yx} & \sigma_{xx} \end{pmatrix} \begin{pmatrix} E_x \\ E_y \end{pmatrix} \Leftrightarrow \begin{cases} j_x = \sigma_{xx} E_x + \sigma_{xy} E_y \\ j_y = \sigma_{yx} E_x + \sigma_{xx} E_y \end{cases} \quad (2.29)$$

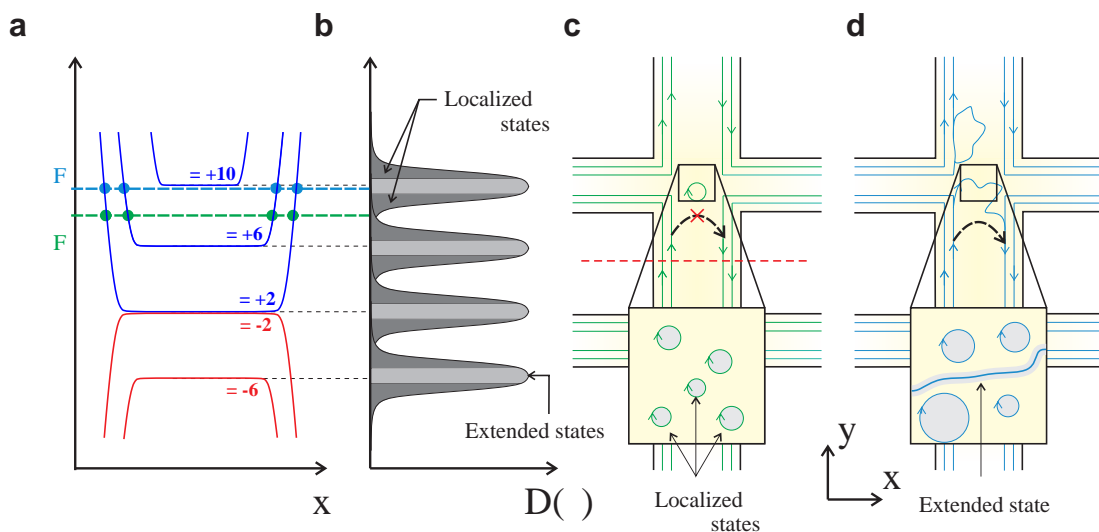


Figure 2.8: **Conduction model under the Quantum Hall regime.** **a**, Cross-sectional view (red dashed line in panel **c**) of the energy spectrum. **b**, Broadened Landau levels. The states whose Fermi level ε_F lies within the light gray region are considered extended. Otherwise, the states remain localized (dark gray region) **c**, Representation of the localized states within the sample surface. A percolation path to counter-propagating edges states is non-probable. **d**, The extended states can link counter-propagating edges states.

The quantum Hall effect is nothing else than the experimental manifestation of the Landau quantization introduced in Section 2.2. Indeed, the quantized steps in resistivity (Fig. 2.7) or conductivity, can be expressed as a function of the Landau levels N (Section 2.2) or, alternatively, as a function of the filling factor ν . The conductivity is then defined as:

$$\sigma_{xy} = \pm g_s g_v \left(N - \frac{1}{2}\right) \frac{e^2}{h} = \nu \frac{e^2}{h}, \quad (2.30)$$

where $g_s = 2$ and $g_v = 2$ are the spin and valley degeneracies and the filling factor ν can be understood as a the number of occupied states $\nu = \pm 4(N - 1/2)$. This dimensionless parameter varies as function of B -field and charge carrier density. In fact, ν strictly defines the number of charge carriers per flux quanta in a specific material:

$$\nu = \frac{n}{n_B} = \frac{hn}{eB}, \quad (2.31)$$

where n is the charge carrier density and $n_B = B/\phi_0 = eB/h$ is nothing more than the magnetic field in units of flux quanta $\Phi_0 = h/e$.

Bulk and edge model under QHE

Within the bulk and at finite B -fields, the charge carriers are expected to cycle in cyclotron orbits and therefore not contribute to the electron transport. However, the presence of disorder not only transforms the landau levels into a collection of broadened

Gaussian distributions (Fig. 2.8b) but also converts the transport into extended or localized states [30]. Impurities, defects and inhomogeneities that could contribute to the random potential fluctuations, lead to the broadening of the DOS around each of the Landau levels. The extended states (Fig. 2.8d) have a finite amplitude within a vast extension inside the bulk, whereas the localized states (Fig. 2.8c) are confined into small regions [31]. Any variation in Fermi energy ε_F or magnetic field modifies the Landau level occupancy (Fig. 2.8b) and thus the transport model inside the Bulk (Fig. 2.8c and d). For Fermi energies close the Landau level energies $\varepsilon_{\pm}(N)$ (dashed blue line in Fig. 2.8a), extended states form within the bulk. In that situation, percolating paths are expected to exist between the two boundaries of the sample (marked in light blue in Fig. 2.8d). Contrary, charge carriers which energies lies in the tails of a Landau level (dashed green line in Fig. 2.8a) describe closed trajectories around closed equipotential lines (marked green in Fig. 2.8c). This states are hence localized, they are not able to connect both boundaries and therefore to not modify the net current.

The edge states picture, elaborated by Marcus Büttiker [32–34], follows the Landauer approach in which conduction is viewed in terms of transmission and reflection of charge carriers. In the quantum Hall (QH) regime, one dimensional conductance channels, also called edge channels, are formed along the edges of a 2DEGs (Fig. 2.8c and d). These edge channels/states are associated to the skipping orbit motion of the charge carriers under magnetic fields. The edge states are expected to form at the edges of the 2DEGs, where the Landau levels bend-up due to confinement of the potential (Fig. 2.8a). At the intersections with the Fermi level (Fig. 2.8a) arise the conductive states. The spatial separation between counter-propagating conductive channels, due to the insulating bulk, suppresses the back-scattering of the charge carriers. This model, develop by B. I. Halperin [35] M. Büttiker [32], is a single particle picture that does not include electron-electron interactions or macroscopic electrostatic effects. S. Komiyama et. al proposed in [36] how to include electrostatic first order effects in the edge state picture. In graphene, D. A. Abanin developpt a conformal invariant approach [37] to account for the shape-dependent potential distributions in the quantum Hall regime.

2.3 Description of graphene ribbons

From the theoretical description introduced in previous chapter, we know that graphene has a linear density of states with no energy gap [18]. A band-gap, the defining feature of all semiconducting materials, lies at the core of every electronic logic-device since it allows the discrete control between a conductive and an insulating state. Even so, graphene offers other remarkable characteristics such as an unprecedented electron mobility at room temperature that makes it appealing for electronics [38, 39]. Thus, there has been quite an effort to overcome the lack of a band-gap since its discovery in 2004 [18].

In all materials, the band structure of the macroscopic crystal is modified as soon its dimensions approach the length-scale of the charge carriers' wavelength (λ_F). In a quasi-one dimensional (1D) system, the continuous band structure is transformed into

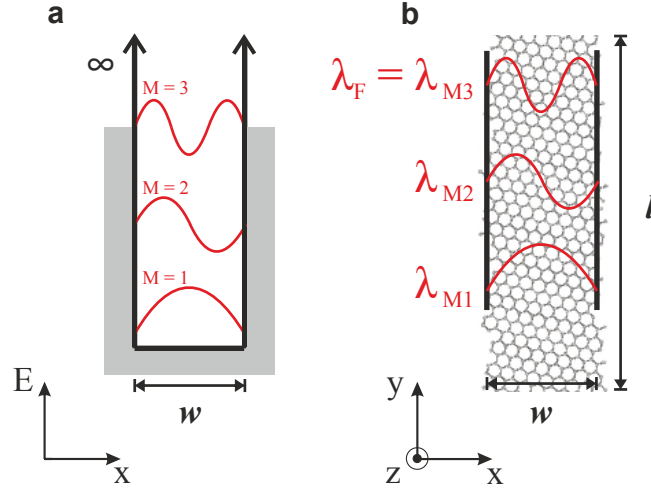


Figure 2.9: **"Particle in a box" problem.** **a** An infinite potential barrier mimics the effect of the infinite electrostatic potential at the edges of a 1D system. The red traces represent the electron's wave-functions for the first three states ($M = 1, 2$ and 3). **b** Schematic representation for the confinement quantization in a quasi-1D graphene ribbon. The wavelengths of the allowed subbands or modes (M), at a certain Fermi energy, appear in red (note that, all wavelengths $\lambda_M > \lambda_F$ fulfilling boundary conditions will participate to transport).

a collection of discrete energy subbands, traditionally referred in transport experiments as "modes" (M) [40]. The schematics shown in Fig. 2.9a illustrate the "particle in a box" situation applied to a one-dimensional (1D) material (Fig. 2.9b), where the length is infinite compared to the width ($l \gg w$).

The electron waves, confined in the quasi-1D quantum well, become standing waves fulfilling periodic boundary conditions. The perpendicular (to the 1D-material axis) wavelength and momentum for a specific mode ($\lambda_{\perp, M}$ and $k_{\perp, M}$, respectively) are defined as $\lambda_{\perp, M} = \frac{2w}{M}$ and $k_{\perp, M} = \frac{M\pi}{w}$. An estimation of the energy subband spacing (ΔE) and the energy band-gap (ΔE_{con}) are given by $\Delta E_{con} = 2 \Delta E = 2 \hbar v_F \Delta k = 2 \hbar v_F \pi / w$. Numerically, a $w = 45 \text{ nm}$ wide 1D channel would lead to an estimated energy spacing of $\Delta E \approx 45 \text{ meV}$ and an energy gap of $\Delta E_{con} \approx 90 \text{ meV}$. To a first order approximation and neglecting any contribution from the crystallographic orientation of the edges, the same analysis is valid for 1D slices of graphene, known in literature as graphene "constrictions" or "nanoribbons". When adding the orientation of the graphene lattice and thus the configuration of the edges into the problem, one finds strong similarities with the case of carbon nanotubes (CNTs). CNTs can be regarded as rolled-up stripes of graphene, hence it is intuitive to think that the underlying physics is common to both. In CNTs, the energy gap or position of the subbands depend on the diameter and the orientation of the nanotube [41]. In graphene ribbons, and for the ideal situation of no disorder and perfect edges, the dispersion relation shows no energy band-gap for zigzag ribbons and either a metallic or semiconducting behavior for armchair. To understand this statement, we first need to define the width of a N-armchair/N-zigzag graphene nanorib-

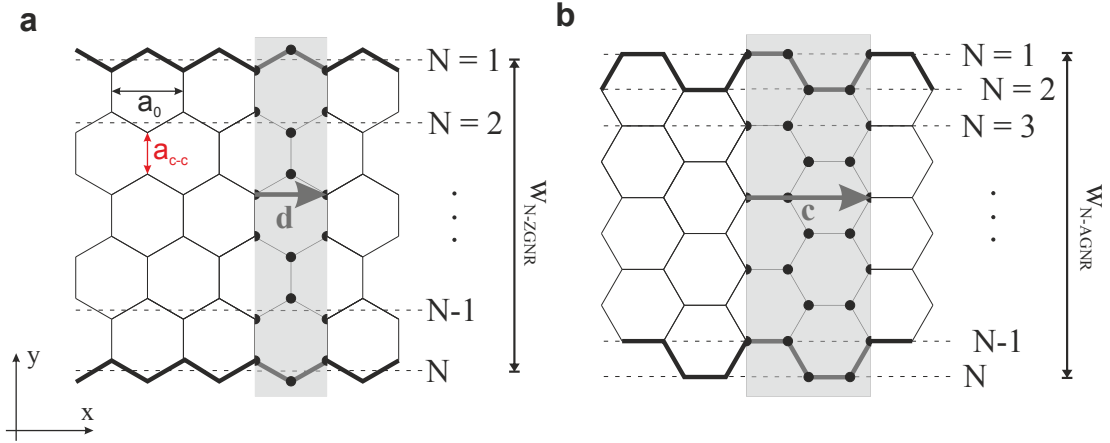


Figure 2.10: **Real-space crystallographic description.** Crystal structure of zigzag (a) and armchair (b) ribbons. In each case we indicate the number of lines/dimers (N) for zigzag/armchair ribbons and the unit cell (emphasized in gray). The ideal lattice constants of the ribbons are $|\mathbf{d}| = a_0 = \sqrt{3} a_{C-C}$ and $|\mathbf{c}| = \sqrt{3} a_0$.

bon (w_{N-AGNR}/w_{N-ZGNR}), with N being the number of dimers/lines (Fig. 2.10): $w_{N-AGNR} = \frac{1}{2}(N-1)a_0$ and $w_{N-ZGNR} = \frac{\sqrt{3}}{2}(N-1)a_0$, with $a_0 = \sqrt{3}a_{C-C}$ and $a_{C-C} = 1,42 \text{ \AA}$ (distance between carbon atoms). The real space crystal structure of a zigzag and armchair ribbon as function of N is shown in Fig. 2.10. The unit vector \mathbf{c} (\mathbf{d}) denotes the translational vector, or lattice constant, of an armchair (zigzag) ribbon in real space (Fig. 2.10 and Fig. 2.11a).

In the zone-folding approximation method, it is useful to understand the unit-cell of a N -AGNR (N -ZGNR) as a repetition of the zero-dimensional (0D) unit cell defined by \mathbf{c} and \mathbf{d} (black dashed rectangle in Fig. 2.11a). In reciprocal space, the shorter (longer) side of the rectangular Brillouin zone (BZ) (black dashed lines in Fig. 2.11b) are defined by the corresponding \mathbf{c}^* (\mathbf{d}^*) wave-vector which describe the one-dimensional BZ of armchair (zigzag) ribbons. The global band structure of graphene ribbons having armchair (zigzag) edges is then predicted by projecting the 2D graphene BZ onto the corresponding axis \mathbf{c}^* (\mathbf{d}^*) using the zone-folding technique (Fig. 2.11b). The linear dispersion relation originating at the \mathbf{K} - and \mathbf{K}' -points are expected to appear (after folding) at around $k = 0$ ($k = 2\pi/3$) for armchair (zigzag) ribbons. All ZGNR are then metallic since their allowed k_{\perp} in reciprocal space, represented as slices parallel to the ribbon axis, will undeniably intersect the \mathbf{K} -points at $k = 0$. Note that the $k = 0$ represents the first harmonic of the ground state fulfilling boundary conditions. In Fig. 2.11b, we represent the four ground states ($N = 1, 2, 3$ and 4) of the N -AGNR and N -ZGNR.

More complex tight-binding and Dirac equation based calculations [43] are in good agreement with the aforementioned description. Fig. 2.11c shows tight-binding simulations of armchair and zigzag ribbons as function of the number of dimers/lines respectively. Simulations have been performed with Kwant, a Python package for numerical

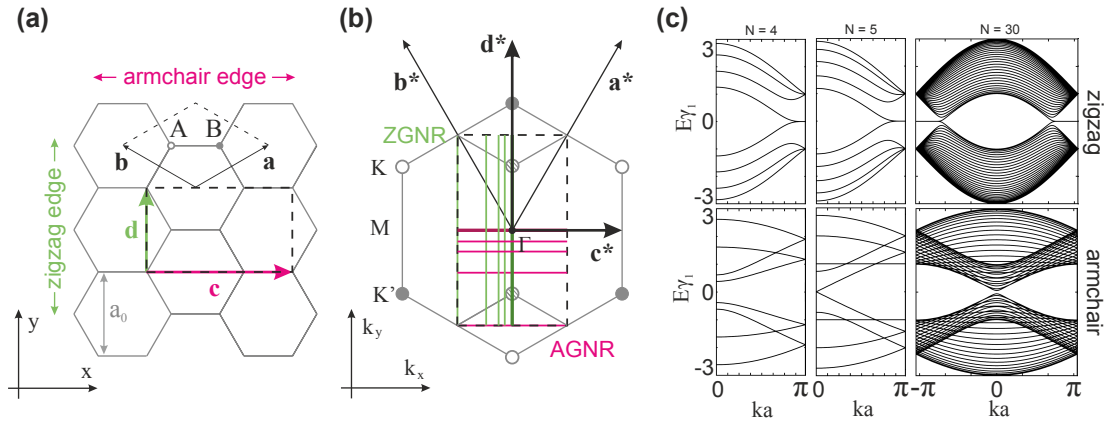


Figure 2.11: **Zone-Folding approximation.** Representation of the 0D unit cell (dashed black lines) in real (a) and reciprocal space (b). The unit cell of 2D graphene is also plotted for comparison in (a). The vectors \mathbf{c} and \mathbf{c}^* (\mathbf{d} and \mathbf{d}^*) relate to armchair (zigzag) configurations in real (a) and reciprocal (b) space, respectively. (b) The four ground states ($N = 1, 2, 3$ and 4) of the N -armchair (N -AGNR) and N -zigzag (N -ZGNR) ribbons are plotted in red and green, respectively. The zone folded first Brillouin zone of graphene leads to two double degenerate Dirac cones at the position of null momentum. (c) Tight-binding model of the energy π -band structure of armchair and zigzag ribbons with various widths, $N = 4, 5$ and 30 (Calculations done in KWANT [42]).

quantum transport calculations based on a tight-binding approach [42]. As expected, the zigzag configuration shows a metallic behavior for any given width since the \mathbf{K} -points are already crossed at zero momentum (Fig. 2.11b). Armchair ribbons are metallic when the number of dimers (N) equals $N = 3m - 1$ and semiconducting otherwise, being m an integer number ($m \in \mathbb{N}$). An armchair ribbon of $N = 5$ is therefore metallic, as shown in Fig. 2.11c.

References

1. Saito, R. *et al.* Trigonal warping effect of carbon nanotubes. *Phys. Rev. B* **61**, 2981 (2000).
2. Semenoff, G. W. Chiral symmetry breaking in graphene. *Phys. Scr.* **T146**, 014016 (2012).
3. Schneider, M. *et al.* Local sublattice symmetry breaking for graphene with a centrosymmetric deformation. *Phys. Rev. B* **91**, 161407(R) (2015).
4. Wallace, P. R. The band theory of graphite. *Phys. Rev.* **71**, 622 (1947).
5. Dresselhaus, M. S. Graphite Fibers and Filaments. *Springer-Verlag and Berlin*, vol. 5 (1988).
6. Painter, G. S. & Ellis, D. Physical Properties of Carbon Nanotubes. *Phys. Rev. B* **1**, 4747 (1970).
7. Saito, R. Physical Properties of Carbon Nanotubes. *Imperial College Press, London* (1998).
8. Sarma, S. D. Electronic transport in two-dimensional graphene. *Rev. Mod. Phys.* **83**, 407 (2011).
9. Kekulé, A. Semiconductor Nanostructures: Quantum States and Electronic Transport. *Oxford University Press* (2010).
10. Goerbig, M. O. Electronic properties of graphene in a strong magnetic field. *Review of Modern Physics* **83**, 112–123 (2010).
11. Semenoff, G. W. *et al.* Condensed-Matter Simulation of a Three-Dimensional Anomaly. *Phys. Rev. Lett.* **53**, 2449 (1984).
12. Qaiumzadeh, A. *et al.* The effect of sublattice symmetry breaking on the electronic properties of doped graphene. *New Journal of Phys.* **11**, 095023 (2009).
13. Weitz, R. T. *et al.* Nanomaterials: Graphene rests easy. *Nature Nanomaterials* **5**, 699 (2010).
14. Kekulé, A. *Bulletin de la Societe Chimique de Paris* **3**, 98 (1865).
15. Kekulé, A. *Annalen der Chemie und Pharmazie* **137**, 129 (1866).
16. Bena, C. *et al.* Remarks on the tight-binding model of graphene. *New J. Phys.* **11**, 095003 (2009).
17. Ashcroft, N. & Mermin, N. Solid State Physics. *Saunders College Publishing International Edition* (1976).
18. Novoselov, K. S. *et al.* Electric Field Effect in Atomically Thin Carbon Films. *Science* **306**, 666–669 (2004).
19. Neto, A. H. C. *et al.* The electronic properties of graphene. *Reviews of Modern Physics* **81**, 109–110 (2009).
20. DiVincenzo, D. P. *et al.* Self-consistent effective-mass theory for intralayer screening in graphite intercalation compounds. *Phys. Rev. B* **29**, 1685 (1984).
21. Dean, C. R. *et al.* Boron nitride substrates for high-quality graphene electronics. *Nature Nanotechnology* **5**, 722–722 (2010).

22. Giovannetti, G. *et al.* Substrate-induced band gap in graphene on hexagonal boron nitride: Ab initio density functional calculations. *Phys. Rev. B* **76**, 073103 (2007).
23. Watanabe, K. *et al.* Direct-bandgap properties and evidence for ultraviolet lasing of hexagonal boron nitride single crystal. *Nature Materials* **3**, 404–409 (2004).
24. Wang, L. *et al.* One-Dimensional Electrical Contact to a Two-Dimensional Material. *Science* **342**, 614–617 (2013).
25. Xue, J. *et al.* Scanning tunnelling microscopy and spectroscopy of ultra-flat graphene on hexagonal boron nitride. *Nat. Mat.* **10**, 282 (2011).
26. McClure, J. W. Diamagnetism of Graphite. *Phys. Rev.* **104**, 666 (1956).
27. Novoselov, K. S. *et al.* Room-Temperature Quantum Hall Effect in Graphene. *Science*, **315**, 5817, 1379 (2007).
28. Von Klitzing, K. *et al.* New Method for High-Accuracy Determination of the Fine-Structure Constant Based on Quantized Hall Resistance. *Phys. Rev. Lett.* **45**, 494 (1980).
29. Aschcroft, N. & Mermin, N. Solid state physics. *Saunders College and Orlando* (1976).
30. Huckestein, B. Scaling theory of the integer quantum Hall effect. *Rev. Mod. Phys.* **67**, 357 (1995).
31. Kramer, B. Localization: theory and experiment. *Rep. Prog. Phys.* **56**, 1469–1564 (1993).
32. Büttiker, M. Absence of backscattering in the quantum Hall effect in multiprobe conductors. *Phys. Rev. B* **38**, 9375 (1988).
33. Büttiker, M. The quantum Hall effect in open conductors. *Semiconductors and semimetals* **35**, 191–277 (1992).
34. Davies, J. The physics of low dimensional semiconductors. *Cambridge University Press, Chap. 9* (1998).
35. Halperin, B. I. Quantized Hall conductance, current carrying edge states, and the existence of extended states in a two-dimensional disordered potential. *Phys. Rev. B* **25**, 2185 (1982).
36. Komiyama, S. The physics of low dimensional semiconductors. *Phys. Rev. B* **54**, 2067 (1996).
37. Abanin, D. A. Conformal Invariance and Shape-Dependent Conductance of Graphene Samples. *Phys. Rev. B* **78**, 035416 (2008).
38. Morozov, S. *et al.* Giant Intrinsic Carrier Mobilities in Graphene and Its Bilayer. *Phys. Rev. Lett.*, **100**, 016602 (2008).
39. J.H.Chen *et al.* Intrinsic and extrinsic performance limits of graphene devices on SiO₂. *Nature Nanotechnology* **3**, 206–209 (2008).
40. Lin, Y.-M. *et al.* Electrical observation of subband formation in graphene nanoribbons. *Phys. Rev. B*, **78**, 161409 (2008).
41. Saito, R. *et al.* Physical properties of carbon nanotubes. *Imperial College Press* (1998).

42. Groth, C. W. *et al.* Kwant: a software package for quantum transport. *New J. Phys.* **16**, 063065 (2014).
43. Wakabayashi, K. *et al.* Electronic transport properties of graphene nanoribbons. *New Journal of Physics* **11**, 095016 (2009).

Within this chapter I will introduce the three different fabrication methods used throughout this thesis. I will start by the simplest process, i.e the fabrication of graphene devices on a SiO_2 substrate, to end up with the more elaborated hBN-graphene-hBN structures. Every fabrication method represented a huge step forward in device quality. This chapter, together with the associated experimental findings, highlight the importance of the fabrication technique on the transport phenomena (Section 2.1).

3.1 Graphene on SiO_2

This fabrication method represents the fastest way of building graphene devices, from the amount of processing time and difficulty involved. I will introduce the etching and metalization steps in this part, even though these fabrication steps are common to all fabrication methods. A schematic overview of the process is provided in Fig. 3.1. The process-flow starts with the evaporation of metal markers on a wafer scale. In order to increase the yield of graphene flakes on the substrate's surface during the exfoliation process, it is important to maximize the distance between metal markers. The wafers are commercially available from "NOVA Electronics materials" with a $\sim 285\text{ nm}$ dry thermally oxidated silicon layer on top. The thickness of the oxide layer is crucial to increase the contrast of the light through the graphene flake with respect to the surroundings [1]. Silicon bulk is heavily p-doped to allow conduction at low temperatures. Indeed, the Silicon layer is used as a back-gate electrode to tune the charge carriers concentration in graphene.

To start with, I spin-coat a double layer of polymethyl methacrylate (PMMA) over a 10" SiO_2 wafer and expose the designed marker field via electron beam lithography (EBL). Prior evaporation of the $5\text{ nm}/50\text{ nm}$ Chromium/Gold metal markers, I immerse the written wafers in PMMA-resist developer for ~ 60 seconds. The chromium layer is crucial to increase the adhesion to the substrate. The process is finalized with a lift-off of the residual metal to remove. The resulting wafer is diced in $7 \times 7\text{ cm}$ chips prior spin-coating of a protective photo-resist layer. Graphene can then be deposited on surface of the processed chips.

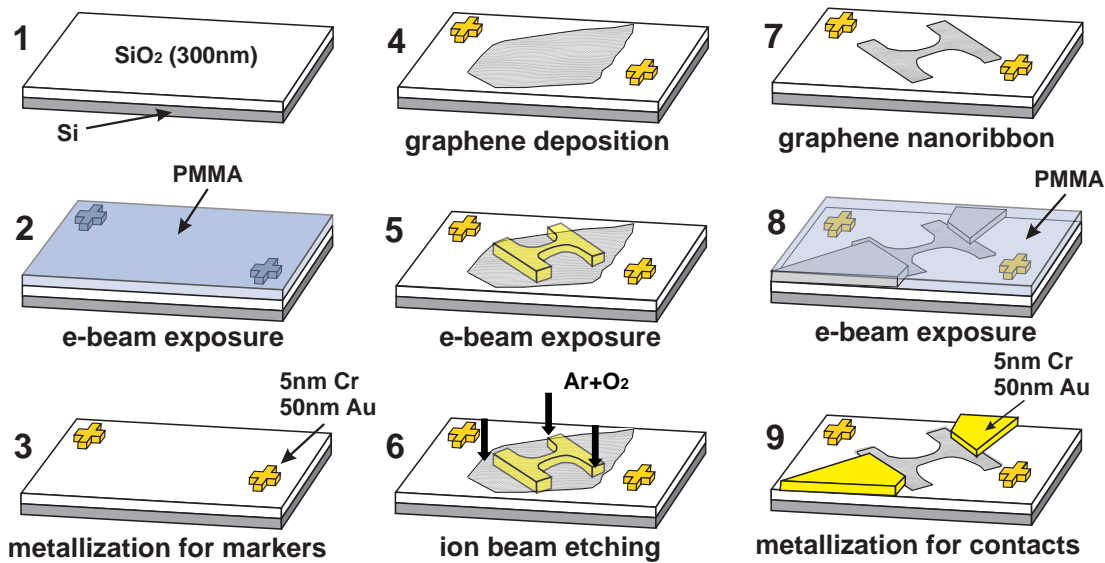


Figure 3.1: **Schematics of the fabrication process.** Process flow for the fabrication of graphene devices. Graphene flakes are mechanically exfoliated from graphite and deposited onto the SiO_2 substrates. The highly doped Si substrate serves as a back-gate electrode. Electron beam lithography (e-beam) and reactive ion etching (RIE) are used to structure the graphene devices. An additional e-beam step and a lift-off process are needed to electrically contact the devices.

To exfoliate graphene flakes, I use the "scotch-tape" technique developed by Novoselov et al. [2]. The working principle stems from the weak van der Waals forces sticking the graphite layers together in a graphite crystal (Fig. 3.2a). An adhesive tape (Fig. 3.2b) provides enough sticking force to progressively exfoliate the graphite crystal by repeatedly attach and detach the tape (Fig. 3.2b). The graphene flakes adhered to the scotch tape are transferred into the SiO_2 chips by gently pressing the 7×7 cm chips into the sticky tape. The yield of large flakes can be increased by extensively cleaning the surface of the SiO_2 chips and/or by doing the process in a dry atmosphere. A plasma oxygen step also helps in preparing the surface for the deposition of graphene. For further details refer to [3]. Graphene flakes of over $50 \mu m$ in length can be obtained with this fabrication method (Fig. 3.2c).

Raman spectroscopy

Once on the substrate, although it is possible to give a good estimate on the single- or bi-layer nature of the flakes under the optical microscope [1], the selected flakes are analyzed by Raman spectroscopy. Raman imaging is a non invasive tool, which does not require any other specific treatment than placing the samples under a laser spot. Raman spectroscopy is based on the inelastic scattering of the induced electron-hole pairs in the material.

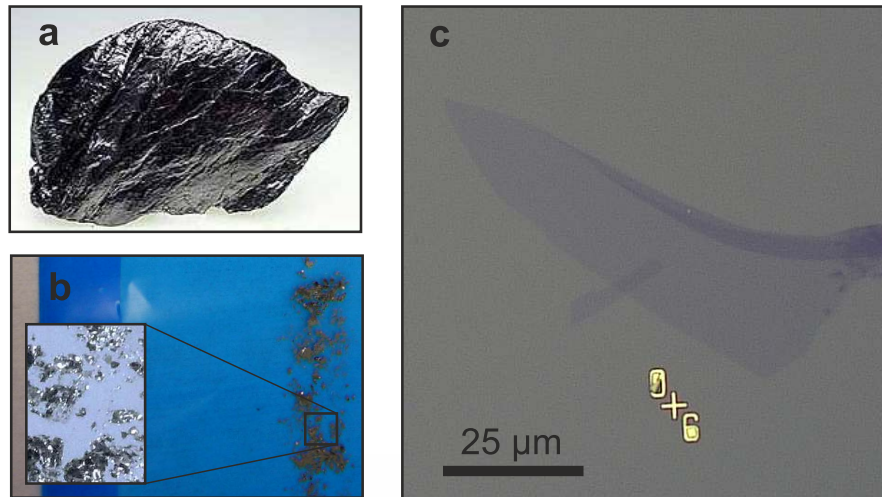


Figure 3.2: **Mechanical exfoliation of graphene, "scotch-tape" technique.** **a**, Raw source material for graphene, a Highly Ordered Pyrolytic Graphitic (HOPG) crystal. **b**, Rests of graphite lying on top of a scotch tape. The exfoliation process progressively splits the graphite layers until a single flake crystal, i.e. graphene, is detached. The exfoliation process yield bigger flakes when done in a dry atmosphere. The time in which the SiO_2 substrate is in contact with the "scotch-tape" influences the density of graphite residues transfer onto the SiO_2 substrate. **c**, Optical microscope picture of a graphene flake with over $50\ \mu m$ in length, deposited onto a SiO_2 substrate.

A laser beam provides a monochromatic excitation energy and the scattered photons are collected by a Charged Coupled Device (CCD) camera. The modifications in the wave-length of the collected light (Raman shift) is intrinsically related to the scattering processes involved. The spectrum of graphene is characterized by two well defined G- and 2D-lines (Fig. 3.3). The 2D-line gives insightful information on the number of layers [4]. For single-layer graphene, the 2D peak is defined by a single Lorentzian whereas for bi-layer graphene, the line-shape is the contribution of four slightly shifted Lorentzian. The reason of the sub-peaks contribution is understood from the degeneracy of the dispersion relation, giving rise to additional Raman processes. For a more detailed description of the Raman spectra refer to [5].

Patterning and contacting steps

To carve the shape of the graphene nanostructures, it is necessary to rely on precision cutting techniques that limit the amounts of defects or contamination. For this purpose I rely on a reactive ion etching (RIE) method in combination of a hard mask (made of Cr or PMMA). The etching process is essentially based on the directional bombardment of argon atoms under an argon/oxygen atmosphere. A chemical etching process, enhanced by the plasma atmosphere, happens simultaneously. Thus, this method comprises an anisotropic etching process with a chemical reactivity.

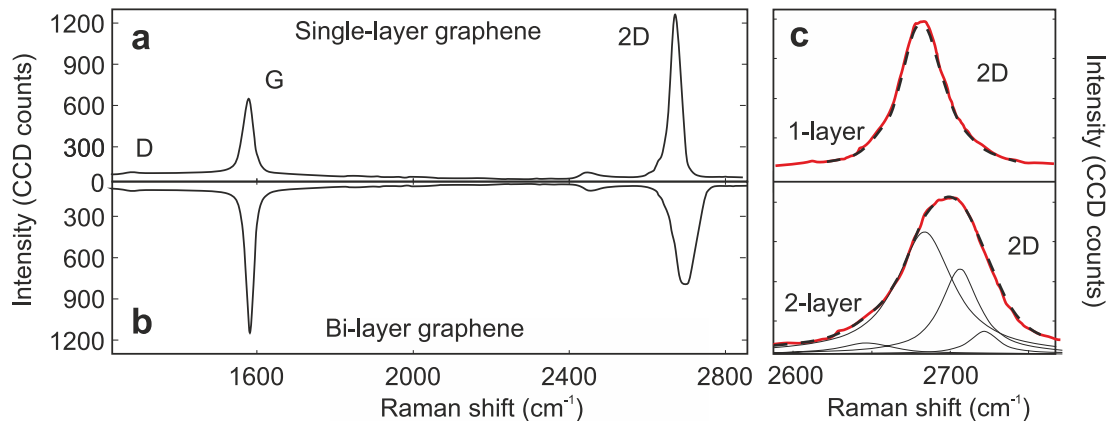


Figure 3.3: **Characteristic Raman spectra of exfoliated graphene.** **a** and **b**, Raman spectrum of single- (panel a) and bi-layer (panel b) graphene. The D, G and 2D lines are indicated in panel a. **c**, Direct comparison between the 2D peak of a single and bi-layer graphene. The 2D-line shape for single layer graphene can be modeled by a Lorentzian. The 2D peak (red trace) of a bi-layer flake is composed of four Lorentzians (black trace).

Prior the etching step, the samples are spin-coated with a layer of PMMA resists and written by EBL. After development, the resulting etch mask undergoes RIE. The process is relatively fast, as it takes ~ 8 seconds to carve the unwanted surface. The exact recipes and a description of the processing parameters can be found in appendix A. I note that, all fabrication methods have specific parameters and some differences, e.g I use a *Cr* etching mask for structuring the hBN-graphene-hBN devices (details in appendix A). An AFM image of a graphene device after the RIE process is shown in Fig. 3.4.

To contact the etched devices I follow a standard EBL procedure prior evaporation of a *Cr/Au* layer. As a final step, the undesired metal is removed via a lift-off process. The Chromium layer (5 nm) increase the adhesion of the metal structure onto the *SiO*₂ surface. It is known that *Au* does not attach properly to *Si* oxide. It is also worth mentioning that *Cr/Au* can withstand a post-step in Hydrofluoric acid (*HF*), either to suspend the graphene structure or to clean rests of contaminants [6]. Many combinations of metal have been tried to improve the contact resistance of the metal-graphene interface [7–9]. Although lower contact resistances are desired in transport experiments, most of the structures throughout this thesis are designed in a four-terminal configuration, eliminating any contribution from the contact resistance. As a last step, the *SiO*₂ chip is glued to a standard chip carrier (Kyocera C-QFN PB-C88084) with silver-paste and two-component glue (UHU). I wire-bond the samples with a semi-automatic wedge bonder (TPT HB06). Samples can then be directly mounted in the probe tube of a measuring set-up (for details refer to [10]).

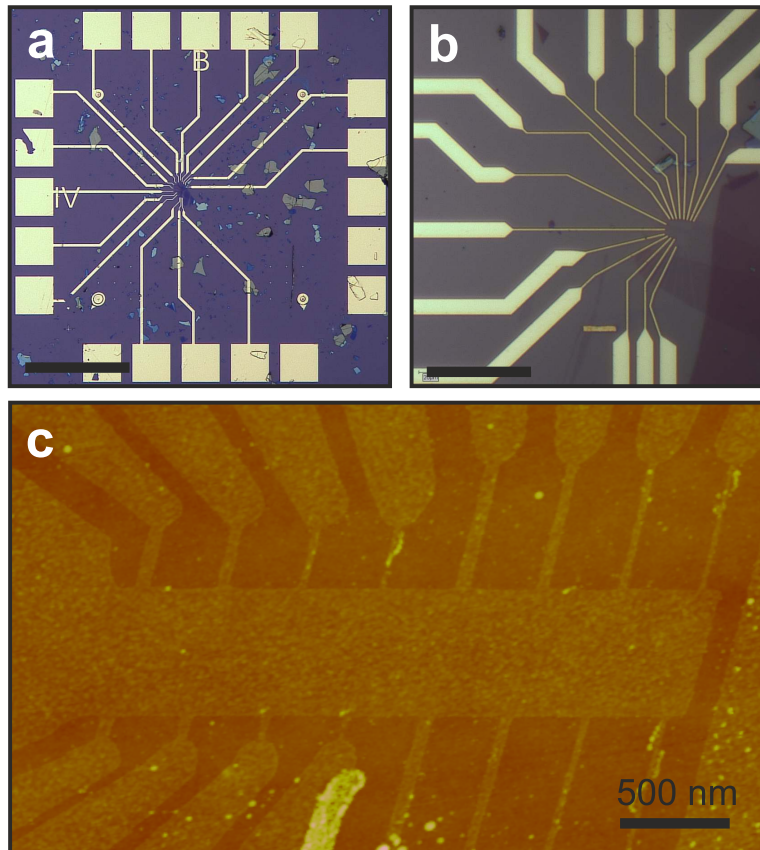


Figure 3.4: **Fabricated graphene devices.** **a** and **b**, Connections lines from the Bondpads (big gold squares) down to the graphene-based electrodes (visible in panel c). The scale bars are 500 nm and $20\ \mu\text{m}$ in panels a and b, respectively. **c**, Atomic Force Microscope (AFM) image of the contacted graphene ribbons' array.

3.2 Graphene on hBN

This section illustrates the fabrication steps involved in the fabrication of graphene devices on hexagonal Boron Nitride (hBN) substrates. As introduced in Section 2.1, hBN appears as a suitable substrate material for graphene. The fabrication process consists of the mechanical exfoliation of both agents, the graphene and the hBN substrate, and the transfer process of the former onto the latter. The main idea of this transfer process follows the guidelines presented in [11], appropriately adapted to our requirements.

Once again, I start by mechanically exfoliating some hBN flakes on top of a $7 \times 7\text{ cm}$ SiO_2 chip. The method is analogous to the exfoliation of graphene (see Section 3.1). It is worth mentioning that the hBN crystals, as a 3D layered material, have a weak interlayer binding compared to the intralayer forces. The "scotch-tape" exfoliation technique is hence as successful as for graphene. Optical pictures of hBN flakes are shown in

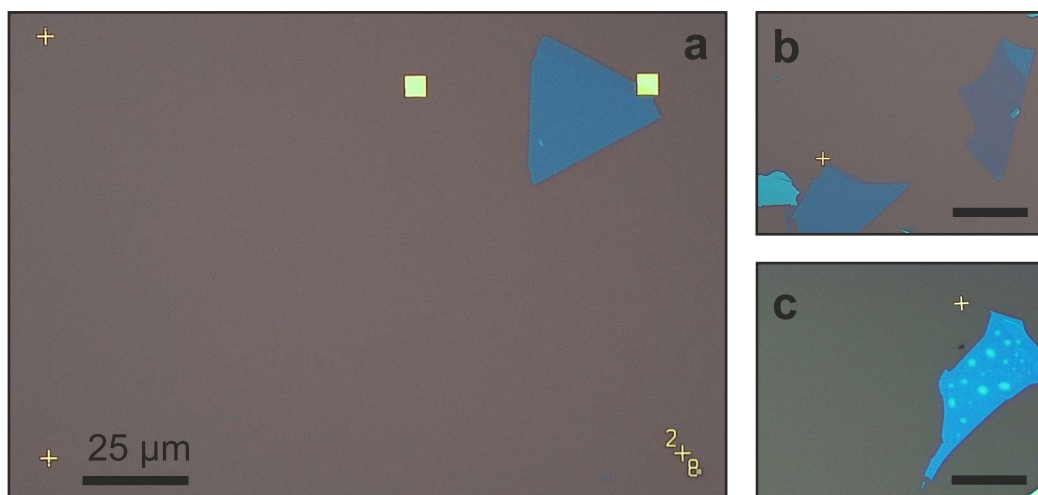


Figure 3.5: **hBN as a suitable substrate for graphene.** **a** and **b**, Optical microscope images of hBN flakes (light blue color) on a SiO_2 (dark gray color). The contrast in color of the flakes decreases the thinner the flakes are (panel b). **c**, hBN flake showing visible traces of residues (brighter spots on the hBN flake). Residues accumulated during the fabrication process are most probably trapped within the hBN flake and the substrate.

Fig. 3.5, where I can see the change in contrast as a function of the layer thickness. At that stage, it is also important to visually inspect the hBN flakes. Flakes having rest of residues are discarded (Fig. 3.5c). I choose hBN flakes of a thickness around 30-50nm (colored light turquoise under the optical microscope). This value should be taken into account when metalizing the final structures.

Even though I could, at that stage, try to exfoliate graphene on the hBN covered chip, the yield would be too low for making it viable. Instead, I use an alignment process based on micro-manipulators to deposit graphene on top of a selected hBN flake. The process allows to transfer graphene on specific spots with a precision of a few microns.

To succeed, the hBN flake have to be as large as possible, reaching average sizes of around $10\ \mu m$ (Fig. 3.5) with our exfoliation method. The graphene flakes are deposited on a polymer stack previously spin-coated on a $7 \times 7\ cm$ chip. The bottom part is a $100\ nm$ -thick water-soluble layer of polyvinyl alcohol (PVA) and the upper part a $\sim 200\ nm$ thick layer of PMMA. Graphene is exfoliated on top of that polymer stack. Although the visibility is decreased, choosing the appropriate thickness of the PMMA layer ($\sim 200\ nm$) ensures the graphene to be found under the optical microscope (dashed lines Fig. 3.6 a and b).

To lift the PMMA layer, the chip with the polymer stack with the graphene is placed onto the water surface, inside a petri dish (Fig. 3.5c). The PVA layer dissolves and the PMMA detach from the SiO_2 chip, resting on the surface of the water (black arrow in

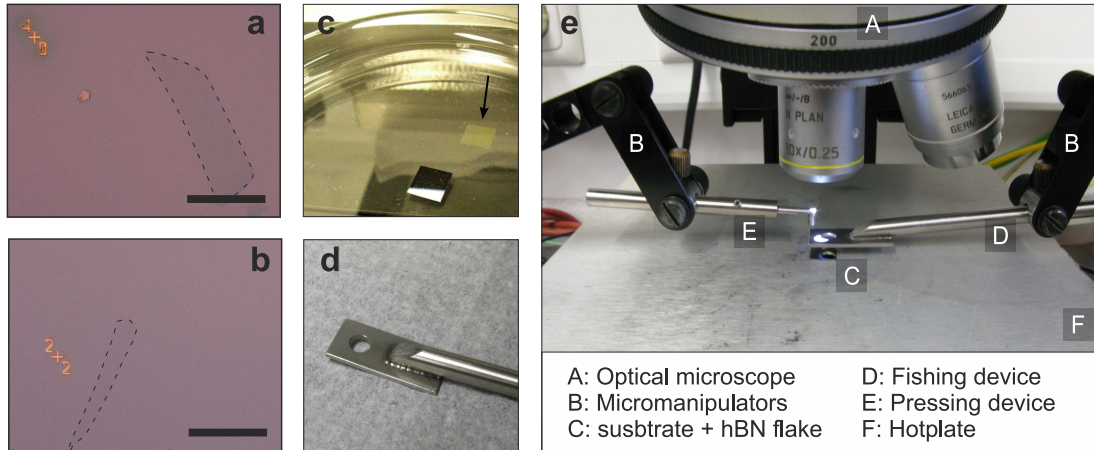


Figure 3.6: **"Fishing" fabrication technique.** **a** and **b**, Optical microscope images of two graphene flakes deposited onto PVA/PMMA stacks. Due to a change in contrast, the flakes are barely visible even under the optical microscope, thus highlighted with black dashed lines. **c**, After placing the SiO₂/PVA/PMMA/graphene stack (panels **a** and **b**) on the water surface, the PVA dissolves and the SiO₂ chip sinks to the bottom of the water recipient. The PMMA/graphene stack remains on surface (black arrow). The stack is visible by naked eye and can therefore be caught with the help of a "fishing device". **d**, Picture of the "fishing device" used to take the floating PMMA/graphene stack (panel **c**). **d**, Picture of the transfer apparatus. The fishing and the pressing devices are operated by micro-manipulators under an optical microscope. the PMMA+graphene stack is pressed over the selected hBN flake. Pictures **c** and **e** are reprinted from [12].

Fig. 3.5c). With the help of a fishing device (Fig. 3.5d), the PMMA is fished and placed under an optical microscope with a micro-manipulator setup (Fig. 3.5e). The fishing devices is nothing else than a metal structure with a hole in it (Fig. 3.5d). It is crucial to place the graphene flake inside the hole of the fishing device, in order to see it under the optical microscope afterward.

After leaving the fishing device dry (the process can be shortened by the use of a hot plate a 40°C), I align the graphene flake on top of the targeted hBN flake. I progressively higher the chip until the SiO₂ surface reaches contact with the PPMA stack. To force the contact between PMMA and chip I use a pressing device (Fig. 3.5e). Graphene and hBN flakes have to be perfectly aligned and in close contact before applying the pressing device, otherwise misalignment may occur. Heating up the hot plate underneath the chip (Fig. 3.5e) up to 100°C helps to bring in contact the PMMA and the SiO₂. The PMMA layer literally melts and stick on surface. A strong change in image contrast is visible under the optical microscope.

Once the transfer method is finalized, the samples are heavily contaminated from handling the samples in ambient conditions and the PMMA stack remains still on sur-

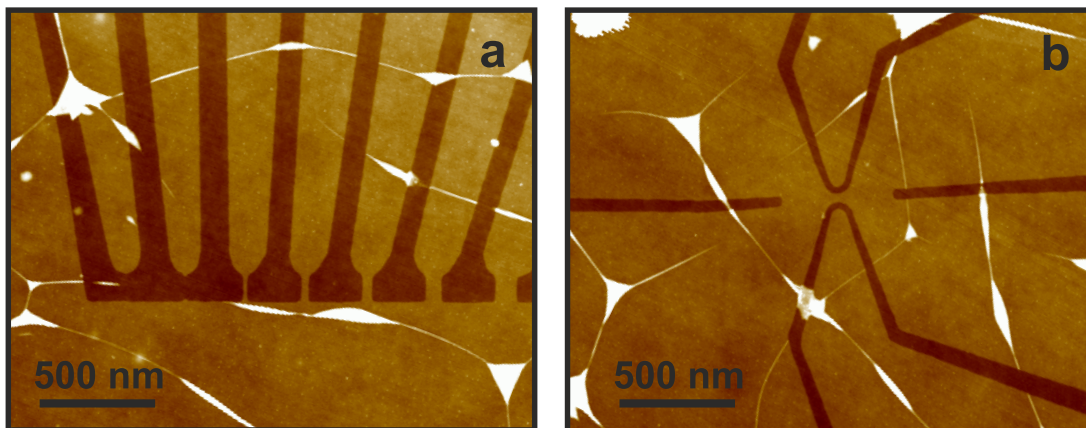


Figure 3.7: **Graphene devices on hBN substrate.** **a** and **b**, AFM images of a two-terminal graphene nanoribbons' array (panel a) and a four-terminal side-gated constriction (panel b) after an extensive chemical cleaning step. Samples have been annealed in a H_2 atmosphere (refer to text) to reduce the amount of processing contaminants. Bubbles and ripples are common to all samples fabricated with this technology. The devices are located away from the bubbles.

face. Samples follow an extensive chemical cleaning step by immersing the SiO_2 chips in warm acetone for four to five hours. I rinse with isopropyl alcohol afterwards. The chemical cleaning removes most of the residues and prepare the samples for the patterning and contacting steps. An AFM image of a set of graphene devices on hBN substrate can be found in Fig. 3.7. I emphasize that, as a final processing step, samples undergo a thermal annealing treatment once contacted. For further details on the annealing process refer to [13].

3.3 Encapsulated hBN-graphene-hBN

This transfer method is based on the method develop by Wang et al. [14]. Although the basic idea is similar to the "fishing" technique, samples issued from this fabrication method are noticeably cleaner. In fact, the process is entirely done in clean-room. Comparatively, this is a less time-consuming method and the yield is higher. All in all, once this technique is mastered and for the kind of devices we are interested in, there are no reason to use the previous fabrication methods. A schematic representation of the process is shown in Fig. 3.8. The process starts with a glass slide covered with tape and spin-coated with PMMA polymer. I exfoliate hBN flakes onto this stack. The optical picture Fig. 3.9a shows the contrast of a hBN flake on that glass structure.

Separately, I prepare a SiO_2 chip with a graphene flake on top. Under the mask aligner (Fig. 3.8), I align the graphene flake with the hBN flake located on the glass stack. Once

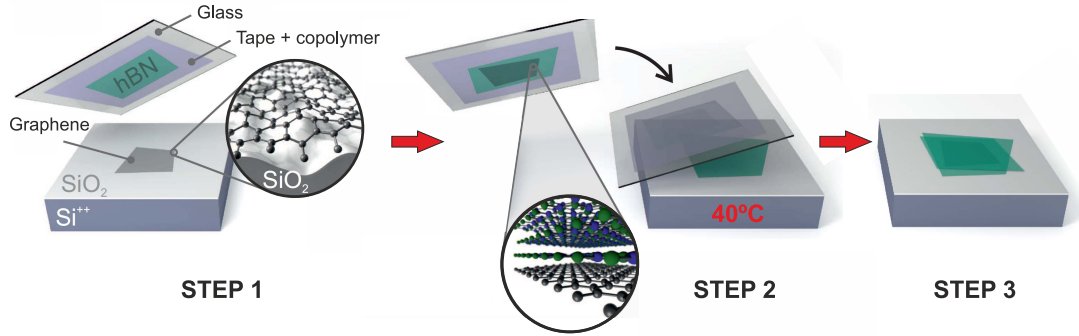


Figure 3.8: **"Pick up" transfer technique.** Process flow illustration of the "pick up" transfer method, also referred as "dry transfer technique" in the text. Under the mask aligner, I bring the glass stack (tape + copolymer + hBN flake) into contact with the selected graphene flake (step 1). I do not apply any temperature at this point. Once released, the graphene flake sticks to the hBN. With the added graphene layer, I press the glass stack onto a targeted hBN flake (step 2). I finish the transfer method by chemically cleaning the hBN-graphene-hBN heterostructure (step 3).

aligned, I bring both flakes into contact (step 2 in Fig. 3.8). Contact is recognized by a change in contrast under the optical microscope of the mask aligner. Temperature is not necessary, although slightly warming up ($T = 40^{\circ}\text{C}$) the silicon chip can help.

Right after, I release/lift the stack. Due to the strong Van-der Waals forces between the two atomically flat materials (graphene and hBN), the graphene flake detaches with ease from the SiO_2 surface.

As a next step, I prepare another SiO_2 chip with hBN flakes on top. Later on, I deposit the whole glass/tape/PMMA/hBN/graphene onto the pristine hBN flake of the freshly prepared SiO_2 chip (step 2 in Fig. 3.8). This step is, once again, done with the mask aligner. Yet, the sample holder is heated up to 90°C . The PMMA layer melts and the whole stack attaches to the SiO_2 chip. The resulting hBN-graphene-hBN stack, lying on the SiO_2 (step 3 in Fig. 3.8), has to be extensively cleaned with acetone for two to three hours and thereafter rinsed with Isopropanol. The sample is then ready for its next processing step. It is important to note that graphene does not come into contact with organic solvents or polymers during the whole process.

Possibly, the biggest advantage of this fabrication method stems from the fact that graphene is protected by the hBN flakes against impurities. Moreover, during the fabrication process of hBN-graphene-hBN nano-structures the graphene layer is protected against any kind of solvents.

Fig. 3.8b and c show optical and AFM images of the hBN-graphene-hBN heterostructure. Visible under AFM inspection (Fig. 3.8c), we observe bubble-like features in a

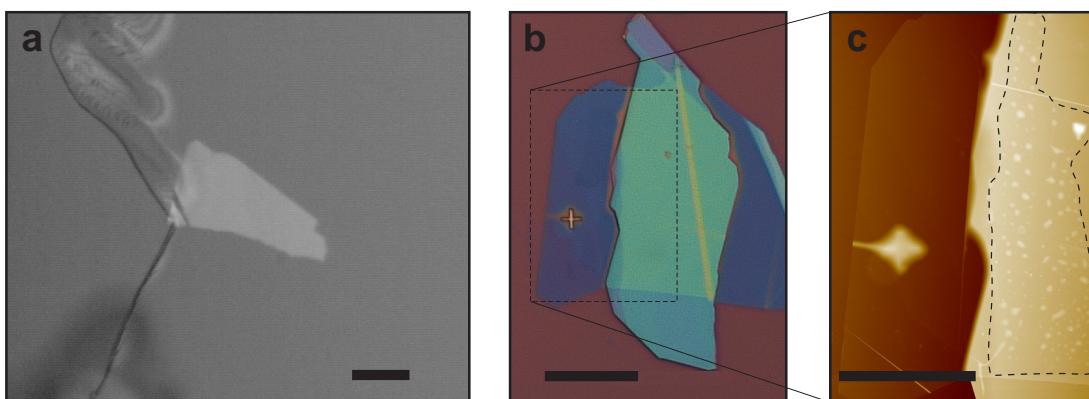


Figure 3.9: "**Pick up**" transfer technique. **a**, Optical microscope image of an hBN flake exfoliated onto the glass/tape/copolymer stack. **b**, Optical image of a finish hBN-graphene-hBN heterostructure. The graphene flake is hardly visible. **c**, AFM image of the hBN-graphene-hBN heterostructure in panel b. The graphene flake can be distinguish (dashed black lines), as well as the bubbles forming in the graphene. All scale bars represent $25\ \mu\text{m}$.

very similar way as for fishing fabrication method (Fig. 3.7). The bubbles are typically found in hBN-graphene heterostructures and originated from rest of hydrocarbons that contaminate the hBN surface. Trapped in between the hBN and graphene layers, the aforementioned hydrocarbons agglomerate and form bubbles [15].

References

1. Blake, P. *et al.* Making graphene visible. *Appl. Phys. Lett.* **91**, 063124 (2007).
2. Novoselov, K. S. *et al.* Electric Field Effect in Atomically Thin Carbon Films. *Science* **306**, 666–669 (2004).
3. Dauber, J. Master's thesis. *RWTH Aachen university* (2011).
4. Ferrari, A. *et al.* Raman Spectrum of Graphene and Graphene Layers. *Phys. Rev. Lett.* **97**, 187401 (2006).
5. Dresselhaus, M. S. *et al.* Characterizing Graphene and Graphite and Carbon Nanotubes by Raman Spectroscopy. *Annual Review of Condensed Matter Physics* **1**, 89–108 (2010).
6. Dauber, J. *et al.* Reducing disorder in graphene nanoribbons by chemical edge modification. *Appl. Phys. Lett.* **104**, 083105 (2014).
7. Watanabe, E. *et al.* Low contact resistance metals for graphene based devices. *Diamond and related Materials* **24**, 171–174 (2012).
8. Chaves, F. A. *et al.* Physical model of the contact resistivity of metal-graphene junctions. *Appl. Phys. Lett.*, **115**, 164513 (2014).
9. Politou, M. *et al.* Transition metal contacts to graphene. *Appl. Phys. Lett.*, **117**, 153104 (2015).
10. Volk, C. Ph.D. thesis, RWTH Aachen University (2015).
11. Dean, C. R. *et al.* Boron nitride substrates for high-quality graphene electronics. *Nature Nanotechnology* **5**, 722–722 (2010).
12. Foster, F. Master's thesis. *RWTH Aachen university* (2011).
13. Engels, S. Ph.D. thesis. *RWTH Aachen University* (2015).
14. Wang, L. *et al.* One-dimensional electrical contact to a two-dimensional material. *Science* **342**, 614–617 (2013).
15. Haigh, S. J. *et al.* Crosssectional imaging of individual layers and buried interfaces of graphene-based heterostructures and superlattices. *Nat. Mater.*, **11**, 764 (2012).

Disordered graphene nano-structures

4.1 Experimental evidences of a diffusive transport behavior

This section has been partly published in:

Disorder induced Coulomb gaps in graphene constrictions with different aspect ratios.

B. Terrés, J. Dauber, C. Volk, S. Trellenkamp, U. Wichmann and C. Stampfer
Appl. Phys. Lett. **98**, 032109 (2011).

Besides the wide-spread theoretical description of nano-structured graphene ribbons discussed above, the transport characteristics of real devices is certainly influenced by the presence of disorder. Even if most of graphene's properties [1] are well described in terms of non-interacting (or weakly interacting) Dirac fermions [2, 3], the transport behavior becomes heavily influenced by electron interactions once the dimensions of the graphene devices approach the nanometer scale. [1].

The fact that disorder-associated phenomena did not show-up in bulk graphene experiments remained a puzzle in the physics of graphene for a while. Klein tunneling [4], or the unimpeded penetration of pseudo-relativistic particles through high and wide potential barriers, revealed the physic principles of that distinctive phenomena [4]. In nano-structured graphene though, Klein tunneling does not hold and the transport behavior is characterized instead by disorder-driven tunneling processes [5].

In the following section we will introduce transport measurements on lithographically etched two-terminal graphene ribbons on SiO_2 substrates of different widths (w) and lengths (l). We will initially characterize the transport behavior at high charge carrier densities, i.e. away from the charge neutrality point (noted V_0) and extract some significant electrical parameters, e.g. the contact resistance R_C and carrier mobility μ . Thereafter, we will restrict ourselves to the region of reduced conductance, i.e. transport gap, and extract the relevant energy scales (energy gaps). These extracted energies will be compared to the theoretically expected energy scales for the case of single-particle wave confinement, introduced in Section 2.3.

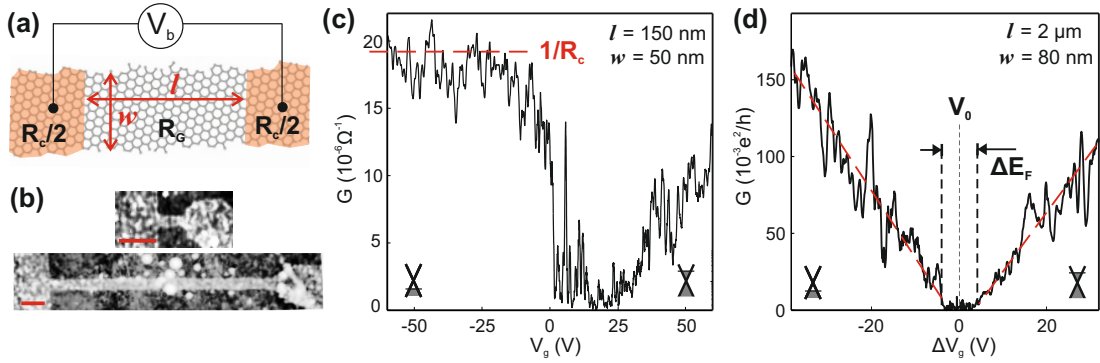


Figure 4.1: **(a)** Schematics representation of a two-terminal graphene nanoribbon. The *Au/graphene* contact resistance (R_C) is represented in orange as a resistance in series. The bias voltage (V_b) is applied symmetrically to the device. The length (l) and the width (w) appear in red. **(b)** Atomic Force Microscopy (AFM) scans of the 2-terminal devices measured in panels (c) and (d). The scale bars represent 200 nm . **(c)** and **(d)** Back gate characteristics at $V_b = 300\ \mu\text{V}$ of the graphene ribbons shown in (b) (dimensions indicated in panels). The saturation (panel (c)) and the linear fits to the conductance (panel (d)) are marked in red. The dashed black lines represent the limits of the transport gap (ΔE_F) and the charge neutrality point (V_0) in panel (d). Measurements at $T = 1.7\text{ K}$.

This section is revelatory of the divergences between the theoretical expectations and real-world measurements, supporting the conclusion that, in realistic devices, disorder plays a major role in defining the transport behavior.

Under a Drude model approximation, the electrical transport of graphene is mainly determined by the carrier density (n) and the carrier mobility (μ). To extract meaningful values of conductivity and thus mobility, it is important to identify the contact resistance of the metal-graphene interfaces. The contact resistance in two-terminal graphene devices can be extracted from the asymptotic saturation of the conductance at high carrier densities. This situation is visible in short and wide ribbons (Fig. 4.1c), where the conductance of the graphene channel (Fig. 4.1a,b) is expected to be highest. Considering equal contact resistances at both side-ends of the ribbon (see schematic in Fig. 4.1a), the conductance can be defined as:

$$G = \frac{1}{R_G + R_C} = \frac{1}{\frac{1}{ne\mu} \cdot \frac{l}{w} + R_C} = \frac{1}{\frac{1}{(\alpha(V_g - V_0))e\mu} \cdot \frac{l}{w} + R_C}, \quad (4.1)$$

where R_C and R_G are the contact and the graphene resistances, $\alpha = 7 \times 10^{10}\text{ cm}^{-2}\text{V}^{-1}$ is the lever arm (or capacitive coupling to the back gate), n the charge carrier density and e the electron charge. From the expression above, G tend to R_C^{-1} when $R_C \gg R_G$. Fig. 4.1c illustrates this asymptotic saturation of G . We extract a rough estimation of the contact resistance ($R_C \approx 50\text{ k}\Omega$). Note that R_C could be easily determined for a four-terminal configuration of the contacting skim, by comparing the two- and four-terminal conductance.

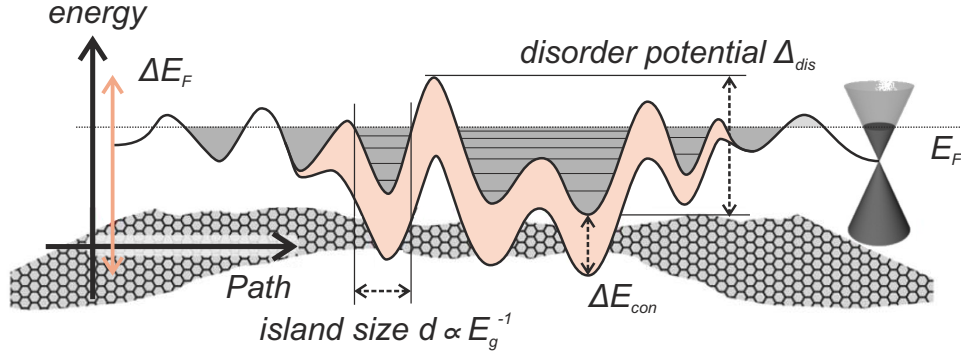


Figure 4.2: Illustration of the potential landscape along the graphene constriction. The formation of charged islands or quantum dots at low densities is due to the presence of a fluctuating potential Δ_{dis} . The related energy scales are discussed in the main text. Picture adapted from [6].

As shown in Fig. 4.1d, the conductance traces of narrow graphene ribbons conserve the overall linear dependence of G as function of the back gate voltage V_g . This feature originates from the linear density of states (DOS) characteristic of bulk graphene (see Section 2.1). As mentioned, this linear behavior is more likely to appear at moderate carrier densities, where the effect of the contact resistance merely contributes. A linear fit (neglecting fluctuations) to the conductance (red dashed lines in Fig. 4.1d) gives a rough estimation of the field-effect carrier mobility $\mu = \frac{\Delta G}{\Delta V_g} \frac{1}{\alpha e} \frac{l}{w}$. The extracted values for the electrons and holes are $\mu_e \approx 300 \text{ cm}^2/(\text{Vs})$ and $\mu_h \approx 360 \text{ cm}^2/(\text{Vs})$, respectively. These values are much smaller than the typical values found in large graphene flakes on SiO_2 substrate ($\mu \approx 5000 - 10000 \text{ cm}^2/(\text{Vs})$) [1]. This first comparison suggest graphene ribbons to be more affected by disorder than bulk graphene. At that point, this statement is somehow vague since a proper definition of disorder is missing. We will nonetheless describe it as a random, non-uniform potential distribution along the conductance path. Later on we will discuss more in detail its nature and characteristics.

As observed in Fig. 4.1d, the evolution of G is superimposed with aperiodic, yet reproducible fluctuations. These fluctuations have been commonly attributed to local resonances and/or *Universal Conductance Fluctuations* (UCF) [7–11] in literature. Both scenarios reveal the presence of a highly disordered potential landscape (Fig. 4.2) but UCFs require the phase information of the electrons to be conserved. Phase coherent transport has been demonstrated in bulk graphene [8–11] as well as in graphene nanoribbons [12, 13]. The contribution of these coherent interferences is usually viewed as corrections to the semi-classical conductance (4.1) and it manifests in transport measurements at zero magnetic field (B field) as UCF or as *weak localization* (WL) phenomena when measured as function of B field. Coherent transport measurements will be introduced more in detail in the following sections, we decided to introduce the concept of localization during this section in order to characterize the transport behavior and highlight the disordered nature of the electron path in graphene nanoribbons.

In diffusive systems at low temperatures, when the scattering processes are considered

elastic due to the freeze-out of phonons modes, almost all carriers scatter-off static potentials. In that situation, to get an estimate of the length-scale between scattering processes, i.e. free path l_e , one can express the conductivity in the region of linear conductance (Fig. 4.1d) using the Einstein relation:

$$\sigma = DOS(E_F) e^2 D, \quad (4.2)$$

where σ is the conductivity, D is the diffusion constant and $DOS(E_F)$ is the density of states evaluated at the Fermi energy E_F :

$$DOS(E_F) = \frac{8\pi|E_F|}{\hbar^2 v_F^2} \quad \text{with} \quad E_F = \hbar v_F \cdot \sqrt{\pi\alpha V_g}. \quad (4.3)$$

At $V_g = -10 V$ we obtain a Diffusion constant $D \approx 0,002 m^2/s$, that translates into a mean free path of $l_e \approx 4 nm$. Note that this value is more than one order of magnitude smaller than the ribbon width ($W = 80 nm$), being the Diffusion coefficient D and the mean free path l_e related through:

$$l_e = 2D/v_F. \quad (4.4)$$

All the experimental observations discussed above (low mobility, sharp and reproducible conductance resonances and a short mean free path) are thus revelatory of a diffusive system.

4.1.1 Transport characteristics close to the charge neutrality point: Disorder-induced Coulomb gaps in graphene constrictions

From now on, we will restrict ourselves to the region of suppressed conductance, or transport gap ΔE_F . In this energy range around the charge neutrality point V_0 , the presence of disorder is even more pronounced. In fact, it was the experimental study of the observed energy gaps in graphene nanoribbons [5, 14–23] that led to the disorder-induced Coulomb blockade interpretation [5, 23, 24] of the transport behavior. The linear fits to the conductance on the electron- and hole-sides (marked in red in Fig. 4.1d) define the size of the transport gap $\Delta E_F \approx 8 V$ that, once converted into energy through:

$$\Delta E_F (eV) = 2\hbar v_F \sqrt{\pi\Delta V/2} = \hbar v_F \sqrt{2\pi\Delta V}, \quad (4.5)$$

yields to an estimated $\Delta E_F \approx 840 meV$. Compared with the theoretical expectations in the absence of interactions for a $w = 80 nm$ ribbon ($\Delta E_{con} \approx 50 meV$, see wave confinement in Section 2.3), the extracted gap is more than one order of magnitude higher. This observation can be naturally justified by the formation of electron-hole puddles [26] at low carrier densities due to the presence of the aforementioned potential fluctuations (Fig. 4.2). Within this picture, Coulomb blockade arises from the tunneling/charging events of the carriers from puddle to puddle. It is important to note that, even though standard theory of Coulomb blockade (classical theory developed by Kulik and Shekter [27, 28]) neglects an electronic/wave-confinement level spacing within the charged puddle region, a confinement gap ΔE_{con} (Fig. 4.2) is necessary to prevent Klein tunneling

effects and assure localization within the electron-hole puddles. The schematic representation in Fig. 4.2 depicts this scenario and introduces the so-called effective energy gap E_g and the transport gap ΔE_F energy scales. The effective energy gap E_g refers to the charging energy of the smallest isolated islands [5, 23] and it is therefore heavily influenced by the width of the ribbon. The transport gap ΔE_F though, is directly related to the amplitude of the disorder potential fluctuations (marked as Δ_{dis} in Fig. 4.2). This energy scale corresponds to the range in V_g in which the electronic transport is characterized by coulomb blockade physics. These two well-defined energy scales define the transport around the Dirac cone of realistic nano-scaled devices. Indeed, a closer look inside the transport gap region (Fig. 4.3b,c, or refer to [5]), reveals a series of Coulomb resonances characteristic of tunneling processes. The strong localization of the charge carrier wave-functions leads to the suppression of phase coherence between successive tunneling processes. Hence, the scenario presented so far describes the observed low temperature gaps in terms of the geometric considerations of isolated localized states, neglecting effects associated to interference phenomena between puddles (e.g. resonant tunneling). To justify this assumption, the line-shape of a narrow resonance inside the transport gap (Fig. 4.3c) has been fitted by [5]:

$$G \approx \cosh^{-2}(e\alpha_g\delta V_g/2.5k_B T_e), \quad (4.6)$$

where $\alpha_g \approx 0.2$ is the lever arm or capacitive coupling to the back-gate electrode and $\delta V_g \approx V_g - V_g^{peak}$. The extracted electron temperature $T_e \approx 2.1K$ is close to the base temperature of the measuring system, leading to the conclusion that Coulomb blockade is a good approximation to the tunneling processes since the broadening of the peak is mainly limited by temperature rather than lifetime of the resonance. Under this assumption, we will compare the extracted energy gaps E_g of two-terminal graphene

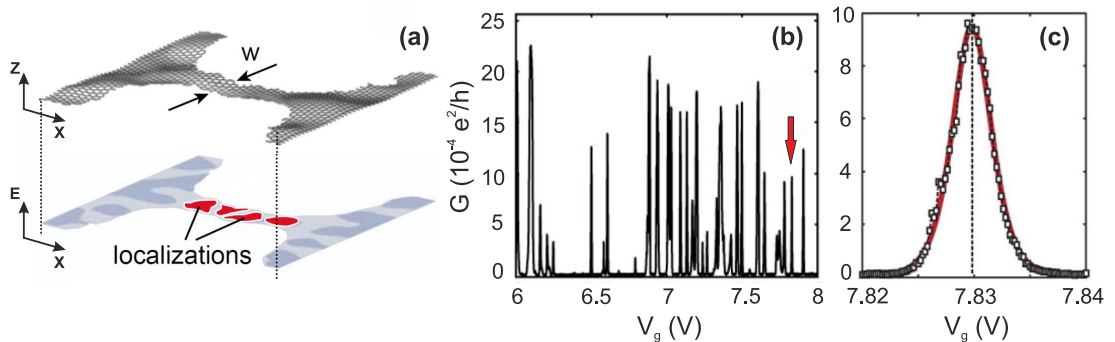


Figure 4.3: In-situ representation of the potential landscape introduced in Fig. 5 along the length and width of the graphene nanoribbon. The formation of charged islands (localizations) at low densities is marked in red. Picture adapted from [25]. (b) High resolution close-up inside the transport gap showing a large number of sharp resonances attributed to charging effects (re-printed from [5]). (c) Close-up and line-shape fitting (red trace) of a single resonance (see red arrow in panel (b)) (re-printed from [5]).

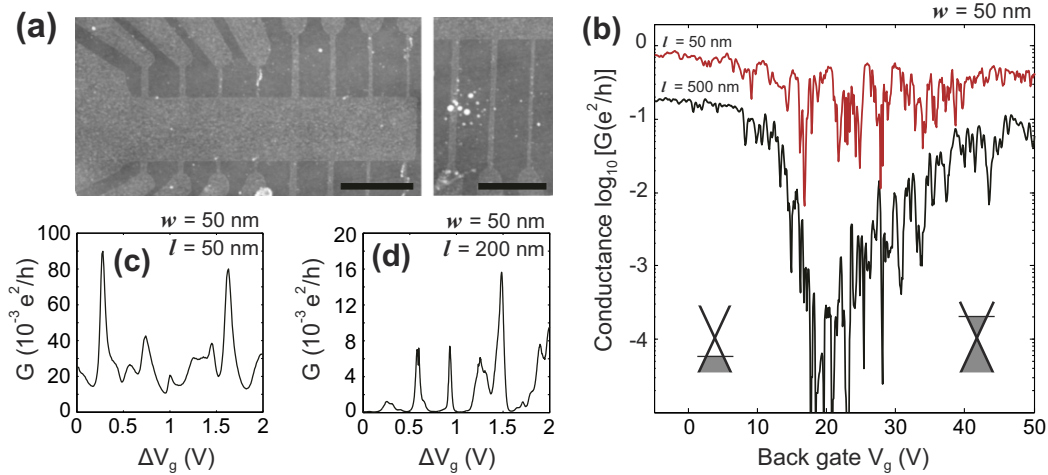


Figure 4.4: **(a)** Scanning force microscope images of etched graphene constrictions on SiO_2 substrate with different lengths (l) and widths (w). The scale bars represents $1 \mu\text{m}$. **(b)** Back gate characteristics at $V_b = 500 \mu\text{V}$ for two graphene constrictions with width $w = 50 \text{ nm}$ and different lengths $l = 50 \text{ nm}$ (red trace) and $l = 500 \text{ nm}$ (black trace). **(c)** and **(d)** Conductance peaks in the transport gap region for two different constrictions, $w = l = 50 \text{ nm}$ (c) and $w = l/4 = 50 \text{ nm}$ (d) at $V_b = 100 \mu\text{V}$.

nanoribbons with a Coulomb blockade-based model from [24]:

$$E_g = \frac{a}{W} e^{-bW}, \quad (4.7)$$

where $a = 2 eV$ and $b = 0.026 \text{ nm}$.

In following section, we will present the systematic study of the energy gap in graphene ribbons as function of the length l and width w (Fig. 4.4a). In particular, we will focus on graphene constrictions in the regime where $l \approx w$. In this regime, the Coulomb charging energy E_g (also called effective energy gap previously, see Fig. 4.2) is still predominantly determined by the width [5, 23]. However, the overall conductance level is strongly influenced by the length of the constriction. Most interestingly, we show that in very short constrictions, Coulomb blockade-like diamonds with high transparency can be observed.

In Fig. 4.4b, we show the conductance G as a function of the back-gate voltage V_g for two 50 nm wide constrictions with different lengths $l = 50 \text{ nm}$ and $l = 500 \text{ nm}$, measured at $V_b = 500 \mu\text{V}$. The transport gap (roughly between 17 and 30 V), separates hole from electron transport, as indicated by the two lower inserts in Fig. 4.4b [29]. While for the 500 nm constriction the conductance is strongly suppressed in this regime (G values down to $10^{-5} e^2/h$), we observe a significantly increased conductance for the shorter constriction. Nevertheless, a number of pronounced resonances reaching lower conductance values characterize the gap region, in rather good agreement with the measurement on the longer constriction (compare also Fig. 4.5a and Fig. 4.5b). A close-up

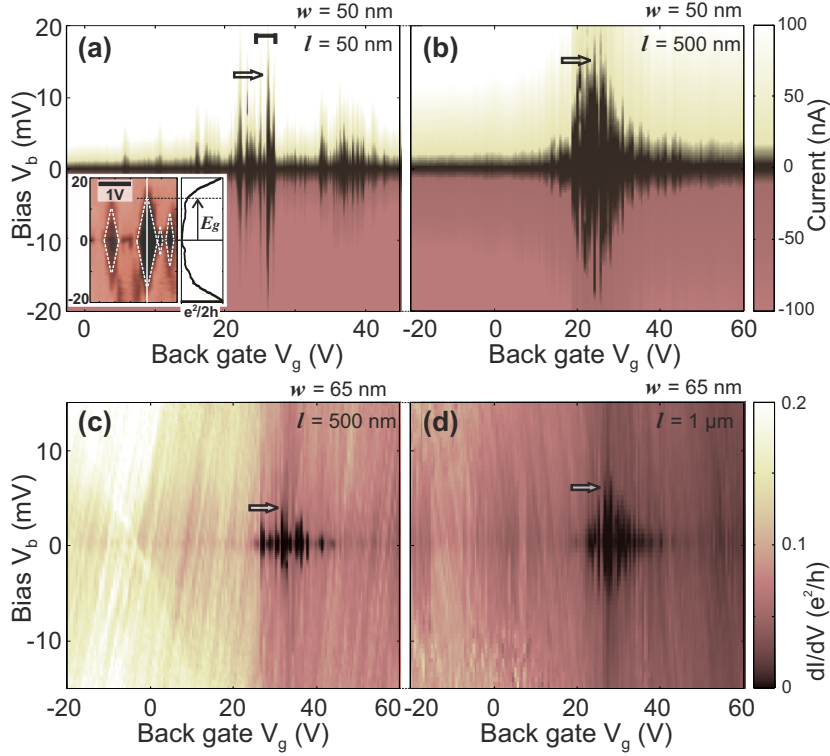


Figure 4.5: (a) and (b) Color plot of the source-drain current as a function of V_g and V_b for two constrictions of $w = 50 \text{ nm}$ and $l = 50 \text{ nm}$ (a), $l = 500 \text{ nm}$ (b). The inset shows differential conductance measurements of the region where the transport gap is most pronounced (see black bar in panel (a)). A cross section through the center of the largest diamond is shown on the right side of the inset, highlighting the definition of the gap E_g . (c) and (d) Differential conductance maps for graphene constrictions of $w = 65 \text{ nm}$ and length $l = 500 \text{ nm}$ (c) and $l = 1 \mu\text{m}$ (d).

of such resonances is shown in Fig. 4.4c and d. These reproducible resonances have been taken at $V_b = 100 \text{ V}$ within transport gap. We observe neither complete pinch-off nor strong Coulomb blockade behavior, as it is found for longer constrictions with the same width. For example, in Fig. 4.4c we show data recorded on a 50 nm long ($w = 50 \text{ nm}$) constriction. The overall conductance level differs significantly to the 200 nm long constriction of the same width (Fig. 4.4d); however, the typical V_g spacing between the resonances is comparable. In Fig. 4.5a and b, we show 2D plots of current as a function of V_b and back gate voltage for the two 50 nm wide constrictions with $l = 50 \text{ nm}$ (a) and 500 nm (b). In good agreement with earlier studies [5, 15, 19, 21, 22], we find regions of suppressed current with an extension of E_g/e in the V_b direction (see arrows). By plotting higher-resolution measurements of the differential conductance, one can see that the region of suppressed current is composed of individual diamonds (see inset in Fig. 4.5a). The energy gap (E_g) corresponds to the charging energy of the largest diamond [5, 23] as highlighted in the inset (see arrow in Fig. 4.4a). Interestingly, this energy scale only weakly depends on the constriction length. By comparing

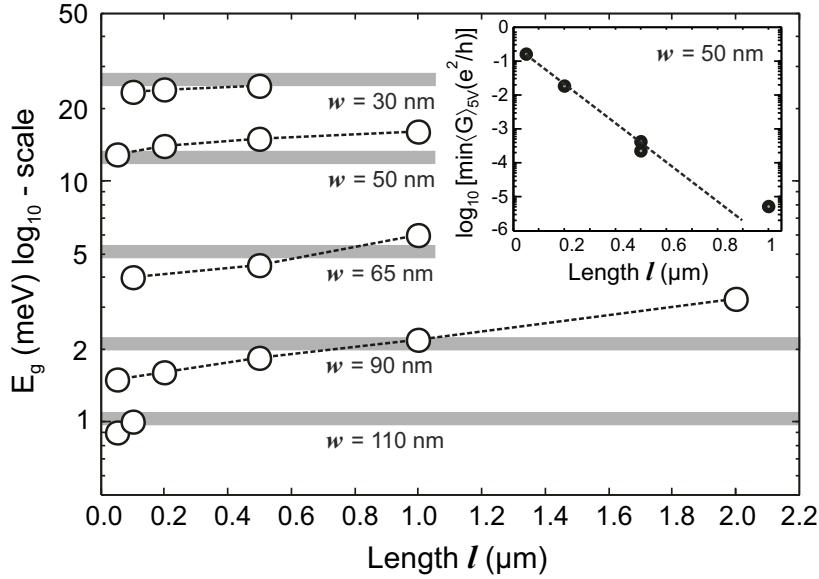


Figure 4.6: Energy gap E_g as a function of length l for a number of different graphene constrictions of different widths w (see labels and data points connected by dashed lines). The horizontal gray lines represent $E_g = a/w e^{-bw}$, where $a = 2 eV$ and $b = 0.026 nm^{-1}$ are taken from [24]. The inset shows the minimum value of the running averaged conductance G as function of length (running average interval of $5 V$ in back gate voltage).

Fig. 4.5a and Fig. 4.5b, we observe only a small difference in E_g between the $50 nm$ ($E_g = 13 meV$) and $500 nm$ ($E_g = 15 meV$) long constriction, allowing the conclusion that the smallest island or localized state is predominantly a function of the width w . The main difference can be found in the back gate coverage of the observed gaps. The shorter the constriction, the fewer islands (or localized -edge- states) are in the constriction, leading to fewer charging events. Consequently, the current is suppressed in smaller and fewer gate voltage regimes. However, the smallest island is found to be roughly length-independent (this is also true for $l < w$). The definition of the transport gap in back-gate voltage [18, 20] used as a figure of merit in earlier work, is hard to define for very short constrictions since it is considered to strongly depend on the disorder potential [5, 21, 23] which becomes very sample dependent, due to lack of averaging.

Similar behavior can also be seen for a $65 nm$ wide, $500 nm$, and $1 \mu m$ long constriction, as shown in Fig. 4.5c and Fig. 4.5d, respectively. Here, we plot the differential conductance as a function of V_b and V_g . In both measurements, a maximum charging energy of around 4.5 and $6 meV$ can be observed (see arrows). In total, we studied roughly 20 graphene constrictions on three different samples. In Fig. 4.6, we summarize the extracted energy gaps E_g as a function of the length for five different widths [30]. It can be seen that E_g strongly depends on the width, finding good agreement with earlier experiments and theoretical models [22, 24]. In particular, we compare our results with the model from Ref. [24], where the energy gap is approximated by $E_g = a/w e^{-bw}$ (see gray bars in Fig. 4.6) (see also Refs. [15, 20, 24]). In contrast to the weak E_g -length de-

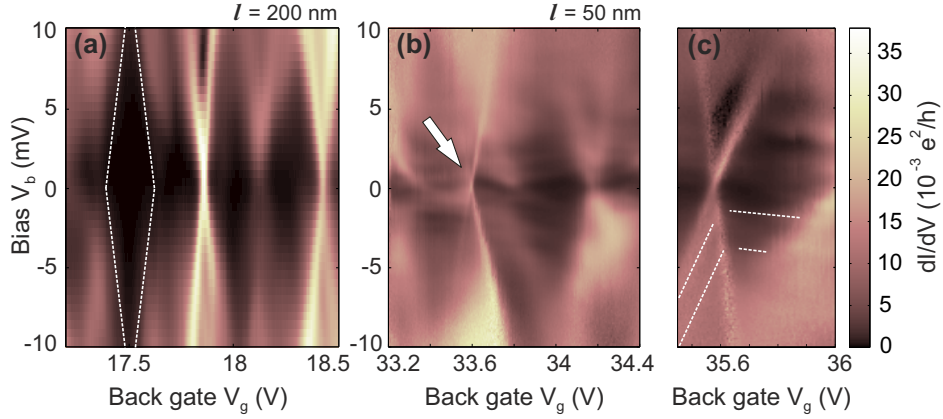


Figure 4.7: Differential conductance vs BG voltage and bias voltage of 200 nm (a) and 50 nm (b) and (c) long graphene constriction of width 50 nm. (a) Distinct diamonds of fully suppressed conductance can be observed (see white dashed line). (b) and (c) Similar data taken on a 50 nm long constriction. Diamonds at an elevated conductance level can be observed. Sharp resonances (white arrow in panel (b)) and features of increased conductance inside the diamonds (horizontal dashed lines in panel (c)) can be observed.

pendence, we observe a rather strong length dependence of the minimum conductivity, as shown by the inset in Fig. 4.6. The minimum value of the running averaged conductance decreases exponentially with increasing constriction length. This fits well with the scenario where localizations or tunneling processes are dominating the transport through the constrictions. Moreover, it shows that by making graphene constrictions very short, we can obtain a conductance level close to e^2/h .

More insights on the transparency of the shorter constrictions is gained by focusing on a small back-gate voltage range, as shown in Fig. 4.7. Here, we show high-resolution differential conductance dI/dV_b plots for different constriction lengths with constant width ($w = 50$ nm). Measurements on a 200 nm long constriction (Fig. 4.6a) show well distinguishable diamonds of suppressed conductance, in good agreement with earlier studies. In shorter constrictions ($w = 50$ nm) (Fig. 4.6b and c), we observe diamonds where the conductance is not fully suppressed, most likely because of strong coupling to localized states or isolated charged islands. Moreover, we observe faint lines of increased conductance inside the diamonds aligned with features outside the diamonds, which might be due to inelastic co-tunneling (see, e.g., dashed lines in Fig. 4.6c). According to recent experiments by Han et al. [22] the average hopping length L_c is in the range of $w \leq L_c < 2w$. Consequently, it is likely that for very short constrictions, L_c exceeds l ($l < w \leq L_c$) so that transport in short constrictions is no longer effectively one dimensional, resulting in several transport channels in the constrictions. This would account for (i) the strong increase in conductance and (ii) the appearance of very sharp features in the conductance (see, e.g., arrow in Fig. 4.6b), which could result from interference effects or Fano resonances.

In summary, in this section we characterize and present transport measurements on graphene nano-constrictions with different aspect ratios. We showed that the strongly width-dependent disorder induced energy gap is roughly length-independent, whereas the overall conductance level depends strongly on the length. In the gap region of very short graphene constrictions, a conductance level close to $0.1e^2/h$ can be reached, making these structures potential prime candidates for exploring Fano resonances, as we will see in Section 4.4.3, and Kondo physics in graphene nanostructures.

References

1. Geim, A. K. *et al.* The rise of graphene. *Nature Materials* **6**, 183–191 (2007).
2. Gonzalez, J. *et al.* Continuum approximation to fullerene molecules. *Phys. Rev. Lett.*, **69**, 172 (1992).
3. Peres, N. M. R. *et al.* *Phys. Rev. B*, **73**, 125411 (2006).
4. Katsnelson, M. I. *et al.* Chiral tunnelling and the Klein paradox in graphene. *Nature Physics* **2**, 620–625 (2006).
5. Stampfer, C. *et al.* Energy Gaps in Etched Graphene Nanoribbons. *Phys. Rev. Lett.* **102**, 056403 (2009).
6. Stampfer, C. *et al.* Tunable Graphene Single Electron Transistor. *Nano Lett.* **8**, 2378 (2008).
7. Beenakker, C. W. J. *et al.* Quantum Transport in Semiconductor Nanostructures. *Solid State Phys.* **44**, 1–228 (1991).
8. Kharitonov, M. Y. *et al.* Universal conductance fluctuations in graphene. *Phys. Rev. B* **78**, 033404 (2008).
9. Morozov, S. V. *et al.* Strong Suppression of Weak Localization in Graphene. *Phys. Rev. Lett.* **97**, 016801 (2006).
10. Horsell, D. *et al.* Mesoscopic conductance fluctuations in graphene. *Solid State Commun.* **149**, 1041–1045 (2009).
11. Lundeberg, M. B. *et al.* Spin-resolved quantum interference in graphene. *Nature Physics* **5**, 894–897 (2009).
12. Minke, S. *et al.* Phase coherent transport in graphene nanoribbons and graphene nanoribbon arrays. *Phys. Rev. B* **86**, 155403 (2012).
13. Berger, C. *et al.* Electronic Confinement and Coherence in Patterned Epitaxial Graphene. *Science* **312**, 1191–1196 (2006).
14. Chen, Z. *et al.* Graphene nano-ribbon electronics. *Physica E* **40** (2007).
15. Han, M. Y. *et al.* Energy Band-Gap Engineering of Graphene Nanoribbons. *Phys. Rev. Lett.* **98**, 206805 (2007).
16. Li, X. *et al.* Chemically Derived and Ultrasoft Graphene Nanoribbon Semiconductors. *Science*, **319** (2008).
17. Wang, X. *et al.* Room-Temperature All-Semiconducting Sub-10-nm Graphene Nanoribbon Field-Effect Transistors. *Phys. Rev. Lett.*, **100**, 206803 (2008).
18. Molitor, F. *et al.* Transport gap in side-gated graphene constrictions. *Phys. Rev. B*, **79**, 075426 (2009).
19. Liu, X. L. *et al.* Electrostatic confinement of electrons in graphene nanoribbons. *Phys. Rev. B*, **80**, 121407 (2009).
20. Molitor, F. *et al.* Energy and transport gaps in etched graphene nanoribbons. *Semicond. Sci. Technol.*, **25**, 034002 (2010).
21. Gallagher, P. *et al.* Energy and transport gaps in etched graphene nanoribbons. *Phys. Rev. B*, **81**, 115409 (2010).

22. Han, M. Y. *et al.* Electron Transport in Disordered Graphene Nanoribbons. *Phys. Rev. Lett.*, **104**, 056801 (2010).
23. Todd, K. *et al.* Quantum Dot Behavior in Graphene Nanoconstrictions. *Nano Lett.* **9**, 416 (2009).
24. Sols, F. *et al.* Coulomb Blockade in Graphene Nanoribbons. *Phys. Rev Lett.* **99**, 166803 (2007).
25. Güttinger, J. Ph.D. thesis. *ETH, Zurich* (2011).
26. Neto, A. H. C. *et al.* Edge and surface states in the quantum Hall effect in graphene. *Phys. Rev. B* **73**, 205408 (2006).
27. Shekhter, R. I. Zero anomalies in the resistance of a tunnel junction containing metallic inclusions in the oxide layer. *Sov. Phys. JETP*, **36**, 747 (1973).
28. Kulik, I. O. Kinetic phenomena and charge discreteness effects in granulated media. *Sov. Phys. JETP*, **41**, 308 (1975).
29. *All samples are slightly p-doped most likely due to residual resist on the graphene structures.*
30. *Since the extracted gap E_g is strongly disorder dependent, the error bars are around 5 – 10%, in agreement with earlier studies. For clarity error bars are not shown explicitly in Fig. 4.6.*

4.2 Evidences of a bulk-induced disorder

4.2.1 Magnetically confined quantum dots

In nano-structured graphene devices, edges and bulk contribute to the overall disorder. To characterize the nature of the potential fluctuations, we study the transport characteristics of magnetically confined quantum dots arising from bulk disorder. At finite magnetic fields, the localized states, induced by the potential fluctuations within the bulk, i.e. bulk disorder, break into a collection of interacting equipotential regions and/or quantum dots (QDs). Transport studies through these magnetically confined quantum dots have been carried by scanning tunneling spectroscopy (STS) [1] as well as by direct electronic transport measurements [2]. However, on the latter [2], the magnetically confined QDs were distorted by the PN-NP junctions underneath the metal contacts as well as being partly delimited by the edges of the graphene device. Even though the tunneling processes in QDs are governed by Coulomb interactions and/or by confinement of the wave-like charge carriers, the disorder induced by the rough edges has been hindering the observation of clear wave-like phenomena [3]. Indeed, once the edge disorder removed, the wave nature of the charge carriers emerged, both in transport [4] as in optical measurements [5, 6]. More importantly, the localized states sitting at the graphene edges are known to charge and discharge as a function of the Fermi energy (see Section 6.2), heavily modifying the capacitive coupling and thus making the interpretation of the charging energies unreliable. All in all, the proposed device represents an alternative route to study QDs in graphene, where the presence of bulk disorder and a perpendicular magnetic field assist in building QDs without the limitations introduced by edges. Also in this section, and from the bias spectroscopy data of the magnetically confined QDs, we report the observation of phonon-mediated excited states. Results highlight the importance of electron-phonon interactions in graphene resting on SiO_2 substrates.

The device under study is based on a graphene nano-constriction in series with wide graphene leads (Fig. 4.8a). The wide leads are contacted by 5/100 nm Cr/Au metal electrodes (Fig. 4.8a). The constricted area is used to inject the charge carriers into a magnetically confined QD forming within the lead region, in a similar way a STM tip would locally probe a specific area on the material [1]. The magnetically confined QD has been measured in a 2-terminal configuration (red trace in Fig. 4.8b) by applying a constant bias voltage $V_b = 350 \mu V$ between the source I_S and drain I_D leads (Fig. 4.8a). The two additional voltage probes (noted V_A and V_B in Fig. 4.8a) offer the possibility to measure the device in a 4-terminal configuration (blue trace in Fig. 4.8b).

The SiO_2 substrate is known to induced fair amounts of disorder in graphene on a characteristic length-scale of $\xi_{dis} \sim 30 - 100 nm$ [7]. SiO_2 has been therefore chosen as substrate to increase the probability of forming relatively small QDs with a diameter in the order of the disorder length-scale ($d \approx \xi_{dis}$). Two symmetric side gates V_{SG1} and V_{SG2} (Fig. 4.8a) are build along the edges of the device to disclose the location of the QDs within the sample and the overall charge carrier density is tuned via a back-gate

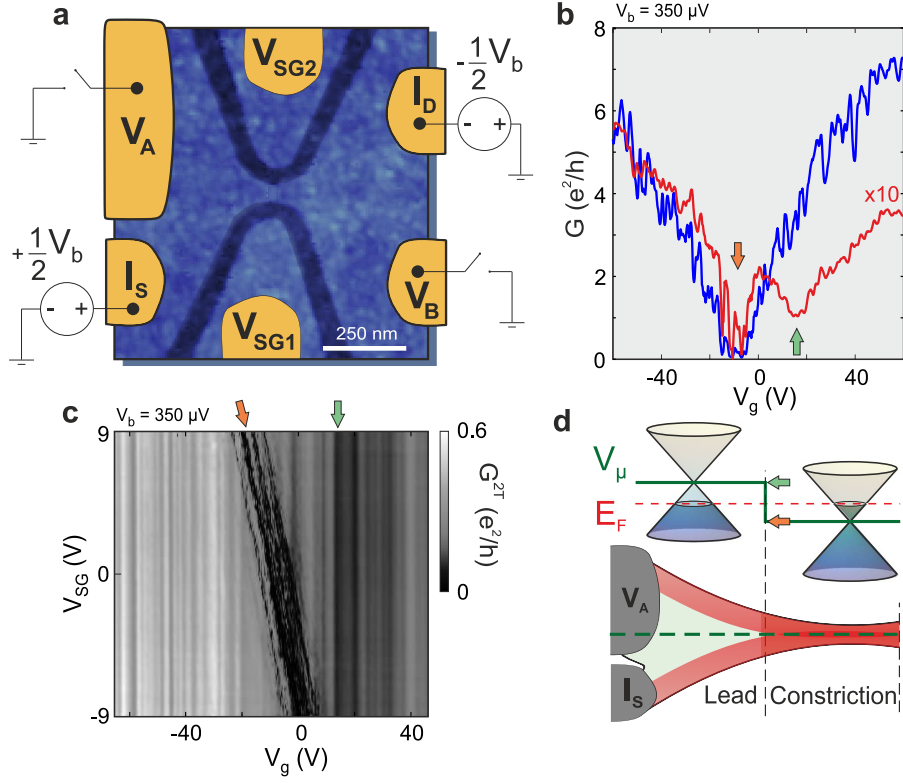


Figure 4.8: **Side-gated graphene constriction and doping distribution.** **a**, False-colored atomic force microscope (AFM) image of a 80 nm -wide graphene constriction. Metal contacts, graphene and SiO_2 -substrate are shown in yellow, blue and dark blue, respectively. The electrical transport is measured in a 2-terminal (I_S and I_D leads) configuration. The side-gate voltages V_{SG1} and V_{SG2} can be operated independently. The metal contacts V_A and V_B are kept open during the 2-terminal operation, allowing to probe the bulk region in the quantum Hall effect (QHE) regime (refer to Fig. 4.9). **b**, 4- and 2-terminal (multiplied by 10) conductance (blue and red traces, respectively). The charge neutrality point of the leads and the constriction are indicated by green and orange arrows, as in panels c and d. $T = 1.7\text{ K}$. **c**, 2-terminal conductance G^{2T} as a function of V_g and a symmetric side-gate voltage $V_{SG} = V_{SG1} = V_{SG2}$ at $T = 1.7\text{ K}$. **d**, Schematic representation of the electrochemical potential V_μ along the graphene device (dashed green line). The green and orange arrows mark the position of the charge neutrality point from leads and constriction.

voltage V_g applied directly to the Si^{++} layer of the Si/SiO_2 chip.

In this section, we report on the observation of charge localization effects through magnetically confined quantum dots solely defined by compressible strips in the Quantum Hall effect (QHE) regime. The device under study was measured in a variable temperature insert (VTI) in magnetic fields ranging from 0 to 9 Tesla. At zero B-field,

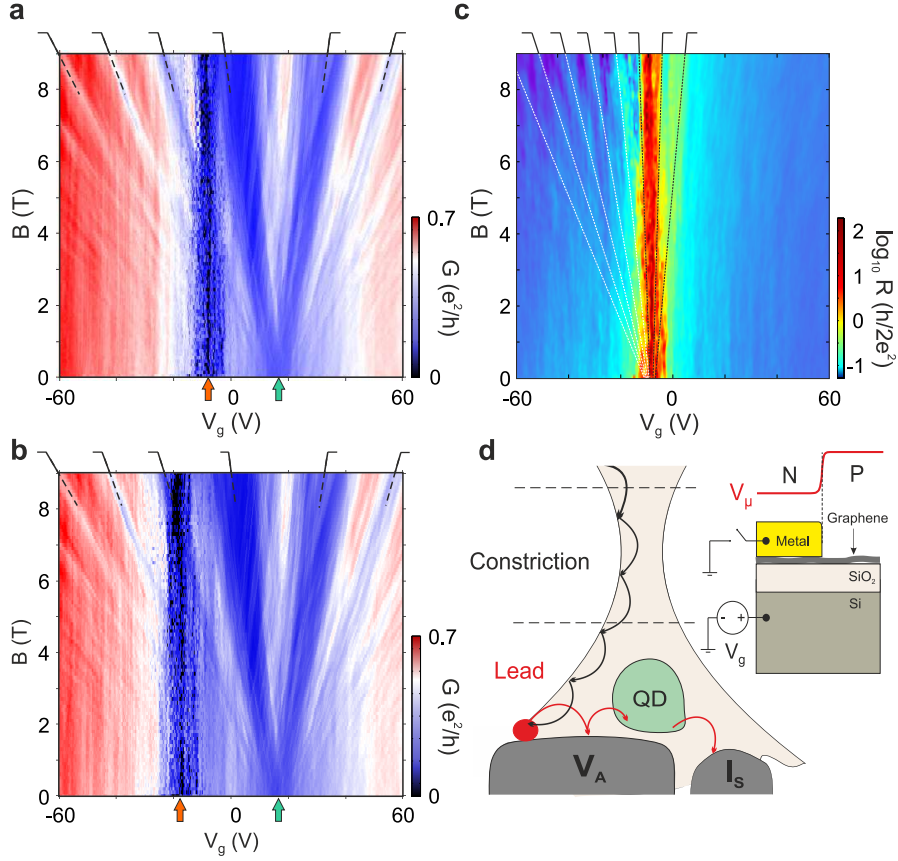


Figure 4.9: **Magnetic field dependence.** **a**, Landau fan of the device shown in Fig. 4.8a, measured in a 2-terminal configuration for $V_{SG1} = V_{SG2} = 0 V$ ($T = 2 K$). The orange and green arrows mark the position of the transport gap and the origin of the Landau fan, respectively. The onsets of the LLs are indicated by black lines **b**, Same as panel a for $V_{SG1} = V_{SG2} = 9 V$. The position of the transport gap (orange arrow) is noticeably shifted. **c**, Landau fan measured in a 4-terminal configuration. The position of the transport gap (red color), coincide with the origin of the Landau fan. The dashed lines represent the theoretical evolution of the Landau levels. **d**, Schematic representation in the QHE regime of the cyclotron orbits in a 2-terminal and a 4-terminal configuration (red and black arrows, respectively). The red point indicates the voltage drop during a 4-terminal operation. The inset shows the PN/NP junction formation underneath the voltage probes.

conductance fluctuations (Fig. 4.8b) typical of disordered graphene (see Section 4.1) already reveal the disordered nature of the transport characteristics. At finite magnetic fields, onsets of Landau quantization are visible for the electron- and hole-transport regimes of the 2- and 4-terminal configurations (see upper black lines in Fig. 4.9a-c). Before discussing how the potential fluctuations develop under finite magnetic fields, it is convenient to clarify the striking differences between the 2- and 4-terminal magneto-transport data (compare panels a and b with panel c in Fig. 4.9).

Doping distribution

In the 2-terminal configuration (red trace in Fig. 4.8b) the voltage range with the lowest level of conductance, i.e. transport gap (see Section 4.1), is attributed to the narrowest graphene region along the electronic path, in that case the graphene constriction (Fig. 4.8a and d). The position of the transport gap in the back-gate voltage axis is noted $V_{cons} \approx -8.5 V$ (orange arrows in Fig. 4.8b-d and Fig. 4.9) and it is expected to depend on an applied side-gate potential V_{SG} (Fig. 4.8a). This is indeed visible in Fig. 4.8c, where we show the 2-terminal conductance as a function of V_g and a symmetric side-gate voltage ($V_{SG} = V_{SG1} = V_{SG2}$). The transport gap evolves as a function of V_{SG} whereas the overall conductance remains unchanged. A second deep in the 2-terminal conductance, noted $V_{lead} \approx 16.6 V$ (green arrow in Fig. 4.8b) is also visible in the 2-terminal conductance map of Fig. 4.8c and it represents the charge neutrality point (CNP) of the bulk graphene region, since it does not depend on the side-gate potential V_{SG} . This behavior is revelatory of a PN/NP junction along the transport path (Fig. 4.8d).

The same situation applies under finite magnetic fields (Fig. 4.9). Again, two distinctive energy scales are recognized. The transport gap (orange arrows in Fig. 4.9a and b) depends on the applied side-gate potential (compare panel a and b of Fig. 4.9) and its back-gate voltage value V_{cons} is the same as in Fig. 4.8b. The CNP of the leads is once more indicated by green arrows (Fig. 4.9b) and it overlaps with the origin of the Landau fan, meaning that the Landau quantization forms within the graphene leads.

The charge neutrality point of the constriction $V_{cons} \approx -8.5 V$ and of the leads $V_{lead} \approx 16.6 V$ (orange and green arrows in Fig. 4.8c and Fig. 4.9a-b) have an associated doping level $n_{cons} = \alpha_{cons} V_{cons} \approx -6 \times 10^{11} cm^{-2}$ and $n_{lead} \approx 1.2 \times 10^{12} cm^{-2}$, where the lever arms α_{cons} and α_{lead} are extracted from the Landau level fans of Fig. 4.9a and c.

All in all, we identified two regions along the graphene device having specific levels of doping. The situation is schematically depicted in Fig. 4.8d, where the Dirac cones of the leads and the constriction lie at different energy levels. This marked difference in doping is expected when considering the edges of graphene as a major source of disorder, e.g doping (see red color along the edges of the graphene device in sketch of Fig. 4.8d). We will demonstrate this assumption later on in Section 4.4.2 by proving the length of the graphene constrictions as being the resonant cavity of Fabry-Pérot-like interferences.

Pathway of the edge states

At high magnetic fields, in the QHE regime, the path of the measured skipping orbits depends on the configuration of the contacts (Fig. 4.9d). In a 4-terminal configuration, the edge states propagate from source I_S to drain I_D (Fig. 4.8a) although the edge state path that is effectively measured is determined by the location where the voltage is probed via the V_A and V_B voltage terminals. The edge state path that is measured in a 4-terminal configuration is represented by a black trace in Fig. 4.9d.

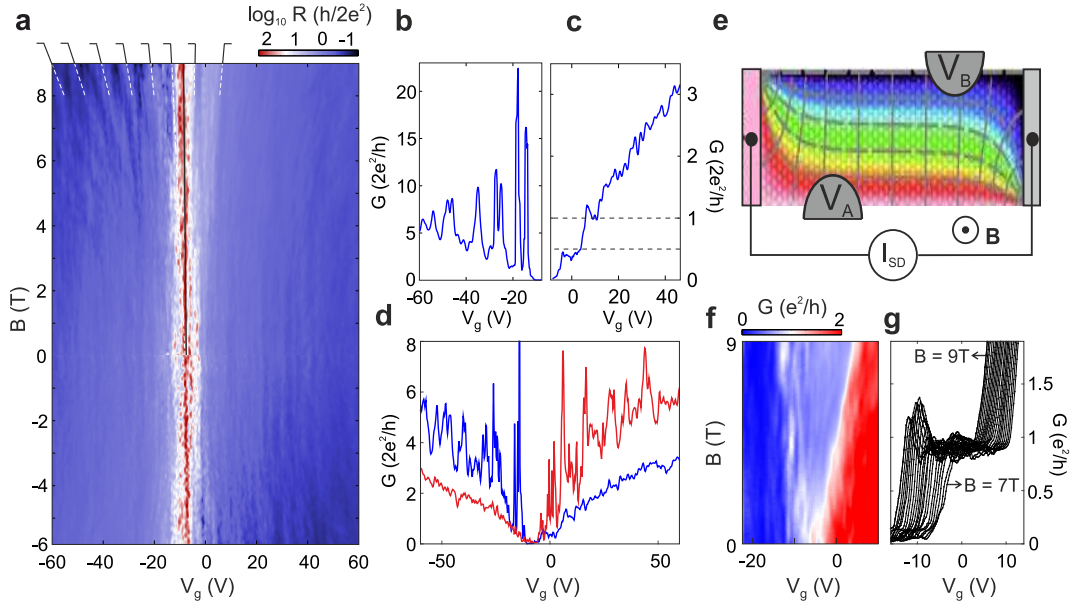


Figure 4.10: **Degeneracy lifting and asymmetry of the Hall potential.** **a**, 4-terminal Landau fan of the device shown in Fig. 4.8a, measured at $T=2\text{ K}$ ($V_b=350\ \mu\text{V}$). **b**, **c**, Line-cuts of G at $B=9\text{ T}$ as a function of back-gate voltage, for the holes (**b**) and electron (**c**) transport regimes. **d**, Line-cuts at $B=+6$ and -6 T (blue and red trace, respectively) of panel **a**, underlining the asymmetry of the hall potential distribution between the potential probes (V_A and V_B in panel **e** and Fig. 4.8a). **e**, Theoretical calculation of a symmetric Hall potential distribution highlighting the formation of hot spots (adapted from [8]). **f**, **g** Color map and conductance traces of the $\nu = e^2/h$ Hall plateau for a second cool-down of the same device. The conductance traces (from $B=7$ to 9 T in steps of 0.1 T) are shifted horizontally for clarity.

In a 2-terminal configuration the measured path comprises the whole travel from source I_S to drain I_D contact. In that case, two different scenarios are a priori possible. In a first case, the edge state may continue underneath the voltage probes V_A/V_B until reaching the Source/Drain lead. We consider this case quite unlikely since the high carrier density of the metal contacts may screen any potential inhomogeneities in the graphene underneath and, as shown in Fig. 4.9a-b and Fig. 4.11a-c, the 2-terminal conductance is cluttered from sharp resonances related to charged puddles with dimensions on the order of $d \approx 80\text{ nm}$ (refer to Fig. 4.16). Moreover, the metallic nature of the voltage probes surely modifies the capacitive coupling of the graphene region underneath. In that case, the origin of the Landau fan would be associated to the doping level of the metal-covered graphene. Instead, we observe the Landau level fan developing at the back-gate voltage value V_{leads} (green arrow in Fig. 4.8 and Fig. 4.9), which correspond to the CNP of the leads measured at zero Tesla.

In the second case scenario, the edge state path follows the boundary of the metal

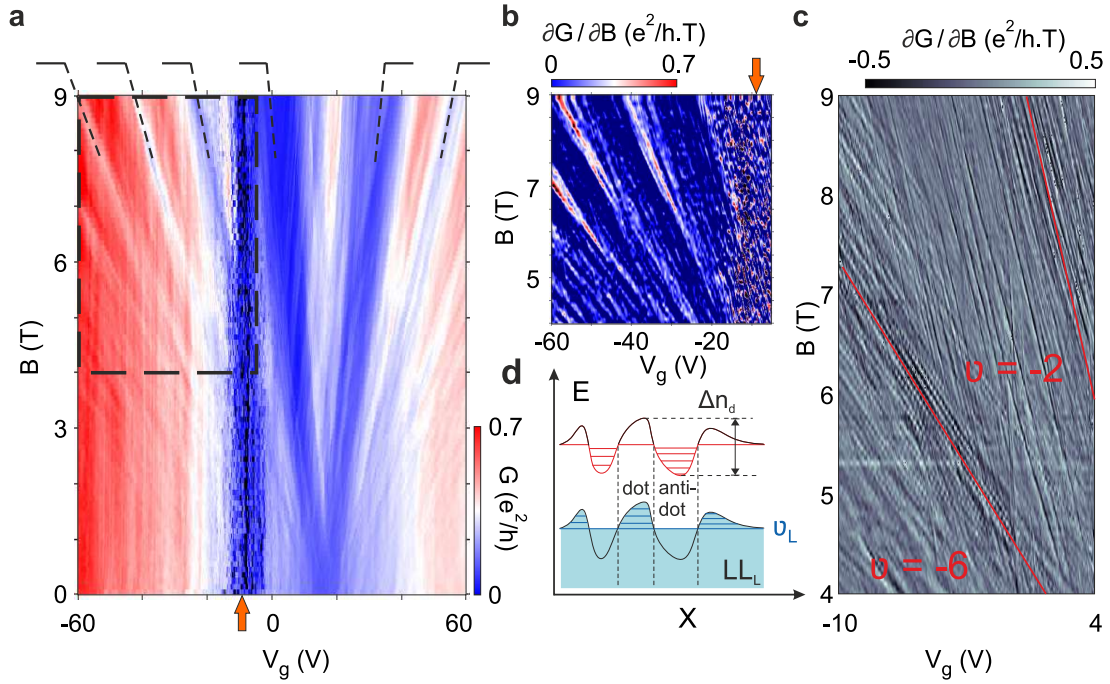


Figure 4.11: **Nature of localization in the Quantum Hall regime.** **a**, 2-terminal Landau fan re-plotted from Fig. 4.9a. **b**, Derivative $\partial G/\partial B$ inside the black dashed box of panel a. The rich structure of parallel lines indicates the position of the Landau levels (LLs). The orange arrow marks the transport gap (also visible in panel a). **c**, High resolution map of the localized states at $\nu = -2$ and $\nu = -6$. Each line/resonance represents the charging event of a localized state. All lines/resonances within the same Quantum phase have an equal slope in the $B - V_g$ plane. **d**, Schematic representation of the confined incompressible patches, represented with their discrete states for dots (blue trace) and anti-dots (red trace) arising from the disorder fluctuations Δn_d , in the quantum Hall regime. The successive lower and upper states ν_L and ν_u see the same potential landscape. The lower Landau level LL_L is colored in light blue.

contact as indicated in Fig. 4.9d by a red "skipping orbit" trace. In order to reach the drain lead I_D , the charge carriers quit the graphene edge and surround the PN/NP junction formed underneath the metal contact V_A . Actually, any metal probe built over the graphene, like the metal electrodes V_A and V_B , may create a potential difference as schematically described in Fig. 4.9d. This build-up PN/NP junction arises from the electric-field screening and the doping induced by the metal contacts on surface of graphene [9, 10]. During a 2-terminal measurement (Fig. 4.9a and b) the voltage probes V_A and V_B (Fig. 4.8a) may thus allow to probe the bulk region (marked as "Lead" Fig. 4.9d) and measure localized states within the bulk (colored in light green in Fig. 4.9d).

At finite B-fields and for the 4-terminal configuration the measured edge state path

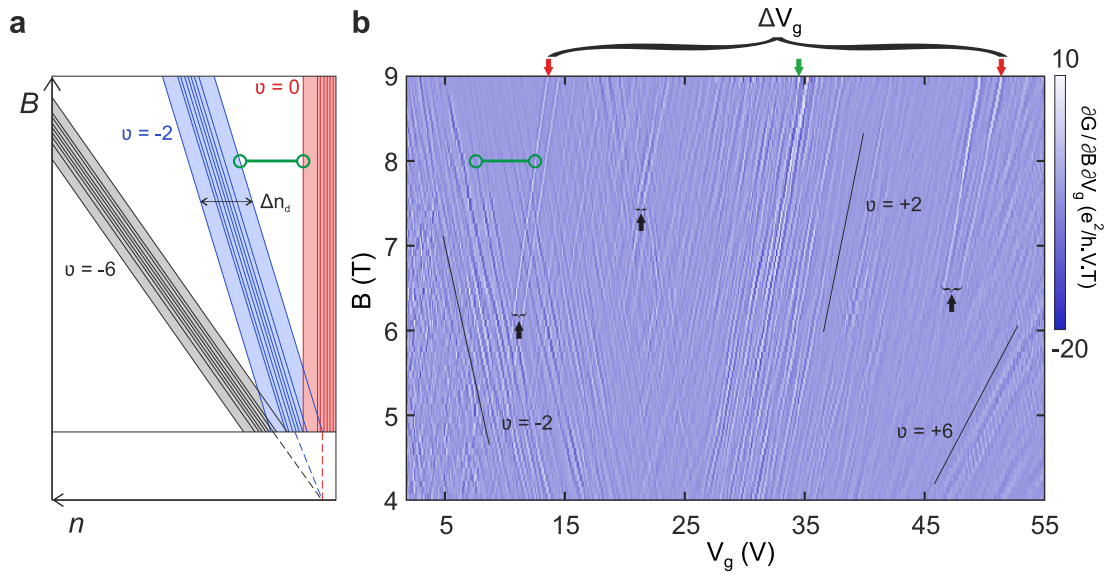


Figure 4.12: **Disorder fluctuations in the (B, V_g) plane.** **a**, Each localized state in the (B, n) plane gives rise to a line that runs parallel to its associated filling factor ν . The strong potential fluctuations in our sample increase the probability to probe individual charging events (marked in green) at the limits of the Landau level region (color shaded). **b**, Derivative of the transconductance $\partial G / \partial V_g \partial B$ around the charge neutrality point of Fig. 4.9a. The rich structure of parallel lines becomes denser around the LLs' position (the green arrow indicates the center of the LL associated to $\nu = +2$). The red arrows mark the left and right foremost resonances, defining the amplitude the disorder fluctuations ΔV_g . The isolated resonances marked in green are probed in Fig. 4.14. The resonance pairs of equal intensity associated to localized states at $\nu = +2$ are indicated by black arrows.

(black trace in Fig. 4.9d) reflects the quantum Hall evolution of the constriction (Fig. 4.9c). The position of the transport gap (high resistance region in Fig. 4.9c) superimposes with the origin of the Landau level fan. Moreover, the capacitive coupling extracted from the 4-terminal Landau fan $\alpha_{cons} \approx 7 \times 10^{10} \text{cm}^{-2} \text{V}^{-1}$ is higher than the value obtained from the 2-terminal measurement $\alpha_{leads} \approx 4.2 \times 10^{10} \text{cm}^{-2} \text{V}^{-1}$. These differences are expected when we consider the narrower graphene constriction to be better coupled to the back-gate than the bulk [11]. The lever arm, or capacitive coupling, is extracted by comparing the Landau quantization model to the measurements (see Section 6.1).

A closer look at the magnetic evolution of the 4-terminal conductance (Fig. 4.10) reveals insightful information on the electronic structure of the graphene constriction. A line-cut at $B = 9 \text{T}$ of the Landau fan in Fig. 4.10a reveals a strong asymmetry of the voltage measured between the V_A and V_B probes (Fig. 4.8a). Indeed, the Landau level quantization manifests as conductance oscillations on the hole-side of the transport regime (Fig. 4.10b), although on the electron-side (Fig. 4.10c) Hall conductance plateaus are clearly visible. Same observations have been reported on 2-terminal Quantum Hall

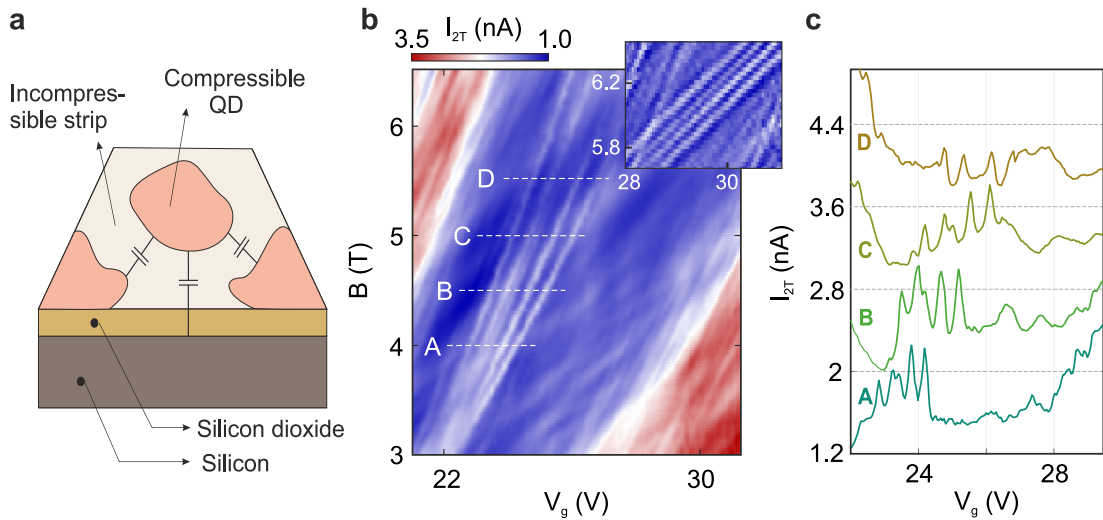


Figure 4.13: **Isolated charging events.** **a**, Representative sketch of the graphene surface tearing into compressible regions in the quantum Hall regime. The magnetically confined QDs (light red) are capacitively interacting with the surroundings. **b**, Close-up of four adjacent resonance lines issued from incompressible patches at $\nu = +2$. Inset shows four isolated charging events associated to $\nu = +6$. **c**, Coulomb blockade peaks from the resonance lines shown in panel b, measured at finite values of B-field. The spacing between peaks increase as a function of B-field.

measurements on suspended graphene devices [12, 13] and the explanation has been attributed to asymmetries in the Hall voltage distribution [8, 14]. To corroborate this point, we measure the Landau fan for negative B-field values (Fig. 4.10a). The line cuts at $B = +6$ and -6 T (blue and red traces in Fig. 4.10f, respectively) proves the conjecture that asymmetric hot spots are indeed present in our graphene device (Fig. 4.10e) and that disorder inhomogeneities lie presumably at the origin of the asymmetries in the hall voltage distribution [13, 14].

Once discussed the observation of the QH regime in our sample, the fine details of the electronic structure come into play. The lifting of four-fold degenerate Landau levels is apparent for electron-side of the Landau fan (Fig. 4.10c, f and g), where the presence of well defined Hall plateau at $\nu = +1$ confirms the broken symmetry nature of the quantum Hall sequence.

The nature of localization at finite magnetic fields.

As mentioned in the introduction, the proposed device allows us to investigate localization phenomena in graphene with the possibility to tune both the charge carrier density and the magnetic field. At finite B -fields we observe sets of localization resonances packed around the evolution of the Landau levels (Fig. 4.11b and c). This behavior is expected to happen as a Landau level approaches initial/complete filling and the density of states available is unable to flatten the bare disorder potential (see Fig. 4.11d)

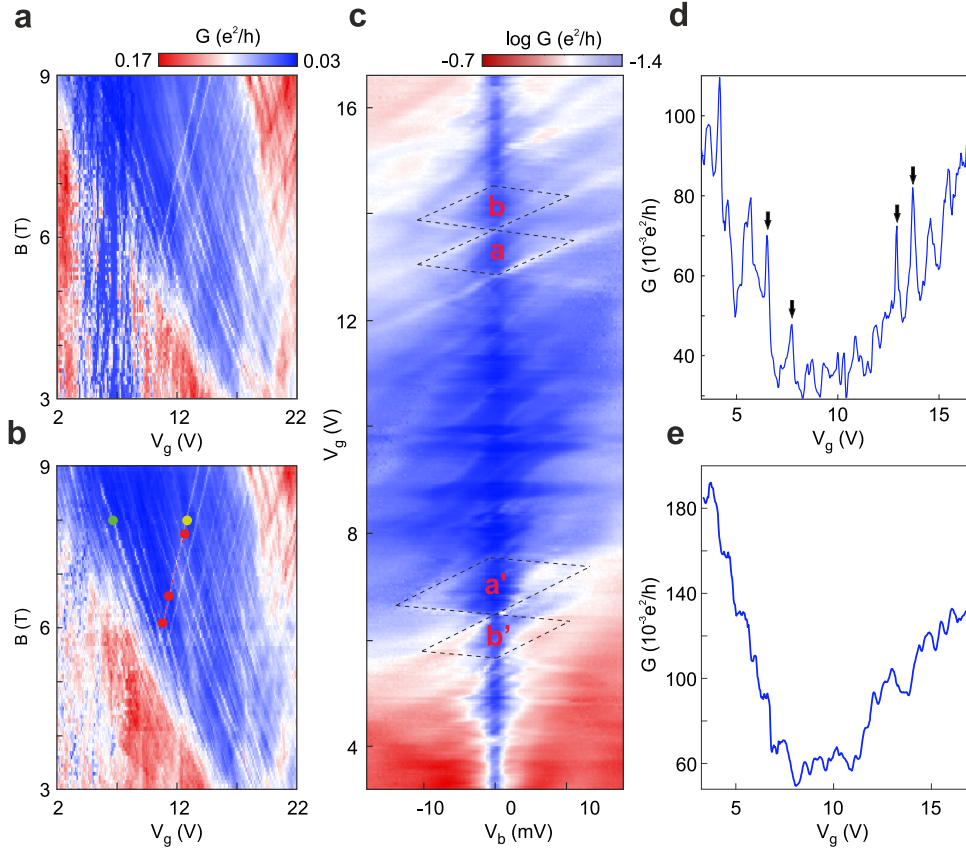


Figure 4.14: **Single electron charging of magnetically confined states.** **a** and **b**, High-resolution maps of the Landau fan shown in Fig. 4.11a. The evolution of the charging events (resonances) in the (B, V_g) plane are independent to the configuration of the side gates ($V_{SG1} = V_{SG2} = 0 V$ in panel a and $V_{SG1} = V_{SG2} = 9 V$ in b). The green and yellow dots indicate the resonances probed in panel c. The yellow and red dots highlight the acquisition points of the bias spectroscopy measurements in Fig. 4.16a-d. **c**, Bias spectroscopy measurements of the $\nu = +2$ (upper diamonds) and $\nu = -2$ (lower diamonds) states at $B = 8 T$ and $T = 15 mK$, as a function of bias V_b and back-gate V_g voltage for $V_{SG1} = V_{SG2} = 9 V$. The number of charge carriers is fixed in each diamond. The labels a, b and a', b' indicate the number of electrons and holes, respectively. **d**, **e**, Conductance line-cuts of the conductance map in panel c, showing the consecutive Coulomb resonances at $V_b = 0 V$ (black arrows in panel d) and its evolution into conductance steps at high-bias voltages $V_b \approx -12 mV$ (panel e).

[15, 16]. Potential barriers emerge and eventually form compressible regions enclosed by incompressible strips [15, 17], thus creating the so-called magnetically confined QDs (Fig. 4.13a and Fig. 4.16f). Fig. 4.11c shows two distinct groups of localized states around the $\nu = -2$ and $\nu = -6$. The resonances/lines are cluttered around well develop QHE phases which therefore helps in determining the location of the LLs in the $B - V_g$

plane. As we can see in Fig. 4.11a, the onsets of LLs are marked by dashed black lines at the top of the Landau fan. These positions correspond to regions with higher density of resonances (red colored regions in Fig. 4.11b).

For the sake of completeness we will review the basics of localization under Quantum Hall regime [15, 16]. We sketch the expected evolution of the localized states in the $B - V_g$ plane in Fig. 4.12a, with a measured data set appearing in Fig. 4.12b. As reported in literature [15], the number of states or resonance lines within each phase should be constant and independent on the B -field. Moreover, each group of resonances forms strips of constant width Δn_d that relates to the amount of disorder in the sample (Fig. 4.11d). Furthermore, the localized states with an equal slope in the $B - V_g$ plane belong to the same underlying phase. In fact, the slope of the resonance lines is proportional to $\Delta B/\Delta V_g = h/e\nu$ since the filling factors are proportional to the flux quanta enclosed by the magnetically confined area $\nu = hn/eB$ (see Section 2.2). Owing to these experimental observations, the single-particle description (wave-confinement) of the localization phenomena does not hold. Specifically, if one considers the states of the magnetically confined QDs arising from wave-function confinement quantization, any increase of the B -field, and thus of the number of flux quanta through the resonant cavity, should make shrink its dimensions in order to keep the filling factor constant. Instead, although the filling factor is conserved for a varying B -field, the number of localized states appears also constant, which is in clear conflict with the expected increase of localized states per unit surface when their dimensions shrink as a function of B -field. For a more detailed argumentation please refer to [15, 16].

The energy scale associated to the disorder potential fluctuations (Fig. 4.12b) is relatively large $\Delta n_d \approx \hbar v_F \sqrt{\pi \alpha_{leads} \Delta V_g} \approx 145 \text{ meV}$, which indicates the strong doping fluctuations within our sample ($\Delta V_g \approx 38 \text{ V}$, see Fig. 4.12). Although strong disorder is usually undesired, in our case it increases the probability to probe individual localized states at the boundaries of a quantum phase (marked by red arrows in Fig. 4.12b). An example of isolated resonant lines are shown in Fig. 4.13b, along with line-cuts of the conductance at finite magnetic fields (Fig. 4.13c). The bias spectroscopy of the resonances shown in Fig. 4.13 can be found in Section 8.1.

It is important to note that resonances associated to a quantum phase $\nu = \pm 2$ should evolve in pairs (see Fig. 4.14b). Similarly, the regions issued from regions at $\nu = \pm 4, \pm 6, \dots$ should evolve in groups of four (see inset of Fig. 4.13b), owing to the spin- and valley-degeneracy of the half-integer Landau levels in graphene [1].

Eventhough the resonances should in principle run parallel to each other as a function of magnetic fields [15], we observe them to slightly split as a function of magnetic field (Fig. 4.14f and resonance pairs marked by a black arrow in Fig. 4.12b). Their evolution in the $V_g - B$ plane (Fig. 4.12 indicates that the splitting may be indeed related to the lifting of the four-fold degeneracy discussed previously for the constriction region (Fig. 4.10). Same conclusions were suggested in [1] to account for the increased energy splitting between charging peaks in STS experiments.

Bias spectroscopy of localized states under B -fields.

Having isolated charging lines in the $V_g - B$ allows to probe them via bias spectroscopy measurements (Fig. 4.14). We study the resonance lines marked by green circles in Fig. 4.12 and by a green and a yellow dot in Fig. 4.14b as a function of bias voltage V_b . A detailed plot of the conductance as a function of back-gate V_g and bias V_b voltages (Fig. 4.14c) reveal diamond-like structures characteristic of Coulomb blockade physics (dashed white lines in Fig. 4.14c). The bias spacing of each individual diamond is the energy required to add an additional charge carrier into the system (E_{add}). The charging phenomena is observed for an anti-dot (marked in red in Fig. 4.11d) of a $\nu = +2$ phase region, and for a dot (marked in blue in Fig. 4.11d) of a $\nu = +2$ exhaustion region. Their respective electronic filling sequence is labeled "a" and "b" for the anti-dot system, and "a'" and "b'" for the dot (Fig. 4.14c). A line-cut of the conductance at $V_b = 0 V$ (Fig. 4.14d) shows the well known Coulomb resonances, where the energy spacing between consecutive charging peaks is equal to the charging energy E_{add} . At high bias voltages ($V_b \approx -12 mV$), the conductance develops from a Coulomb peaks structure to equidistant steps in conductance (Fig. 4.14e). It is important to note that the charging peaks start to develop at around $B = 3.5 T$ (Fig. 4.14a, b and f) and remain visible up to $B = 9 T$, meaning that the magnetically confined QDs are stable for a wide-range of B -fields.

Once the localized states identified, we will give further insights on where the QDs are located within the sample. As observed in panel a and b of Fig. 4.14, the measured Landau level evolution corresponds to a graphene region located far from the edges (i.e. bulk graphene), since a change in the side-gate potential (V_{SG1} and V_{SG2} in Fig. 4.8a) just modifies the position of the transport gap (associated to the edges and constriction). Fig. 4.14a shows a close-up region around $\nu = \pm 2$ for $V_{SG1} = V_{SG2} = 0 V$ and Fig. 4.14b for $V_{SG1} = V_{SG2} = 9 V$. The same behavior is observed in the bias spectroscopy measurements for the two configurations of the lateral gates (Fig. 4.15). Both for $V_{SG1} = V_{SG2} = 0 V$ (panels a-b) and $V_{SG1} = -V_{SG2} = 9 V$ (panels c-d), the charging events (diamonds plots inside the black rectangles in Fig. 4.15b and c) remain unaffected, whereas the transport gap regions (delimited by black dashed lines) are modified.

High resolution maps of the "a" electron charging event (see bias spectroscopy data in Fig. 4.16a-d) show clear excited states. The diamond plots have been taken at finite values of magnetic fields ($B = 6.1, 6.6, 7.7$ and $8 T$). As observed, the charging energy $E_C \approx 10.5 meV$ is constant as a function B -field, with variances in the order of $\sim 0.5 meV$. We conclude that the magnetic field does not modify the dimensions of the QD and may thus be purely determined by disorder and the electrostatics. This result, represents the first experimental demonstration supporting the hypothesis introduced by S.Illani in [15].

Presence of the excited states and implications.

The observation of excited states in graphene QDs has been widely reported in literature [18, 19] but it is significant the fact that excited states occur in the quantum Hall regime. To demonstrate that the analyzed QD is in the Quantum Hall regime, we

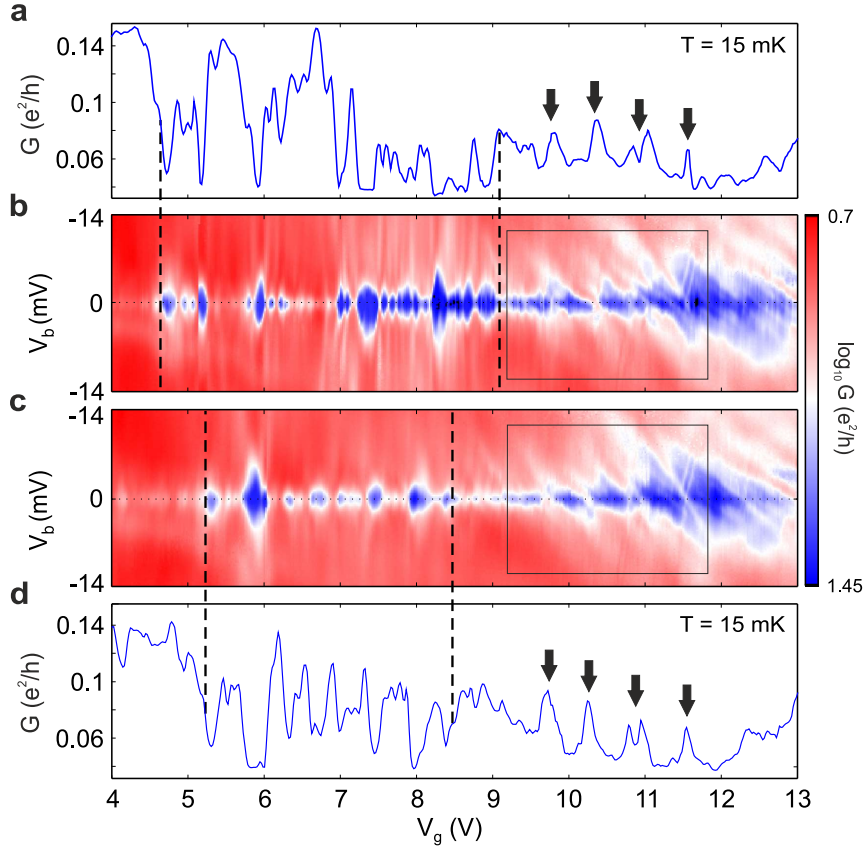


Figure 4.15: **Side-gate dependence of the confined states.** **a, d**, 2-terminal conductance traces at $V_b = 0 V$, extracted from the bias spectroscopy maps shown in panel **b** and **c**, respectively. The four consecutive Coulomb peaks are marked by black arrows. The transport gap region is delimited by dashed black lines. **b, c**, Bias spectroscopy maps measured at $B = 6 T$ and $T = 15 mK$ for $V_{SG1} = V_{SG2} = 0 V$ (**b**) and $V_{SG1} = -V_{SG2} = 9 V$ (**c**). The regions inside the black rectangles are qualitatively unaffected by a lateral potential (V_{SG1}, V_{SG2}).

map the position in the back-gate voltage axis of the first charging event from the "a" diamond as a function of magnetic field (Fig. 4.16e). The extracted values (indicated by red dots in Fig. 4.14a-d) clearly superimpose the evolution of the magnetic resonance, confirming that the magnetically confined QD follows the $\nu = +2$ quantum phase [15, 16]. A schematic representation of a magnetically confined QD in the QHE regime is shown in Fig. 4.16f, with the edge states represented in red.

To understand the implications of having excited states in magnetically confined QDs we briefly review the basic operation of QDs and Single Electron Transistors (SETs). The term SET is used when all quantum mechanical energy scales can be neglected compared to the electrostatic contributions. For SETs, the energy needed to tunnel one charge carrier into the system is solely determined by the addition energy $E_{add} = e^2/C_{tot}$, also known as charging energy E_C [20]. In that case, C_{TOT} is the self-

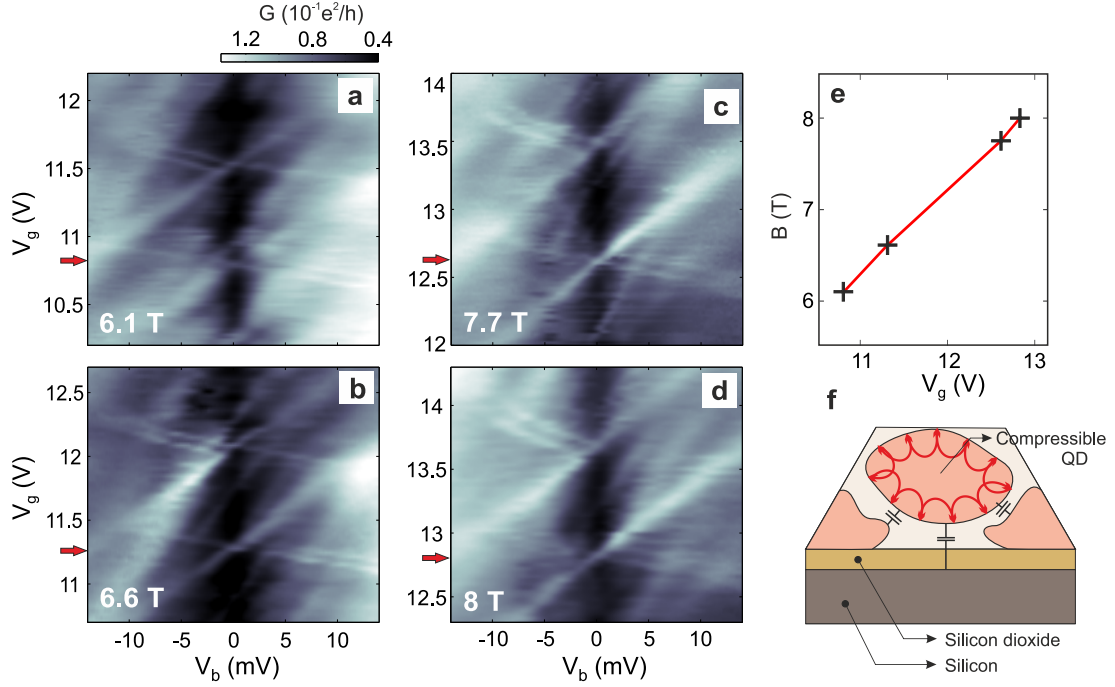


Figure 4.16: ***B*-field dependence of the magnetically localized states.** **a, b, c** and **d**, High resolution measurements of the diamond associated to the electron "a" in the quantum Hall phase $\nu = +2$, measured at $T = 15 \text{ mK}$ and $B = 6.1, 6.6, 7.7$ and 8 T (panels a, b, c and d, respectively). Excited states are visible in all diamonds. **e** Magnetic evolution of the first tunneling event, noted "a" in Fig. 4.14, of the QD as a function of back-gate voltage V_g . The crosses correspond to the values in back gate voltage extracted from panels a to d (red arrows) where the charging events happen. **f** Schematic representation of a magnetically confined QD. The skipping orbit inside the confined area highlights that the QD is itself in the quantum Hall regime.

capacitance of the charged island of diameter d . In QDs though, the addition energy is defined as $E_{add} = e^2/C_{tot} + \Delta$, where Δ is the so-called level spacing that stems from the size confinement of the electron wave-function.

The distinction between QDs and SET is done by comparing its dimensions to the Fermi wave-length (λ_F). For small enough charged island, i.e. for island dimensions in the order of the Fermi wave-length ($d \sim \lambda_F$), the charged island is considered to behave as a QD and Δ applies in the calculation of the addition energies $E_{add} = e^2/C_{tot} + \Delta$. Otherwise, i.e. for $d \gg \lambda_F$, we define the charged island as a SET and the size confinement contribution Δ can be discarded for the calculation of $E_{add} = e^2/C_{tot}$ [20].

Although not strictly correct, the observation of excited states in bias spectroscopy measurements is usually directly attributed to the presence of electronic excited states [18]. Their associated energy-scale is calculated as a single-particle level spacing $\Delta = \hbar v_F / (d\sqrt{N})$, where $v_F \approx 10^6 \text{ m/s}$ is the Fermi velocity [21] and N the number of charge carriers in the dot [18, 20]. In our case (see Fig. 4.16 and Fig. 8.3), the extracted values

of level spacing Δ of our magnetically confined QD for $B=6.1, 6.6, 7.7, 8T$ are mostly equal, with $\Delta \approx 1.2 \pm 0.1 meV$. The fact to have a constant, B -field independent Δ is in contradiction with the expected $(1/\sqrt{N})$ -dependency of Δ . As shown in Fig. 4.16e and Fig. 4.14 (see red and yellow points in panel b) the charging phenomena is attributed to a magnetically confined region in the quantum Hall phase $\nu=+2$. Owing to $\nu=(hn)/(eB)$ and the fact that magnetic QD is not supposed to change its dimensions as a function of B -field (see argumentation in [15, 16]), we would therefore expect an increase in the number of charge carriers inside the QD as a function of magnetic field. The fact to observe a charge carrier independent energy of the excited states when the charge island surely changes its number of carriers as a function of B -field, is already a first indication that we are not dealing with electronic excited states.

Even though, we can still estimate the single particle level spacing using the model of a quantum mechanical harmonic oscillator [20] for the quantized states $\Delta = hv_f/2L_c$, where L_c is the length-scale of the resonant cavity (see Section 4.4.2). Under QHE conditions we expect the wave-function of the charge carriers to couple to the circumference L_c of the QD rather than to its diameter. Furthermore, this expression for Δ does not depend on the charge carriers inside the QD, which conveys with the experimental observations (Fig. 4.16). We therefore obtain a length-scale $L_c \approx 1.7\mu m$ from the $\Delta \approx 1.2 meV$ extracted from measurements. The associated diameter reads $d_1 = L_c/\pi \approx 550 nm$.

To put this diameter value d_1 into perspective, we will compare it to the diameter of the the QD considering just the electrostatic contributions. Neglecting the confinement energy, the addition energy is then solely determined by $E_{add} = e^2/C_{TOT}$, which enables a much rigorous read-out of the energy scales. Here we extract an addition energy $E_{add} \approx 12.0 meV$ (Fig. 4.16 and Fig. 8.3), Using a disc model, we can estimate the effective charge island diameter to be $d_2 = e^2/(4\epsilon_0\epsilon E_{add}) \approx 80 nm$, with $\epsilon = (1 + 4)/2$.

This value of diameter ($d_2 \approx 150 nm$) is comparatively much smaller than the diameter extracted from excitation energy ($d_1 \approx 550 nm$). We attribute this strong disagreement between both extracted diameters as a indication that the excited states observed in the bias spectroscopy data are not issued from electronic excited states.

During recent years, conjectures arose whether the enhanced conductance lines parallel to the edges of the Coulomb diamonds, i.e. excited states, are undoubtedly due to transport through excited states [22]. Possible scenarios leading to similar effect in the bias spectroscopy measurements have been proposed, such as modulation of the tunnel coupling due to resonances in the constrictions [23, 24] and phonon mediated transport effects [25].

Due to the lack of constrictions in our QD system, where the QD is magnetically confined around a potential valley, we discard fluctuations of the density of states in the constriction as possible origin for the lines of enhanced differential conductance outside the Coulomb diamonds. Instead, we suggest these lines as being the result of phonon mediated transport in our graphene QDs on Silicon dioxide substrates. In fact, it has been shown that such lines can also appear due to phonon mediated transport in suspended quantum dots in different material systems [26–28]. Indeed, this results may

explain the lack of excited states found in graphene QDs studies on hBN substrate [3].

A rather important implication of our results, points out that the observation of excited states does not directly implies the presence of electronic excited states (i.e size confinement effects) and that, in graphene QDs on Silicon dioxide substrates, phonon-electron interactions may be a relevant effect.

Conclusions.

In this section we developed a reliable and reproducible way of studying Coulomb blockade-based QDs in graphene. The device under study appears as a valid experimental turnaround to overcome the limitations introduced by the edges and/or the constriction barriers in traditional etched QDs. An altered local density of states, an A-B sub-lattice symmetry breaking or a modulation of the tunnel coupling due to resonances in the constrictions, have been traditionally identified as a source of uncertainty for the proper identification of size-confinement effects in graphene. Under finite magnetic fields, we firstly unveil the differences and the characteristics transport paths of the two- and four-terminal configurations of the conductance on graphene quantum point contacts. We identify the presence of resonances and localization effects within the bulk region and we focus our analysis on an individual magnetically confined QD. The magnetic evolution of the charging events and its accurate analysis allow us to rule-out size confinement effects as the origin of the excited states. More importantly, we suggest electron-phonon interactions as the mechanism behind the observed lines of enhanced differential conductance outside the Coulomb diamonds.

References

1. Jung, S. *et al.* Evolution of microscopic localization in graphene in a magnetic field from scattering resonances to quantum dots. *Nature Physics* **7**, 245–251 (2011).
2. Moriyama, S. *et al.* Field-induced confined states in graphene. *Appl. Phys. Lett.* **104**, 053108 (2014).
3. Engels, S. *et al.* Etched graphene quantum dots on hexagonal boron nitride. *Appl. Phys. Lett.* **103**, 073113 (2013).
4. Wang, X. *et al.* Graphene nanoribbons with smooth edges behave as quantum wires. *Nature Nanotechnology* **6**, 563–567 (2011).
5. Ryu, S. *et al.* Raman Spectroscopy of Lithographically Patterned Graphene Nanoribbons. *ACS Nano* **5** (5), 4123–4130 (2011).
6. Terrés, B. *et al.* Raman spectroscopy on mechanically exfoliated pristine graphene ribbons. *Physica status solidi (b)* **12**, 251, 2551–2555 (2014).
7. Xue, J. *et al.* Scanning tunnelling microscopy and spectroscopy of ultra-flat graphene on hexagonal boron nitride. *Nat. Mat.* **10**, 282 (2011).
8. Kramer, T. *et al.* Theory of the quantum Hall effect in finite graphene devices. *Phys. Rev. B* **81**, 081410(R) (2010).
9. Giovannetti, G. *et al.* Doping Graphene with Metal Contacts. *Phys. Rev. Lett.* **101**, 026803 (2008).
10. Xia, F. *et al.* The origins and limits of metal graphene junction resistance. *Nature Nanotechnology* **6**, 179–184 (2011).
11. Vera-Marun, I. J. *et al.* Quantum Hall transport as a probe of capacitance profile at graphene edges. *Appl. Phys. Lett.* **102**, 013106 (2013).
12. Du, X. *et al.* Fractional quantum Hall effect and insulating phase of Dirac electrons in graphene. *Nature* **462**, 192–195 (2009).
13. Williams, J. R. *et al.* Quantum Hall conductance of two-terminal graphene devices. *Phys. Rev. B* **80**, 045408 (2009).
14. Abanin, D. A. Conformal Invariance and Shape-Dependent Conductance of Graphene Samples. *Phys. Rev. B* **78**, 035416 (2008).
15. Ilani, S. *et al.* The microscopic nature of localization in the quantum Hall effect. *Nature* **427**, 328–332 (2004).
16. Martin, J. *et al.* The nature of localization in graphene under quantum Hall conditions. *Nature Physics* **5**, 669–674 (2009).
17. Lee, D. S. *et al.* Transconductance Fluctuations as a Probe for Interaction-Induced Quantum Hall States in Graphene. *Phys. Rev. Lett.* **109**, 056602 (2012).
18. Schnez, S. *et al.* Observation of excited states in a graphene quantum dot. *Appl. Phys. Lett.* **94**, 012107 (2009).
19. Volk, C. *et al.* Probing relaxation times in graphene quantum dots. *Nature Communications* **4**, 1753 (2013).

20. Kekulé, A. *Semiconductor Nanostructures: Quantum States and Electronic Transport*. Oxford University Press (2010).
21. Neto, A. H. C. *et al.* The electronic properties of graphene. *Reviews of Modern Physics* **81**, 109–110 (2009).
22. Jacobsen, A. *et al.* Finite-bias spectroscopy of a three-terminal graphene quantum dot in the multilevel regime. *Phys. Rev. B* **89**, 165413 (2014).
23. Molitor, F. *et al.* Observation of excited states in a graphene double quantum dot. *EPL (Europhysics Letters)* **6**, 89 (2010).
24. Güttinger, J. *et al.* Graphene quantum dots in perpendicular magnetic fields. *Physica status solidi B* **246**, 11, 2553–2557 (2009).
25. Roulleau, P. *et al.* Coherent electron phonon coupling in tailored quantum systems. *Nature Communications* **2**, 239 (2011).
26. Weig, E. M. *et al.* Single-Electron-Phonon Interaction in a Suspended Quantum Dot Phonon Cavity. *Phys. Rev. Lett.* **92**, 046804 (2004).
27. Sapmaz, S. *et al.* Tunneling in Suspended Carbon Nanotubes Assisted by Longitudinal Phonons. *Phys. Rev. Lett.* **96**, 026801 (2006).
28. Leturcq, R. *et al.* Franck Condon blockade in suspended carbon nanotube quantum dots. *Nature Physics* **5**, 327–331 (2009).

4.3 Evidences of an edge-induced disorder

In the following section I will analyze the crystallographic fingerprints of clean graphene edges. Samples will be investigated by means of Raman spectroscopy experiments, allowing us to characterize the edge quality of our newly developed fabrication technique. Results will be compared to the abundant literature on Raman spectroscopy measurements on scattering-related phenomena at the graphene edges [1–7].

4.3.1 Raman spectroscopy on mechanically exfoliated pristine graphene ribbons

This section has been published in:

Raman spectroscopy on mechanically exfoliated pristine graphene ribbons
B. Terrés, S. Reichardt, C. Neumann, K. Watanabe, T. Taniguchi and C. Stampfer
Physica Status Solidi B **251**, 2551-2555 (2014)
© 2014 WILEY-VCH Verlag GmbH & Co. KGaA

Graphene nanoribbons have been extensively studied in the past years [8–13], mainly due to their promise of an electronic band-gap making them interesting for electronic applications. Confinement of electrons in these nano-scaled structures is predicted to form a quasi one-dimensional system [9] with its properties strongly depending on the configuration of the edges [14, 15]. However, experimental and theoretical studies have revealed graphene nanoribbons to be extremely sensitive to small amounts of disorder, in particular to edge disorder [16, 17]. In fact, the transport characteristics of nano-structured graphene ribbons are mainly dominated by statistical Coulomb blockade effects [12, 18]. Improvements on the fabrication techniques allowing for cleaner edge configurations are therefore of great importance and may not only improve the transport properties [19] but also enable the investigation of the unique vibrational properties of these graphene nanostructures [1]. Despite theoretical work [2, 3] there are - to our knowledge - only a few optical characterization studies of graphene nanoribbons [4, 5].

Raman spectroscopy of carbon materials, in general, has been identified as a powerful tool for determining the number of graphene layers [20, 21], the local amount of strain and doping [22], and for studying electron-phonon interactions [15, 23–25] and therefore the electronic properties themselves.

In this work, we report on Raman spectroscopy measurements on non-etched graphene ribbons of various widths (from ~ 15 to 160 nm) resulting from peeling-off a graphene flake on the boundary region of a hexagonal boron nitride (hBN) flake and its underlying SiO₂ substrate. We show that the characteristic signatures of single-layer graphene are well preserved and that the configuration of the edges is more regular compared to previously studied graphene ribbons fabricated by state-of-the-art reactive ion etching (RIE) techniques [4, 5]. Moreover, the analysis of the full width at half maximum (FWHM) of the G- and 2D-line (Γ_G and Γ_{2D}) as well as the frequency of the G- and 2D-line (ω_G and ω_{2D}) provide strong indications of finite size and/or edge effects [2, 3, 5].

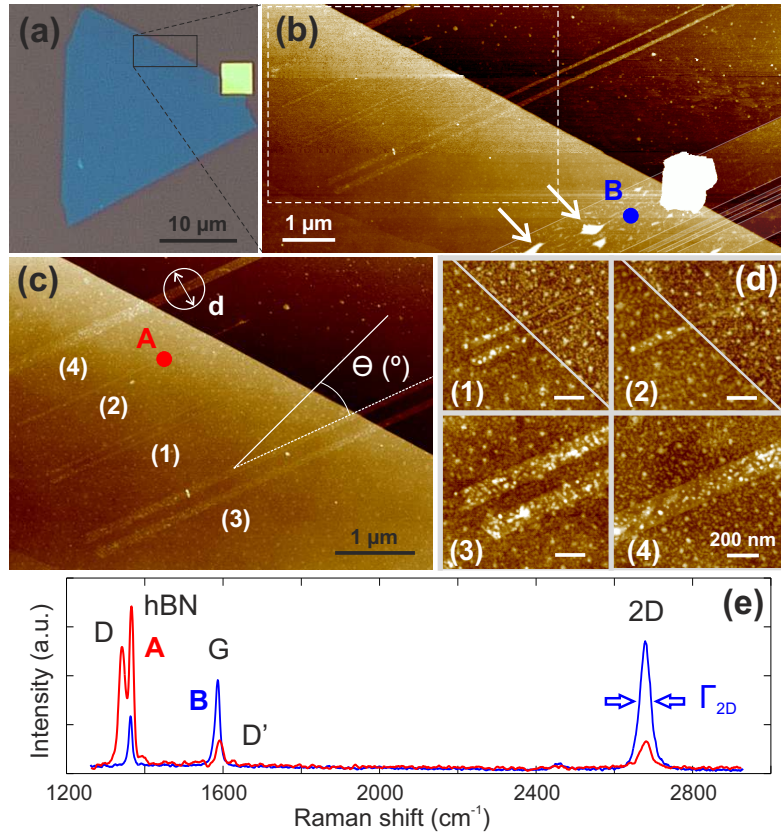


Figure 4.17: **a**, Optical microscope image of a ~ 30 nm thin hBN flake (light blue color) on top of a Si/SiO₂ substrate (grey color). **b**, **c**, and **d**, Scanning force microscope (SFM) images taken in the region highlighted by the black box in panel (a). **c**, SFM close-up image of the white-dashed box in panel (b). In this region the ribbons are separated by a distance of around $1 \mu\text{m}$, twice as large as the spot-size $d \approx 500$ nm (white circle) of the linearly polarized laser with an angle θ . **d**, SFM close-ups of the ribbons (1), (2), (3) and (4), also displayed in panel (c). Ribbons (1) and (2) do not have a constant width, as highlighted in the two upper subpanels of panel (d). We show the wider and narrower ends of these ribbons. **e**, Characteristic Raman spectra of bulk graphene on hBN [acquisition point B in panel (b)] and of ribbon (2) [acquisition point A, panel (c)].

Fabrication.

The fabrication of the graphene ribbons is based on purely mechanical exfoliation of graphite. We initially prepared Si/SiO₂ samples with deposited hBN flakes (Fig. 4.17a). The hBN flakes have been mechanically exfoliated from pure hBN crystals and deposited onto the Si/SiO₂ substrate. Thereafter, the samples were immersed in a piranha solution, 3:1 mixture of sulfuric acid (H₂SO₄) and 30% hydrogen peroxide (H₂O₂), for 3 minutes and later rinsed with ultrapure water. This cleaning procedure has a similar effect on the SiO₂ surface than a plasma etching step prior deposition of the graphene

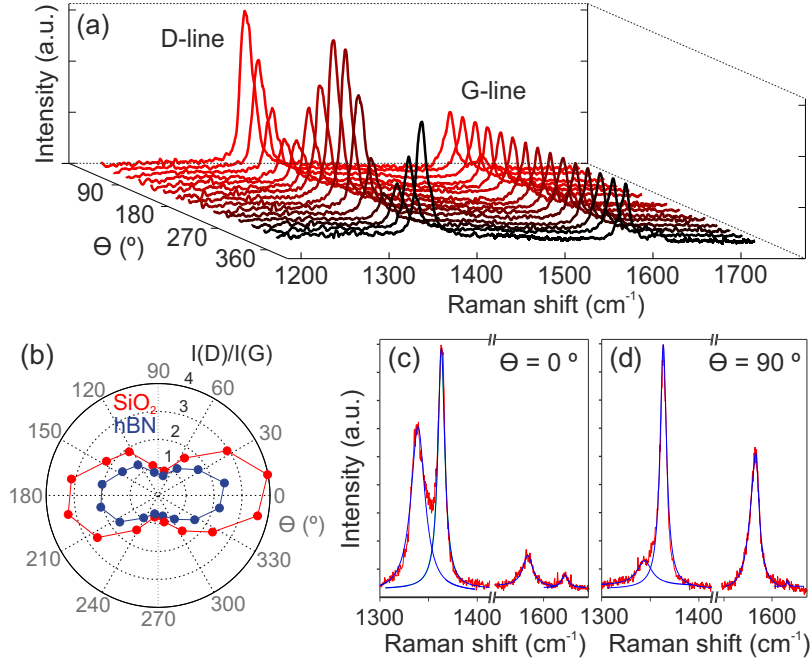


Figure 4.18: **a**, Raman spectra (D- and G-line) of the ribbon (3) on SiO₂ as a function of the polarization angle θ (see Fig. 4.17c). The difference in polarization angle between subsequent traces is $\theta = 22.5^\circ$. The Raman spectra are normalized to the G-line maximum height and shifted for clarity. **b**, Polar plot of $I(D)/I(G)$ as a function of θ for ribbon (3) on both hBN (blue trace) and SiO₂ (red trace) substrates. **c**, and **d**, Raman spectra of ribbon (4), on the hBN substrate, at $\theta = 0^\circ$ (c) and 90° (d). The Lorentzian fits to the data are shown in blue.

flakes. Both methods are supposed to hydroxylate the SiO₂ surface [26] and therefore increase the local adhesion of graphene to the surface. The Raman spectrum of graphene on such a treated SiO₂ substrate is characterized by a very slight increase of the FWHM of the 2D-line [27]. The hBN flakes are known to be chemically inert and therefore not affected by the piranha solution at room temperature [28]. Interestingly, we nonetheless observe an increase in doping of graphene on hBN compared to graphene regions resting on SiO₂.

While the hBN flakes have been directly deposited on the SiO₂ substrate, the graphene flakes have been prepared on top of a ≈ 300 nm-thick layer of polymethylmethacrylate (PMMA) previously spin-coated on a glass slide [29]. Raman spectroscopy was used to identify and select individual single-layer graphene flakes [20, 30]. The resulting graphene-PMMA-glass stamp was then mounted in a mask-aligner in such a way that the graphene flake could be aligned on top of the hBN-SiO₂ piranha-treated chip [31]. Once on top of the hBN-SiO₂ target region, the two flakes were brought into contact. This process was repeated until some parts of the graphene flake stuck to the hBN-SiO₂ surface. This technique utilizes van der Waals adhesion to peel-off the graphene ribbons (shown in Fig. 4.17a), the hBN substrate is therefore important for this fabrication

process since graphene adheres more strongly to the hBN than SiO₂ [31]. The yield of this fabrication process is nonetheless low and neither the position nor the width of the obtained graphene ribbons is controllable. Therefore, this fabrication method is - in its present form - irrelevant from a technological point of view, but it is extremely valuable since it allows the Raman (and potentially transport) investigation of non-etched, i.e. pristine, graphene ribbons. Moreover, we would like to emphasize that these graphene ribbons were never in contact with any spin-coated polymer resist typically involved in the fabrication of etched ribbons, nor with any solvents such as acetone, isopropanol or even water.

An optical microscope image of a fabricated sample is shown in Fig. 4.17a. For simplicity, we grouped the ribbons of similar width and labeled them as (1)-(4) (shown in Fig. 4.17c). The widths were extracted from scanning force microscope (SFM) images (Fig. 4.17b, c and d), resulting in a width of $W \approx 160$ and 120 nm for the ribbons (4) and (3). The widths of the ribbons (1) and (2) differ significantly between left and right ribbon ends (see upper panels in Fig. 4.17d). Specifically, ribbons (1) and (2) have a varying width from $W \approx 40$ to 15 nm [ribbon (1)] and $W \approx 45$ to 20 nm [ribbon (2)]. In the following, we will therefore refer to the average width $W \approx 25, 35, 120$ and 160 nm of the ribbons (1), (2), (3) and (4). The Raman data were recorded using a laser wave length of 532 nm ($\hbar\omega_L = 2.33$ eV) through a single-mode optical fiber whose spot size is limited by diffraction. The measurement setup is a commercially available confocal Raman Microscope Alpha 300R from Witec, whose laser is linearly polarized. The sample was fixed to a high-precision rotation mount model PRM-1 from Thorlabs, in order to manually adjust the polarization laser direction relative to the ribbon axis (see inset in Fig. 4.17c). A long working distance focusing lens with numerical aperture of 0.85 is used to obtain a spot size of approximately 500 nm (circle in Fig. 4.17c). Characteristic Raman spectra of the narrow ribbon (2) and bulk graphene, both on the hBN substrate, are presented in Fig. 4.17e. The Raman spectra (labels A and B in Fig. 4.17b and 1c) show the prominent G-line (≈ 1582 cm⁻¹) as well as the single Lorentzian-shaped 2D-line (≈ 2675 cm⁻¹) as expected for graphene. No defect induced D-line (≈ 1340 cm⁻¹) or D'-line (≈ 1620 cm⁻¹) are observed on the bulk graphene region (acquisition point B), which confirms that the fabrication method does not induce defects into the graphene flake. In both spectra, a third prominent sharp peak arises at ≈ 1365 cm⁻¹, which is attributed to the Raman-active LO phonon of hBN [32].

Characterization of the edges

In order to characterize the edges and in particular the edge roughness of the graphene ribbons, we performed polarization angle dependent Raman measurements. Fig. 4.18 shows the Raman spectra of the ribbons (3) ($W \approx 120$ nm, Fig. 4.18a and b) and (4) ($W \approx 160$ nm, Fig. 4.18c and d) as function of the polarization angle θ of the incident light (see inset in Fig. 4.17c). For each ribbon and each polarization angle, a spectrum has been recorded and the G-, D- and hBN-lines were fitted with a single Lorentzian line shape (see examples in Fig. 4.18c and d). In agreement with previous work [4, 6, 7, 33], the D-line intensity $I(D)$ appears to be strongest for polarization parallel to the edge and reaches a minimum for the perpendicular polarization $\theta = 90^\circ$. This

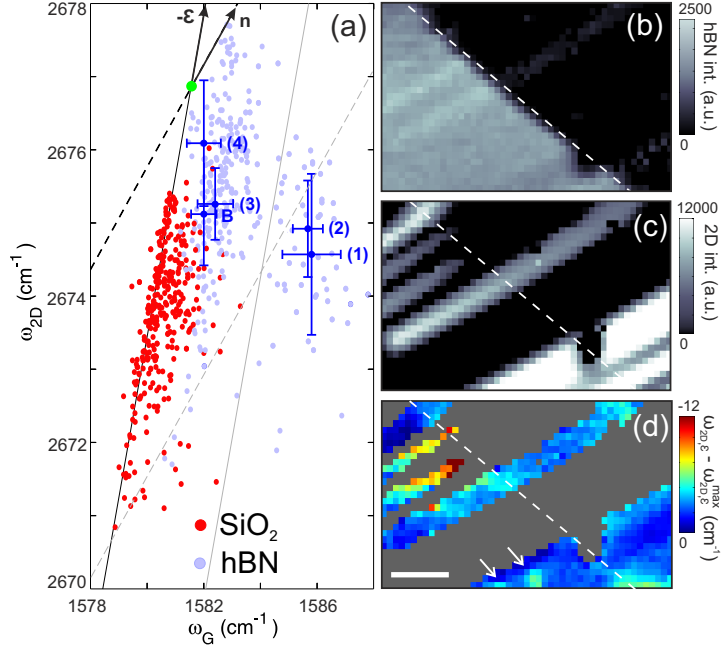


Figure 4.19: **a**, Correlation between ω_{2D} and ω_G at $T = 300$ K. The descriptions of the black and gray axis as well as the color code are introduced in the main text. **b**, and **c**, False-colored Raman maps of $I(\text{hBN})$ and $I(2D)$. The boundary between the hBN and SiO_2 substrates in panel b is marked with a white dashed line. The individual ribbons (1), (2), (3) and (4) are well differentiated from each other. **d**, Map of the local 2D-line shifts due to strain $\omega_{2D,\varepsilon}$ obtained after projecting all the Raman data points onto the strain axis [solid black line in panel (a)] relative to its maximum value [$\omega_{2D,\varepsilon}^{max}$, green point in panel (a)]. The scale bar is $2\mu\text{m}$.

can be observed in Fig. 4.18a, where each Raman spectrum corresponds to a different polarization angle θ , starting from $\theta = 11.25^\circ$ to $\theta = 348.75^\circ$ in steps of 22.5° . Every trace in this plot is normalized to the maximum intensity of the G-line and shifted in the intensity and frequency axis for clarity. For the rest of the analysis, we compare the ratio $I(D)/I(G)$ using the peak area of the fitted Lorentzian function as a measure of intensity. In Fig. 4.18b we show a corresponding polar plot which illustrates the expected mirror planes at $\theta = 0^\circ$ and $\theta = 90^\circ$ [6, 33]. Raman spectra with Lorentzian fits for the direction of maximum and minimum D-line intensity ($\theta = 0^\circ$ and $\theta = 90^\circ$, respectively) of ribbon (4) are presented in Fig. 4.18c and d.

According to Ref. [7] and assuming that $I(G)$ does not depend on θ , a lower bound for the edge disorder correlation length $\xi \approx 2v_F/(\omega_L b)$ can be estimated from the ratio $b = I(D)_{min}/I(D)_{max}$ between the lowest and highest normalized D-line intensity ($I(D)_{min}/I(G)$ and $I(D)_{max}/I(G)$, respectively). For the ribbon (4) (Fig. 4.17c and d), we obtain the lowest intensity ratio of $b \approx 0.055$ (Fig. 4.18c and d), which yields a correlation length of $\xi \approx 10$ nm. This value is significantly higher than the correlation length of $\xi \approx 1$ nm reported on plasma etched graphene nanoribbons [4] and therefore

suggests that the graphene ribbons have a more regular crystallographic orientation of the edges.

Strain, doping and finite size effects

For a more detailed investigation of the dependence of the Raman spectra on the width of the graphene ribbons, we study spatially resolved Raman maps of the sample. In particular, we recorded a Raman map of the $6\ \mu\text{m}$ by $10\ \mu\text{m}$ sample region shown in Fig. 4.17b with a spatial oversampling of 200 nm and an integration time of 15 s (with a laser spot size of 500 nm and a laser power of $\approx 1\ \text{mW}$). The corresponding Raman maps of the hBN-line and the 2D-line intensities, $I(\text{hBN})$ and $I(2D)$, are shown in Fig. 4.19b and c. One can identify the hBN and SiO_2 substrates and the graphene ribbons (1)-(4), partly crossing both substrates. In the lower right corner of Fig. 4.19c, bulk graphene is also observed. By means of the so-called vector decomposition method introduced by Lee et al. [22], we analyze the presence of strain and/or doping variations in our sample. Accordingly, we plot the dependence of the G-line (ω_G) and the 2D-line (ω_{2D}) positions (i.e. frequencies) for all the Raman spectra recorded in the inspected area (Fig. 4.17b) in Fig. 4.19a. The red points show the extracted Raman data from spectra recorded on bulk graphene and ribbons, both on SiO_2 , whereas the light blue points are from graphene regions resting on hBN. The blue data points with error bars show the average values of ω_G and ω_{2D} obtained for every individual graphene ribbon (1)-(4) and bulk graphene (B) on the hBN substrate (see labels in Fig. 4.19a).

The solid and dashed lines indicate the slopes of the strain and large-scale doping axis according to Ref. [22]. Please note that we do not know the exact origin of these two axis and, for simplicity, we marked the same origin as in Ref. [22] (see green point in Fig. 4.19a). Interestingly, the red cloud of data points clearly follows a slope of $\Delta\omega_{2D}/\Delta\omega_G = 2.2$ (solid black line), characteristic of uniaxial strain - in good agreement with Lee et al. [22] -. Both red and main light blue data clouds appear to be offset by $\approx 2.2\ \text{cm}^{-1}$ in the ω_G axis with a direction parallel to the strain axis. This offset is understood as a difference in induced doping [23] between the SiO_2 and the hBN substrates (extracted doping difference: $\Delta n \approx 2 \times 10^{11}\ \text{cm}^{-2}$), most likely due to the treatment with the piranha solution of the hBN surface. More interestingly, Fig. 4.19a suggests that the narrowest ribbons [(1) and (2)] are subject to stronger doping compared to bulk graphene and the wider ribbons. This is noticeable from their mean positions [labeled (1) and (2) in Fig. 4.19a], which are at the very right of this plot (see right gray dashed line of slope 2.2). However, there is an inconsistency with the line width of the G-peak that will be discussed in the following section.

Interestingly, the same ribbons [(1) and (2)] seem to have also different strain values compared to bulk graphene and the wider ribbons [(3) and (4)] (see lower dashed line). This finding is highlighted after projecting all (ω_{2D} ; ω_G) points onto the strain axis (the obtained values are labeled as $\omega_{2D,\epsilon}$). In Fig. 4.19d we show the corresponding spatial map of the difference $\omega_{2D,\epsilon} - \omega_{2D,\epsilon}^{\text{max}}$ relative to its maximum value $\omega_{2D,\epsilon}^{\text{max}}$. Here, we show that the strongest deviations are clearly for the two most narrow ribbons (see yellow and red regions in Fig. 4.19d). Please note that in bulk graphene, the values decrease close to the hBN edge and on bubbles (marked by white arrows in Fig. 4.17b and Fig. 4.19d), which is a further sign that this quantity is indeed related to strain.

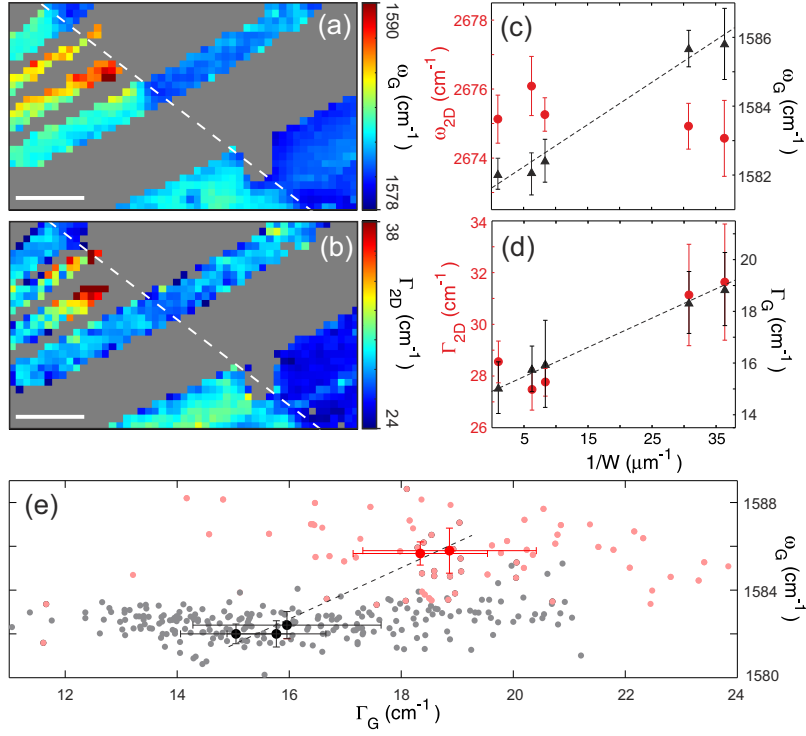


Figure 4.20: **a**, and **b**, Local distribution of ω_G and Γ_{2D} , respectively. The scale bars are $2\mu\text{m}$. **c**, Averaged ω_G and ω_{2D} for every individual graphene ribbon on hBN as function of $1/W$. **d**, Averaged Γ_G and Γ_{2D} for the individual graphene ribbons on hBN as function of $1/W$. **e**, Correlations between Γ_G and ω_G for the ribbons and bulk graphene on the hBN substrate. The light red data points correspond to the narrowest ribbons (1) and (2) with their respective averages marked in red. The ribbons (3), (4) and bulk graphene (B) appear as gray data points with their average values in black. The error bars in all the panels are half the standard deviation.

For a more quantitative analysis of the dependence of the Raman G- and 2D-modes on the ribbon width, we analyze the changes in frequency and broadening of the G-line as well as ω_{2D} and Γ_{2D} as a function of the averaged ribbon width W . Apart from the aforementioned difference in doping between the hBN and SiO_2 substrates (Fig. 4.19a), the spatial representation of ω_G (Fig. 4.20a) reveals a stiffening of the G-line for the narrower ribbons (1) and (2), which is in agreement with Fig. 4.19a and earlier work [5]. Fig. 4.20c shows ω_G and ω_{2D} as a function of the inverse averaged width ($1/W$) for the different ribbons. Interestingly, we observe an increase of ω_G as function of $1/W$ (see dashed line in Fig. 4.20c), meaning that the smaller the ribbon the stiffer the G-line. This is commonly attributed to edge doping and/or confinement effects [5]. The 2D-line frequency ω_{2D} does not show any substantial dependence with the width of the ribbons (see red data points in Fig. 4.20c). In Fig. 4.20d we show that also the G- and 2D-peak line widths (Γ_G and Γ_{2D}) increase with decreasing ribbon width W . This width dependent broadening might be an indication of finite size effects [34]. In

order to exclude doping effects for the increase of Γ_G , we show the dependence of ω_G as function of Γ_G (re-plotting the data shown in Fig. 4.20c and d) in Fig. 4.20e. In complete disagreement with experimental results on bulk graphene [15, 24, 25] and theory [35] on doping dependent Landau damping, we observe an increase of ω_G with increasing Γ_G . For bulk graphene, exactly the opposite has been observed in earlier experiments [15, 24, 25]. Finally, from Fig. 4.17a and d we can estimate a maximum strain difference in the narrow ribbons. Assuming uniaxial strain, we extract a maximum strain difference on the order of 0.23% [22]. It is important to note that according to Ref. [36] these values cannot explain the observed maximum broadening of the G-line (Fig. 4.17e), making edge effects and/or finite size effects a prime candidate to explain our experimental findings.

Conclusion

In summary, we discussed Raman spectroscopy measurements on lithography-free fabricated graphene ribbons made by direct exfoliation of graphene on hBN flakes. Despite a prominent doping of the hBN substrate, most probably induced by the fabrication process, we were able to perform polarization dependent measurements that confirm a more regular crystallographic orientation of the ribbon edges. The reported values of correlation length ξ are one order of magnitude higher than on graphene ribbons fabricated by plasma etching techniques. This direct comparison reveals the otherwise expected roughness of the edges in plasma etched graphene nanoribbons.

Analysis of the frequency and broadening of the G- and 2D-line show prominent differences between the narrowest ribbons (≈ 15 and 20 nm) and the widest ones (bulk graphene included), suggesting the presence of confinement and/or edge effects in these narrow structures. The results of this work highlight the disordered nature of the crystallographic termination at the edges of traditional plasma etched graphene nanoribbons, and emphasizes that further developments in the fabrication process yielding cleaner graphene samples with regularly oriented edges may enhance both the vibrational and electronic characteristics of graphene devices.

References

1. Saito, R. *et al.* Raman spectra of graphene ribbons. *J. Phys.: Condens. Matter* **22**, 334203 (2010).
2. Gillen, R. *et al.* Vibrational properties of graphene nanoribbons by first-principles calculations. *Phys. Rev. B* **80**, 155418 (2009).
3. Bischoff, D. *et al.* Symmetry properties of vibrational modes in graphene nanoribbons. *J. Appl. Phys.* **109**, 073710 (2011).
4. Gillen, R. *et al.* Raman spectroscopy on etched graphene nanoribbons. *Phys. Rev. B* **81**, 205426 (2010).
5. Ryu, S. *et al.* Raman Spectroscopy of Lithographically Patterned Graphene Nanoribbons. *ACS Nano* **5** (5), 4123–4130 (2011).
6. Cancado, L. G. *et al.* Influence of the Atomic Structure on the Raman Spectra of Graphite Edges. *Phys. Rev. Lett.* **93**, 247401 (2004).
7. Casiraghi, C. *et al.* Raman Spectroscopy of Graphene Edges. *Nan. Lett.* **9**, 1433–1441 (2009).
8. Han, M. Y. *et al.* Energy Band-Gap Engineering of Graphene Nanoribbons. *Phys. Rev. Lett.* **98**, 206805 (2007).
9. Lin, Y.-M. *et al.* Electrical observation of subband formation in graphene nanoribbons. *Phys. Rev. B* **78**, 161409 (2008).
10. Wang, X. *et al.* Room-Temperature All-Semiconducting Sub-10-nm Graphene Nanoribbon Field-Effect Transistors. *Phys. Rev. Lett.*, **100**, 206803 (2008).
11. Molitor, F. *et al.* Transport gap in side-gated graphene constrictions. *Phys. Rev. B* **79**, 075426 (2010).
12. Gallagher, P. *et al.* Disorder-induced gap behavior in graphene nanoribbons. *Phys. Rev. B* **81**, 115409 (2010).
13. Terrés, B. *et al.* Disorder induced Coulomb gaps in graphene constrictions with different aspect ratios. *Appl. Phys. Lett.* **98**, 032109 (2011).
14. Son, Y.-W. *et al.* Energy Gaps in Graphene Nanoribbons. *Phys. Rev. Lett.* **97**, 216803 (2006).
15. Yan, J. *et al.* Electric Field Effect Tuning of Electron-Phonon Coupling in Graphene. *Phys. Rev. Lett.* **98**, 166802 (2007).
16. Wang, X. *et al.* Graphene nanoribbons with smooth edges behave as quantum wires. *Nature Nanotechnology* **6**, 563–567 (2011).
17. Kosynkin, D. V. *et al.* Longitudinal unzipping of carbon nanotubes to form graphene nanoribbons. *Nature* **458**, 872–876 (2009).
18. Stampfer, C. *et al.* Energy Gaps in Etched Graphene Nanoribbons. *Phys. Rev. Lett.* **102**, 056403 (2009).
19. Tombros, N. *et al.* Quantized conductance of a suspended graphene nanoconstriction. *Nature Physics* **7**, 697–700 (2011).

20. C.Ferrari, A. Raman spectroscopy of graphene and graphite: Disorder and electron phonon coupling and doping and nonadiabatic effects. *Solid State Commun.* **143**, 47 (2007).
21. Malard, L. M. *et al.* Raman spectroscopy in graphene. *Phys. Rep.* **473**, 51 (2009).
22. Lee, J. E. *et al.* Optical separation of mechanical strain from charge doping in graphene. *Nature Communications* **3**, 1024 (2012).
23. Chen, C.-F. *et al.* Controlling inelastic light scattering quantum pathways in graphene. *Nature* **471**, 617–620 (2011).
24. Stampfer, C. *et al.* Raman imaging of doping domains in graphene on SiO₂. *Appl. Phys. Lett.* **91**, 241907 (2007).
25. Pisana, S. *et al.* Breakdown of the adiabatic Born Oppenheimer approximation in graphene. *Nature Materials* **6**, 198–201 (2007).
26. Tiberj, A. *et al.* Reversible optical doping of graphene. *Scientific Reports* **3**, 2355 (2013).
27. Wang, Q. H. *et al.* Understanding and controlling the substrate effect on graphene electron-transfer chemistry via reactivity imprint lithography. *Nature Chemistry* **4**, 724–732 (2012).
28. Altun, A. O. *et al.* Boron nitride stamp for ultra-violet nanoimprinting lithography fabricated by focused ion beam lithography. *Nanotechnology* **18**, 465302 (2007).
29. Zomer, P. J. *et al.* A transfer technique for high mobility graphene devices on commercially available hexagonal boron nitride. *Appl. Phys. Lett.* **99**, 232104 (2011).
30. Graf, D. *et al.* Spatially Resolved Raman Spectroscopy of Single-, Few-Layer Graphene. *Nano Lett.* **7**, 238 (2007).
31. Wang, L. *et al.* One-Dimensional Electrical Contact to a Two-Dimensional Material. *Science* **342**, 614–617 (2013).
32. Geick, R. *et al.* Normal Modes in Hexagonal Boron Nitride. *Phys. Rev.* **146**, 543 (1966).
33. Gruneis, A. *et al.* Inhomogeneous optical absorption around the K point in graphite and carbon nanotubes. *Phys. Rev. B* **67**, 165402 (2003).
34. Ferrari, A. *et al.* Interpretation of Raman spectra of disordered and amorphous carbon. *Phys. Rev. B* **61**, 14095–14107 (2000).
35. Ando, T. *et al.* Anomaly of Optical Phonon in Monolayer Graphene. *J. Phys. Soc. Jpn.* **75**, 124701 (2006).
36. Mohiuddin, T. M. G. *et al.* Uniaxial strain in graphene by Raman spectroscopy: G peak splitting and Grüneisen parameters and sample orientation. *Phys. Rev. B* **79**, 205433 (2009).

4.4 Reduction of edge-disorder via electrostatic gating

4.4.1 Electrical transport indications of a reduced disorder

The mobility of the charge carriers in graphene is strongly dependent on interactions with impurities and/or the substrate. As introduced in Section 4.4, the transport characteristic at zero Tesla of our graphene devices on SiO_2 is heavily influenced by the presence of disorder. From a structural point of view, it appears rather reasonable to differentiate between edges and bulk disorder. Whereas the latter has been extensively studied ([1–4] and Section 4.2.1), the limitations introduced by the edges of graphene has been mostly treated in literature from crystallographic considerations [5–7]. In theory, one would expect the wave-function of the charge carriers to be heavily distorted by the anisotropic nature of the graphene edges. A locally modified density of states, e.g. breaking of the A-B sub-lattice symmetry, as well as an irregular crystallographic orientation of the edges [7] may hamper the observation of clear wave-function confinement phenomena in etched graphene nano-structures. Actually, newly developed fabrication methods yielding to uniform edge terminations showed unambiguous signs of wave-like phenomena, both in transport [8] as in optical measurements [9, 10]. However, eventhough such lattice considerations surely play an important role defining the electronic properties of graphene nano-structures, the potential fluctuations introduced by the chemical compounds attached to the edges may be more significant in real world conditions. Ambient and/or processing impurities leading to chemical functionalization of the edges may heavily alter the transport fingerprints [11].

Throughout this section, we study the dependence of the transport behavior of a graphene constriction under influence of an applied side-gate voltage. We will reveal the edges of graphene as being a major source of potential fluctuations. This section is revelatory of an edge-characteristic disorder with a rapidly-varying spatial fluctuation compared to bulk disorder. More importantly, we introduce a way to reduce the aforementioned disorder by applying an electrostatic potential close to edges of the devices. These findings may indeed be relevant for other 2D materials, as the abrupt termination of the 2D material, i.e. the edges, are a common issue.

To fabricate the samples, we mechanically exfoliated graphene flakes and deposited them onto a highly p-doped Si substrate. We verified the single-layer nature of the selected graphene flakes via Raman spectroscopy measurements [12]. The nano-structured graphene device shown Fig. 4.21a, b has been patterned by electron-beam (e-beam) lithography of a $\sim 120\text{ nm}$ -thick resist etching mask. The unprotected graphene was removed by a reactive ion etching (Ar/O_2 plasma) process. After removing the residual resist, the graphene devices were contacted with Cr/Au electrodes. Prior measuring, samples were immersed in a 1% buffered Hydrofluoric acid (HF) solution. This cleaning procedure proved to remove dopants and/or absorbents and therefore disorder in graphene [13].

Samples were measured in a pumped He^4 system at $T \approx 1.6\text{ K}$ and in a dilution refrigerator at $T \approx 15\text{ mK}$. The conductance through the constrictions was recorded by

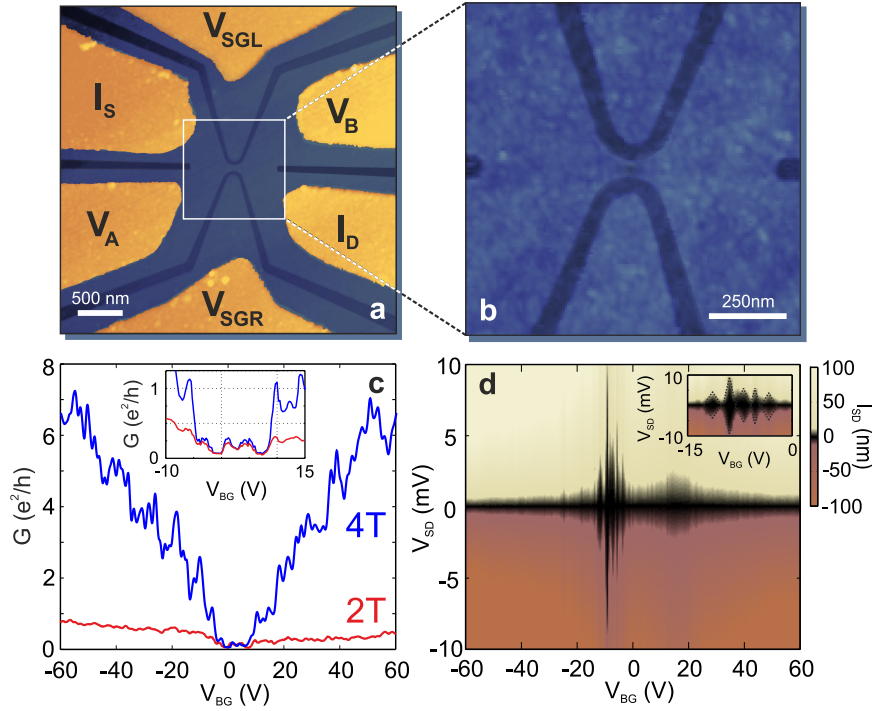


Figure 4.21: **Device fabrication and electrical characterization.** **a**, **b**, False-colored Atomic Force microscope (AFM) images of a side-gated graphene constriction of width $W = 70 \text{ nm}$ and length $L \approx 150 \text{ nm}$, contacted in a 4-terminal configuration. The Cr/Au metal electrodes, the SiO_2 substrate and the graphene are represented in yellow, dark blue and blue color, respectively. The conductance G is measured after applying a bias voltage $V_b = 350 \mu\text{V}$ between the source and drain terminals (I_S , I_D). The voltage is measured between terminals V_A and V_B . The left side-gate electrode (V_{SGL}) and right side-gate electrode (V_{SGR}) can be tuned individually. **c**, 4-terminal (blue trace) and 2-terminal (red trace) conductance G as a function of V_{BG} for the graphene device shown in panels **a** and **b**. The inset shows a close-up view inside the transport gap region. **d**, Color plot of the source-drain current (I_{SD}) as a function of V_{BG} and source-drain voltage V_{SD} . The inset reveals the diamond-like features inside the transport gap region.

low-frequency lock-in techniques after adding an AC bias voltage of $100 \mu\text{V}$. To locally tune the electrostatic potential at the edges of the graphene constriction, a couple of lateral graphene gates has been placed 40 nm away (Fig. 4.21a, b). These side-gate electrodes can be operated symmetrically ($V_{SGL} = V_{SGR}$) or anti-symmetrically ($V_{SGR} = -V_{SGL}$). Samples were designed in a four-terminal configuration (Fig. 4.21a) to withdraw any spurious contribution from the metal-graphene interface and the graphene leads. A comparison between 2- and 4-terminal conductance is shown in Fig. 4.21c. As expected, both traces are qualitatively similar inside the low conductance region, i.e. transport gap (inset of Fig. 4.21c), showing that, close to the charge neutrality point,

the graphene region of lowest conductance is actually the constriction area. At higher charge carrier densities, the 2- and 4-terminal conductances differ substantially from each other (Fig. 4.21c). Quantitatively, we observe high levels of conductance for the 4-terminal configuration, as well as robust and reproducible oscillations superimposed to the conductance trace.

Even though the current cannot be completely pinched-off in these 70 nm-wide constrictions (inset of Fig. 4.21c), the transport gap still exhibits a diamond-like pattern (Fig. 4.21d), suggesting that the transport mechanism inside the transport gap is mostly dominated by statistical Coulomb blockade, in good agreement with earlier work [14–17].

Fig. 4.22 shows the conductance G as a function of the back-gate voltage V_{BG} for a symmetric ($V_{SGR} = V_{SGL}$) and an anti-symmetric ($V_{SGR} = -V_{SGL}$) configuration of the side-gate potentials. Away from the charge neutrality point, i.e. at high carrier densities, the conductance displays robust and reproducible resonances. These quasi-periodic oscillations of the conductance (arrows in Fig. 4.22a) are apparently undisturbed as a function of symmetric side-gate potentials (Fig. 4.22a,b,d, and e) and yet become remarkably disturbed under increasing anti-symmetric potentials (Fig. 4.22c and f). These effects reveal a sudden and significant change in the scattering landscape along the electronic path under application of an anti-symmetric potential. Contrary, a symmetric side-gate potential seems to tune the charge carrier density without any noticeable modification of the scattering/disorder landscape. These initial experimental observation seems to indicate the prominent contribution of the potential landscape to the conductance and its dependence with a anti-symmetric side-gate potential.

It is important to note the absence of a net contribution to the charge carrier density under anti-symmetric operation of the side-gates (Fig. 4.22c and f). This can be seen by looking at the position of the charge neutrality point (dashed white line in Fig. 4.22c), which remains vertical as a function of side-gate voltage potentials. This behavior suggests that both left (V_{SGL}) and right (V_{SGR}) side-gates couple equally to the constriction.

The same behavior is observed at different temperatures (see temperatures in Fig. 4.22). Although at high temperatures $T = 20\text{ K}$ (Fig. 4.22a and d) the resonances not only decay in amplitude but their periodicity changes, suggesting that resonant scattering and/or coherent contributions are present in our devices. We note that all resonances (black arrows in Fig. 4.22a) under symmetric side-gate potentials evolve according to the very same relative lever arm α_{rel} as the conductance minimum, also called charge neutrality point V_{CNP} (white dashed lines in Fig. 4.22a, b). We are therefore dealing with resonances happening in the constricted area. The relative lever arm α_{rel} is a relative measure of the electrostatic coupling between the side-electrodes and the constriction Δ_{SG} , defined by comparing it to the back-gate vs constriction coupling Δ_{BG} . Basically $\alpha_{rel} = \Delta_{BG} / \Delta_{SG} \approx 0.5$.

Even if the overall charge carrier density is tuned by the symmetric potentials, we do not observe at high energies any apparent modification of the transport characteristics as a function of a symmetric side-gate potential. This can be understood looking at the numerical simulation of the electrostatic potential distribution across the graphene

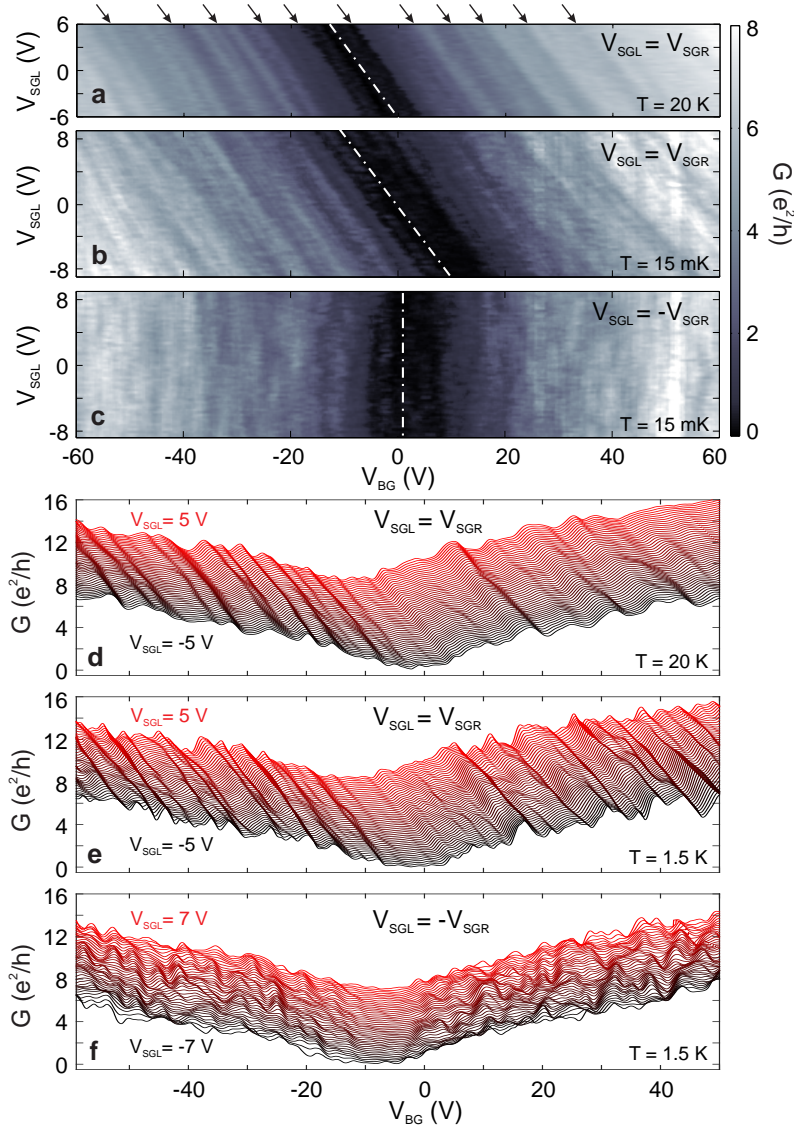


Figure 4.22: **Influence of an applied side-gate potential at high carrier densities.** **a**, **b** and **c**, 4-terminal conductance maps as a function of the back-gate voltage V_{BG} and the left side-gate voltage V_{SGL} for a symmetric $V_{SGL} = V_{SGR}$ (panel a and b) and an anti-symmetric $V_{SGL} = -V_{SGR}$ (panel c) configuration of the side-gate potentials. The charge neutrality point V_{CNP} is indicated by a white dashed line. **d**, **e**, and **f**, 4-terminal conductance traces versus V_{BG} for a symmetric, $V_{SGL} = V_{SGR}$ (panel d and e), and an anti-symmetric, $V_{SGL} = -V_{SGR}$ (panel e), configuration of the side-gate potentials. The traces are shifted upwards in the G -axis for clarity. Temperatures are indicated in the panels.

nanoribbon (Fig. 4.23).

The numerical simulations within this section are performed with `nextnano`³ software [18, 19], a simulation package based on Fortran90-code that provides electrostatic

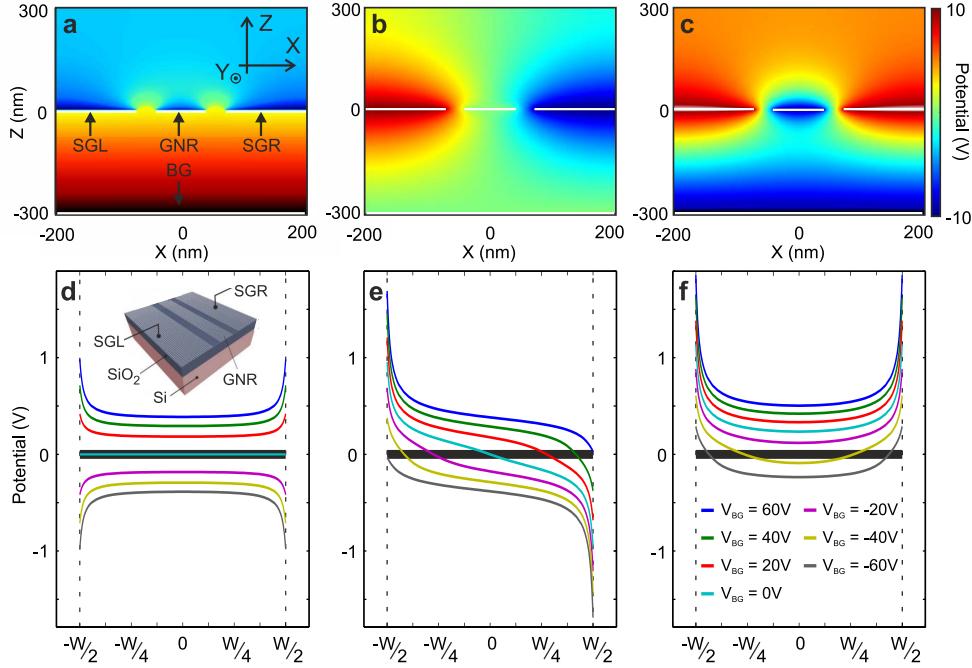


Figure 4.23: **Disorder-reduction in the quantum Hall regime.** **a**, **b**, and **c**, Transverse line-cut of the electrostatic potential around the graphene nanoribbon (GNR) the side-gate (SGR, SRL) and the back-gate (BG) electrodes (represented in white), for the following configurations: $V_{BG} = 10\text{ V}$, $V_{SGL} = V_{SGR} = 0\text{ V}$ in panel a, $V_{BG} = 0\text{ V}$ and $V_{SGL} = -V_{SGR} = 9\text{ V}$ in panel b, and $V_{BG} = -10\text{ V}$ and $V_{SGL} = V_{SGR} = 9\text{ V}$ in panel c. The ribbon potential is zero in all panels. **d**, **e**, and **f**, Transverse line-cut of the electrostatic potential in the graphene nanoribbon of width $W = 80\text{ nm}$, for the electrode configurations shown in panels a, b and c, respectively. The color code in panel f indicates the potential applied to the back-gate.

simulation in one, two and three dimensions, for different nanodevice geometries and an extensive materials database, including graphene. As an important feature, we note that quantum mechanical effects, like wave-function confinement and quantum capacitance, are taken into account.

Fig. 4.23a,b and c show the cross-section of the electrostatic potentials across a 80 nm -wide graphene nanoribbon *GNR* with lateral gates *SGR/SGL* and a back-gate *BG* (inset of Fig. 4.23d) for different potential configurations of the electrodes (see figure captions). As observed in Fig. 4.23, the 2D nature of graphene induce a strong potential inhomogeneity along the edges. At the sharp edges of the graphene nanoribbon, the potential develops a $1/\sqrt{x}$ singularity (Fig. 4.23d). This strong inhomogeneity has been analytically predicted [20, 21] and experimentally demonstrated [22]. Therefore, at high carrier densities, the effect of the lateral gates is redundant since the back-gate electrostatic potential already increases the local potential at the edges. Close to the charge neutrality point though, when the back-gate electrode is tuned to zero voltage, the influence of lateral potential is rather significant (cyan trace in Fig. 4.23e and f). We

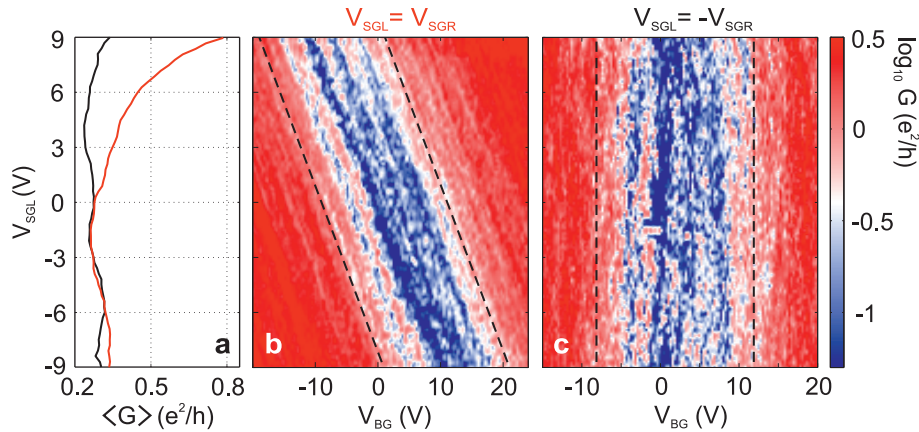


Figure 4.24: **Reduction of disorder inside the transport gap.** **a**, Averaged conductance $\langle G \rangle$ as a function of V_{SGL} for a back-gate voltage interval $\Delta V_{BG} = 20 V$ within the black dashed lines inside the transport gap of panel b (red trace) and panel c (black trace). **b**, **c**, Color maps of the 4-terminal conductance G for a symmetric ($V_{SGL} = V_{SGR}$) and an anti-symmetric ($V_{SGL} = -V_{SGR}$) configuration of the side-gate potentials (panels b and c, respectively), measured at $T = 15 mK$.

therefore expect to see a considerable dependence of the transport behavior as a function of the side-potentials inside the transport gap. Indeed, close the charge neutrality point, i.e. for low back-gate voltages, the potential profile induced by the back-gate is predominantly flat (see cyan trace in Fig. 4.23d).

Experimental evidences are found in Fig. 4.24, where we show a close-up of the conductance inside the transport gap as a function of back-gate and side-gate voltages. Sweeping the side-gate potentials anti-symmetrically ($V_{SGL} = -V_{SGR}$) seems to randomize the conductance traces without any apparent pattern (Fig. 4.24c). In fact, this behavior was already observed at high carrier densities (Fig. 4.22c and f) where an anti-symmetric potential appeared to change the scattering landscape and therefore its electronic transport fingerprints (Fig. 4.27f). Contrary, for high symmetric potentials ($V_{SGL} = V_{SGR} \geq 4 V$), the overall conductance inside the transport gap gradually increases (Fig. 4.24b). To evaluate the change in conductance we calculate $\langle G \rangle$ defined as the averaged conductance within a back-gate voltage interval of $\Delta V_g = 20 V$ around the charge neutrality point (region between the dashed black lines in Fig. 4.24b and c). $\langle G \rangle$ is calculated for $V_{SGR} = V_{SGL}$ and $V_{SGR} = -V_{SGL}$ (panel b and c of Fig. 4.24, respectively). At high side-gate voltages (Fig. 4.24a), the value of $\langle G \rangle$ for symmetric potentials is ~ 3 times higher than for the anti-symmetric case (compare red and black traces in Fig. 4.24).

These results confirm that a symmetric side-gate potential influences the transport behavior mainly around the charge neutrality point and supports the conjecture, supported by electrostatic simulations (Fig. 4.23), that at high back-gate voltages the potential at the edges is already augmented. This effect is known as fringe-fields in literature [22] and it is expected to arise in 2D materials that are gated by a comparatively large

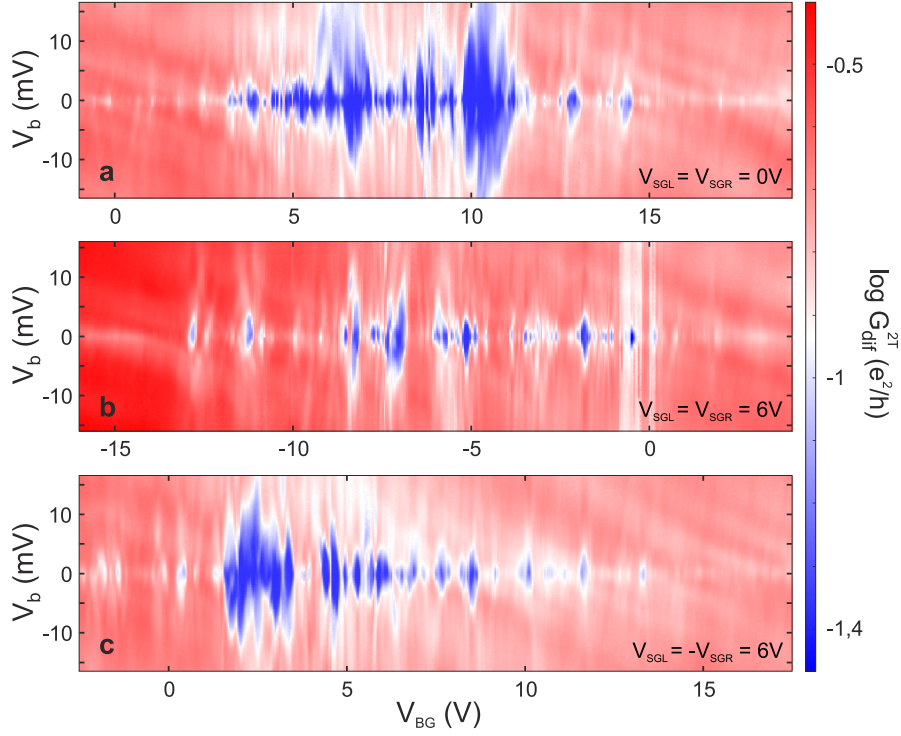


Figure 4.25: **Reduction of disorder inside the transport gap.** **a**, **b**, and **c**, 2-terminal differential conductance $G = dI/dV$ in log scale, as a function of bias V_b and back gate voltage V_{BG} for $V_{\text{SGL}} = V_{\text{SGR}} = 0\text{V}$ (panel a), $V_{\text{SGL}} = V_{\text{SGR}} = 6\text{V}$ (panel b) and $V_{\text{SGL}} = -V_{\text{SGR}} = 6\text{V}$ (panel c). The Temperature was set to $T = 15\text{mK}$ for all measurements.

parallel electrode. More importantly, these first results suggest an important reduction of disorder potential under symmetrically applied lateral potentials.

This reduction in disorder is supported by bias spectroscopy measurement (Fig. 4.25). At $V_{\text{SGL}} = V_{\text{SGR}} = 0\text{V}$ the bias spectroscopy shows the traditional diamond-like features of disordered graphene constrictions [14–17]. Setting the side-gate potentials to $V_{\text{SGL}} = V_{\text{SGR}} = 6\text{V}$ and $V_{\text{SGL}} = -V_{\text{SGR}} = 6\text{V}$ allows to compare the effects of a symmetric and anti-symmetric potential on the transport characteristics (Fig. 4.24b and c, respectively) and deduce the effects of the applied side-gate configuration on the potential landscape (Fig. 4.26 and Fig. 4.27).

Starting with the bias spectroscopy data from Fig. 4.25 and following the model introduced by Stampfer et. al. [23], we attribute the biggest diamond to the smallest charged island along the constricted area. A zoom-in map of the biggest diamonds can be found in Fig. 4.27a, b and c. The diamond extension E_g/e in the bias voltage direction (red arrows in Fig. 4.27a, b and c) is directly related with the dimensions of the smallest charged island. We extract the largest energies $E_g \approx 10, 14$ and 5meV for the configurations $V_{\text{SGL}} = V_{\text{SGR}} = 0\text{V}$, $V_{\text{SGL}} = -V_{\text{SGR}} = 6\text{V}$ and $V_{\text{SGL}} = V_{\text{SGR}} = 6\text{V}$ (Fig. 4.27a, b and c, respectively). Which correspond to the island diameters $d \approx 180, 120$ and 350nm . The diameter d of the charged island is estimated using a simple disc model,

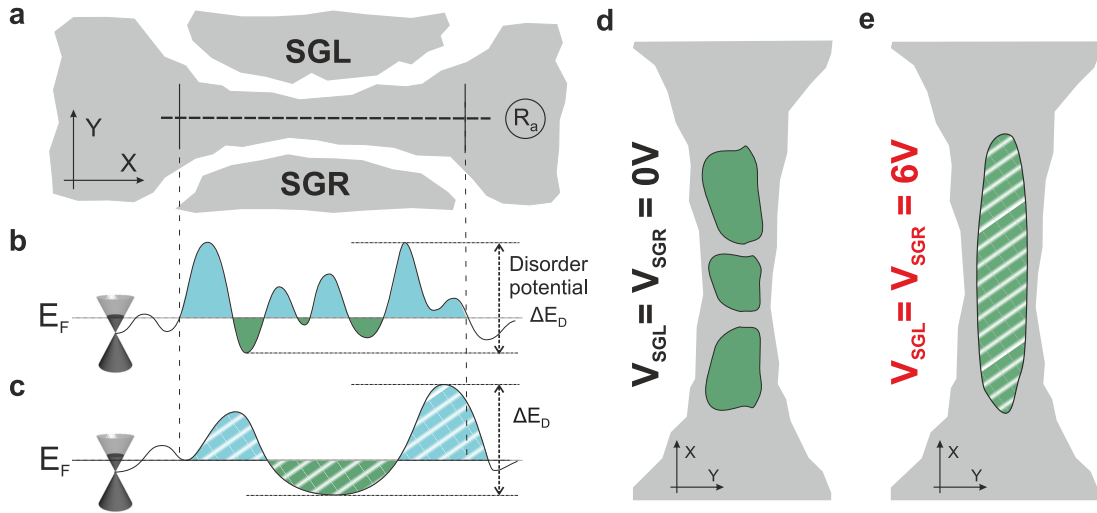


Figure 4.26: **Sketch of the potential distribution under finite side-gate potentials.** **a**, Sketch of a graphene nanoribbon with the right and left side-gate electrodes indicated by *SGR* and *SGL*, respectively. The dashed and solid gray lines indicate the ribbon axis and the limits of the constriction, respectively. **b** and **c**, Line-cut of the disorder fluctuations along the ribbon axis (dashed gray line marked R_a in panel a) for $V_{SGL} = V_{SGR} = 0 V$ (panel b) and $V_{SGL} = V_{SGR} = 6 V$ (panel c). The dimensions of the dots (solid and dashed green colored) and anti-dots (solid and dashed blue colored) depend on the disorder potential (marked ΔE_D), the Fermi Energy E_F and the side-gate potentials (V_{SGL} and V_{SGR}). **d**, and **e**, Schematic representation of the dots' dimensions and their spatial distribution, for a side-gate potential $V_{SGL} = V_{SGR} = 0 V$ (panel d) and $V_{SGL} = V_{SGR} = 6 V$ (panel e). For simplicity, we discard the representation of the anti-dots.

with $d = e^2 / (4\epsilon_0\epsilon_{eff}E_g)$ and $\epsilon_{eff} = (1 + 4)/2 = 2.5$, where ϵ_{eff} is the effective dielectric constant including the vacuum and SiO_2 contributions. We can therefore conclude that, under high symmetric potentials, there is a substantial increase in the dimensions of the charged islands that may also explain the overall increase in conductance. Notice that the conductance background in Fig. 4.25b is higher than for panels a and c of the same figure.

To visualize the effects of the side-gates on the potential landscape along the graphene ribbon, we schematically represent the evolution of the electron-hole puddles for the symmetric configuration of the side electrodes in Fig. 4.26. Depicted in blue and green we show the dots and anti-dots forming along the electronic path. In these sketches it is not represented the quantum confinement energy gap separating the hole- and electron-like charged puddles, as described in Fig. 4.2. As suggested by the bias spectroscopy measurements of Fig. 4.25 and Fig. 4.27a-c, the increase in conductance upon application of symmetric side potential (Fig. 4.24a) is due to the broadening of the localized states along the electronic path. The localized states are extended (Fig. 4.26e) owing to a longer lengthscale of the disorder potential fluctuations ΔE_D (Fig. 4.26c) under

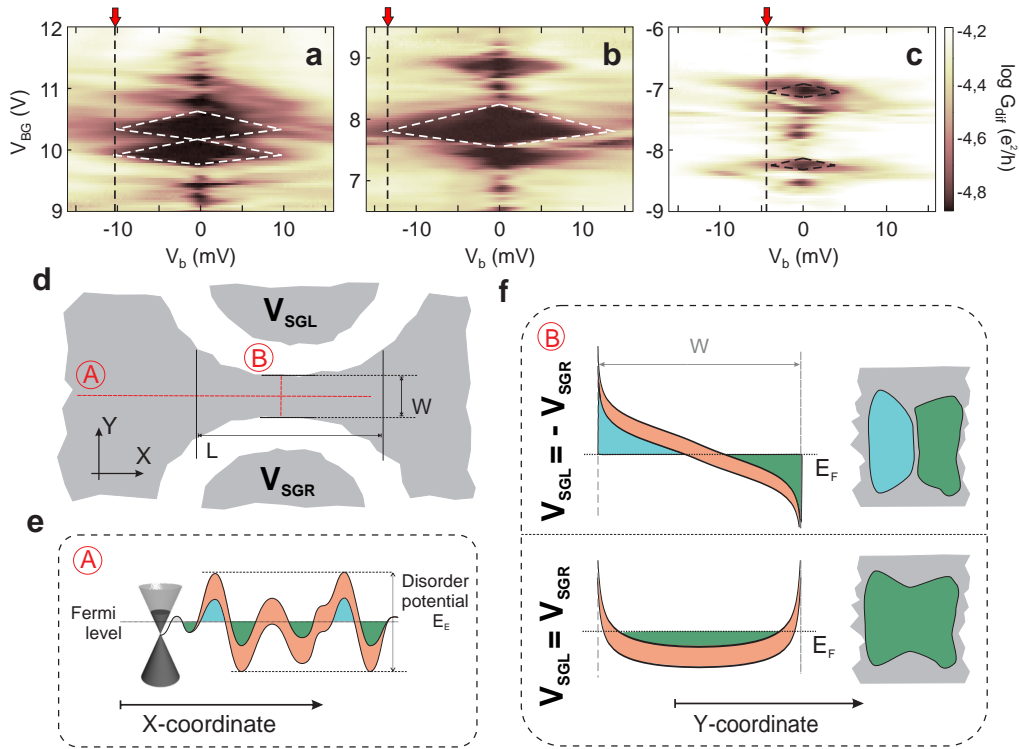


Figure 4.27: **Effect of an anti-symmetric side-potential.** **a**, **b**, and **c**, Zoom-in bias spectroscopy measurements showing the biggest diamond (dashed white lines) inside the transport gap for $V_{SGL} = V_{SGR} = 0 V$ (panel a), $V_{SGL} = -V_{SGR} = 6 V$ (panel b) and $V_{SGL} = V_{SGR} = 6 V$ (Panel c). Data has been taken at $T = 1.7 K$. **d**, Schematics of a graphene nanoribbon of width W and length L , with the left and right side-gate electrodes indicated by SGR and SGL , respectively. **e**, Line-cut of the disorder fluctuations along the ribbon axis (red line B in panel d), the confinement energy gap appears in orange. **f**, Line-cut of the disorder potential along the ribbon width (red line A in panel d), for anti-symmetric ($V_{SGL} = -V_{SGR} = 6 V$) and symmetric $V_{SGL} = V_{SGR} = 0 V$ side-potentials. The Fermi energy is marked by a dashed gray line. The resulting distribution and size of the dots (green) and anti-dots (blue) is represented aside.

symmetric side-gate potentials.

Alternatively, we represent a possible schematic representation of the localized states distribution for an anti-symmetric potential (Fig. 4.27). In that case, the tilting of the potential across the constriction (see simulations in Fig. 4.23e) may force an effective splitting of the electron-hole puddle (Fig. 4.27f). This description is again (see Section 4.1) only valid in the presence of a quantum confinement energy gap (ΔE_{con} in Fig. 4.2 and represented in orange in Fig. 4.27e and f). This confinement energy has been estimated in literature [23] as $\Delta E_{con}(W) \approx \gamma \pi a_{C-C}/W$, where $\gamma \approx 2.7 eV$ and $a_{C-C} = 0.142 nm$ [23, 24]. Effectively, the size of the charged islands should decrease approximately by half after applying an anti-symmetric potential (Fig. 4.27f), which is

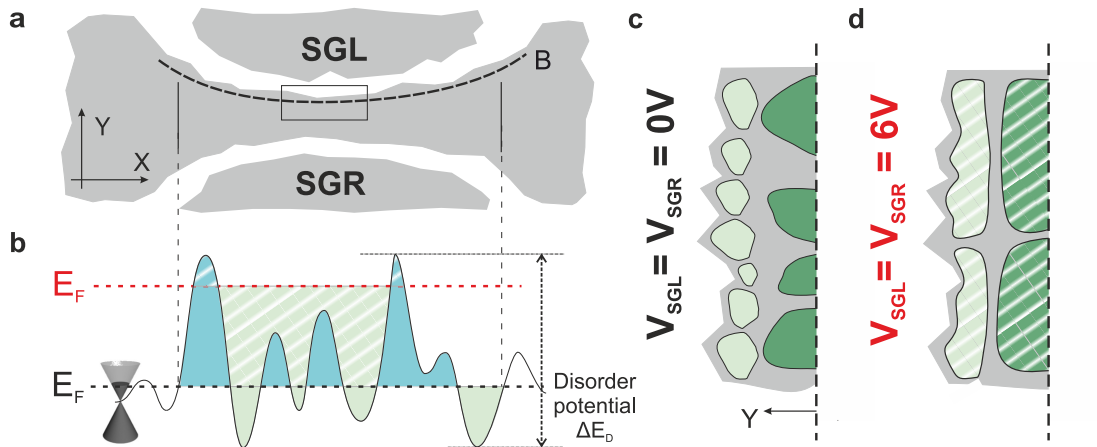


Figure 4.28: **Schematic interpretation of the disorder reduction process.** **a**, See description in Fig. 4.26a. **b**, Disorder fluctuations line-cut along the ribbon edges (dashed gray line marked B in panel a). The dimensions of the dots (solid and dashed green colors) and anti-dots (solid and dashed blue colors) depend on the disorder potential (marked ΔE_D) and the Fermi Energy (E_F) along the edge of the constriction. The change in Fermi energy (E_F) upon application of a symmetric potential ($V_{SGL} = V_{SGR} = 6V$) is shown in red and the corresponding change in the dots/anti-dots dimensions in dashed colors. **c**, and **d**, Schematics representation of the dots' dimensions and their spatial distribution inside the black box of panel a, for a side-gate potential $V_{SGL} = V_{SGR} = 0V$ (panel c) and $V_{SGL} = V_{SGR} = 6V$ (panel d). For simplicity, we discard the representation of the anti-dots. The light and dark green colors highlight the localized states along the edges and the ribbon axis, respectively.

in reasonable fair agreement with the extracted energy scales from panels a, b and c of Fig. 4.27 (see red arrows).

Up to this point, we essentially described the experimental findings and relate them to the dimensions of the electron-hole-puddles. Although this link appeared straightforwardly, the connection between an applied side-gate voltage and the modification of the potential landscape is still missing. Indeed, one may expect any applied potential to tune the Fermi energy E_F without severely modifying the potential topography. In our case though, a locally applied potential at the edges of the graphene constrictions appeared to heavily smooth the potential inhomogeneities. In the following, we will introduce a conceptual description of this process by relating it to the edge-induced disorder. Even though the description is merely an interpretation exercise and/or a possible case scenario, it may help to the outlook and further investigations on the topic.

The graphene nanoribbons within this section are fabricated by reactive ion etching processes. This plasma process is extremely reactive on the graphene edges and the crystallographic orientation of the edges are expected to be highly inhomogeneous. First experimental observation supporting this statement can be found in Section 4.3.1, where

we found a correlation length ξ of exfoliated graphene ribbons one order of magnitude higher than for plasma etched ones. As shown theoretically [25], in non-regular edge crystal structures as the one expected for RIE etched ribbons, just with three or four zigzag sites per sequence (understanding sequence as any length with a regular crystal pattern) are enough to exhibit a non-negligible edge state. These edge states, not to be mistaken with the edge states in the QHE regime, can be understood as a charge density distribution localized at the edges of the graphene ribbons [25]. In Section 6.2 we bring further evidences of these strongly edge-bounded states in ballistic graphene nanoribbons and their charging effects in transport. We can therefore understand these edge states as a direct consequence of the crystal disorder. We will from now on refer to this crystal disorder and any dopants or chemical functionalization at the edges as edge-induced disorder.

In Fig. 4.28 we depict the edge states as hole or electron-puddles (represented in light blue and light green colors) of a length-scale much smaller than the extension of the localized states within the ribbon center region (represented in dark green color Fig. 4.28c and d). The spatial extension of the edge states is believed to be in the nanometer scale (~ 2 to 10 nm [25]) whereas the charge puddles are in the order of $\sim 100\text{ nm}$ (see Section 4.2.1, Section 4.4.1 or Section 4.4.3 for an estimation of the charged puddle dimensions). The spatial extension of the edge states can be seen in Fig. 4.28c and in Fig. 4.28b as a line-cut of the disorder potential long the ribbon edges (black dashed line in Fig. 4.28a).

We will start by assuming that the extension of the charge puddles within the ribbon bulk depend on the length-scale of the edge-induced disorder, also called correlation length ξ (see section Section 4.3.1). We would expect that the shorter ξ the smaller the localized states within the nanoribbon bulk. In this scenario, an applied lateral potential is expected to increase the Fermi energy E_F at the edges (see E_F marked in red in Fig. 4.28b). The effect, or potential difference induced by the side-gate electrodes, is very small at the center/axis of the ribbon (see cyan trace in Fig. 4.23f). This elevated E_F at the edges, may then enlarge the edge states, as indicated in dashed light green color in Fig. 4.23a and f. The consequence of enlarging this edge states seems therefore to extend the localized states (dashed dark green puddles in Fig. 4.23f). In other words, upon application of a side-gate potential we shield the intrinsic correlation length ξ of the edges, smoothing the disorder fluctuation along the electronic path (dashed dark green puddles in Fig. 4.23f).

This section is revelatory of the role of disorder in the transport properties of graphene constrictions. We emphasize the direct link between conductance and bulk disorder and propose a possible connection accounting for the effects of the edge-induced disorder on the transport characteristics. More importantly, the experimental findings suggest an important reduction of disorder via symmetrically applied lateral potentials. This electrostatic approach to reduce disorder may not only be relevant for graphene but to any 2D material where the edge/boundaries are not defined by a smooth electrostatic potential, like in traditional 2D electron gases (2DEGs), but rather by the abrupt termination of the material.

4.4.2 Observation of Fabry-Pérot oscillations as a proof of disorder reduction

As stated in Section 4.2.1, close to the charge neutrality point, graphene nanodevices show low levels of conductance superimposed with sharp but reproducible conductance peaks/fluctuations (see Fig. 4.1). This low energy range is known as "transport gap" and its underlying physics is driven by statistical Coulomb blockade.

Although the conductance oscillations (Coulomb peaks) are observed all along this low-energy range (see Section 4.2.1), its nature is sooner related to the classical diffusive motion of electrons [26] rather than to quantum interference effects. In fact, these sharp resonances arise from the potential fluctuations along the electronic path together with the lack of coherence of the charge carriers. Inside the transport gap, the charge carriers lose their coherence by tunneling along the conductive path, presumably due to the weak coupling between successive charge puddles. The lack of coherence has been demonstrated by fitting the shape of these conductance peaks by a Gaussian line-shape [27, 28] (refer to Fig. 4.3).

At high energies though, similar conductance fluctuations are also observed, although its underlying physics is different. Contrary to the particle-like behavior (statistical Coulomb blockade picture) of the charge carriers inside the transport gap, at higher energies, the oscillations mostly relate to wave-like phenomena. quantum interference effects become increasingly important as soon as the electron phase coherence length becomes comparable to the size of the device. Analogous results have been observed in carbon nanotubes (CNT) [27, 29, 30], where resonant tunneling effects, also called Fabry-Pérot interferences, arose thanks to the coupling of the electron wave-functions to a resonant cavity. In that case, a single conductance resonance line-shape is well described by a Lorentzian function [27], which is related to energy uncertainty [28] rather than thermal broadening (Coulomb blockade scenario).

As observed in Fig. 4.21c, Fig. 4.22 or Fig. 4.29a, these quasi-periodic conductance oscillations are clearly distinguishable when represented as a function of a symmetric side-gate potential. As we mentioned in previous section (Section 4.4.1), the symmetric potential tunes the overall charge carrier density without modifying the scattering landscape. We therefore observe the resonances evolving parallel to each other, following the same relative lever arm α_{rel} . These oscillations have a characteristic periodicity in the order of $\Delta V_{BG} \approx 4V$. Traditionally, the periodicity in the V_{BG} -axis, or as a function of the bias voltage V_b , exhibits an inverse dependence as function of the cavity length L . Extracting this length-scale L directly from the measurements may allow us to determine the physical cavity where the wave-like carriers are coupling to. For an experimental demonstration in CNTs please refer to [29]. We therefore expect to extract the dimensions of the resonance cavity by taking a closer look at the differential conductance $G_{diff} = dG/dV_b$ as a function of back-gate and bias voltages (Fig. 4.33). As shown by the bias spectroscopy measurements at $T = 1.7 K$ (Fig. 4.33b), the positions of the dG/dV_b dips evolve smoothly as a function of V_b and V_{BG} , forming a mesh of crisscrossing dark lines. The dips in dG/dV_b (dark lines) are more pronounced than the typical dG/dV_b peaks characteristic of Coulomb diamonds [26]. A change in V_{BG} or V_b

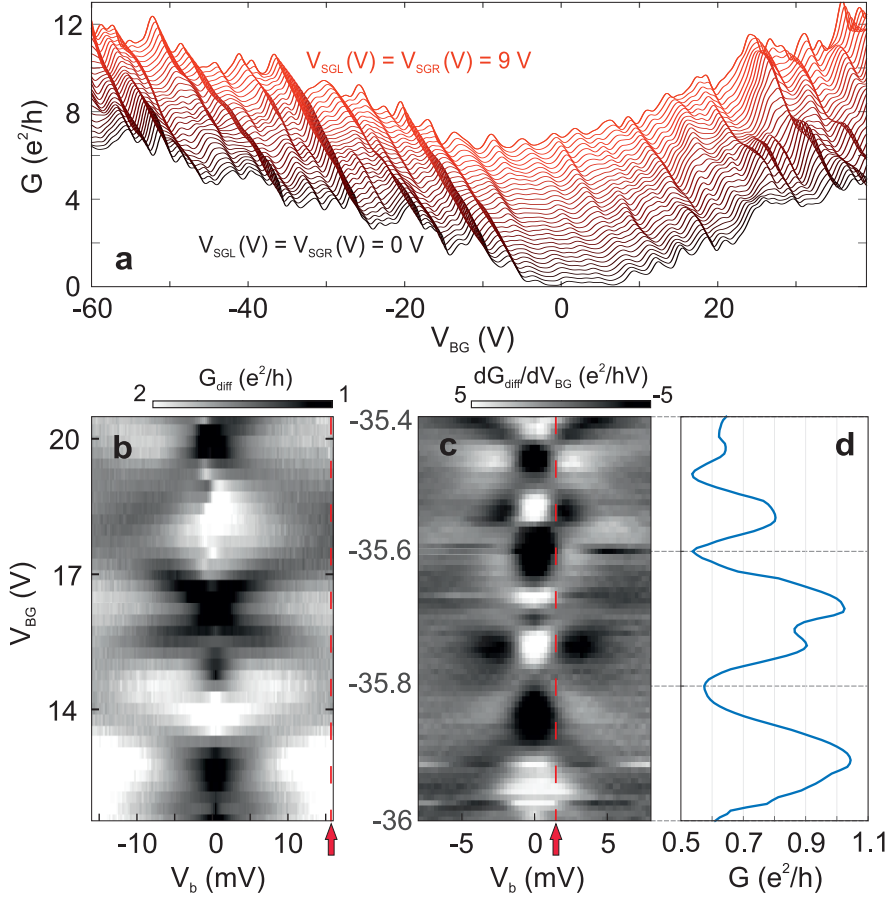


Figure 4.29: **Energy-scale of the conductance oscillations.** **a**, G traces for the 70 nm -wide device shown in Fig. 4.21 as a function of symmetric side-potentials, from $V_{SGL} = V_{SGR} = 0\text{ V}$ (black trace) to $V_{SGL} = V_{SGR} = 9\text{ V}$ (red trace). Traces are shifted upwards in the G -axis for clarity. Measured at $T = 1.7\text{ K}$. **b**, Differential conductance G_{diff} vs. V_{BG} and V_b of the characteristic conductance oscillations seen in panel a. We extract a Energy scale $V_C \approx 16\text{ meV}$ (red dashed line and red arrow). Measured at $T = 1.7\text{ K}$. **c**, and **d**, Differential conductance G_{diff} vs. V_{BG} and V_b of the same device as in panel a, measured at $T = 15\text{ mK}$. A much lower energy scale $V_C \approx 3\text{ meV}$ (red dashed line and red arrow) is also observed, characteristic of a rapidly varying conductance oscillations (panel d).

thus modulates the Fermi energy of the charge carriers in graphene and hence changes the Fermi wave-number $k = 2\pi/\lambda$. The dG/dV_b oscillations are thus attributed to a modification of momentum k_F . We extract an energy scale $E_c = e V_C \approx 16\text{ meV}$ (dashed red line in Fig. 4.29b). The resonant length L is related to the energy E_c by:

$$\lambda_F = \frac{2\pi}{k_F} = \frac{2L}{M} \Leftrightarrow \Delta k = \frac{\pi}{L} \Rightarrow E_c = \Delta E = \hbar v_F \Delta k = \frac{\hbar v_F}{2L}, \quad (4.8)$$

where M is the number of modes coupling to the cavity of length L at the Fermi energy E_F , and ΔE (Δk) is the energy (momentum) spacing between successive sub-

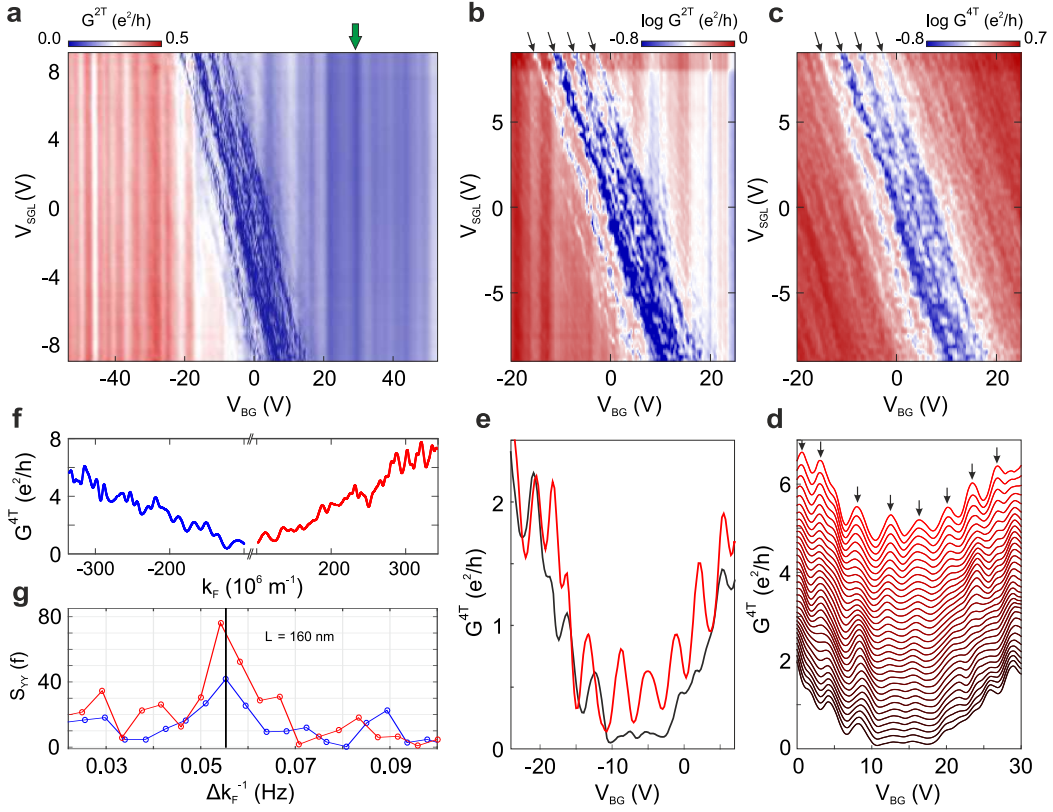


Figure 4.30: **From particle- to wave-like phenomena.** **a**, and **b**, 2-terminal conductance G^{2T} as a function of V_{BG} and a symmetric side-gate voltage $V_{SGL} = V_{SGR}$, measured at $T = 1.7 K$, for two different cool-downs of the same device. The black arrows indicate the parallel resonances arising at high values of symmetric potential (panel b) and the green arrow the charge neutrality point (CNP) of the leads (panel a). **c**, 4-terminal conductance G^{4T} as a function of V_{BG} and $V_{SGL} = V_{SGR}$, measured at $T = 1.7 K$. **d**, 4-terminal conductance traces from $V_{SGL} = V_{SGR} = 0 V$ (black trace) to $V_{SGL} = V_{SGR} = 9 V$ (red trace) in steps of $0.3 V$. Traces are shifted in steps of $0.15 V$ in the G – axis and $\Delta V_{BG} = V_{SGL} \times \alpha_{rel}$ in the V_{BG} – axis for clarity, where α_{rel} is the relative lever arm (Fig. 4.22). **e**, Comparison between the conductance G^{4T} at $V_{SGL} = V_{SGR} = 0 V$ (black trace) and $V_{SGL} = V_{SGR} = 9 V$ (red trace). The red trace is shifted $V_{SGL} \times \alpha_{rel} \approx 4.5 V$ in the V_{BG} – axis. **f**, Conductance G^{4T} represented as a function of k_F (refer to text). **g**, We determine the dimensions of the resonant cavity $L \approx 160 nm$ via the Fourier transform (FFT) study of the trace shown in f. Bias voltage is $V_b = 350 \mu V$ in all panels.

bands, also known as level spacing. We thus extract a characteristic length-scale $L = \hbar v_F / 2E_C \approx 140 nm$ from the extracted energy scale in Fig. 4.33b (red dashed line and arrow). This dimension is in the order of the constriction length $L_c \approx 150 nm$. We attribute the resonance path of the charge carriers to the back- and forth-scattering along the constriction length, presumably due to the PN-NP junctions building at the

bottle neck of the constriction with the leads (for more details see Section 4.2.1 or Fig. 4.8d). These findings represent another experimental proof supporting the situation depicted in Fig. 4.8d. Similarly, it is also possible to extract a characteristic length-scale L from the conductance oscillations as a function of V_{BG} . Once represented as a function of momentum $k_F = \sqrt{\pi\alpha V_{BG}}$, the pseudo-period of the oscillations Δk_F is directly proportional to the dimensions of the cavity $\Delta k_F = \pi/L$ (for more details please refer to Section 6.1). We extract a length-scale of $L \approx 160 \text{ nm}$, which is in fairly good agreement with the dimensions extracted from the bias spectroscopy measurements.

Moreover, at low temperatures, we also observe conductance fluctuations with a considerably smaller periodicity $\Delta V_{BG} \approx 0.2 \text{ V}$ (Fig. 4.29c and d). After extracting their energy scale $E_c \approx 16 \text{ meV}$ (Fig. 4.29c), we obtain a resonance length of $L \approx 700 \text{ nm}$, in agreement with the distance between constriction and metal contacts (Fig. 4.21a). Once the fundamental resonant periodicities in our graphene structure has been characterized, we focus on the effects of a symmetric potential inside the transport gap. As mentioned above, although the conductance traces are superimposed with resonant oscillations of a characteristic periodicity, at $V_{SGL} = V_{SGR} = 0 \text{ V}$, the transport gap does not show any traces of resonance pattern (black trace in Fig. 4.30d). By increasing the symmetric potential, resonant oscillations gradually develop inside the transport gap (Fig. 4.30). This effect is visible in the 2- and the 4-terminal conductance (Fig. 4.30a and b, respectively). Qualitatively, these oscillations behave equally as the ones observed at higher charge carrier densities (Fig. 4.27a). They evolve parallel to each other with the same relative lever arm (black arrows in Fig. 4.30a and b). A direct comparison of the conductance trace at $V_{SGL} = V_{SGR} = 0 \text{ V}$ and $V_{SGL} = V_{SGR} = 9 \text{ V}$ (black and red trace in Fig. 4.30d, respectively) reveal the striking differences between the two conductance traces close to the charge neutrality point.

Within this section we demonstrated the classical-to-quantum transition within the whole energy range of graphene nanodevices. Results suggests the possibility for nanometer-sized electronic elements that make use of quantum coherence. Compared to CNTs, where the fabrication of coherence devices is limited to the metallic ones [29], graphene devices are not limited by the chirality of their crystal structure, thus making them a far better candidates for the realization of quantum mechanical devices.

More importantly, we proof that edge disorder is significantly reduced by applying a symmetric side-gate potential. Close to charge neutrality point, an energy range that has been traditionally driven by Coulomb blockade physics, the disorder fluctuations have been reduced to the point where charge carriers started to develop hints of the wave-like behavior, i.e. quantum interference phenomena. These findings open the door to further reduce the effects of the edges and their inherent induced disorder potential, in graphene and other 2D materials.

4.4.3 Fano resonances as a proof of disorder reduction

In previous Section 4.4.1 we introduced the effects of an applied side-gate potential on the disorder landscape. Effectively, we assumed the charged puddles along the graphene constriction to increase in size under the effect of a symmetric side-gate potential. Thus reducing the amount of localized states that the charge carriers need to overcome to travel between source and drain leads (see sketch in Fig. 4.26). These assumptions were deduced by looking at the charging energies of the biggest diamond (see Fig. 4.27) as well as the dimensions of the transport gap in the bias spectroscopy measurements (Fig. 4.25). At that point, we presumed the edge disorder, due to a rough crystallographic orientation at the edges and/or the presence of trap states/contaminants, as being linked to the amount of disorder fluctuations, i.e. the number of charged puddles, along the electronic path. Either way, by operating the side-gate electrodes, we locally tune the potential at the graphene edges, which appears to enlarge the size of the localized states along the constriction axis (see sketch in Fig. 4.28). At the limit, under high side-gate potentials, we would thus expect the charged puddles to broaden beyond the constriction length, effectively building a quasi-1D channel between source and drain leads (Fig. 4.31).

In this section, we report on the experimental observation of a quasi-1D electronic system building along a graphene constriction. The 1D nature of the conductance path develops after shrinking the contribution of the disorder fluctuations by a symmetric side-gate potential (see Section 4.4.1). The 1D-like channel is identified via its coherent interference with a zero-dimensional (0D) system. The coherent interference between

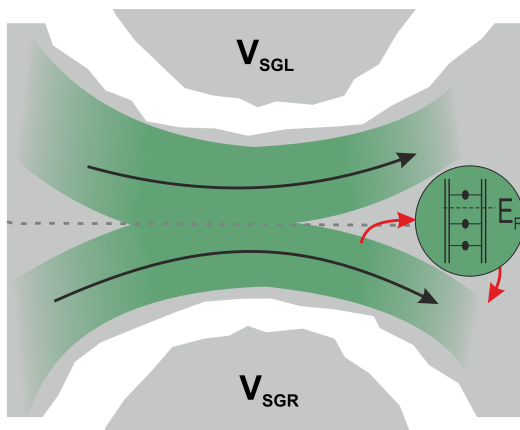


Figure 4.31: **Proposed interference path.** Schematic representation of a possible Fano system formed by a direct coherent quasi 1D-system and a resonant path, e.g. quantum dot. The 1D system is assumed to arise along the electronic path upon application of a symmetric side-gate potential. The location of the QD is justified by comparing its electrostatic coupling γ , i.e. relative lever arm, compared to the capacitive coupling of the Coulomb resonances within the transport gap (see discussion in text).

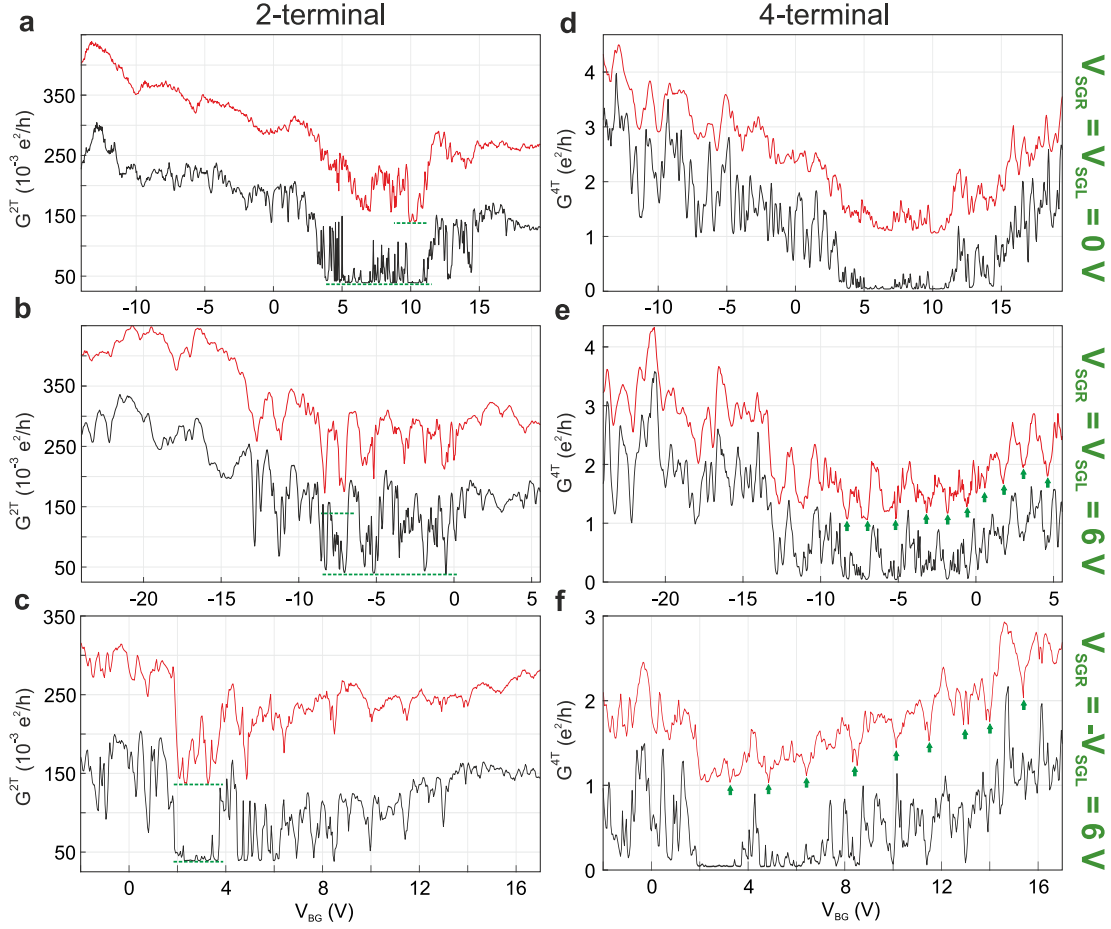


Figure 4.32: **Side-gate dependence of the Fano resonances.** **a**, **b** and **c**, 2-terminal conductance traces measured at $V_b = 250 \mu V$ (black traces) and $V_b = 5.5 mV$ (red traces) for $V_{SGL} = V_{SGR} = 0 V$, $V_{SGL} = V_{SGR} = 6 V$ and $V_{SGL} = -V_{SGR} = 6 V$ (panels **a**, **b** and **c**, respectively). The red traces are shifted $0.5 e^2/h$ units up in the conductance axis for clarity. **d**, **e** and **f**, Same as **a**, **b** and **c**, measured in a 4-terminal configuration. The green arrows indicate the position of quasi-periodic Fano line-shapes. All data panels have been recorded at $T = 15 mK$ and $B = 0 T$. The red traces are shifted $0.5 e^2/h$ units up in the conductance axis for clarity.

the 1D and 0D systems form a Fano-like interference pattern, visible in both the 2- and 4-terminal conductance. Results bring further evidences on the effects of a side-gate potential in flattening the disorder (refer to Section 4.4.1). Moreover, we appoint side-gated constrictions as a reliable route to fabricate Fano-resonance based quantum interference devices in graphene.

The Fano resonance (FR) is a universal physical effect that was successfully described by Fano in terms of interference between a resonant and a continuum, i.e. a non-resonant, state. This phenomenon is thus expected to arise in two-path elec-

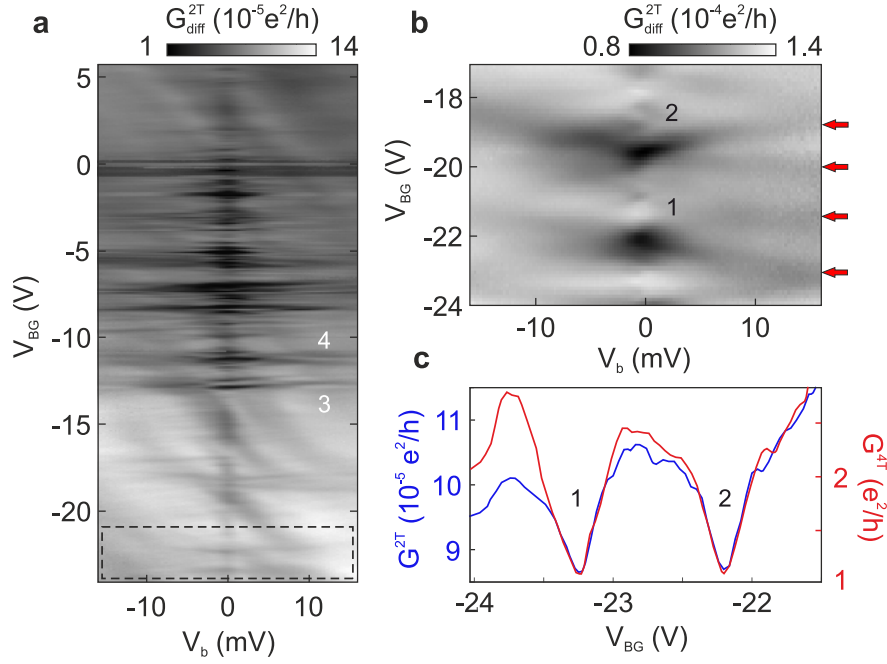


Figure 4.33: **Traces of Fano resonances at $B=0$ T, $V_{\text{SGL}}=V_{\text{SGR}}=6$ V and $T=15$ mK.** **a**, Bias spectroscopy measurements of the 2-terminal differential conductance G_{diff}^{2T} . **b**, Zoom-in map inside the region of elevated conductance (dashed-line region in panel a). The Fano resonances are highlighted by red arrows at high bias voltages **c**, 2- and 4-terminal conductance traces of the Fano resonances "1" and "2" (panel b), measured at $V_b = 0$ V. The complete 2- and 4-terminal back-gate traces can be found in Fig. 4.32 and Fig. 4.35. We label the Fano resonances from "1" to "4".

tronic transport measurements where the coherence of the charge carriers is conserved. The observation of Fano line-shapes has previously been observed in carbon nanotubes (CNTs), where the 1D nature of the channel and its interference with a resonant path yielded the observation of such phenomenon [31]. In graphene though, the observation of Fano resonances has yet to be reported, presumably due to the disordered nature of the graphene nano-structures and hence the difficulty of building coherent quasi-1D systems. As illustrated in Fig. 4.31, the effect of strong side-gate potential may enlarge the size of the localized states beyond the constriction length thus creating an effective 1D channel (represented in green in Fig. 4.31). In order to produce Fano interferences, this continuum path has to coherently interfere with a resonant path, e.g. localized state or quantum dot. In our case we propose the QD to be located at the bottle neck of the graphene constriction, as depicted in Fig. 4.31. We will later on support this assumption by looking the electrostatic coupling of the QD relative to the back-gate and side-gate electrodes.

Following the theory from Fano [32, 33], we describe the voltage-dependent conduc-

tance $G(V_{BG})$ of a Fano line-shape as follows:

$$G(V_{BG}) = G_{non} + G_{int}(V_{BG}), \quad (4.9)$$

where G_{non} denote the non-interfering contribution of the 1D channel to the conductance and G_{int} is the Fano, i.e. coherent contribution, defined as:

$$G_{int}(V_{BG}) = A \frac{(\epsilon + q)^2}{\epsilon^2 + 1} \quad \text{and} \quad \epsilon = \frac{\alpha(V_{BG} - V_0)}{\Gamma/2}, \quad (4.10)$$

hence, the Fano resonances are expected to appear in transport measurements as sharp dips in conductance [31] with ϵ being a dimensionless parameter and A , V_0 and Γ the amplitude, position and width of the Fano resonance, respectively. The lever arm α relate in that case to the electrostatic coupling of the quantum dot to the back-gate. The asymmetry parameter q is proportional to the ratio of the transmission amplitudes of the resonant and non-resonant paths. Although this parameter is considered a real quantity in the original Fano theory [34], and will be considered so in the first part of this section, it must be treated as a complex number in general [35]. This parameter leads to resonant (symmetric conductance peak) and anti-resonant transmission (symmetric dip) for $q \rightarrow \infty$ and $q \rightarrow 0$, respectively. In all other situations, e.g. $q = 1$, the Fano resonances have an asymmetric characteristic line shape (Fig. 4.34a). In our system, the lever arm $\alpha \approx 0.27 \text{ meV/mV}$ is directly estimated from the differential conductance at finite source-drain voltages V_b (Fig. 4.37a) [36].

Fano resonances at zero Tesla

Initially, we will analyze the differences in the conductance traces as a function of back-gate voltage for the different configurations of the side-gate potential (Fig. 4.32). The

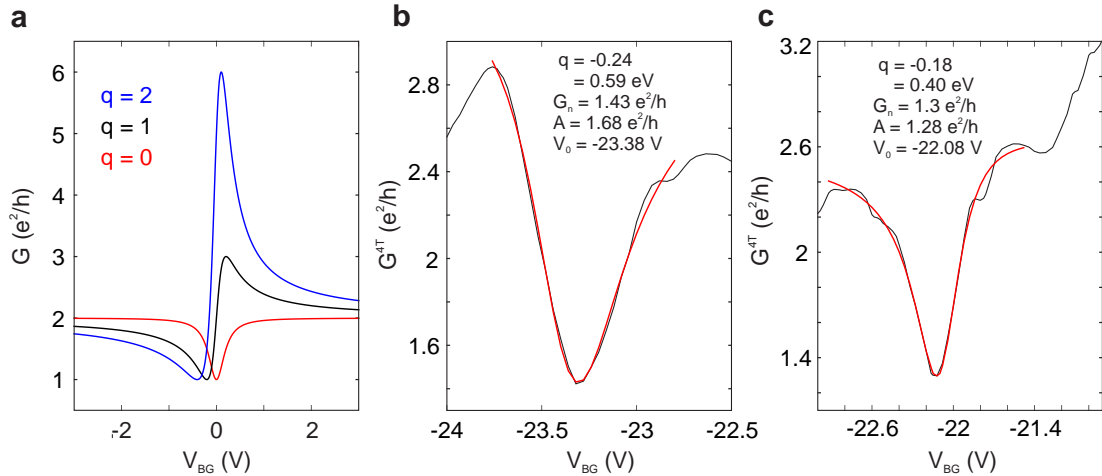


Figure 4.34: **Comparison with the Fano theory.** **a**, Theoretical Fano line-shapes from Eq. 4.10, represented for different values of $q \in \mathfrak{R}$. **b** and **c**, Conductance of the Fano peaks noted 1 and 2 in Fig. 4.33c, measured at $V_b = 3 \text{ mV}$. The data is fitted with the Fano line-shape expression in Eq. 4.10.

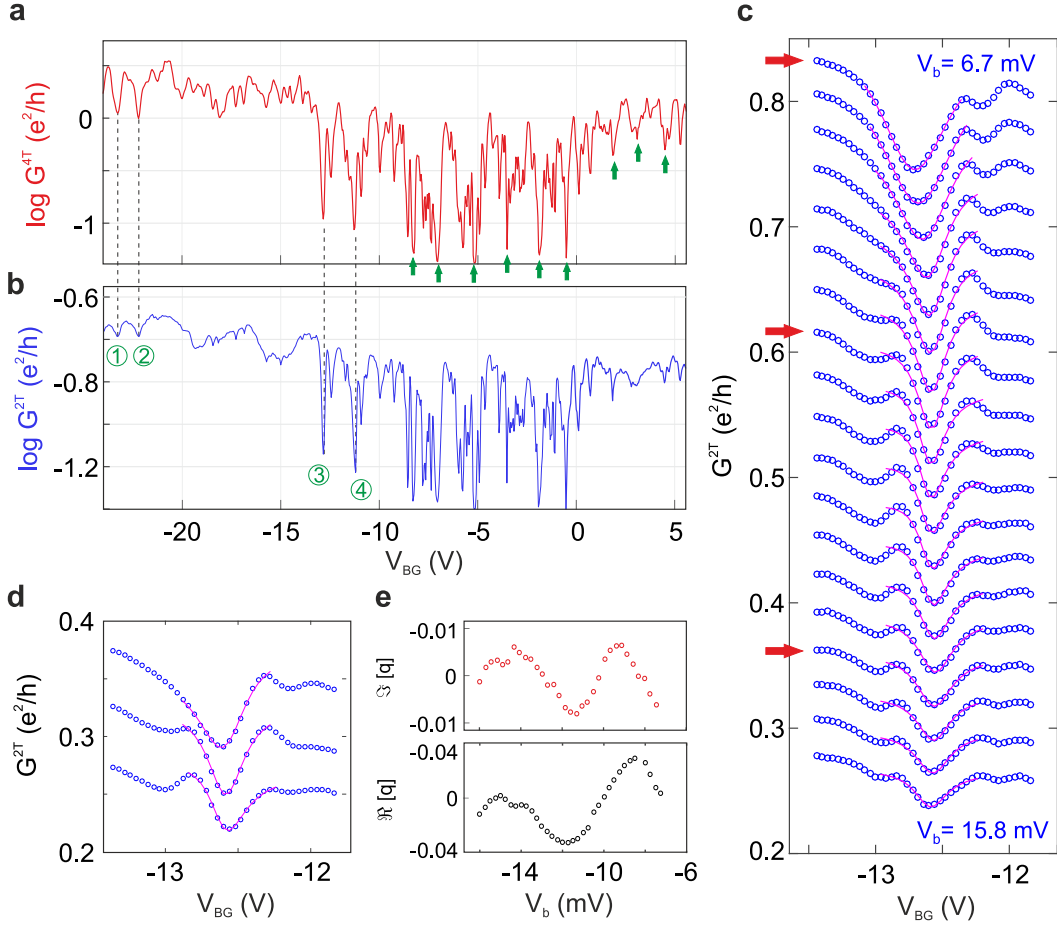


Figure 4.35: **Traces of Fano interference at $V_{SGL}=V_{SGR}=6\text{ V}$, $B=0\text{ T}$ and $T=15\text{ mK}$.** **a** and **b**, 2- and 4-terminal conductance measured at $V_b=250\text{ }\mu\text{V}$, from the measurement shown in Fig. 4.33b. The green arrows indicate the position in V_{BG} of the quasi-periodic Fano lines for the electrons side. For the holes side, we label the Fano resonances from "1" to "4". **c**, Bias evolution of the Fano line-shape labeled "4" in panel b, measured from $V_b=6.7\text{ mV}$ to $V_b=15.8\text{ mV}$ in steps of 0.5 mV . **d**, Fano line-shapes at the bias voltages marked by a red arrow in panel c. **e**, Extracted $\Re[q]$ and $\Im[q]$ by fitting the Fano model (see Eq. 4.11) to the Fano line-shapes of panel c.

aim of this section is to emphasize that the application of a side-gate potential contribute to the appearance of Fano resonances. As observed in Fig. 4.32, not only the levels of conductance are increased upon application of a side-gate potential (compare the base ground conductance marked by an horizontal green dashed line in panels a, b and c of Fig. 4.32) but sharp and periodic dips in conductance are clearly distinguishable when applying a side-gate potential, i.e. for $V_{SGL}=V_{SGR}=6\text{ V}$ or $V_{SGL}=-V_{SGR}=6\text{ V}$ (see green arrows in panels e and f of Fig. 4.32, respectively). The sharp dips in conductance are visible for both the 2- and 4-terminal measurements (compare left and right

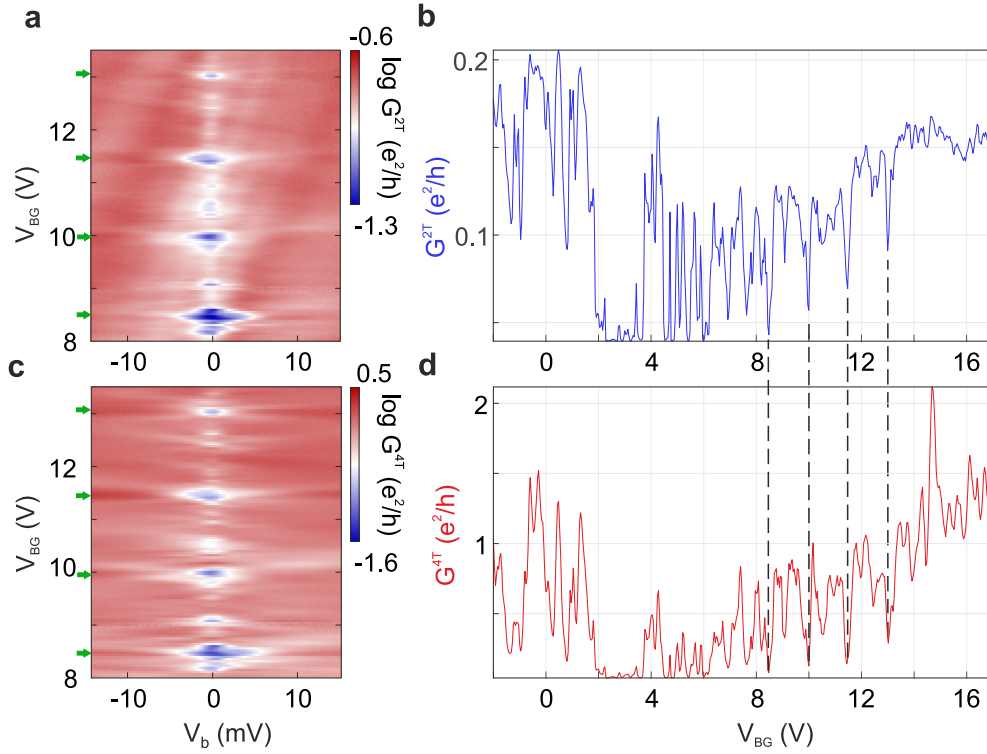


Figure 4.36: **Traces of Fano interference at $V_{SGL} = -V_{SGR} = 6$ V, $B = 0$ T and $T = 15$ mK.** **a** and **b**, 2-terminal conductance map (panel a) for $V_{SGL} = -V_{SGR} = 6$ V showing four equidistant Fano resonances. The associated conductance line-cut at $V_b = -1$ mV (panel b) has the position of the Fano line-shapes highlighted by black dashed lines. **c** and **d**, Same as panels a and b for the 4-terminal configuration. The periodic position of the Fano resonances in the V_{BG} -axis is indicated by green arrows in panel a and by dashed black lines in panels b and d.

panels in Fig. 4.32) and at low and high bias voltages (compare black and red traces in Fig. 4.32). Although there are also sharp and reproducible dips in conductance for $V_{SGL} = V_{SGR} = 0$ V (panels a and d of Fig. 4.32), we do not observe any evident periodic pattern. For intrinsic Fano resonances (FRs) one would expect a regular periodic pattern of FRs to evolve as a function of energy or, alternatively, back-gate voltage [31]. The observation of this periodic sequence of Fano resonances indicate that the charge along the 1D-like path conserve their coherence and the QD remains stable with equidistant Coulomb charging events within the back-gate voltage range. Without any side-gate potential applied ($V_{SGL} = V_{SGR} = 0$ V), a higher number of localized states are supposed to contribute to transport, burying the 1D nature of the direct path and/or randomizing their overall coherent contribution, hence obscuring any clear periodic Fano resonance pattern.

To corroborate the sharp and reproducible dips in conductance observed in Fig. 4.32 as being Fano-based interferences, we will first turn our attention to the bias spec-

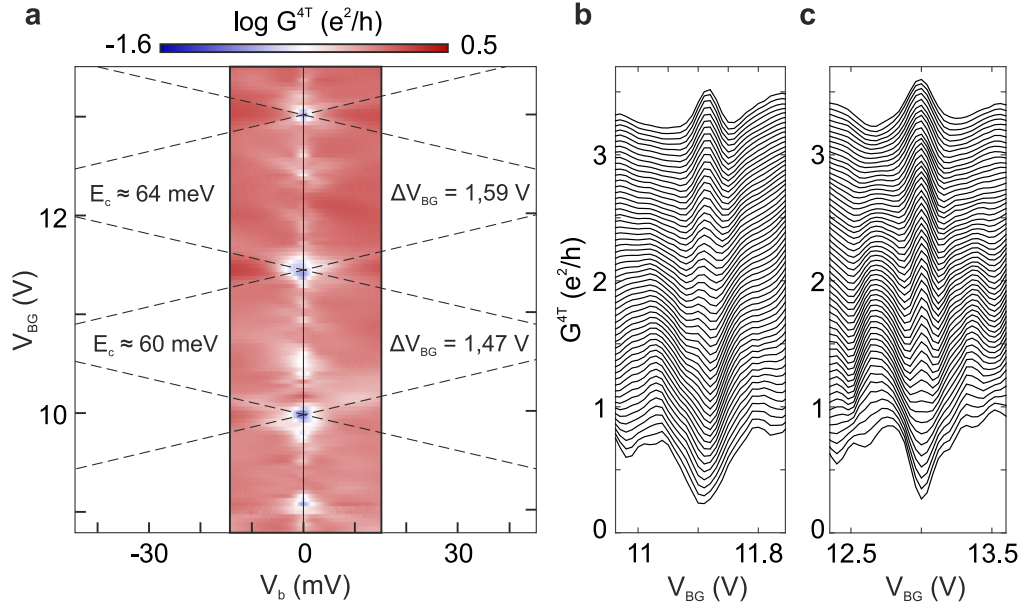


Figure 4.37: **Associated energy scales at $V_{SGL} = -V_{SGR} = 6\text{ V}$, $B = 0\text{ T}$ and $T = 15\text{ mK}$.** **a**, Re-plotted bias spectroscopy map from Fig. 4.36c. The diamonds are highlighted by dashed black lines and the extracted energies are indicated inside each diamond. **b** and **c**, 4-terminal conductance line-cuts from $V_b = 0\text{ mV}$ (lowest trace) up to 14 mV (upper trace) in steps of 0.25 mV , of the Fano-lines at $V_{BG} \approx 11.5\text{ V}$ (panel b) and $V_{BG} \approx 13\text{ V}$ (panel c) in panel a and Fig. 4.36c.

troscopy measurements at high side-gate potentials ($V_{SGL} = V_{SGR} = 6\text{ V}$) (Fig. 4.33). In that configuration, the finite bias measurements show the same quasi periodic distribution of dips in conductance appearing in panels b and e of Fig. 4.32. Within the high conductance region (voltage range from $V_{BG} \approx -11\text{ V}$ to -24 V of Fig. 4.33a or Fig. 4.32b, e) the overall conductance is above $G^{4T} \sim 1e^2/h$ (or $G^{2T} \sim 0.015e^2/h$ for the 2-terminal conductance), a level of conductance comparable to the non-resonant contribution expected for a quasi-1D channel (Eq. 4.10). The sharp resonance conductance dips are on the order of $\sim 1e^2/h$ for the 4-terminal conductance (red trace in Fig. 4.33c). These resonance features conserve the same line-shape in both the 2- and 4-terminal conductance (blue and red trace in Fig. 4.33c). As shown in Fig. 4.33b (zoom-in measurement inside the dashed black box of Fig. 4.33a) the individual dips in conductance at $V_b = 0\text{ V}$ linearly split as a function of bias voltage into two conductance dips (see red arrows in Fig. 4.33b and resonances 3 and 4 in Fig. 4.33a, or in Fig. 4.36 and Fig. 4.37 for the anti-symmetric configuration of the side-gate potentials). This is expected in Fano interferences [31], where the Fano line shapes are indeed the boundaries of adjacent "inverted" Coulomb blockade diamonds. For increasing bias voltages the resonances split in order to follow a diamond-like shape [31]. In Fig. 4.34, we re-plot the resonances number 1 and 2 of Fig. 4.33c with their corresponding fits to the model (Eq. 4.10). The fitting procedure yields similar symmetry values of $q \approx -0.24$ and -0.18 and a comparable broadening of $\Gamma \approx 0.59$ and 0.4 eV for both Fano line-shapes.

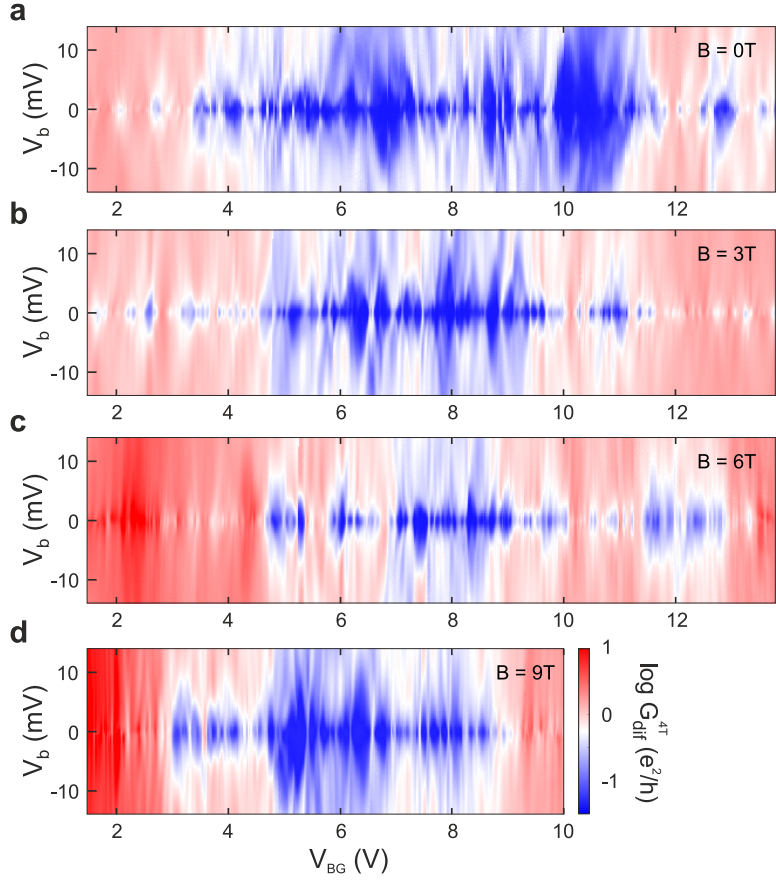


Figure 4.38: **Disorder-reduction under finite magnetic fields.** **a**, **b**, **c** and **d**, Diamond plots inside the transport gap measured at different values of magnetic field $B=0, 3, 6$ and 9 T (panels **a**, **b**, **c** and **d**, respectively), for the 4-terminal differential conductance G_{diff}^{4T} at $V_{SGL} = V_{SGR} = 0\text{ V}$. We observe a gradual decrease in disorder until $B=6\text{ T}$, although the coulomb pattern is conserved in all maps.

Although these values are noticeably broad (we appoint that resonances 3 and 4 in Fig. 4.33c are slightly sharper, with a $\Gamma \sim 0.2\text{ V}$), the height of the Fano peaks, defined as $A(1 + q^2)$, is manifestly larger than $\sim 1 e^2/h$.

Eventhough the Fano conductance model described by Eq. 4.10 is widely used to fit individual Fano line-shapes [31, 36] treating the $|q|$ parameter as a real number conflicts when the asymmetry of the line shape evolves cyclically [33]. This behavior is already visible in Fig. 4.35c and d, where the asymmetry of the Fano line shape for resonance 4 (Fig. 4.35b) depends cyclically as a function of bias voltage. In order to extract meaningful parameters we thus need to introduce q as a complex number [33]. We modified the expression in Eq. 4.10 as follows:

$$G_{int}(V_{BG}) = A \frac{|\epsilon + q|^2}{\epsilon^2 + 1} = A \frac{(\epsilon + \text{Re}[q])^2 + (\text{Im}[q])^2}{\epsilon^2 + 1}, \quad (4.11)$$

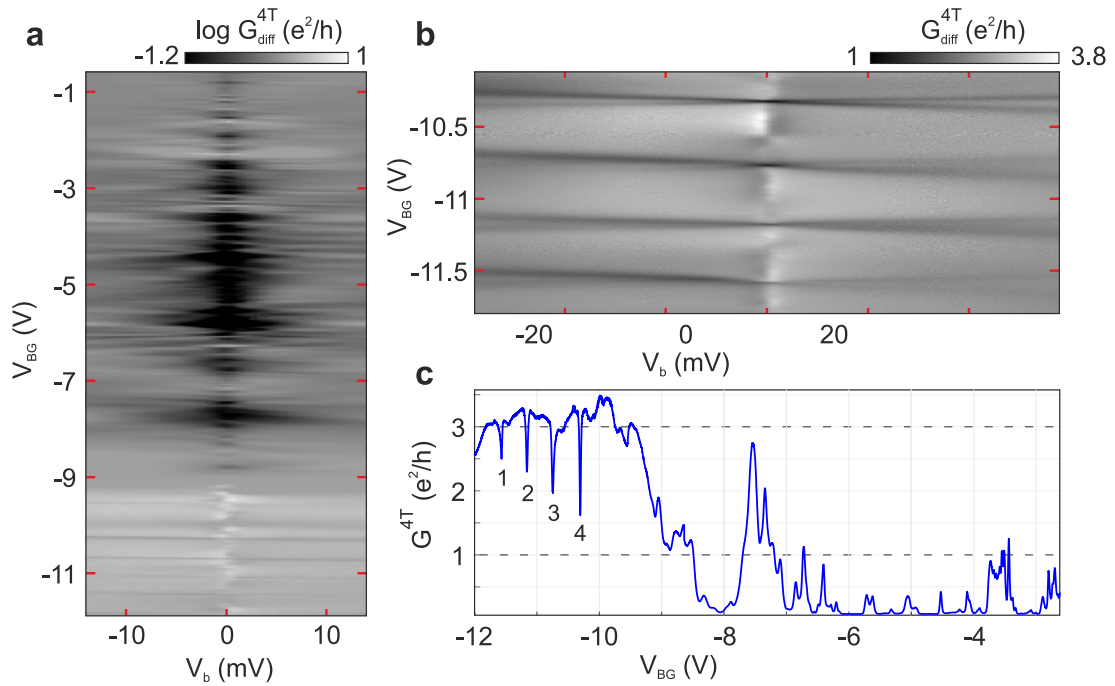


Figure 4.39: **Fano resonances at finite B -fields.** **a, b**, Differential 4-terminal conductance G^{4T} as a function of bias V_b and back-gate voltage V_{BG} measured at $B = 9 T$ under a high symmetric side potential $V_{SGL} = V_{SGR} = 8 V$ ($T = 20 mK$). The close-up region where the Fano resonances appear is shown in panel b. **c**, Conductance trace at $V_b = 0 V$. The Fano dips are labeled from 1 to 4.

Fitting this model of conductance to the measured resonances (see magenta and blue circles in Fig. 4.35c and d for the model and measurements, respectively) provides the real and imaginary part of the complex parameter q ($\Re[q]$ and $\Im[q]$, respectively in Fig. 4.35e), showing a periodic evolution. The rest of parameters in Eq. 4.11 extracted from the fitting routine read $A \approx 0.34 e^2/h$ and $\Gamma \approx 0.08$.

The bias spectroscopy analysis of the antisymmetric case ($V_{SGR} = -V_{SGL} = 6 V$) also reflects the Fano nature of the interference features (Fig. 4.36). The resonances are periodic in the V_{BG} axis ($\Delta V_{BG} \approx 1.5 V$, see distance between green arrows in Fig. 4.36a or in Fig. 4.37) The conductance evolution of the Fano resonances as a function of bias voltage (Fig. 4.36a, c) shows the characteristic splitting of the resonant dip (see dashed lines in Fig. 4.37a) [36]. At zero bias voltage $V_b = 0 V$ the Fano line shape appears as a single sharp dip in conductance, visible in both the 2- and 4-terminal quantities (panels b and d of Fig. 4.36). As expected, the Fano line shape splits for increasing bias voltages V_b (Fig. 4.36a, c) giving insightful information on the resonant path, e.g. the charging energy E_c of the quantum dot (Fig. 4.37a). It is important to emphasize that the differential conductance seems to follow a Coulomb blockade pattern although, in that case, the boundaries of the coulomb diamonds are defined by dips rather than peaks in conductance (Fig. 4.37b). The boundaries of the Coulomb diamonds are ex-

trapolated at high bias voltages (Fig. 4.37a) to extract the energy scale of the quantum dot (dashed black lines in Fig. 4.37a). From the charging energies E_c obtained from the size of the coulomb diamonds in the V_b -axis direction (values marked in Fig. 4.37a), we extract the diameter of the quantum dot $d = e^2 / (4\epsilon_0\epsilon_r E_c)$, where $\epsilon_r = (1 + 4)/2$ [23]. The dimensions of the QD $d \approx 30 \text{ nm}$ are small enough to sit within the constricted region.

Fano resonances at finite magnetic fields

In an attempt to further reduce the influence of the disorder fluctuations and to sharpen the Fano interferences, we analyze the transport behavior of the Fano resonances under finite perpendicular magnetic fields. Finite B -fields have been shown to flatten the contribution of potential fluctuations in electrical transport measurements through graphene nano-structures [37, 38]. Moreover, tuning the magnetic field should allow us to independently control the phase of the Fano interference [33]. As expected, around the charge neutrality point (Fig. 4.38), we observe a decrease of the transport and energy gaps, ΔE_F and E_g , respectively (see Section 4.1 for an introduction to these terms), as a function of magnetic fields up to $B = 6 \text{ T}$. Fig. 4.38 shows the differential conductance G_{diff} vs. V_{BG} and V_b for four different values of magnetic field $B = 0, 3, 6$ and 9 T . The bias spectroscopy map at $B = 9 \text{ T}$ does not follow the trend and shows comparatively larger Coulomb diamonds (compare panel d with previous panels in Fig. 4.38). At $B = 9 \text{ T}$ the Landau quantization is already established in the graphene nanoribbon (see Landau level fan in Fig. 4.10) and the development of the insulating state $\nu = 0$ may mislead the interpretation of the data.

To see whether the Fano line shapes sharpen under high magnetic fields, we repeat the bias spectroscopy measurement shown in Fig. 4.33a now measured at $B = 9 \text{ T}$ and $V_{SGR} = V_{SGL} = 8 \text{ V}$ (Fig. 4.39). At that levels of magnetic field we expect Landau Level quantization to appear even within the constricted region. As expected, at elevated levels of conductance we observe four characteristic Fano resonances for the hole transport regime (Fig. 4.39). A conductance trace at $V_b = 0 \text{ V}$ (Fig. 4.39c) show four sharp conductance dips as well as equidistant Coulomb resonances inside the transport gap.

As discussed previously when introducing the Fano model of conductance (Eq. 4.10) the 1D path contributes to transport with a constant non-energy dependent term. This statement is perfectly valid here, with the equidistant sharp resonances sitting at a level of conductance of $\sim 3e^2/h$. This conductance reveal the lifting of the QHE introduced in Section 4.2.1 or the presence of PN-NP junctions along the electronic path [39]. Considering that degeneracy lifting of the Landau levels applies, the sequence of the conductance plateaus suggest the complete lifting of the first Landau level (LL), i.e. LL0, and the partial lifting of the second Landau level, i.e. LL1, in order to account for the $\sim 3e^2/h$ conductance plateau. The irregular degeneracy of the LL's is in agreement with Section 4.2.1 (Fig. 4.10). It is worth mentioning that at $B = 9 \text{ T}$ the magnetic length $l_b \approx 26/\sqrt{B[\text{T}]} \text{ nm} \approx 9 \text{ nm}$ [40] is smaller than the diameter of the resonant QD measured at zero Tesla ($d \approx 30 \text{ nm}$), thus we expect the QD to be also affected by the

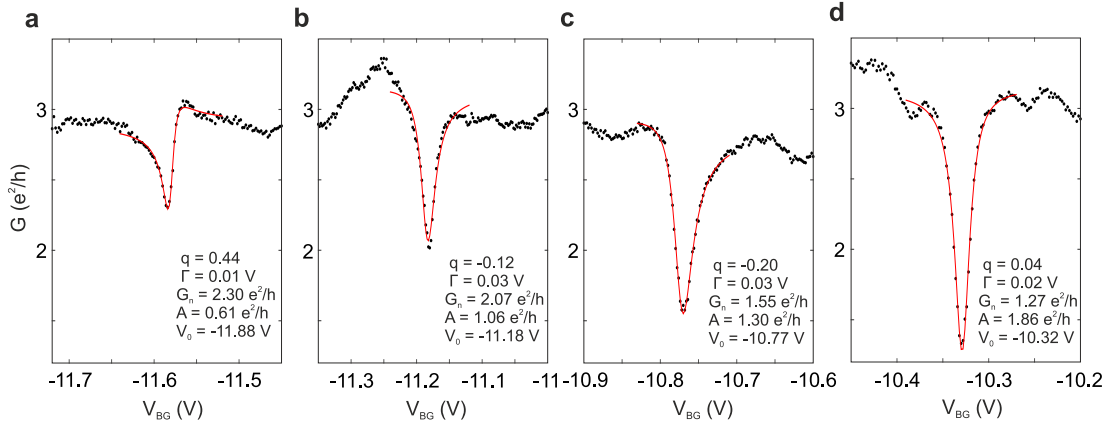


Figure 4.40: **Fano line-shape analysis.** **a, b, c** and **d**, Characterization of the Fano line shapes appearing in Fig. 4.39. The panels **a, b, c** and **d** correspond to the Fano peaks labeled 1, 2, 3 and 4 in Fig. 4.39c. The fitting parameters are show inside the panels.

magnetic field (Fig. 4.43d).

The fitted values G_n , A , Γ , q and V_0 are again extracted by fitting the Fano expression (Eq. 4.10) to the measurements (Fig. 4.40). The Fano resonances appear sharper ($\Gamma \approx 0.02 V$ in Fig. 4.40) but are on the same order of magnitude as at zero Tesla ($\Gamma \approx 0.08 V$ in Fig. 4.35, see corresponding text). Moreover, we find the sign of q to vary between consecutive Fano peaks (Fig. 4.40). These findings suggest the phase of the Fano resonances to be de-phased in respect to each other [33], which is reasonable taking into account that measurements are done at a fixed $B=9 T$ and that there is a constant energy separation between resonances ($\Delta E = \alpha \Delta V_{BG}$ in Fig. 4.41).

Again, we extract the dimensions of the resonant path, e.g. quantum dot (Fig. 4.33a), from the evolution of the Fano resonances as a function of bias and back-gate voltage (Fig. 4.41). The charging energies E_c are obtained from the Coulomb diamond dimensions along the V_b -direction. The extracted E_c are indicated in Fig. 4.41a. The dimensions of the quantum dot are $d \approx 15 nm$, which is smaller than the diameter extracted at zero Tesla ($d \approx 30 nm$ from Fig. 4.37a).

By looking at the evolution of the Fano resonances as a function of side- and back-gate voltages, we can learn on the electrostatic coupling of the quantum dot and therefore its location within the constriction width. Fig. 4.41b and c compares the relative lever arm α_{rel} of the coulomb resonances living inside the transport gap (panel c) and the Fano resonances (panel b) measured at higher levels of conductance. We note that, although we show the 2- and 4-terminal conductance in panels b and c of Fig. 4.41, both quantities are exchangeable as proven in Fig. 4.32. We decided to plot the 2-terminal conductance in panel b to clearly differentiate the Fano resonances from the background. We obtain $\alpha_{rel} \approx \Delta V_{BG} / \Delta V_{SG} \approx 1, 25$ and $1, 47$ for the Coulomb and Fano resonances, respectively. A direct comparison is plotted in Fig. 4.41b with the direction of the Coulomb resonances represented in red. Results suggest the QD responsible for the

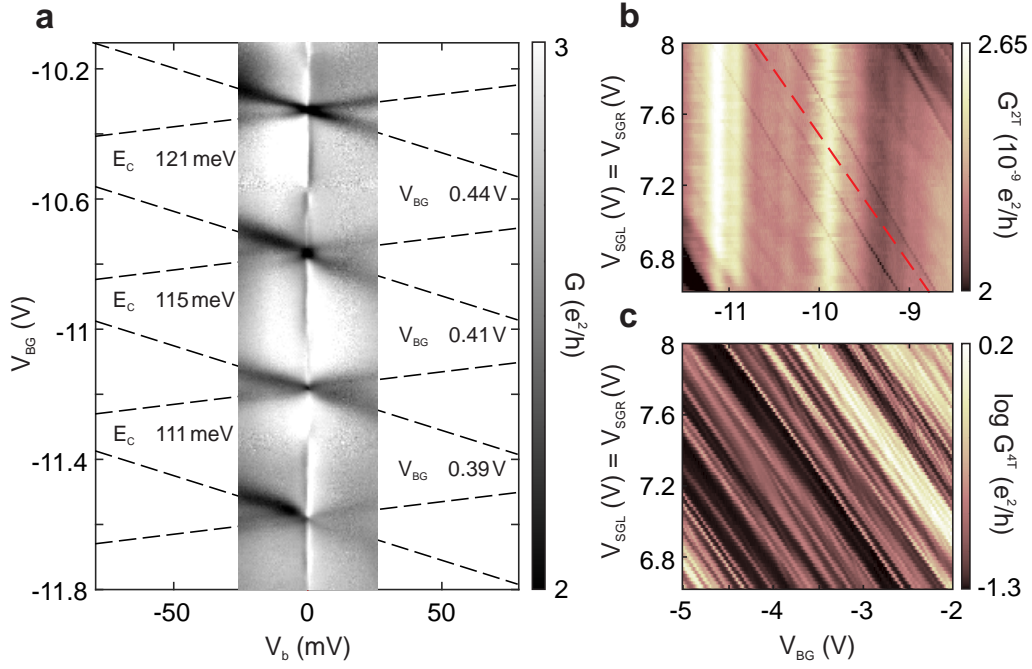


Figure 4.41: **Characterization of the resonant path.** **a**, Four-terminal differential conductance as a function of bias (V_b) and back-gate (V_{BG}) voltages. The zero-bias conductance trace can be seen in Fig. 4.39c. **b**, **c**, Two- and four-terminal conductance maps as a function of V_{BG} and the symmetrically applied side-gate voltages $V_{SGL} = V_{SGR}$.

Fano-like interference to be weakly coupled to the side-gate potentials. We deduce the QD to be located further away from the constriction/edge region as depicted in Fig. 4.31.

The fact that phase coherence is conserved across the Fano interferometer depicted in Fig. 4.31 is essential in Fano theory. In order to estimate the robustness of the interference process, we study the Fano resonances as a function of temperature Fig. 4.42. As shown in Fig. 4.42, there is a clear broadening of the Fano resonance with temperature although the shape is recognizable as a Fano line shape up to temperatures as high as $T \sim 2.8 K$ (Fig. 4.42b). This value of temperature is one order of magnitude higher than for previously reported Fano interferometers on a 2DEG device based on AlGaAs/GaAs [33]. This results may indicate that coherence in graphene is conserved for comparatively higher temperatures than in other 2DEG materials. The question arise whether this particular robustness against temperature can be attributed to the 2D nature of graphene and hence the lack of perpendicular temperature activated phonon modes.

One of the experimental advantages of our system is the spatial separation between the quantum dot and the continuum (Fig. 4.31). It is therefore possible to magnetically control the Fano effect by triggering a perpendicular magnetic field (Fig. 4.43). Sweeping the B -field results in Aharonov-Bohm (AB) based oscillations proportional to the number of flux quanta entering the enclosed region defined by the quantum dot and the resonant path (Fig. 4.31). Fig. 4.43a shows the periodically oscillating Fano

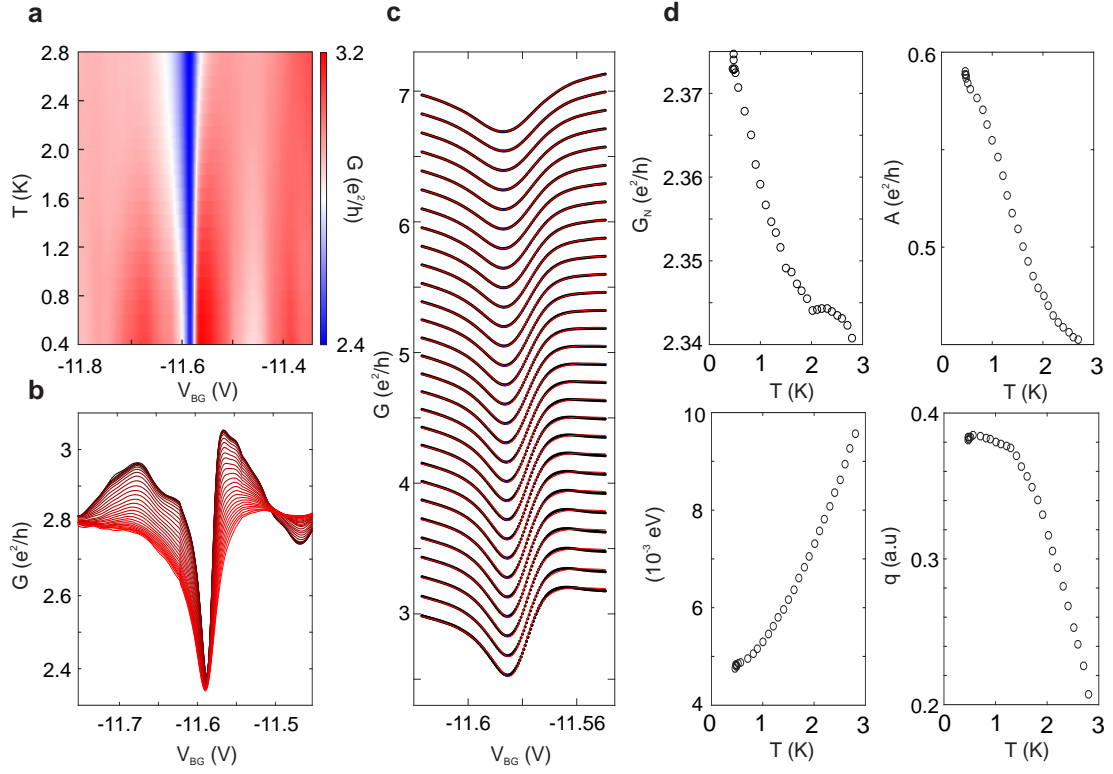


Figure 4.42: **Temperature dependence of the Fano interference.** **a, b,** Temperature dependence of the First Fano line shape (Fig. 4.39c) from $T = 400 \text{ mK}$ up to 2.8 K . **c,** Every individual conductance trace (black data points) is fitted with the conductance model (red solid line) discussed in Eq. 4.10. **d,** The parameters G_N , A , Γ and q are extracted from measurements by the fitting routine shown in panel c.

interferences measured from $B = 7$ to $9 T$. As observed, the asymmetry of the Fano's line-shape evolves with magnetic field. In order to extract meaningful parameters from the magnetic evolution we use Eq. 4.11, where q is defined as a complex number [33]. Issued from the fitting procedure, the periodicity is very much apparent in the real and imaginary part of the asymmetry parameter q ($\Re[q]$ and $\Im[q]$, respectively in Fig. 4.43b and c). From those, we extract an oscillation AB period $\Delta B \sim 1 T$. The diameter d of the area enclosed by the 1D-like path and the quantum dot (Fig. 4.33a) can be calculated as $d = 2\sqrt{\hbar/\pi\Delta B} \approx 70 \text{ nm}$. This value is equal to the dimensions of the $\sim 70 \text{ nm}$ -wide constriction shown in Fig. 4.21a. This result brings further evidences that the Fano interference phenomena may happen at the bottle neck region, most probably between the 1D-like electronic path circulating along the ribbons axis and a 0D-like localized state located further away from the constriction.

Conclusions

This section is revelatory of the effects of a laterally applied electrostatic potential on the transport characteristics of graphene nanoribbons. Close to the charge neutrality

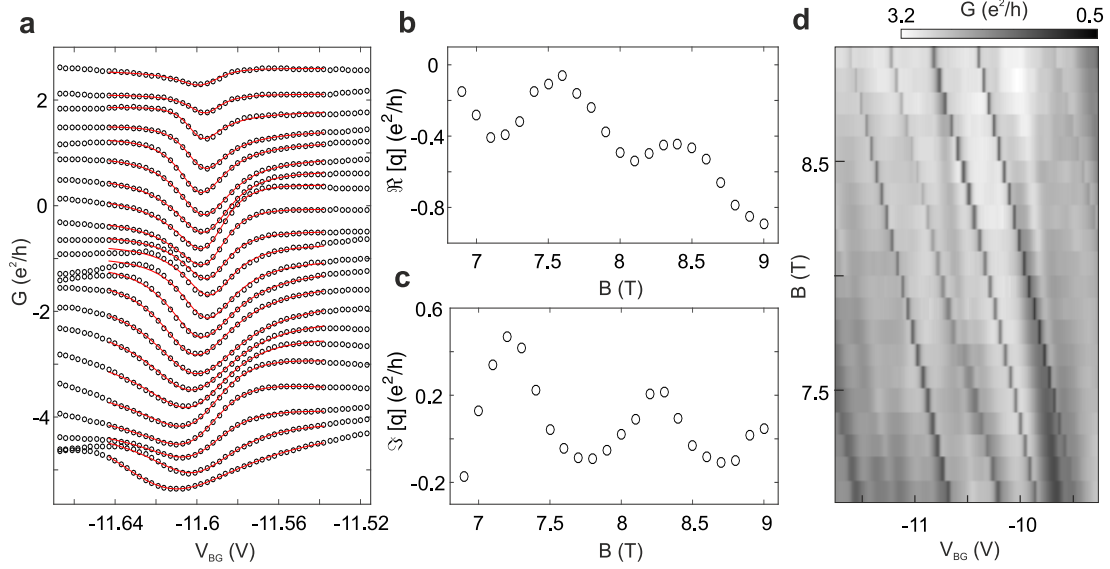


Figure 4.43: **Magnetic control of the Fano interference.** **a**, Conductance traces measured at $T = 100 \text{ mK}$ and different values of magnetic field from $B = 9 \text{ T}$ to 6.9 T in steps of 0.1 T . The open circles and the red solid lines are the data and the fitting procedure, respectively. The traces are incrementally shifted downwards in the G -axis for clarity. The upper most trace ($B = 9 \text{ T}$) has a conductance level of $\sim 3 e^2/h$. **b**, **c**, Obtained $\text{Re}[q]$ (panel b) and $\text{Im}[q]$ (panel c) from the fitting routine (Eq. 4.11). **d**, The results from panels b and c are plotted in the complex q plane. **f**, Conductance map as a function B -field and back-gate voltage for the four resonances under study (see Fig. 4.39c).

point, transport evolves as a function of the side-gate potential from a Coulomb blockade dominated behavior onto an elevated conductance regime where coherence effects start to play an important role. Results bring further evidences on the effects of a side-gate potential in flattening the edge-induced disorder. Throughout this section we studied the Fano interference phenomena in graphene and we identified the robustness in temperature of the interference process compared to GaAs-based interference devices. Results appoint side-gated constrictions as a reliable route to fabricate Fano-resonance based quantum interference devices in graphene.

References

1. Xue, J. *et al.* Scanning tunnelling microscopy and spectroscopy of ultra-flat graphene on hexagonal boron nitride. *Nat. Mat.* **10**, 282 (2011).
2. Martin, J. *et al.* Observation of electron hole puddles in graphene using a scanning single-electron transistor. *Nature Physics* **4**, 144–148 (2008).
3. Deshpande, D. *et al.* Spatially resolved spectroscopy of monolayer graphene on SiO₂. *Phys. Rev. B* **79**, 205411 (2009).
4. Zhang, Y. *et al.* Origin of spatial charge inhomogeneity in graphene. *Nature Physics* **5**, 722–726 (2009).
5. Ihnatsenka, S. *et al.* Conductance quantization in graphene nanoconstrictions with mesoscopically smooth but atomically stepped boundaries. *Phys. Rev. B* **85**, 121407(R) (2012).
6. Mucciolo, E. R. *et al.* Conductance quantization and transport gaps in disordered graphene nanoribbons. *Phys. Rev. B* **79**, 075407 (2009).
7. Ihnatsenka, S. *et al.* Conductance quantization in strongly disordered graphene ribbons. *Phys. Rev. B* **80**, 201407(R) (2009).
8. Wang, X. *et al.* Graphene nanoribbons with smooth edges behave as quantum wires. *Nature Nanotechnology* **6**, 563–567 (2011).
9. Ryu, S. *et al.* Raman Spectroscopy of Lithographically Patterned Graphene Nanoribbons. *ACS Nano* **5** (5), 4123–4130 (2011).
10. Terrés, B. *et al.* Raman spectroscopy on mechanically exfoliated pristine graphene ribbons. *Physica status solidi (b)*, **12**, 251, 2551–2555 (2014).
11. He, K. *et al.* Hydrogen-free graphene edges. *Nature Communications* **5**, 3040 (2013).
12. Ferrari, A. *et al.* Raman Spectrum of Graphene and Graphene Layers. *Phys. Rev. Lett.* **97**, 187401 (2006).
13. Dauber, J. *et al.* Reducing disorder in graphene nanoribbons by chemical edge modification. *Appl. Phys. Lett.* **104**, 083105 (2014).
14. Terrés, B. *et al.* Disorder induced Coulomb gaps in graphene constrictions with different aspect ratios. *Appl. Phys. Lett.* **98**, 032109 (2011).
15. Han, M. Y. *et al.* Energy Band-Gap Engineering of Graphene Nanoribbons. *Phys. Rev. Lett.* **98**, 206805 (2007).
16. Ozyilmaz, B. *et al.* Electronic transport in locally gated graphene nanoconstrictions. *Appl. Phys. Lett.* **91**, 192107 (2007).
17. Stampfer, C. *et al.* Energy Gaps in Etched Graphene Nanoribbons. *Phys. Rev. Lett.* **102**, 056403 (2009).
18. Birner, S. *et al.* Modeling of Semiconductor Nanostructures with nextnano3. *Acta Physica Polonica Series A.* **110**, 2, 111 (2006).
19. Birner, S. *et al.* nextnano: General Purpose 3D Simulations. *Electron Devices and IEEE Transactions* **54**, 9, 2137–2142 (2007).

20. Silvestrov, P. G. *et al.* Charge accumulation at the boundaries of a graphene strip induced by a gate voltage: Electrostatic approach. *Phys. Rev. B* **77**, 155436 (2008).
21. T.Vasko, F. *et al.* Conductivity of a graphene strip, width and gate voltage dependencies. *Appl. Phys. Lett.* **97**, 092115 (2010).
22. Vera-Marun, I. J. *et al.* Quantum Hall transport as a probe of capacitance profile at graphene edges. *Appl. Phys. Lett.* **102**, 013106 (2013).
23. Stampfer, C. *et al.* Energy Gaps in Etched Graphene Nanoribbons. *Phys. Rev. Lett.* **102**, 056403 (2008).
24. White, C. T. *et al.* Conductivity of a graphene strip: Width and gate-voltage dependencies. *Nano Lett.* **7**, 825 (2007).
25. Nakada, K. *et al.* Edge state in graphene ribbons: Nanometer size effect and edge shape dependence. *Phys. Rev. B* **54**, 17954 (1996).
26. Stampfer, C. *et al.* Raman imaging of doping domains in graphene on SiO₂. *Appl. Phys. Lett.* **91**, 241907 (2007).
27. Kamimura, T. *et al.* Carbon Nanotube Fabry Perot Device for Detection of Multiple Single Charge Transitions. *Japanese Journal of Applied Physics* **48**, 025001 (2009).
28. Radosavljevic, M. *et al.* Nonvolatile Molecular Memory Elements Based on Ambipolar Nanotube Field Effect Transistors. *Nano Lett.* **2**, 761–764 (2002).
29. Liang, W. *et al.* Fabry Perot interference in a nanotube electron waveguide. *Nature* **411**, 665–669 (2001).
30. Grove-Rasmussen, K. *et al.* Fabry Perot interference and Kondo effect and Coulomb blockade in carbon nanotubes. *Physica E* **40**, 92–98 (2007).
31. Babic, B. *et al.* Observation of Fano resonances in single-wall carbon nanotubes. *Phys. Rev. B* **70**, 195408 (2005).
32. U.Fano *et al.* Effects of Configuration Interaction on Intensities and Phase Shifts. *Phys. Rev.* **124**, 1866 (1961).
33. Kobayashi, K. *et al.* Mesoscopic Fano effect in a quantum dot embedded in an Aharonov-Bohm ring. *Phys. Rev. B* **68**, 235304 (2003).
34. Fano, U. *et al.* *Nuovo Cimento* **12**, 156 (1935).
35. Clerk, A. A. *et al.* Fano Resonances as a Probe of Phase Coherence in Quantum Dots. *Phys. Rev. Lett.* **86**, 4636 (2001).
36. Kobayashi, K. *et al.* Tuning of the Fano Effect through a Quantum Dot in an Aharonov-Bohm Interferometer. *Phys. Rev. Lett.* **88**, 256806 (2002).
37. Bai, J. *et al.* Very large magnetoresistance in graphenenanoribbons. *Nature Nanotechnology* **5**, 655–659 (2010).
38. Ki, D.-K. *et al.* Crossover from Coulomb Blockade to Quantum Hall Effect in Suspended Graphene Nanoribbons. *Phys. Rev. Lett.* **108**, 266601 (2012).
39. Williams, J. R. *et al.* Quantum Hall Effect in a Gate-Controlled p-n Junction of Graphene. *Science* **317**, 638, 638–641 (2007).

40. Goerbig, M. O. *et al.* Electron interactions in graphene in a strong magnetic field. *Phys. Rev. B* **74**, 161407 (2006).

4.5 Applications: in-plane electronic interconnects

This section has been published in:

Transport in kinked bi-layer graphene interconnects

B. Terrés, N. Borgwardt, J. Dauber, C. Volk, S. Engels, S. Fringes, P. Weber, U. Wichmann, S. Trellenkamp and C. Stampfer

2011 IEEE International Conference Proceeding on Nano/Micro Engineered and Molecular Systems (NEMS)

DOI: 10.1109/NEMS.2011.6017523

As discussed in previous sections, graphene on Silicon dioxide SiO_2 shows a rather disordered behavior. Although the application of graphene in electronics appears thus rather limited, it is still possible to benefit from the planar nature as well as the high current densities withstand by graphene. Within this section, we present transport experiments on kinked bi-layer graphene nanoribbon interconnects. The studied devices consist of approximately 80 nm -wide and $1\ \mu\text{m}$ -long bi-layer graphene nanoribbons with different kink angles. We discuss the ambipolar transport characteristics and show a systematic dependence of the overall conductance as a function of the angle, i.e. the shape of the etched bi-layer graphene nanoribbon. The measurements can be well described with the self-consistent Boltzmann equation for diffusive transport, where the kinked angle appears to have an influence on the effective charge carrier mobility, thus revealing the presence of geometry-dependent ballistic transport effects. These results are crucial for the design and fabrication of future single-layer or bi-layer graphene interconnects in potential all-carbon systems.

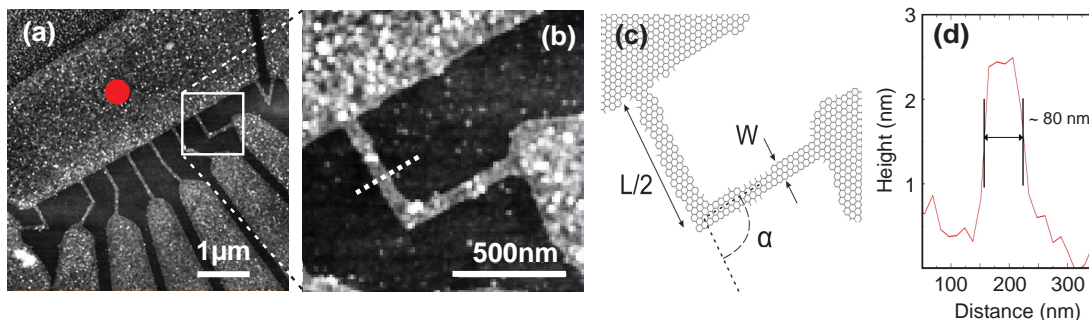


Figure 4.44: **Device characterization.** **a**, Atomic force microscopy (AFM) image of a graphene interconnects array with nanoribbons of $1\ \mu\text{m}$ in length (L) and $\sim 80\text{ nm}$ in width (W). The angle α of the kinks range from 0° to 90° . The location for the Raman acquisition is marked by a red spot. **b**, Close-up image of the $\alpha=90^\circ$ nanoribbon interconnect (white area in panel a). **c**, Schematic representation of a nanoribbon interconnect of panel b. **d**, Cross-sectional analysis along the dashed line shown in panel b. The measured width W is approximately 80 nm .

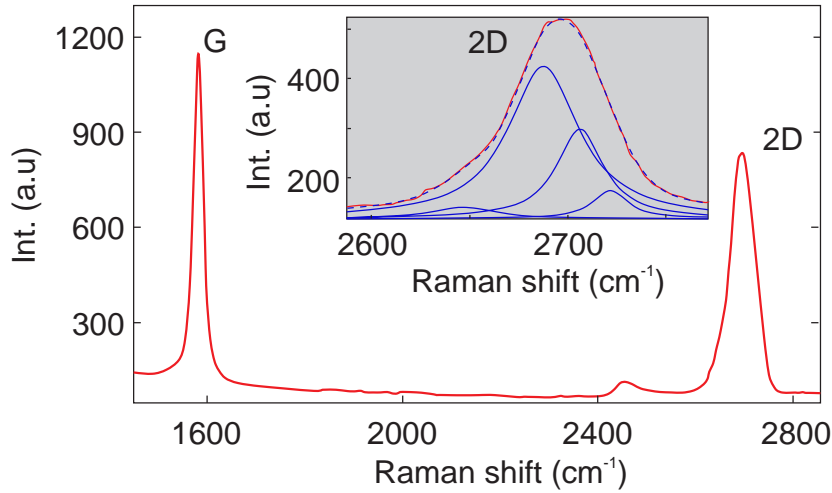


Figure 4.45: **Device characterization.** **a**, Raman spectrum of the graphene flake shown in Fig. 4.44 a and b, measured at the red spot shown in Fig. 4.44 a. The laser spot is located at a distance d away from the graphene interconnects ($d \gg d_L$, with d_L being the laser spot diameter, $d_L \approx 500 \text{ nm}$). The 2D peak (red trace in close-up panel) is fitted by four Lorentzians (shown in blue), which proves the bi-layer nature of the graphene flake.

Introduction

Graphene [1], a monoatomic layer of graphite, and in particular graphene nanostructures [2–4] exhibit unique electronic properties making these materials promising candidates for high-frequency electronics and future nanoelectronics in general [5]. The exceptional high carrier mobility [6] makes graphene particularly attractive not only for amplifiers or switching devices but also for interconnects [7], allowing truly monolithic systems [8]. The improvements on graphene interconnect technology together with recent graphene based logic device developments [9, 10] may suggest that an all-carbon microelectronic technology is potentially achievable. Wafer-scale graphene growth on *SiC* by molecular beam epitaxy (MBE) or chemical vapor deposition (CVD) have already been reported [11, 12], thus allowing the design of large complex electronic circuitry. Moreover, the in-plane design could benefit from the existing semiconductor technology, i.e. the high-resolution lithography.

During the last years extensive studies have been carried out on single-layer graphene nanoribbons and interconnects [7, 13, 14]. Conductance models have been developed and a high conductivity has been predicted for ultra-small graphene nanoribbons becoming superior to state-of-the-art copper interconnects [15]. Moreover, it has been shown that graphene interconnects can withstand high current densities (superior to copper [7]) while providing better thermal conductivity [14]. However, up to now, very little is known about bi-layer or few-layer graphene nanoribbon interconnects. In contrast to single-layer graphene nanoribbons, few-layer nanostructures are expected to be less sensitive to the line edge roughness and may therefore allow higher conductance. Here we report for the first time on transport experiments on bi-layer graphene nanoribbon

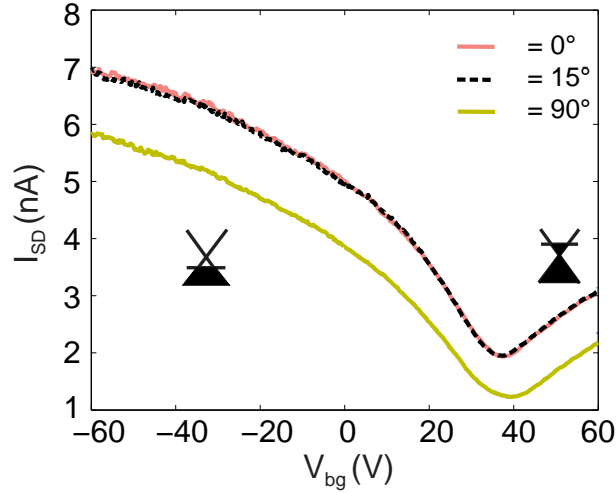


Figure 4.46: **Back-gate characteristics at room temperature.** Source-drain current I_{SD} as a function of back-gate voltage V_{bg} for the nanoribbons with dimensions $L=1\ \mu\text{m}$, $W=80\ \text{nm}$ and kink angles $\alpha=0^\circ$, 15° and 90° . The bias voltage V_b is set to $300\ \text{V}$ during the measurements. Hole and electron regimes are shown. All curves exhibit a minimum in conductance at approximately $40\ \text{V}$ in back-gate voltage, which corresponds to the charge neutrality point. The shift in the charge neutrality point is most likely due to resist residues from the fabrication step. Data from the nanoribbons with $\alpha=0^\circ$ and $\alpha=15^\circ$ appear to be identical.

interconnects with different kink angles. The results are an important step towards an all-carbon microelectronic technology.

The fabrication process of kinked nanoribbon interconnects is extensively discussed in Section 3.1. After evaporation of metal alignment markers on a SiO_2 substrate, bilayer graphene flakes are mechanically exfoliated from natural bulk graphite and deposited onto the insulating $300\ \text{nm}\ \text{SiO}_2$ layer on top of the SiO_2 substrate. Prior deposition of the graphene flakes, the Si substrates are chemically cleaned with Acetone, Dimethylsulfoxide (DMSO) and Isopropanol and heated for 15 minutes on a hot-plate at 180°C to reduce the presence of H_2O molecules on surface. Raman spectroscopy is used to verify the double-layer nature of the investigated graphene [16, 17] (Fig. 4.45). Inset of Fig. 4.45 shows the four Lorentzian peaks characteristic of bi-layer graphene. Electron-beam (ebeam) lithography is used to pattern the etch mask, a $100\ \text{nm}$ -thick layer of Polymethyl Methacrylate (PMMA) resist. A reactive ion etching (RIE) process based on Ar/O_2 plasma is introduced to etch the unprotected bi-layer graphene. Thereafter, the nanoribbons are contacted by e-beam patterned $5\ \text{nm}\ \text{Cr}$ and $50\ \text{nm}\ \text{Au}$ electrodes. An atomic force microscope (AFM) image of the resulting etched bi-layer graphene nanoribbon interconnects can be found in Fig. 4.44a and b. AFM imaging is also used to estimate the length L and the width W of the resulting nanoribbons (see Fig. 4.44d). Finally the samples have been glued with silver paste onto a chip carrier and manually wire-bonded with Au wires by an ultrasonic bonder.

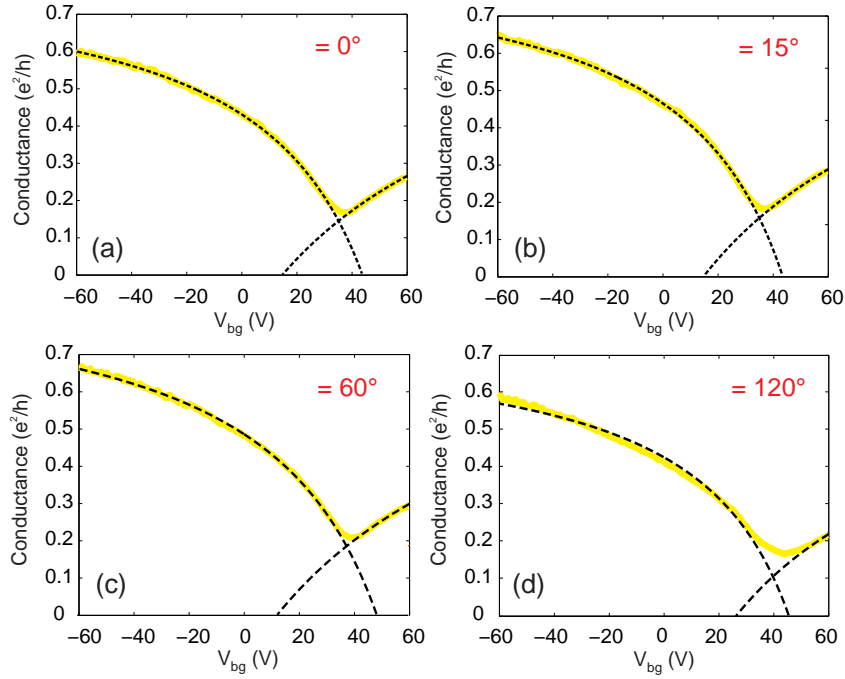


Figure 4.47: **Fitting procedure** Experimental transport data (yellow solid curves) and corresponding fits of the model (black dashed curves) for the nanoribbons with angles $\alpha = 0^\circ$ (a), $\alpha = 15^\circ$ (b), $\alpha = 90^\circ$ (c) and $\alpha = 120^\circ$ (d). Data and model are in reasonable good agreement. All traces are measured at $V_b = 300 \mu V$.

The fabricated samples are measured in a vacuum chamber with a pressure of around $P = 2.10^{-1} \text{ mbar}$. Measurements are performed with a constant bias voltage $V_b = 300 \mu V$ applied between the source (S) and the drain (D) contacts. The source-drain current I_{SD} is then recorded while sweeping the back-gate voltage V_{bg} from -60 V to 60 V . In Fig. 4.46 we show the obtained ambipolar transport characteristics for three different nanoribbon interconnects of kink angles $\alpha = 0^\circ$, 15° and 90° . Interestingly, the curves show almost no difference between the 0° and 15° ribbons, while the current drops significantly for the 90° one. For all three devices the transport behavior can be fully tuned from hole to electron regimes. The observed p-doping ($I_{SD, \min} \approx 40 \text{ V}$) is most likely due to the presence of PMMA resist residues.

Model and discussion

Overall, the observed ambipolar transport characteristic can be approximated by the Drude model. The conductance G of a nanoribbon can be therefore described as $G = G_e + G_h$ where the electron and hole conductance ($G_{e,h}$), both angle dependent, are given by:

$$G_{e,h} = \left[R_c + \frac{L}{W} \cdot \sigma_{e,h}^{-1} \right]^{-1}, \quad (4.12)$$

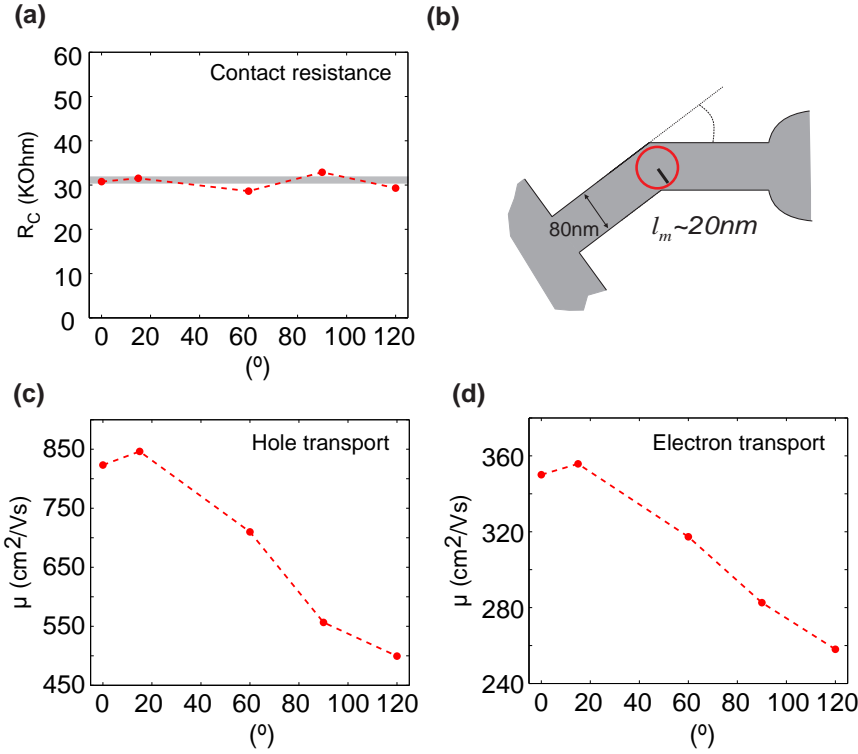


Figure 4.48: **Angle-dependency of the transport characteristics.** **a**, Plot of the contact resistance R_C as a function of different kink angles α . **b**, Schematic illustration of a graphene interconnect of width $W = 80\text{ nm}$ and angle α . The red circle indicates the mean free path, clearly showing that ballistic effects matter when describing the transport mechanism in such devices. **c**, **d**, Effective hole- (panel c) and electron- (panel d) mobilities as a function of the different angles α . Both effective carrier mobilities show a significant angle-dependency, which is a strong indication that ballistic transport plays an important rôle in these devices.

The resistance R_c , which is back-gate voltage independent, is coming from both, source and drain contacts. Both electron (e^-) and hole (h^+) conductivities ($\sigma_{e,h}$) can be approximated by a self-consistent Boltzmann equation for diffusive transport [18], excluding the long-range scattering contributions. Hence, the conductivity is defined as:

$$\sigma_{e,h}(V_{bg}) = [e \cdot n_{e,h}(V_{bg}) \cdot \mu_{e,h} + \sigma_0] \Theta [\pm (V_{e,h}^D - V_{bg})], \quad (4.13)$$

where $n_{e,h}(V_{bg}) = \beta \cdot [\pm (V_{e,h}^D - V_{bg})]$ is the electron and hole carrier concentration [1], $\mu_{e,h}$ the effective charge carrier mobility, σ_0 is the back-gate independent residual conductivity at the charge neutrality point and Θ is the Heaviside function. All samples appear to be slightly p-doped (e.g. Fig. 4.46), most likely due to residues of PMMA on the sample. The devices have not been annealed prior measurements.

The above expression for the conductance can be fitted to the individual transport measurements as shown in Fig. 4.47. The measurements are divided into hole- and

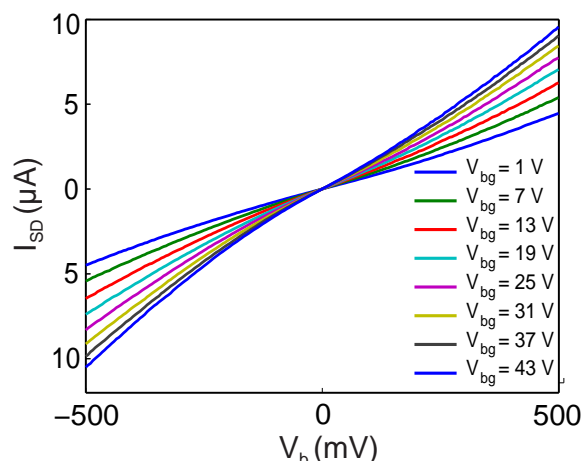


Figure 4.49: **Breakdown current.** Source-drain current I_{SD} versus bias voltage V_b as a function of back-gate voltage V_{bg} for a nanoribbon with dimensions $L = 1 \mu m$, $W = 80 nm$ and angle $\alpha = 0^\circ$. Current densities of up to $10^7 A/cm^2$ can be repeatedly obtained without damaging the device.

electron-regime, which correspond to the left and right hand-side of the charge neutrality point, respectively (see Fig. 4.46). These regimes are treated independently (see black dashed lines in Fig. 4.47). The Contact resistance (R_c) as well as the residual conductivity (σ_0) are fixed to be equal for both holes and electrons regimes. The fit describes the transport characteristic for the different devices reasonably well (compare solid with dashed lines in Fig. 4.47).

In Fig. 4.48 we summarize the different fitting parameters. Results reveal that the contact resistance R_c does not depend on the kink angle α (Fig. 4.48a), whereas the effective charge carrier mobility μ for electron and holes strongly decreases with increased kink angles (Fig. 4.48c and d). Interestingly, the effective mobility is different for electrons and holes, reaching a maximum value of around $850 cm^2/(V.s)$. Compared to bulk graphene, the conductivity achieved by our bi-layer graphene nanoribbon interconnects is rather low. X. Hong et al. [19] claimed mobility values of around $20.000 cm^2/(V.s)$ for single-layer graphene sheets on SiO_2 substrates, whereas C. R. Dean et al. [20] achieved values even three times higher ($60.000 cm^2/(V.s)$) for single-layer graphene sheets on Boron Nitride substrates. Even though bi-layer graphene nanoribbon interconnects show a lower overall effective mobility compared to its single layer counterpart, higher carrier densities can be easily achieved (see Fig. 4.49). During measurements, current densities of up to $10^7 A/cm^2$ were repeatedly reached without damaging the samples.

More importantly, our transport measurements and the angle-dependency of the effective mobility for the electron and hole regimes suggest that the ballistic nature of transport starts playing an important rôle in these graphene structures. In order to compare the mean free path l_m with the length-scale of the nanoribbons, we can extract l_m as follows [6], $l_m = \hbar\mu\sqrt{\pi n}/|e|$, where μ is the effective charge carrier mobility and n is the charge carrier density. Owing to our measurements, the effective charge

carrier mobility can be estimated as $\mu \approx 800 \text{ cm}^2/(\text{V}\cdot\text{s})$, for a nanoribbon of angle $\alpha=0^\circ$. The charge carrier density, which can be derived from the capacitor model [11] as $n = \epsilon\epsilon_0 \cdot V_{bg}/e \cdot d$, can be assumed to be in the order of $n \approx 5 \cdot 10^{12} \text{ cm}^{-2}$. These values give rise to a mean free path of approximately 20 nm , which is on the same length-scale as the nanoribbon width W , and it is clearly exceeding the feature size of the patterned kink structure (Fig. 4.48b). This may explain the observed angle-dependency of the transport parameters (Fig. 4.48).

Conclusions

In this work we present transport measurements on bi-layer graphene nanoribbon interconnects with different kink angles. Results reveal an angle-dependency of both electron- and hole-effective mobilities that highlight the importance of ballistic effects at these length scales. Consequently, the mean free path has to be taken into account when designing such nanoribbon interconnects. Moreover, results suggest that the Drude model used throughout this section would not be able to accurately describe the transport phenomena for smaller devices.

References

1. Neto, A. H. C. *et al.* The electronic properties of graphene. *Reviews of Modern Physics* **81**, 109–110 (2009).
2. Terrés, B. *et al.* Disorder induced Coulomb gaps in graphene constrictions with different aspect ratios. *Appl. Phys. Lett.* **98**, 032109 (2011).
3. Chen, Z. *et al.* Graphene nano-ribbon electronics. *Physica E* **40** (2007).
4. Han, M. Y. *et al.* Energy Band-Gap Engineering of Graphene Nanoribbons. *Phys. Rev. Lett.* **98**, 206805 (2007).
5. Geim, A. K. *et al.* The rise of graphene. *Nature Materials* **6**, 183–191 (2007).
6. Novoselov, K. S. *et al.* Electric Field Effect in Atomically Thin Carbon Films. *Science* **306**, 666–669 (2004).
7. Murali, R. *et al.* Resistivity of Graphene Nanoribbon Interconnects. *IEEE Electron Device Letters*, **30**, 6 (2009).
8. Stampfer, C. *et al.* Energy Gaps in Etched Graphene Nanoribbons. *Phys. Rev. Lett.* **102**, 056403 (2009).
9. Zhang, Q. *et al.* Graphene nanoribbon tunnel transistor. *IEEE Electron Device Lett.* **29** (2008).
10. Meric, I. *et al.* Current saturation in zero-bandgap and top-gated graphene field-effect transistors. *Nature Nanotechnology* **3**, 654–659 (2008).
11. Jobst, J. *et al.* Towards wafer-size graphene layers by atmospheric pressure graphitization of SiC(0001). *Nature Materials* **8**, 203 (2009).
12. Kim, K. S. *et al.* Large-scale pattern growth of graphene films for stretchable transparent electrodes. *Nature* **457**, 706–710 (2009).
13. Murali, R. *et al.* Breakdown current density of graphene ribbons. *Appl. Phys. Lett.* **94**, 244 (2009).
14. Shao, Q. *et al.* High temperature quenching of electrical resistance in graphene interconnects. *Appl. Phys. Lett.* **92**, 202108 (2008).
15. Naeemi, A. *et al.* Conductance Modeling for Graphene Nanoribbon (GNR) Interconnects. *IEEE Electron Device Letters* **28**, 5 (2007).
16. Ferrari, A. *et al.* Raman Spectrum of Graphene and Graphene Layers. *Phys. Rev. Lett.* **97**, 187401 (2006).
17. Graf, D. *et al.* Spatially Resolved Raman Spectroscopy of Single-, Few-Layer Graphene. *Nano Lett.* **7**, 238 (2007).
18. Hwang, E. H. *et al.* Carrier transport in two-dimensional graphene layers. *Phys. Rev. Lett.* **98**, 186806 (2007).
19. Hong, X. *et al.* The quantum scattering time and its implications on scattering sources in graphene. *Phys. Rev. Lett.* **98**, 186806 (2009).
20. Dean, C. R. *et al.* Boron nitride substrates for high-quality graphene electronics. *Nature Nanotechnology* **5**, 722–722 (2010).

5.1 Characterization of the residual disorder

Graphene has emerged as a promising candidate to lead the post-silicon revolution [1, 2]. However, since its discovery, the presence of potential fluctuations has been hindering the observation of a variety of fundamental phenomena expected for intrinsic graphene [2–6]. Hence, right after its discovery, a growing interest developed in order to find suitable substrates for graphene. A milestone was reached in 2010 [7] with the use of hexagonal boron nitride (hBN) as a substrate material. On hBN, graphene was able to achieve comparable performance as for suspended graphene devices [8, 9]. Even though the quality of graphene on this insulating material clearly surpassed the performance of graphene on silicon dioxide, the major leap in device quality came with the complete encapsulation of graphene in between a top- and a bottom-layer of hBN (see Section 3.3 and [10]). This fabrication technology has brought graphene to the forefront of the electronic materials, with levels of quality comparable to conventional III-V 2DEGs materials [11, 12]. Within the layered hBN heterostructure, graphene is exceeding the highest electron mobility at room temperature of any known material to date, with mobilities up to $150,000 \text{ cm}^2/\text{Vs}$ and sheet resistivity below 40 Ohms per square at $n > 4 \cdot 10^{12} \text{ cm}^{-2}$ [10, 13]. These values are indeed equivalent to the theoretical limit imposed by acoustic phonon scattering [14].

Though, for nanostructured graphene devices, comparatively lower carrier mobilities and traces of disorder (see Section 3.3) is what experimentalists have faced so far [15, 16]. To elucidate whether this reduced performance is solely determined by the edges or some bulk disorder still remains within the bulk, we study the remaining potential fluctuations via the localization length ξ in the quantum Hall regime. Measurements are performed in Hall bar devices carved out of hBN-graphene-hBN heterostructures. In this section we will confirm the high quality achieved by our graphene samples issued from patterned hBN-graphene-hBN stacks. The high quality is further demonstrated in Section 6.1 with the electronic transport studies of hBN-graphene-hBN quantum point contacts and nanoribbons, fabricated following the same technique (see Section 3.3).

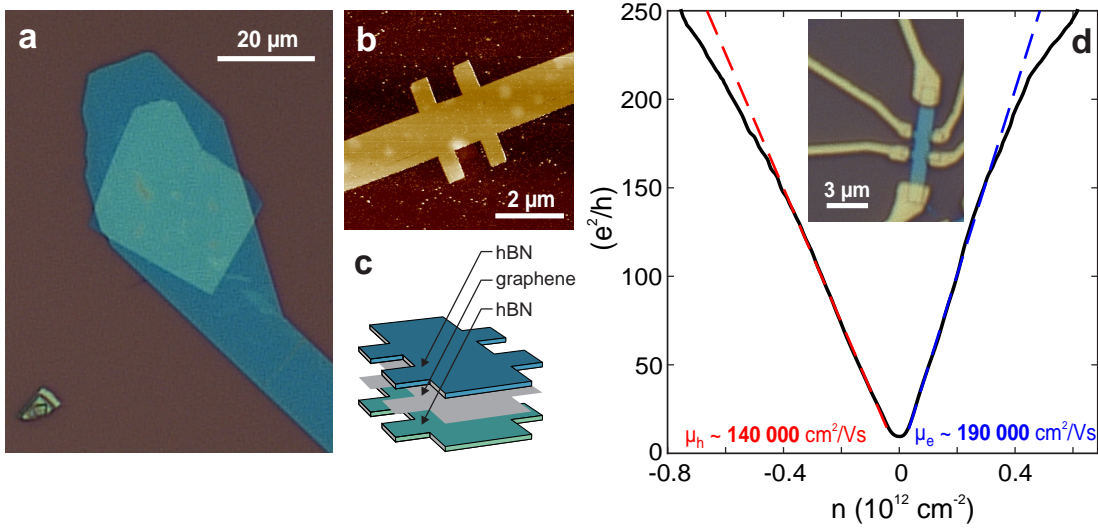


Figure 5.1: **Device fabrication and back-gate characteristics.** **a**, Optical microscope image of an assembled hBN-graphene-hBN stack on SiO_2 substrate, used afterward to fabricate high mobility graphene devices. **b**, Atomic Force Microscope (AFM) image of the resulting Hall-bar device, after patterning the hBN-graphene-hBN stack in panel **a** by reactive ion etching (RIE) techniques. **c**, Schematic representation of layered Hall-bar structure. **d**, Measured conductivity (σ) at $T = 1.7 K$ as a function of charge carrier density (n) of the Hall-bar shown in panel **b**. A constant bias voltage of $V_b = 500 \mu V$ is applied between source and drain contacts. The field-effect mobility is extracted independently for the electron- and hole-side by a linear fit to the conductivity. The inset shows an optical image of the contacted device.

As a first step, we will extract the Drude and the quantum electron mobilities of a Hall bar device to thereafter investigate the nature of the localization phenomena in the quantum Hall (QH) regime. The study of macroscopic Hall bar devices allows us to pin point the limiting characteristic length within our material. In the following, we will show the fingerprints of a well differentiated electronic hopping behavior, which is visible in the temperature evolution of the conductance in the quantum Hall regime.

Since its discovery, the quantum Hall effect has been used in applications from physics to metrology [17]. In graphene, the magnetic evolution of the Landau levels was even used to spatially resolve the capacitance profile of 1D graphene nanoribbons [18]. In this section, we study the saturation energies in a quantum Hall regime as a function of magnetic field and filling factor, to characterize the localization length in hBN-graphene-hBN heterostructures. The integer quantum Hall effect in a two dimensional electron system can be understood as the localization of the states in the tails of individual Landau levels. Within the center of an individual Landau level, the wave functions of the electronic states are delocalized and their extension is governed by the so called localization length $\xi(E)$, i.e. the spatial extension of the wave function. To find out whether $\xi(E)$ lies below or above the dimensions of our sample, we extract the localization length

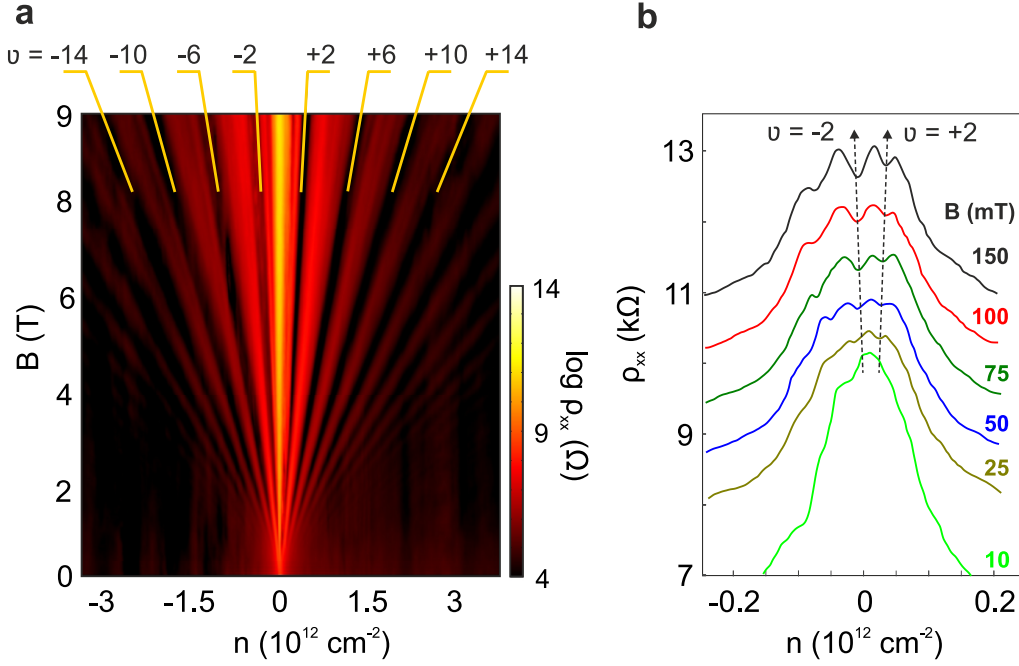


Figure 5.2: **Integer Landau levels quantization and quantum mobility in graphene.** **a**, Landau fan from the graphene Hall-bar device in Fig. 5.1b, measured at $T = 1.7 K$. The characteristic Half-integer quantum Hall effect is well defined at high B-fields. The positions of the filling factors $\nu = \pm 4(N + 1/2)$ with $N = 0, 1, 2, \dots$, are indicated by yellow lines. The electrostatic coupling to the back-gate $\alpha = 6.9 \cdot 10^{10} \text{ cm}^{-2} \text{ V}^{-1}$ is extracted by comparing the data to the model $E_N = \pm \sqrt{2e\hbar v_F^2 N B}$. **b**, The QHE oscillations $\nu = \pm 2$ are already apparent from $B = 50 \text{ mT}$ (blue trace).

$\xi(E)$ via the low temperature evolution of the conduction in the Landau levels tails [19].

The method used to fabricate the sandwiched hBN-graphene-hBN stacks [20] is described extensively in Section 3.3. An optical image of a hBN-graphene-hBN sandwich is shown Fig. 5.1a, with the top- ($\sim 20 \text{ nm}$ -thick) and bottom-layer ($\sim 40 \text{ nm}$ -thick) of hBN appearing in light-green and the SiO_2 substrate in gray. The Hall-bar geometry is carved by reactive ion etching (RIE) (Fig. 5.1b). The resulting 6-terminal Hall-bar device has the active graphene layer still in between the hBN sheets (Fig. 5.1c). The structured device is afterward contacted by 5 nm Chromium (Cr) and 50 nm Gold (Au) metal electrodes (insert of Fig. 5.1d). Measurements have been performed in a variable temperature insert (VTI) using standard Lock-In techniques.

The back-gate characteristics of the Hall-bar device gives a first estimation of the sample quality (Fig. 5.1d). The charge-carrier mobility has been extracted using the Drude formula by fitting the conductivity σ at small charge carrier densities. We deliberately decided to neglect the self-consistent Boltzmann equation since the obtained values of mobility are systematically higher. Hence, the extracted Drude-based values represent

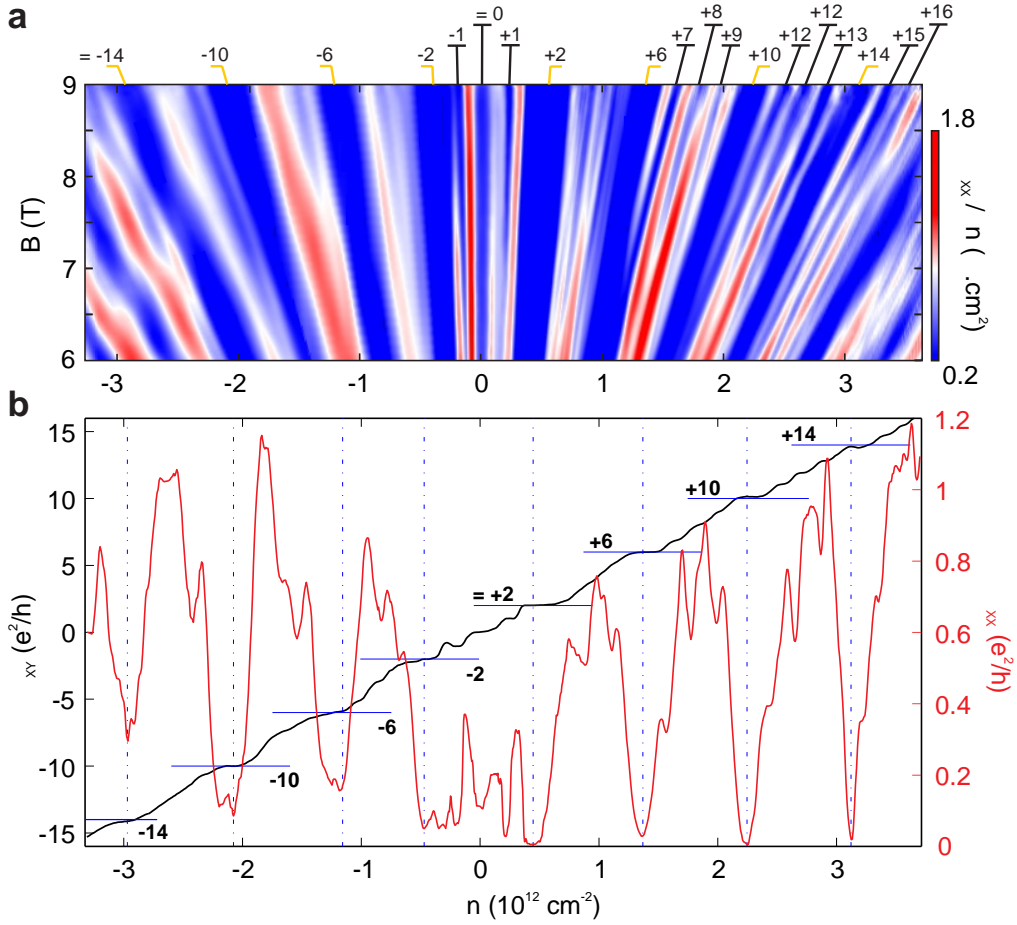


Figure 5.3: **Observation of symmetry broken states in graphene.** **a**, $\partial\rho_{xx}/\partial n$ as a function of magnetic field B and charge carrier density n of the Hall-bar device shown in Fig. 5.1b, measured at $T = 1.7 K$. The complete lifting of the four-fold degenerate Landau levels is visible at high B -fields. **b**, Magnetoresistance σ_{xx} (in red, right axis) and Hall conductivity σ_{xy} (in black, left axis) measured at $B = 9 T$ and $T = 1.7 K$. Apart from the half-integer quantum Hall filling sequence $\nu = \pm 4(N + 1/2)$, indicated by vertical dashed and horizontal solid blue lines, we observe the presence of symmetry broken states.

a lower bound approximation for the electron/hole mobilities. First conductance traces (Fig. 5.1d) at ($T = 1.7 K$) yield mobilities of up to $\mu_e = \frac{\sigma}{en} \approx 190,000 \text{ cm}^2\text{V}^{-1}\text{s}^{-1}$ for the electron-side and $\mu_h \approx 140,000 \text{ cm}^2\text{V}^{-1}\text{s}^{-1}$ for the hole-side. These values are at least two orders of magnitude higher than previously reported mobilities for Hall-bars on SiO_2 substrate [21] and are on the same order of magnitude to comparable hBN-graphene-hBN devices [10, 13]. Although the analysis described above is widely used to evaluate mobilities, it should rather be considered as an estimate. A more appropriate measure of the carrier mobility is obtained by the B-field value in which the Landau levels (LL) oscillations first develop [22]. This value of magnetic field (B_Q) is related to

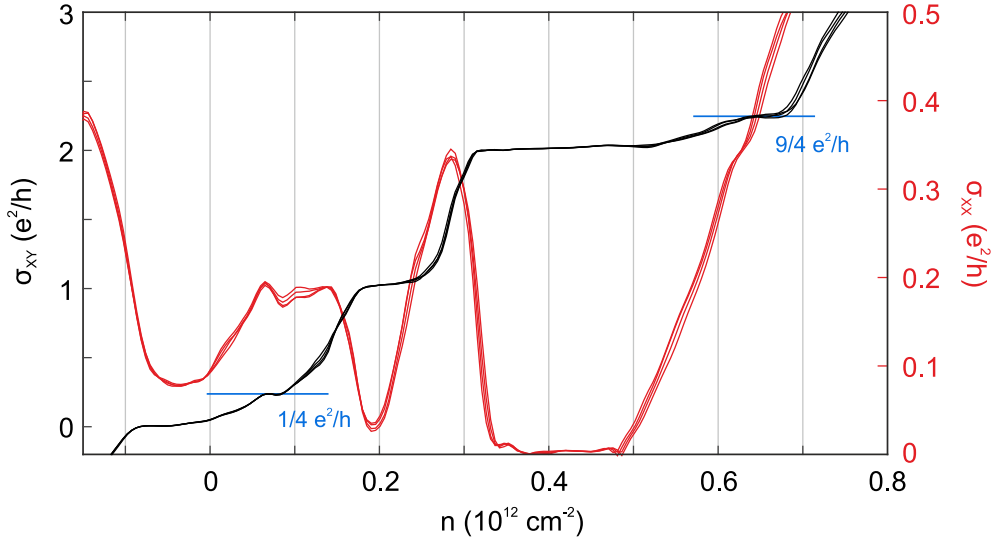


Figure 5.4: **Observation of fractional QH states in graphene.** **a**, Magnetoresistance σ_{xx} (in red, right axis) and Hall conductivity σ_{xy} (in black, left axis) measured at $T = 1.7 K$. Apart from the symmetry broken $\nu = +1$ and the insulating $\nu = 0$ states, we observe the fractional $\nu = 1/4$, and $5/4$ states at high B-fields. Conductance traces from $B = 9$ to $8.8 T$ in steps of $0.05 T$ are superimposed to highlight the local minimum in σ_{xx} and the plateau in σ_{xy} .

the quantum mobility (μ_Q) through $\mu_Q B_Q \equiv w_c \tau_Q = 1$, and it can be understood as the minimal B-field in which the carriers precess along a complete cyclotron radius without scattering. To evaluate the cyclotron radius w_c , one would need to carefully evaluate the small-angle scattering time τ_Q by looking at the SdH oscillations' amplitude as a function of B [23, 24]. As observed in Fig. 5.2b, the LL oscillations are already visible at $B = 50 mT$, which yields $\mu_Q \approx 200,000 \text{ cm}^2 \text{V}^{-1} \text{s}^{-1}$ (Fig. 5.2b), confirming the value of mobility extracted from the back-gate characteristics (Fig. 5.1d).

The high quality of our graphene sample is also visible in the magnetic evolution of the measured conductance. The expected half-integer Landau levels clearly develop at moderate values of B-field (Fig. 5.2b) and degeneracy broken states (splitting of $\nu = \pm 1$), usually associated to the high quality of the samples [25], are also observed (black dashed lines in Fig. 5.2a). Note that the Landau-fan allow us to independently determine the gate coupling (α) of the Hall-bar device (Fig. 5.2). A line-cut at the highest B-field available ($B = 9 T$) reveal a full sequence of symmetry broken states (Fig. 5.3a). They can be easily recognized by local minimums in the longitudinal conductivity σ_{xx} (red trace in Fig. 5.3a) and the formation of conductance plateaus in the transversal conductivity σ_{xy} (black trace in Fig. 5.3a). The observation of the all-integer filling factor sequence $\nu = 0, \pm 1, \pm 2, \pm 3, \dots$ indicate the lifting of the four-fold degenerate Landau levels, supposedly mediated by electron-electron interactions [26, 27]. In the strong quantum limit, these electron-electron interactions can also lead to many-body correlated states, observed as fractional filling factors in the Hall conductance [28].

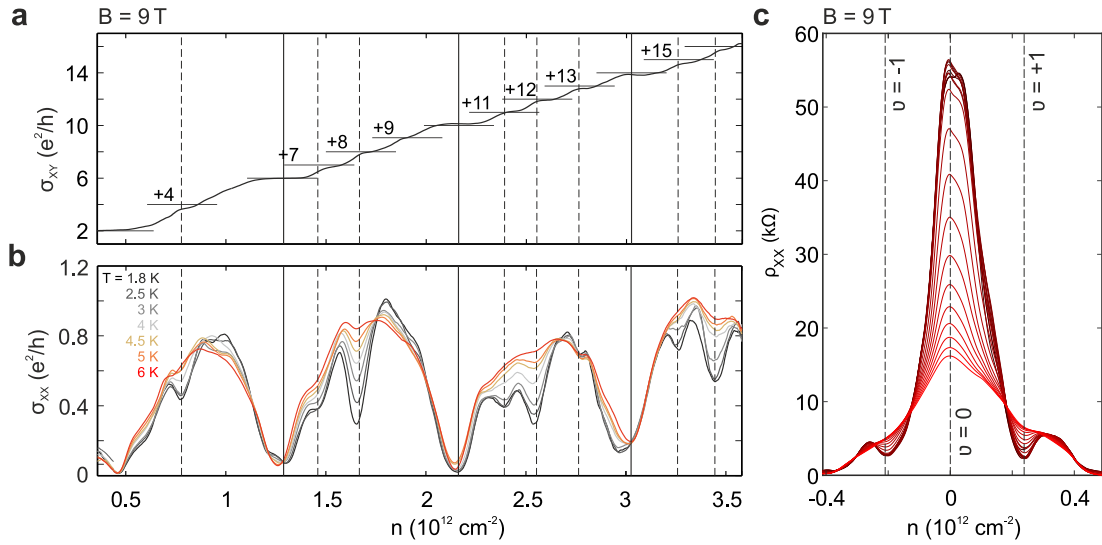


Figure 5.5: **Temperature dependence of the all-integer quantum Hall states.** **a** Hall conductivity σ_{xy} of the device in Fig. 5.1b, measured at $T=1.7\text{ K}$ and $B=9\text{ T}$ **b**, Temperature dependence of the σ_{xx} minimum in the symmetry broken IQHE regime, measured at $B=9\text{ T}$. **c**, Development of the insulating state $\nu=0$ and the broken symmetry state $\nu=\pm 1$, measured at $B=9\text{ T}$. Temperatures are taken from $T=1.7\text{ K}$ (black trace) to $T=15\text{ K}$ (red trace) in steps of 0.8 K .

We report the presence of various fractional quantum Hall states in our device (blue horizontal lines in Fig. 5.3b), most strongly for $\nu=1/4$ and $\nu=5/4$. These fractional states have been previously reported in suspended graphene samples [8, 20, 28], and its observation indicates once more the level of quality achieved by our fabrication technique.

To quantify the energy of these all-Integer QHE states (Fig. 5.3), we measure the temperature dependence of their associated R_{xx} minimum (Fig. 5.5). The temperature dependence of R_{xx} , or alternatively G_{xx} , has been traditionally understood as an activation energy process and it has been widely used to study symmetry-broken [25] and fractional [28] states, in graphene and in traditional 2DEGs [29, 30]. The value of R_{xx} at its local minimum of resistance, for a given symmetry-broken state, is determined as a function of temperature from $\sim 1.7\text{ K}$ to $\sim 9\text{ K}$. As shown in Fig. 5.6, the Arrhenius plots for the R_{xx}^{min} follow, in the high temperature range, a linear behavior characteristic of an activated conduction. The activation energy Δ is determined from $R_{xx}^{min} = R_0 \exp(-\Delta/2T)$. We find that the energy gaps Δ of all degeneracy-lifted states and insulator state ($\nu=0$) show a simply activated temperature dependence over the analyzed range of B-fields (Fig. 5.6). Owing to the exceptional quality of our device, the analysis is accessible at relatively low values of magnetic field ($B=7, 8$ and 9 T).

To start with, the Landau levels (LLs) under study, i.e. $\nu=0, \pm 1, +3, +7, +8, +11 + 12$, show an activation gap that scales approximately linear with the perpendicular B-

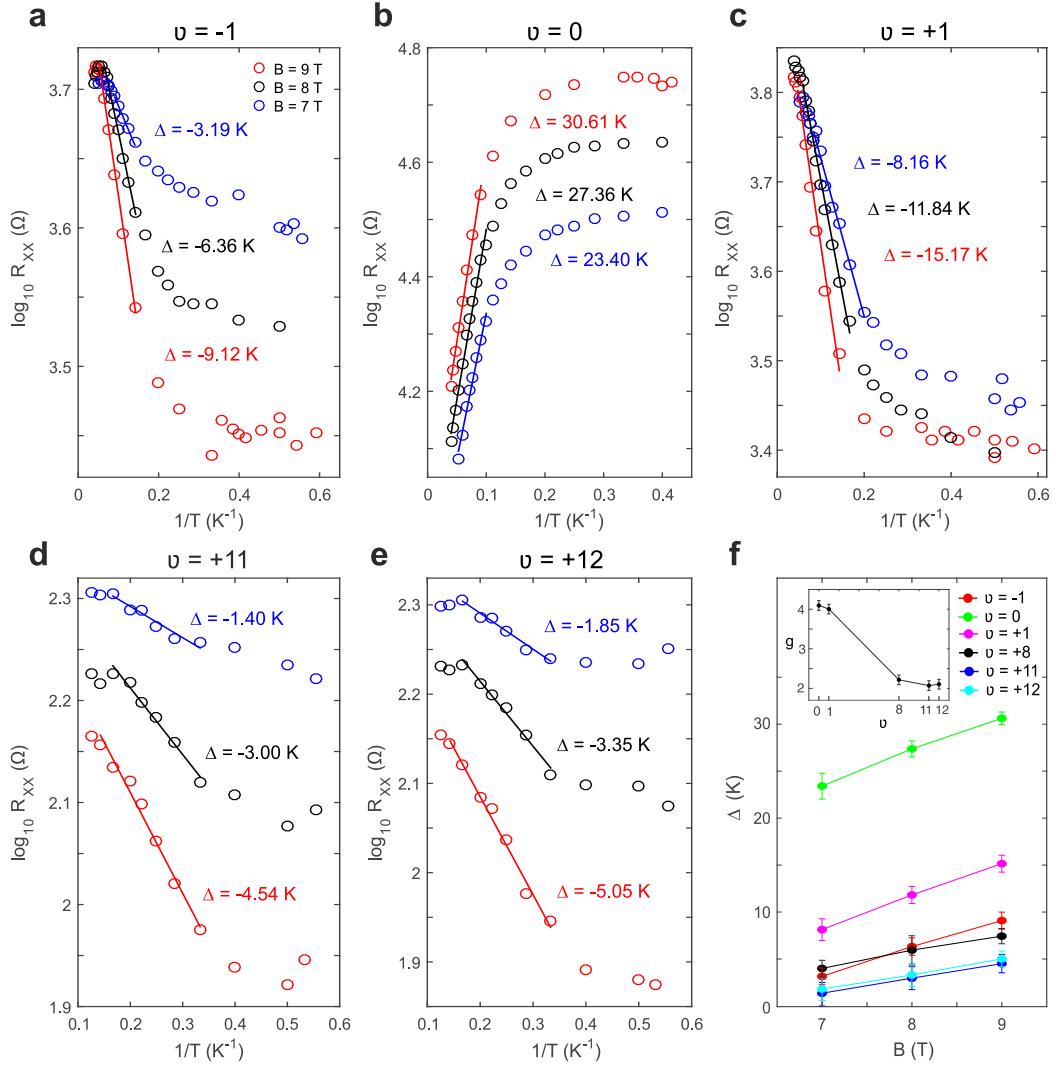


Figure 5.6: **Temperature dependence of symmetry broken states.** **a-e**, Temperature dependence of the R_{xx} minimum at $\nu = -1, 0, +1, +11$ and $+12$, in the symmetry broken IQHE regime. Measurements are taken at $B = 7, 8$ and $9 T$. The energy gaps Δ are extracted by linear fits to the data. **f**, Perpendicular magnetic field evolution of the All-Integer QHE states. Inset shows the enhanced g_{\perp} factors that decrease with increasing LL index.

field (Fig. 5.6f). These results confirm the findings reported in literature [25]. Likewise, the effective gyromagnetic ratio $g_{\perp} = \partial B \cdot \mu_B^{-1}$ [25], where μ_B is the Bohr magneton, are larger than the bare value $g_0 = 2$ and decrease with increasing filling factor index (see inset of Fig. 5.6f), in agreement with quantum Hall ferromagnetism [31]. The temperature evolution from the $\nu = +3, +7, +11$ can be found in Section 8.1. The activation energies of all symmetry broken states is summarized in Tab. 5.1, together with literature values [25].

$B(T)$	$\nu = -1$	$\nu = 0$	$\nu = +1$	$\nu = +3$
9	9.12 K (-)	30.61 K (115 K)	15.17 K (-)	5.77 K (-)
8	6.36 K (-)	27.36 K (97 K)	11.84 K (-)	5.45 K (-)
7	3.19 K (-)	23.40 K (79 K)	8.16 K (-)	6.12 K (-)

$B(T)$	$\nu = +7$	$\nu = +8$	$\nu = +11$	$\nu = +12$
9	3.49 K (-)	7.47 K (7.4 K)	4.54 K (-)	5.05 K (3.9 K)
8	2.53 K (-)	5.98 K (3.5 K)	3.00 K (-)	3.35 K (1.3 K)
7	1.66 K (-)	4.03 K (-)	1.40 K (-)	1.85 K (-)

Table 5.1: Table of the activation energies $\Delta(K)$ as a function of B-field for the filling factors shown in Fig. 5.6 and Fig. 8.4. For comparison, we include in parenthesis the values found in literature [25]. For that, we extrapolate the data from [25] to low magnetic fields.

At the lowest temperatures though ($T \sim 1.7\text{--}3\text{ K}$), R_{xx}^{min} deviates from a simple activation behavior, turning into a rather slowly-dependent temperature evolution (Fig. 5.6). This deviation of the exponential trend is common to all measured filling factors and it is visible for all measured B-fields (Fig. 5.6). Similar observations has been reported on GaAs 2DEGs samples and have been attributed to a variable range-hopping conductance, due to a finite localization of the electrons. This interpretation is valid for the fractional quantum Hall effect (FQHE) [30], as well as for IQHE [32, 33], and it represents a valuable opportunity to characterize the dominating localization length-scales within our high quality sample [34].

At low temperatures, also known as hopping regime, conduction in the Landau level tails decreases with decreasing temperature (Fig. 5.7). At these temperatures, when $k_B T$ is small enough to make the activation to the mobility edge and excitation across potential barriers to neighboring states improbable, conduction is governed by a variable range hopping type of conductance. In this regime electrons or holes are able to tunnel between states within an energy range $k_B T$ leading to a slightly increased conductivity. The temperature dependence of the conductivity in this regime for non-interacting electrons is given by $\sigma_{xx} \propto 1/T \cdot \exp[-(T_0/T)^{1/3}]$. This equation is known as the variable range hoping VRH Mott's law [35]. However, in the QHE regime screening is poor and Coulomb repulsion must be included. This is the Efros-Shklovskii (E-S) VRH regime [36–38], where $\sigma_{xx} \propto 1/T \cdot \exp[-(T_0/T)^{1/2}]$. The localization length at a particular filling factor is $\xi = C e^2 / 4\pi\epsilon\epsilon_0 k_B T_0$ (Fig. 5.7), where C is a dimensionless constant in the order of unity [37] and $\epsilon \approx 4$ is the effective dielectric constant for graphene in between hBN layers.

Fig. 5.7 shows the linear fits to the data and the extracted energies T_0 , for all filling

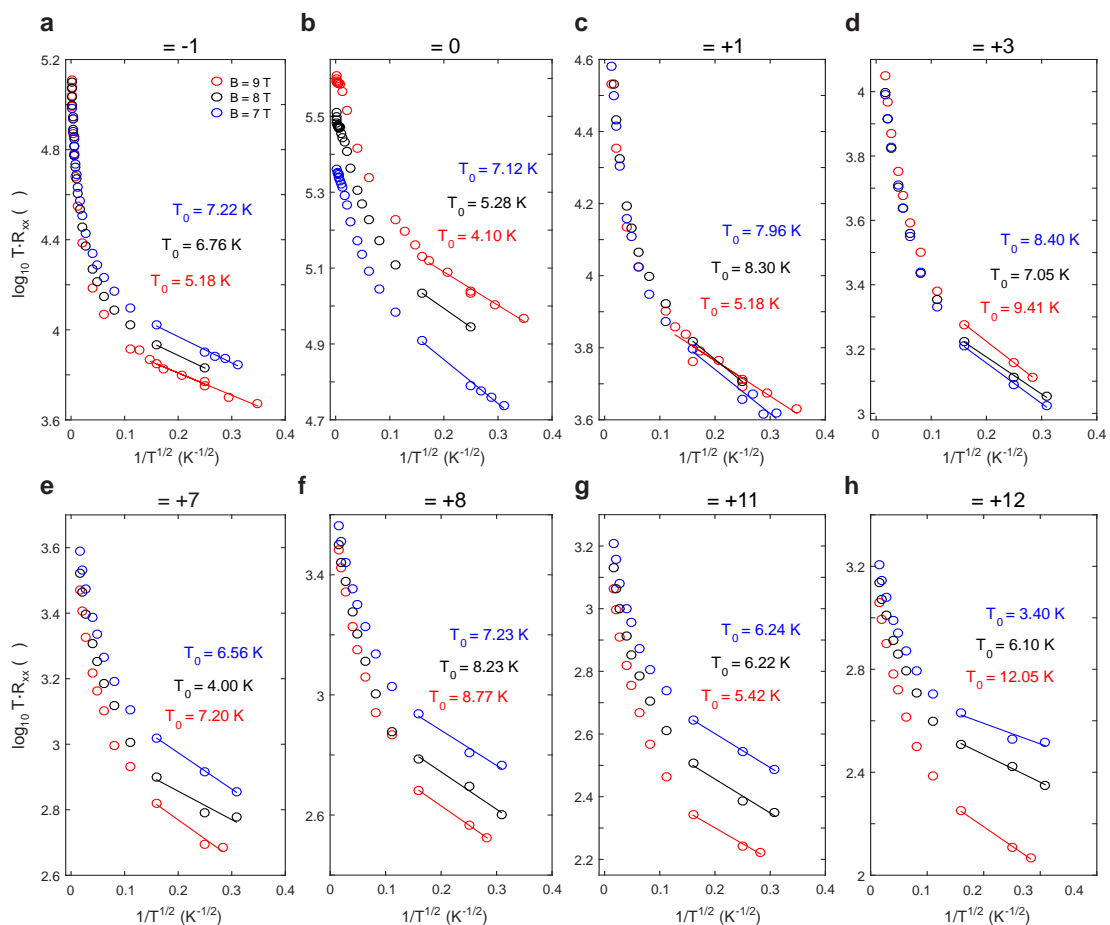


Figure 5.7: **ES-VRH Energy gaps.** Temperature dependence of the R_{xx} minimum in the hopping conductance regime (low temperature range) for $\nu=0, \pm 1, +3, +7, +8, +11$ and $+12$, measured at $B=7, 8$ and 9 T (panels a to h, respectively). The characteristic temperature T_0 is extracted by linear fits to the data.

factors ν . All data points in Fig. 5.7 have been measured within a temperature range from 1.6 K up to 25 K. The resistivity value is extracted from the local minimum of the resistance R_{xx} trace. An zoom-in of the resistivity trace R_{xx} for $\nu = -1$ is shown in Fig. 5.8a-c. Although ξ denotes the typical extension of the electron wave-function, we do not observe any dependence of ξ on ν (see Fig. 8.5). All filling factors have an associated ξ which is close to each other (Fig. 8.5) with an average value of $\sim 1\mu\text{m}$ (Fig. 5.8e). This value is large compared to the localization lengths found in graphene on SiO_2 substrates [38], and it is very close to the dimensions of the Hall bar device of a length $L \approx 2\mu\text{m}$ and width $W \approx 1.2\mu\text{m}$ (Fig. 5.1). Results seems to indicate that the localization length becomes independent of energy and becomes dominated by an intrinsic length scale [39], possibly the $\sim 1.2\mu\text{m}$ width of the sample.

Throughout this section, we studied the quantum Hall state to Hall insulator transition by directly evaluating the localization length ξ in the well understood regime of

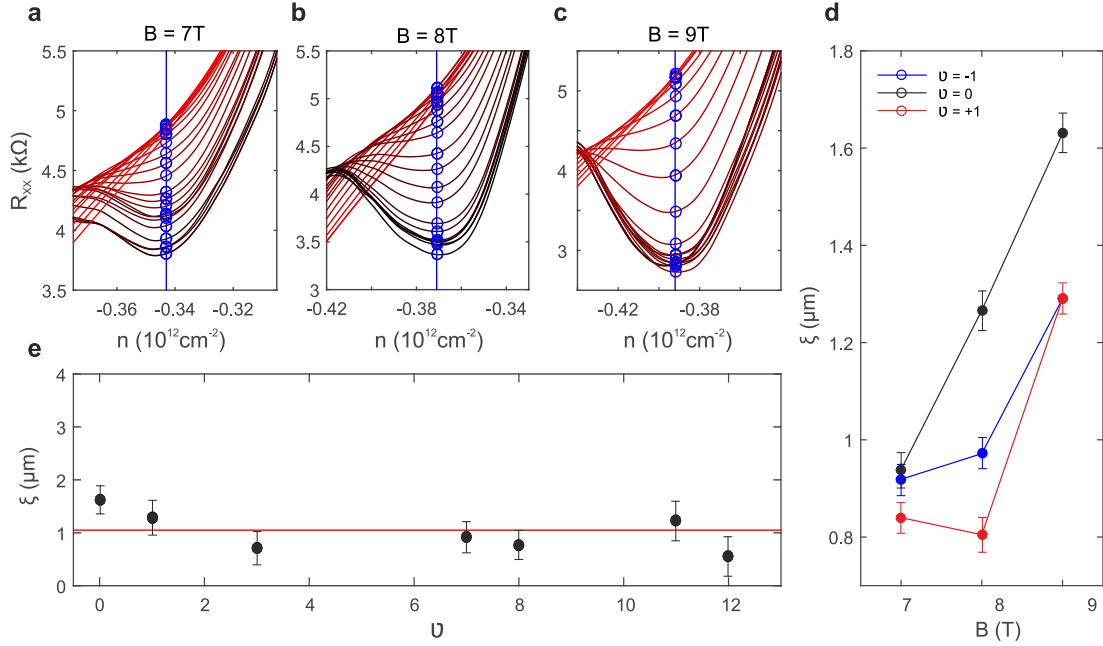


Figure 5.8: **Localization lengths ξ and magnetic field dependence.** **a-c**, Temperature dependence of the resistivity minimum, measured at $B = 7, 8$ and 9T . The temperature varies from 1.6K (black trace) up to 25K (red trace) in steps of 0.5K . The local minimums (marked by a vertical blue line) correspond to the center of the $\nu = -1$ plateau. The saturation of the resistivity is visible for the lower temperatures and it is more pronounced the higher the magnetic field (compare minimums of R_{xx} in panel a and b). **d**, As expected, the localization length ξ is proportional to the B-field. **d**, Extracted ξ (black dots) for the different filling factors ν , measured at $B = 9\text{T}$. The average value ($\xi_{avg} \approx 1\mu\text{m}$) is indicated by a red horizontal line.

variable-range hopping (VRH) conductivity [40]. As it has been shown, VRH dominates the conductance at low temperatures, which allow us to extract the localization length, i.e. the spatial extension of the wave function, as a function of magnetic field and filling factors. We find an approximately equal localization length for all filling factors, which seems indicate that localization in hBN-graphene-devices is limited by the dimension rather than being limited by disorder/scattering.

References

1. Geim, A. K. *et al.* The rise of graphene. *Nature Materials* **6**, 183–191 (2007).
2. Katsnelson, M. I. *et al.* Graphene: carbon in two dimensions. *Materials Today* **10**, (1-2), 20–27 (2007).
3. Martin, J. *et al.* Observation of electron hole puddles in graphene using a scanning single-electron transistor. *Nature Physics* **4**, 144–148 (2008).
4. Ishigami, M. *et al.* Atomic Structure of Graphene on SiO₂. *Nano Lett.* **7**, 1643–1648 (2007).
5. Chen, J.-H. *et al.* Intrinsic and extrinsic performance limits of graphene devices on SiO₂. *Nature Nanotechnology* **3**, 206–209 (2008).
6. Fratini, S. *et al.* Substrate-limited electron dynamics in graphene. *Phys. Rev. B* **77**, 195415 (2008).
7. Dean, C. R. *et al.* Boron nitride substrates for high-quality graphene electronics. *Nature Nanotechnology* **5**, 722–722 (2010).
8. Dean, C. R. *et al.* Multicomponent fractional quantum Hall effect in graphene. *Nature Physics* **7**, 693–696 (2011).
9. Terrés, B. *et al.* Raman spectroscopy on mechanically exfoliated pristine graphene ribbons. *Physica status solidi (b)*, **12**, 251, 2551–2555 (2014).
10. Wang, L. *et al.* One-Dimensional Electrical Contact to a Two-Dimensional Material. *Science* **342**, 614–617 (2013).
11. Dauber, J. *et al.* Ultra-sensitive Hall sensors based on graphene encapsulated in hexagonal boron nitride. *Appl. Phys. Lett.* **106**, 193501 (2015).
12. Banszerus, L. *et al.* Ultrahigh-mobility graphene devices from chemical vapor deposition on reusable copper. *Science Advances* **1**, 6 (2015).
13. Banszerus, L. *et al.* Ballistic Transport Exceeding 28 m in CVD Grown Graphene. *Nano Lett. and* **16**, (2) (2016).
14. Hwang, E. H. *et al.* Acoustic phonon scattering limited carrier mobility in two-dimensional extrinsic graphene. *Phys. Rev. B* **77**, 115449 (2008).
15. Terrés, B. *et al.* Disorder induced Coulomb gaps in graphene constrictions with different aspect ratios. *Appl. Phys. Lett.* **98**, 032109 (2011).
16. Terrés, B. *et al.* Size quantization of Dirac fermions in graphene constrictions. *Nature Communications* (2016).
17. Jeckelmann, B. *et al.* The quantum Hall effect as an electrical resistance standard. *Rep. Prog. Phys.* **64**, 1603 (2001).
18. Vera-Marun, I. J. *et al.* Quantum Hall transport as a probe of capacitance profile at graphene edges. *Appl. Phys. Lett.* **102**, 013106 (2013).
19. Hohls, F. *et al.* Hopping Conductivity in the Quantum Hall Effect: Revival of Universal Scaling. *Phys. Rev. Lett.* **88**, 036802 (2002).
20. Bolotin, K. I. *et al.* Observation of the fractional quantum Hall effect in graphene. *Nature* **462**, 196–199 (2009).

21. Molitor, F. *et al.* Transport gap in side-gated graphene constrictions. *Phys. Rev. B* **79**, 075426 (2010).
22. Mayorov, A. S. *et al.* How Close Can One Approach the Dirac Point in Graphene Experimentally? *Nano Lett.* **12** (9), 4629–4634 (2012).
23. Monteverde, M. *et al.* Transport and elastic scattering times as probes of the nature of impurity scattering in single-layer and bilayer graphene. *Phys. Rev. Lett.* **104**, 126801 (2010).
24. Lonzarich, G. G. *et al.* Electrons at the Fermi surface. *Springford and M. and Ed.; Cambridge University: Cambridge. Chapter 6* (1980).
25. Young, A. F. *et al.* Spin and valley quantum Hall ferromagnetism in graphene. *Nature Physics* **8**, 550–556 (2012).
26. Yan, J. *et al.* Electric Field Effect Tuning of Electron-Phonon Coupling in Graphene. *Phys. Rev. Lett.* **98**, 166802 (2007).
27. Goerbig, M. O. Electronic properties of graphene in a strong magnetic field. *Review of Modern Physics* **83**, 112–123 (2010).
28. Ghahari, F. *et al.* Measurement of the $\nu = 1/3$ Fractional Quantum Hall Energy Gap in Suspended Graphene. *Phys. Rev. Lett.* **106**, 046801 (2011).
29. Tsui, D. C. *et al.* Observation of a fractional quantum number. *Phys. Rev. B* **28**, 2274 (1983).
30. Boebinger, G. S. *et al.* Magnetic Field Dependence of Activation Energies in the Fractional Quantum Hall Effect. *Phys. Rev. Lett.* **55**, 1606 (1985).
31. Nomura, K. *et al.* Quantum Hall Ferromagnetism in Graphene. *Phys. Rev. Lett.* **96**, 256602 (2006).
32. Tsui, D. C. *et al.* Zero-resistance state of two-dimensional electrons in a quantizing magnetic field. *Phys. Rev. B* **25**, 1405 (1982).
33. Ebert, G. *et al.* Hopping Conduction in the Landau-Level Tails in GaAs-AlGaAs Heterostructures at Low Temperatures. *Solid State Commun.* **45**, 625, 625–628 (1983).
34. Moser, J. *et al.* Magnetotransport in disordered graphene exposed to ozone: From weak to strong localization. *Phys. Rev. B* **81**, 205445 (2010).
35. Nicholas, R. J. *et al.* Electron transport in silicon inversion layers at high magnetic fields and the influence of substrate bias. *Surface Science* **98**, 1, 283–298 (1980).
36. Shklovskii, B. I. & Efros, A. L. *Electronic Properties of Doped Semiconductors. Springer-Verlag and Berlin*, (1984).
37. Giesbers, A. J. M. *et al.* Scaling of the quantum Hall plateau-plateau transition in graphene. *Phys. Rev. B* **80**, 241411 (2009).
38. Bennaceur, K. *et al.* Unveiling quantum Hall transport by Efros-Shklovskii to Mott variable-range hopping transition in graphene. *Phys. Rev. B* **86**, 085433 (2012).
39. Koch, S. *et al.* Size-dependent analysis of the metal-insulator transition in the integral quantum Hall effect. *Phys. Rev. Lett.* **67**, 883 (1991).

40. Koch, S. *et al.* Variable range hopping as the mechanism of the conductivity peak broadening in the quantum Hall regime. *Phys. Rev. Lett.* **70**, 3796 (1993).

6.1 Ballistic transport in graphene quantum Point Contacts

This section has been published in:

Size quantization of Dirac fermions in graphene constrictions.

B. Terrés, L.A. Chizhova, F. Libisch, J. Peiro, D. Joerger, S. Engels, A. Girschik, K. Watanabe, T. Taniguchi, S. V. Rotkin, J. Burgdörfer and C. Stampfer
Nature Communications **7**, 11528 (2016)

Quantum point contacts (QPCs) are cornerstones of mesoscopic physics and the central building blocks for quantum electronics. Although the Fermi wave-length in high-quality bulk graphene can be tuned up to hundreds of nanometers, the observation of quantum confinement of Dirac electrons in nanostructured graphene systems has proven surprisingly challenging. In this section, we show ballistic transport and quantized conductance of size-confined Dirac fermions in lithographically-defined graphene QPCs. At high charge carrier densities, the observed conductance agrees excellently with the Landauer theory of ballistic transport, without any adjustable parameter. The width-dependent electrical transport is characterized by reproducible steps in conductance. Experimental data and simulations for the evolution of the conductance steps with magnetic field unambiguously confirm the identification of size quantization in the constriction. Bias spectroscopy and temperature dependent measurements confirm the identification of size quantization as the origin of these steps in conductance. Close to the charge neutrality point, bias voltage spectroscopy reveals a renormalized Fermi velocity ($v_F \approx 1.5 \times 10^6$ m/s) in our graphene QPCs.

The observation of novel transport phenomena in graphene, such as Klein tunneling [1], evanescent wave transport [2], or half-integer [3, 4] and fractional [5, 6] quantum Hall effect, are directly related to the material quality and to the intrinsic relativistic nature of the charge carriers [7]. As the quality of bulk graphene has impressively improved over the last years [8, 9], the understanding of the role and limitations of edges on transport properties of graphene is becoming increasingly important. This is

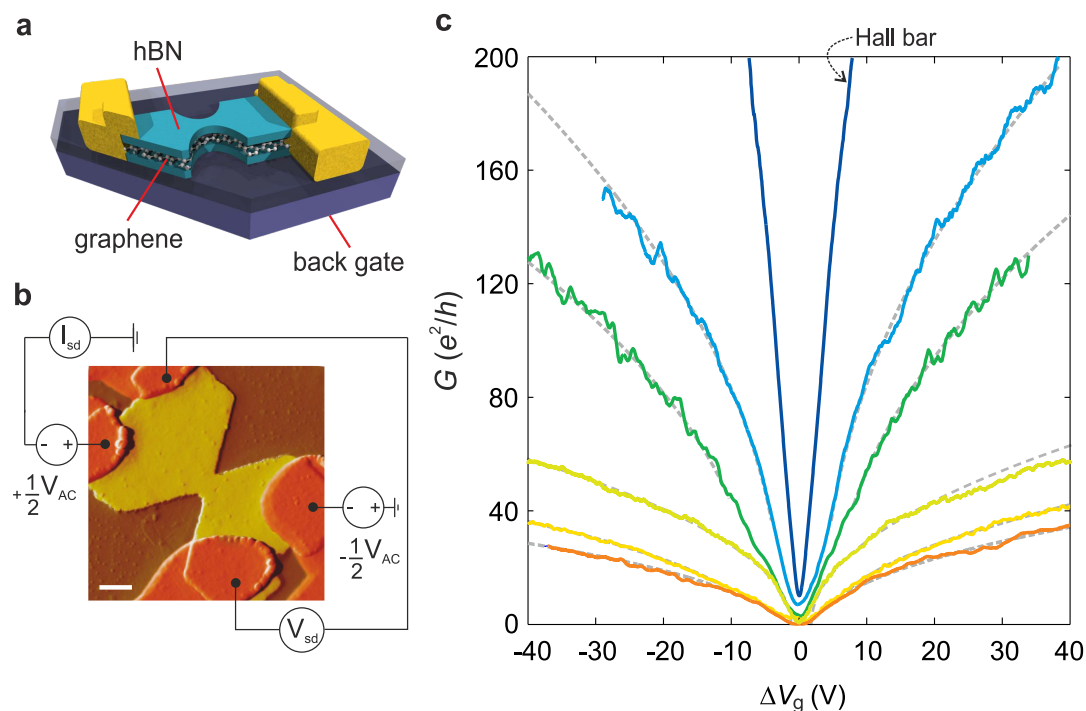


Figure 6.1: **Width-dependent ballistic transport in etched graphene QPCs encapsulated in hBN.** **a**, Schematic illustration of a hBN-graphene-hBN sandwich device with the bottom and top layers of hBN appearing in green, the gold contacts in yellow, the SiO_2 in dark blue and the Si back-gate in purple. **b**, False colored atomic force microscope (AFM) image of a fabricated device. Transport is measured in a four-probe configuration to eliminate any unwanted resistance of the one-dimensional contacts [13]. The orange color denotes the gold contacts, yellow the top layer of hBN and brown the SiO_2 substrate. The scale bar is 500 nm. The differential conductance $G = dI/dV = I_{sd}/V_{sd}$ is measured from an AC excitation voltage $V_{AC} = 250 \mu V_{PP}$. **c**, Low-bias back-gate characteristics of a Hall bar device (see arrow) and of five QPC devices with diff widths ranging from 850 nm to 230 nm (see color code in Fig. 6.6a). The dashed gray lines are fits to the data.

particularly crucial in nanoscale graphene systems where edges can dominate the device properties. Indeed, the rough edges of graphene nanodevices are most probably responsible for the difficulties in observing clear confinement quantization effects, such as quantized conductance [10, 11] and shell filling [12]. So far, signatures of quantized conductance have only been observed in suspended graphene, however with lacking control and information on geometry and constriction width [11]. With further progress in fabrication methods, graphene nano-devices are expected to evolve from a disorder dominated [14] transport behavior to a quasi-ballistic regime, where boundary effects, crystal alignment and edge defects [15] may play a dominant role in defining the transport characteristics. In fact, gaining the control over the graphene edges will open the

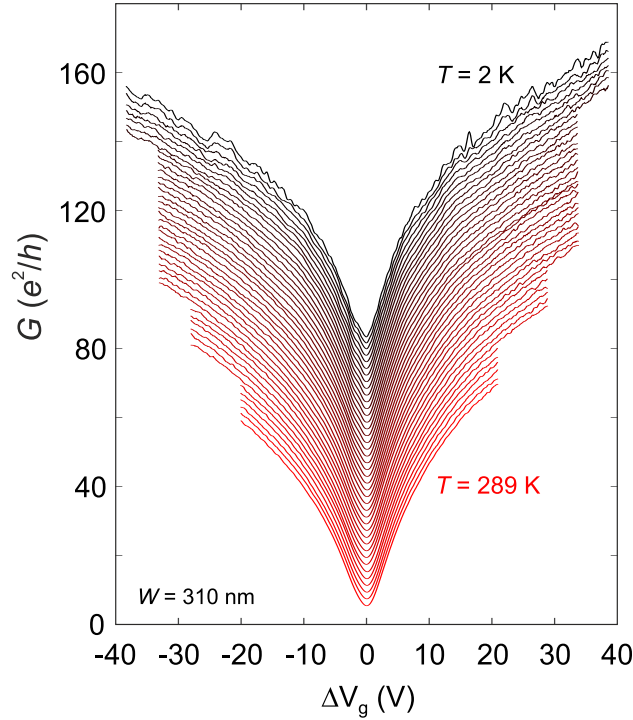


Figure 6.2: **Temperature dependence of the back-gate characteristics for the 310-nm-wide graphene constriction.** Low-bias back-gate dependent four-terminal conductance G as a function of temperature T . The traces are shifted in the conductance axis for clarity. Temperature is recorded from $T = 2$ K (black trace) up to room-temperature ($T = 289$ K, red trace) in steps of 7 K.

door to study interesting edge-related phenomena, such as spin polarization at zig-zag edges [16, 17], valleytronics [18], an unusual Josephson effect [19], magnetic edge-state excitons [20] as well as topologically protected quantum spin Hall states [21].

In this section we report the observation of quantum confinement effects in the ballistic conductance through graphene constrictions acting as quantum point contacts. We prepared a group of graphene devices based on high-mobility graphene-hexagonal boron nitride (hBN) sandwiches on SiO_2/Si substrates and use reactive ion etching (RIE) technique to pattern narrow QPCs (see Section 3.3) with widths ranging from $W \approx 230$ to $1\mu\text{m}$ (Fig. 6.1a,b). The graphene leads are side-contacted [13] by chrome/gold electrodes in a four-terminal configuration to eliminate any unwanted resistance from the one-dimensional contacts. The differential conductance $G = \delta I / \delta V = I_{sd} / V_{sd}$ is measured using standard lock-in techniques with an applied voltage of $V_{AC} = 250 \mu\text{V}_{PP}$ (Fig. 6.1b). A back-gate voltage is applied to the highly-doped Si substrate to tune the carrier density in the graphene, $n = \alpha(V_g - V_g^0) = \alpha\Delta V_g$, where α is the so-called lever arm and V_g^0 is the gate voltage of minimum conductance, i.e. the charge neutrality point (CNP). Thus, tuning the gate voltage V_g changes the Fermi wave-vector $k_F = \sqrt{n\pi}$ of the conducting charge carriers. Fig. 6.1c shows the measured differential

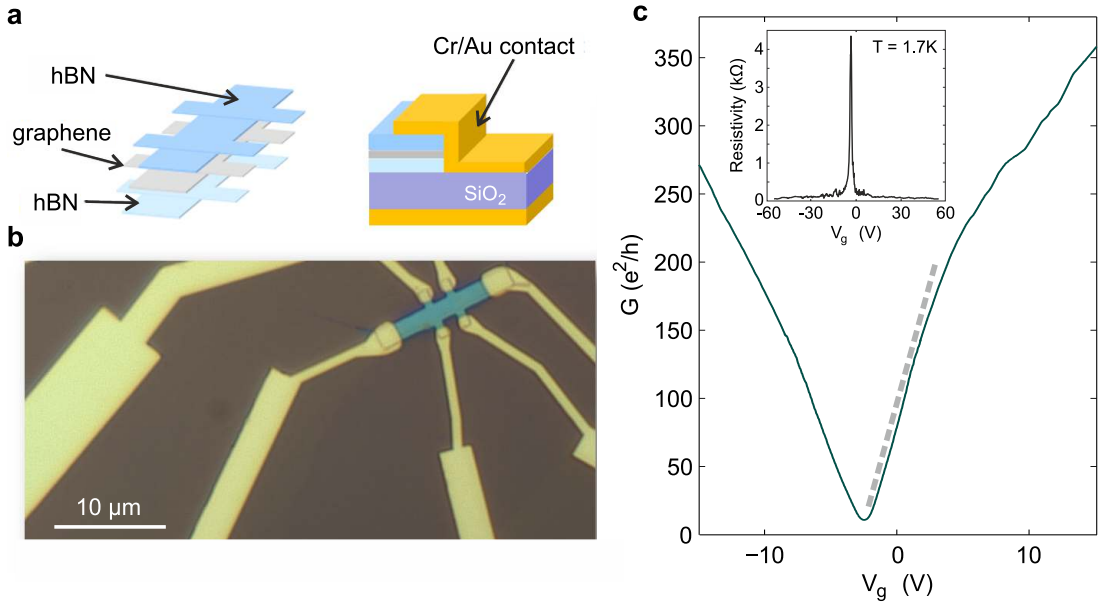


Figure 6.3: **Reference hBN-graphene-hBN sandwich Hall bar device.** (a) Schematic illustration of the hBN-graphene-hBN sandwich hetero-structure and nature of the quasi one-dimensional graphene-metal (Cr/Au) contact. (b) Optical image of an etched and contacted $\sim 1 \mu\text{m}$ -wide hBN-graphene-hBN sandwich Hall bar device. (c) Four-terminal conductance as a function of back gate voltage V_g measured at a constant current of 50 nA and a temperature of 16 K. From the linear slope near the charge neutrality point (see dashed gray line), we extract a carrier mobility of around $150.000 \text{ cm}^2\text{V}^{-1}\text{s}^{-1}$. The inset shows the four-terminal resistivity as a function of gate voltage at lower temperature (1.7 K).

conductance as a function of gate voltage for a number of devices with distinct widths. The observed square-root dependence $G \propto \sqrt{\Delta V_g}$ (see dashed lines in Fig. 6.1c) is a first indication of the ballistic nature of the conductance, that is indeed conserved up to room-temperature (Fig. 6.2). Although the temperature dependent measurements introduced in Fig. 6.2 show a progressive smoothing of the conductance traces with increased temperature (up to $T = 289$ K), the square-root dependence, i.e. the ballistic nature of transport, remains unchanged.

To demonstrate the high electronic quality of our graphene-hBN sandwich structures we show the back-gate characteristic of a reference Hall bar device (Fig. 6.3). From this data (Fig. 6.3c) we extract a carrier mobility in the range of around $150.000 \text{ cm}^2/\text{Vs}$, resulting in a mean free path exceeding $1 \mu\text{m}$ at around $\Delta V_g = 4.6$ V. Thus, the mean free path is expected to clearly exceed all relevant length scales in our constriction devices, giving rise to ballistic transport.

According to the Landauer-Büttiker theory for ballistic transport, the conductance through a perfect constriction increases by an additional conductance quantum e^2/h

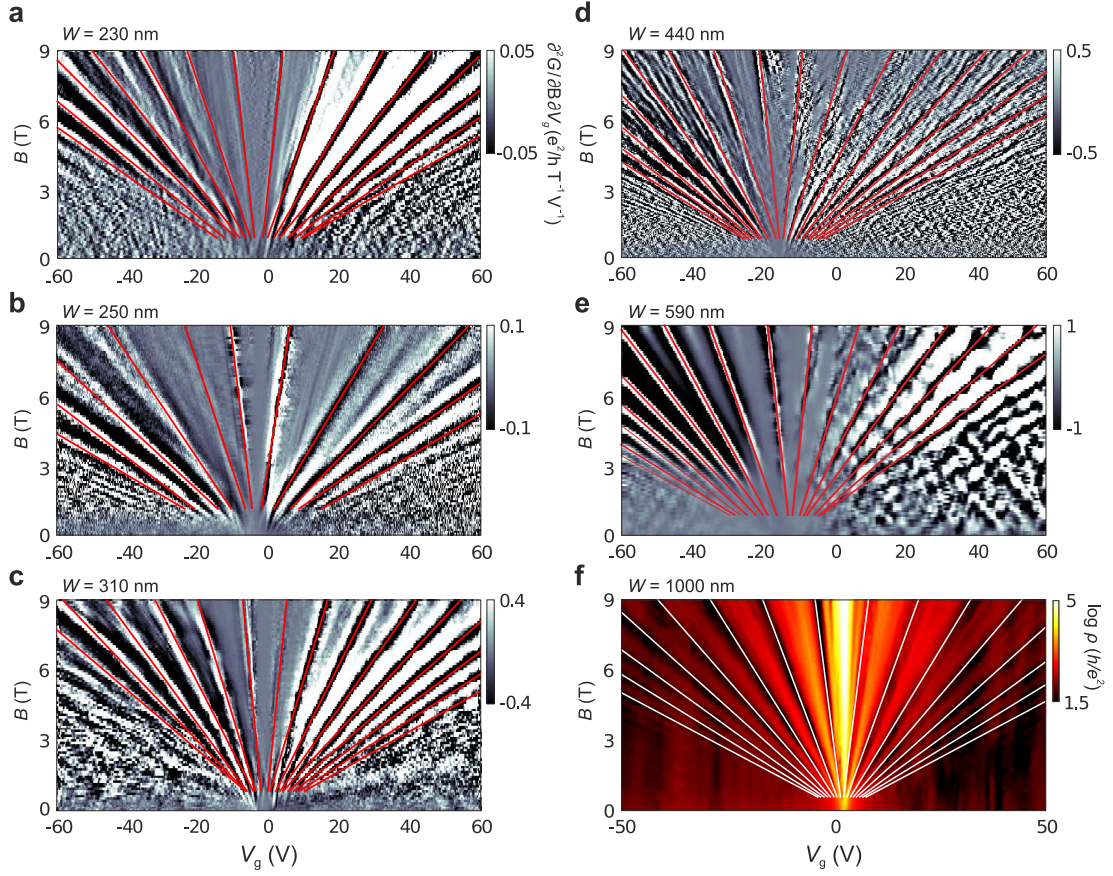


Figure 6.4: **Landau fan and capacitive coupling.** (a)-(e) Second derivative of the longitudinal conductance $\partial^2 G / \partial V_g \partial B$ as a function of magnetic field B and back-gate voltage V_g for six different devices of distinct widths. The red lines follow the evolution of the Landau levels. The slopes of the lines are proportional to the capacitive coupling α . (f) The longitudinal resistivity ρ as a function of B and V_g provide an alternative way to extract α from the position of the Landau levels, marked by white lines.

whenever Wk_F reaches a multiple of π ,

$$G = \frac{4e^2}{h} \sum_{m=1}^{\infty} \theta\left(\frac{Wk_F}{\pi} - m\right), \quad (6.1)$$

where $k_F = \sqrt{\pi n}$ is the Fermi wave-vector, $\theta(k)$ is the Heaviside step function and the factor four accounts for valley and spin degeneracies. For simplicity, we neglected the minor phase contributions due to specific configurations of the graphene edges [22]. The Fourier expansion of Eq. 6.1 yields:

$$G = \frac{4e^2}{h} \frac{c_0 W k_F}{\pi} + \frac{4e^2}{h} \left[\sum_{j=1}^{\infty} c_j \sin(2jWk_F - \phi_j) - \frac{c_0}{2} \right], \quad (6.2)$$

with $c_0 = 1$, $\phi = 0$ and $c_j = 1/(j\pi)$ ($j > 0$) for an ideal constriction. In the presence of

SEM-extracted width W (nm)	α ($10^{10}\text{cm}^{-2}\text{V}^{-1}$)
1000	7.00
850	5.80
590	6.75
440	6.90
310	7.00
280	7.20
250	5.40
230	7.15

Table 6.1: Lever arm α values, extracted from the Landau fans presented in Fig. 6.4, for the seven different devices under study. The geometric widths W are extracted from SEM images (Fig. 6.6b).

rough edges, c_0 is reduced to a value below 1 due to limited average transmission. Likewise, the higher Fourier components c_j are expected to decay in magnitude and acquire random scattering phases $\phi \neq 0$. Consequently, the sharp quantization steps turn into periodic modulations as we will show below. Averaged over these modulations, only the zeroth order term in the expansion [Eq. 6.2] survives. This mean conductance $G^{(0)}$ of a constriction of width W thus features a linear dependence on k_F , or, equivalently, a square-root dependence as a function of back-gate voltage:

$$G^{(0)} \approx \frac{4e^2}{h} \left(\frac{c_0 W k_F}{\pi} - \frac{c_0}{2} \right) = \frac{4e^2}{h} \frac{c_0 W}{\pi} \sqrt{\pi \alpha (V_g - V_g^0)} - \frac{2c_0 e^2}{h}, \quad (6.3)$$

assuming perfect (or energy-independent) transmission of all modes, in agreement with Fig. 6.1.

By measuring the carrier density dependent quantum Hall effect at high magnetic fields [4, 23], we can independently determine the gate coupling α for each device (Fig. 6.4). The derivative of the longitudinal conductance ($\partial G / \partial V_g$) is well suited to identify the evolution of the Landau levels as a function of B-field and gate voltage. The position of the filling factors (FFs) in the B - V_g plane is usually determined by the minimum of the longitudinal resistivity ρ_{xx} (marked in white in Fig. 6.4f). Alternatively, the position of the filling factor corresponds to a maximum and minimum of $\partial^2 G / \partial V_g \partial B$ (marked in red in Fig. 6.4) for the holes- and electrons-side of the Landau fan, respectively. The linear dispersion $E_F = \hbar v_F k_F$ of graphene and its characteristic Landau level quantization $E_N = \pm v_F \sqrt{2\hbar N e B_N}$ (where E_N is the energy of the N^{th} Landau level and v_F the Fermi velocity) determines the Landau level evolution as follows: $B_N = \frac{\alpha_N \hbar}{4N e} V_g + V_0$ with α_N being the gate coupling of every individual Landau level N and V_0 an arbitrary offset accounting for sample doping. The values of coupling α_N diverge for the lowest Landau levels [24], i.e. close to the Dirac point, but rapidly

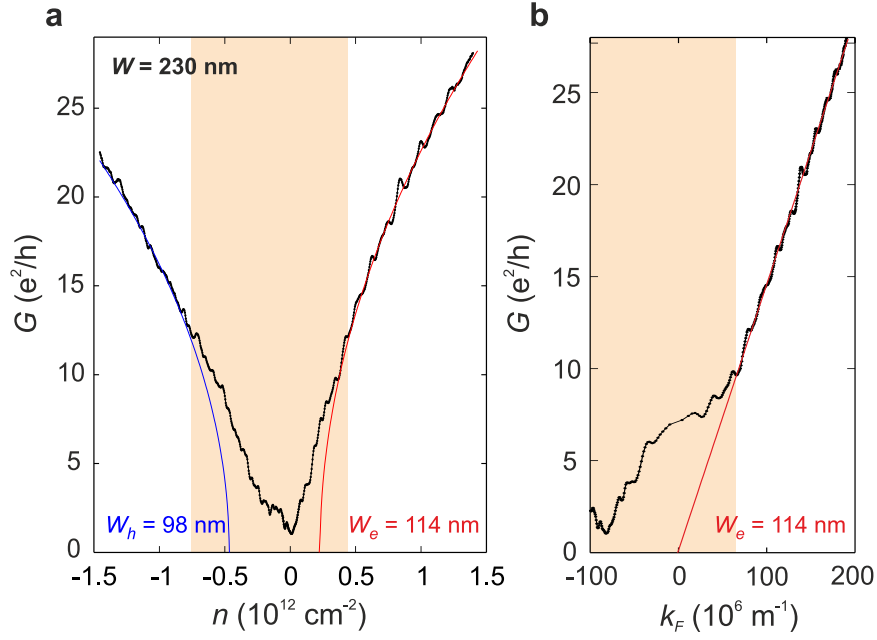


Figure 6.5: **Deviations from the ideal ballistic model of conductance.** (a) and (b) Low-bias four-terminal differential conductance G as a function of charge carrier density n (panel a) and momentum k_F (panel b) of the 230-nm-wide graphene QPC. The shaded orange region denote the deviation from the ideal Landau Büttiker model of conductance $G \propto \sqrt{k_F}$, shown in red and blue for the electron and hole regimes, respectively. By comparing data and model we extract the effective width for hole W_h and electron W_e regimes, shown in blue and red, respectively.

saturates to a constant level of coupling for the higher Landau level indexes. Tab. 8.1 summarizes the extracted saturation values of the lever arms.

With the gate-coupling revealed, we can unfold the dependence of the conductance on V_g and study it as a function of the Fermi wave-number k_F . To linearize the conductance as a function of k_F though, we must initially determine the starting values of gate voltage or carrier density upon which G follows the ballistic model of conductance. A closer look at the trace from the narrowest device $W = 230$ nm (Fig. 6.5) reveals a systematical deviation from the expected square-root dependence at low carrier concentrations, i.e for $n < 0.45 \times 10^{12} \text{ cm}^{-2}$ on the electron side and $n < 0.75 \times 10^{12} \text{ cm}^{-2}$ for the hole side (Fig. 6.5a). This deviation becomes more pronounced close to the charge neutrality point (see orange shaded area in Fig. 6.5). In the ballistic regime, i.e. at high carrier densities, we can fit Eq. 6.3, e.g. the Landauer-Büttiker model of conductance, where n_0^e and n_0^h (or alternatively V_g^{0e} and V_g^{0h}) are the boundary density values for the electron- and hole-side, respectively, and α the lever-arm extracted from the Landau level fan (Fig. 6.4). As expected, the differential conductance G evolves linearly as function of k_F in the ballistic regime (Fig. 6.5b), but but large deviations between data and model become apparent close to the charge neutrality point (see orange-shaded

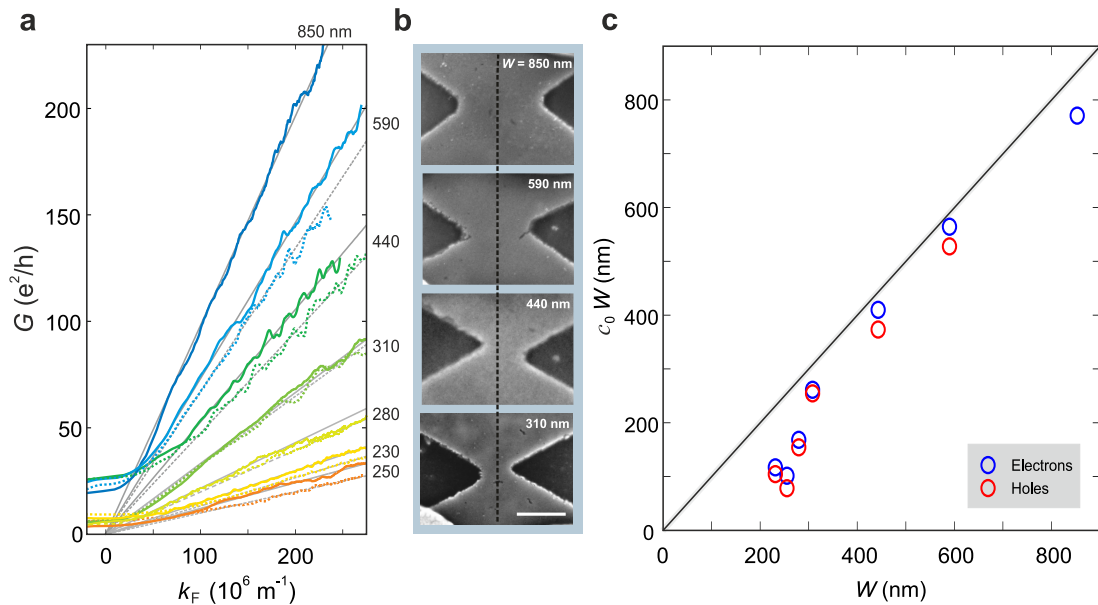


Figure 6.6: **Width-dependent ballistic transport in graphene QPCs.** (a) Low-bias four-terminal differential conductance as a function of k_F for six graphene QPCs of distinct width. The electrons (holes) conductance traces are plotted in solid (dashed) colored lines. The width is extracted, in the high carrier density regime, by fitting the model of conductance (solid and dashed gray lines) to the measurements. (b) Scanning Electron Microscope (SEM) images of four devices. The scale bar is 500 nm. (c) Comparison between the measurement's extracted width $c_0 W$ of panel a, with the SEM-measured width W of panel b.

region in Fig. 6.5b). We conclude that a linear model using a constant gate coupling $k_F = \sqrt{\pi\alpha\Delta V_g}$ is not directly applicable to our graphene constriction devices. Instead, one needs to account for the additional trap states arising from the graphene edges. We will address more in detail the deviations from the ideal model in the following chapter (Section 6.2).

As observed in Fig. 6.6a, at high energies, the conductance evolves linearly as a function of k_F for all graphene QPCs. A linear fit to the slopes (solid and dashed gray lines) allows to extract the product $c_0 W$ (Eq. 6.3) for each device and compare it to the geometrical width W (Fig. 6.6c). The geometrical width (W) of the fabricated QPCs is determined from scanning electron microscopy (SEM) images (Fig. 6.6b), enabling a direct comparison with the data-extracted width $c_0 W$ (Fig. 6.6c). The estimates for $c_0 W$ extracted from $G^{(0)}$ (Eq. 6.3) lie just below the width W , where c_0 decreases for decreasing width. This suggests that for the narrower devices reflections, most likely due to device geometry and edge roughness, are playing a more important role. From the data in Fig. 6.6c we can extract $c_0 \approx 0.56$ for our smallest constriction.

One may also interpret that the effective width of the conduction channel could be, in all cases, smaller than the geometrical width W . However, in the following, we will

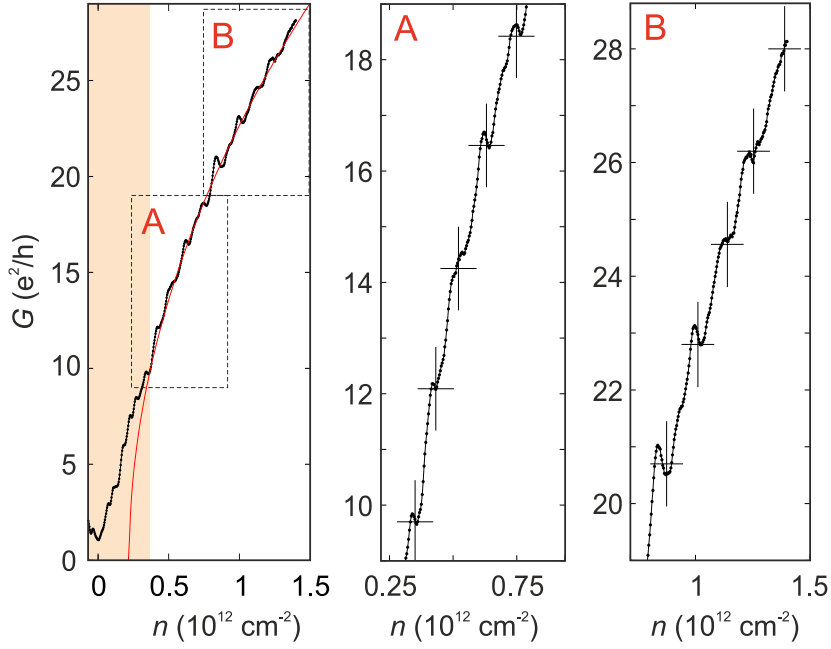


Figure 6.7: **Indications of confinement quantization.** Low-bias four-terminal differential conductance G as a function of n for the 230 nm-wide graphene QPC. Panel A and B are zoom-in of the dashed regions in panel a. The level of conductance and the position in the n -axis of the conductance steps are marked by black crosses.

show that reflections at the rough edges of the constriction are indeed responsible for the deviation of the experimentally extracted $c_0 W$ from the SEM width W .

Superimposed to the overall squared-root behavior of $G(n)$ we find reproducible modulations or steps in conductance (see crosses in Fig. 6.7 and red arrows in Fig. 6.8). The conductance steps are reproducible for several cool-downs (Fig. 6.9) as well as for different devices (Fig. 6.7 for $W = 230$ nm, Fig. 6.8 for $W = 310$ nm and Fig. 6.20 for $W = 230, 250, 280$ and 310 nm). The conductance steps generally show a non-equal steps in conductance ΔG , in the range of $(2 - 4) e^2/h$ (compare conductance steps in Fig. 6.6 and Fig. 6.8). The step height ΔG and its sharpness depend on the carrier density (i.e. k_F). The plateaus do not seem to degrade so heavily at elevated levels of conductance as in traditional III-V semiconductors, conserving fairly visible conductance steps even at conductance values of $\sim 25 e^2/h$ for the 230 nm-wide device (Fig. 6.7) and $\sim 40 e^2/h$ for 310 nm-wide one (Fig. 6.8). More importantly, ΔG seems to depend on the constriction width, in strong good agreement with the transmission coefficient c_0 extracted from the overall conductance trend (Fig. 6.6). Remarkably, we observe a spacing ΔG of the steps close to $\Delta G \approx 2e^2/h \sim c_0 \times 4e^2/h$ for the 280 nm-wide device (with $c_0 \approx 0.56$, see Fig. 6.7) and $\Delta G \approx 4e^2/h \sim c_0 \times 4e^2/h$ for the 310 nm-wide one (with $c_0 \approx 0.98$, see Fig. 6.7).

It is important to note the progressive broadening, in the energy axis (i.e. V_g or n axis), of the conductance steps as a function of energy. This is clearly visible in the

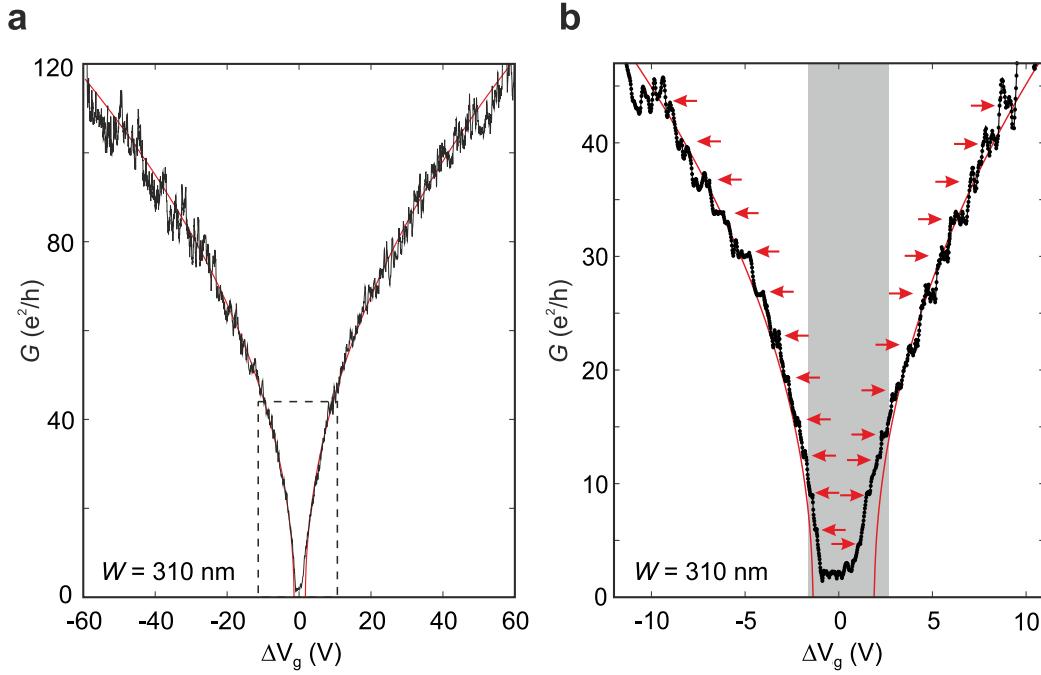


Figure 6.8: **Indications of confinement quantization in the back-gate characteristics of the 310 nm-wide graphene constriction** (a) Low-bias four-terminal conductance G as a function of back gate voltage V_g , measured at $T = 2\text{ K}$. The ideal Landau Büttiker model of conductance $G \propto \sqrt{n}$ is marked in red. (b) Close-up of the conductance G inside the dashed-line region of panel a. The presence of reproducible conductance steps is clearly visible (marked by red arrows). The shaded gray-region denote deviations from the ideal Landauer model (red trace).

electron- and hole-side of the 310 nm-wide device (Fig. 6.8), and it is a direct consequence of the Dirac fermion nature of the charge carriers in graphene.

In the following, we will show that reflections at the rough edges of the constriction are indeed responsible for the deviation of the experimentally extracted $c_0 W$ from the SEM width W). We will initially characterize the nature of these conductance steps via bias spectroscopy and magnetic field dependent measurements.

First supporting evidences of size quantization appear looking at the magnetic field evolution of the conductance plateaus (Fig. 6.10 and Fig. 6.11). Theoretically, the transition from size quantization at zero magnetic field to Landau quantization at high fields is expected to happen when the cyclotron radius $l_c = \sqrt{2N} \cdot l_B$ is smaller than half the device's width W , with $l_B = \sqrt{\hbar/eB}$ being the magnetic length and N a positive integer accounting for the Landau level index. At the crossover, when $2l_c = W$, it is therefore possible to extract the device's width. It is alternatively valid to use the semi-classical relation $l_c = \hbar k_F/eB$, although one must carefully apply this relation in the quantum regime since its solely valid at the boundary, when Landau quantization

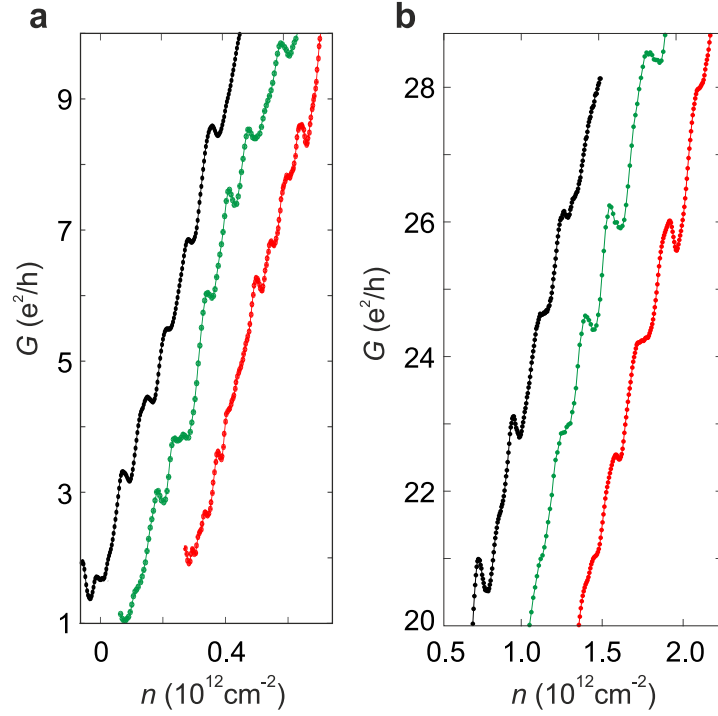


Figure 6.9: **Cool-down dependence of the conductance steps for the 230 nm-wide graphene constriction.** (a) and (b) Four-terminal differential conductance G as a function of charge carrier density n for different cool-downs of the 230 nm-wide graphene QPC, at the low- and high- charge carrier density regimes (panels a and b, respectively). The traces are shifted horizontally for clarity.

comes into play

$$l_c = \sqrt{2N} \sqrt{\hbar/eB} = \hbar k_F / eB \quad \text{when} \quad N = \hbar k_F^2 / 2eB, \quad (6.4)$$

N being directly issued from the Landau quantization in graphene:

$$E = V_F \hbar k_F = V_F \sqrt{2NeB\hbar} \iff N = \hbar k_F^2 / 2eB, \quad (6.5)$$

The magnetic fields fulfilling $B_F = 2\hbar k_F / eW$, noted critical fields (B_F), define thus the transition from quantized conductance to a Landau quantization regime. As observed in Fig. 6.10a (black solid line), the expected boundary limit for a 230 nm-wide ribbon is in good agreement with the beginning of Landau levels' formation. Traces of Landau levels are directly visible above the critical fields, although at $T = 1.7$ K and below the crossover, the conductance is dominated by resonances that obscure the magnetic evolution of the high conductance plateaus. Nonetheless, for the low conductance plateaus (see Fig. 6.10b, c and d), one can track the evolution of the quantized subbands ($B = 0$ T) into its corresponding Landau levels. At higher temperatures, when resonances and scattering effects are expected to vanish, the transition is observed even for the highest conductance plateaus (Fig. 6.11). For comparison, we calculate the evolution of the size quantization as function of magnetic field using the shape of our

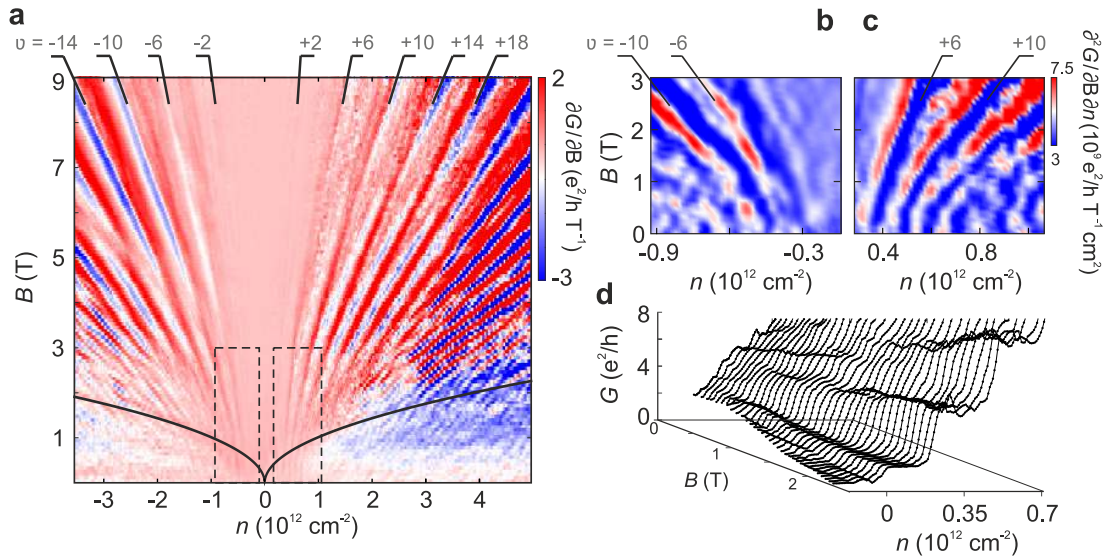


Figure 6.10: **Magnetic-field evolution of the size quantization at $T = 1.7$ K.** (a) Landau level fan of the 230 nm-wide graphene QPC. The formation of Landau levels emerges at high magnetic fields. For B-fields above the critical field B_F (solid black line), i.e. for cyclotron radius l_c smaller than half the constriction's width W , the Landau level quantization dominates over the size quantization. (b) and (c) Derivative plots of the transconductance in the dashed-line regions in panel a. The evolution of the lowest quantization plateaus with magnetic field is clearly visible. (d) The magnetic field evolution of the subbands is also visible in the differential conductance from a different cool-down of the same device, also measured at 1.7 K.

device (extracted from the AFM figure) as the only adjustable parameters (green traces Fig. 6.11b and c). We employ the modular recursive Green's function method [25] with the contribution of the magnetic field modeled via a Peierls phase factor. To compute the local density of states, we superpose the calculated eigenstates using Arnoldi-Lanczos factorization. We find remarkably good agreement with measurements, supporting the notion that the observed kinks are, indeed, unambiguous signatures of size quantization.

More importantly, and opposed to what has been previously established [11], results reveal that the associated confinement states are four-fold degenerate and heavily affected by resonances and back-scattering across the sample. Thus, transport appears to have a particularly reduced transmission coefficient ($c_0 \approx 0.5$), which is also recognizable from the distorted-shape of the conductance plateaus [26]. The results support that the divergences between geometrical and extracted widths Fig. 6.6c are indeed due to a reduced transmission coefficient ($c_0 \approx 0.5$ for the narrowest devices).

Disorder, due to bulk imperfections (situation A in Fig. 6.12d) and crystallographic dislocations at the edges, or "rough" edges, (situation B in Fig. 6.12d) may lead to scattering processes which result in reflections of the charge carriers back to the reservoir, i.e. back-scattering. In adiabatic III-V heterostructures, the shape of the devices

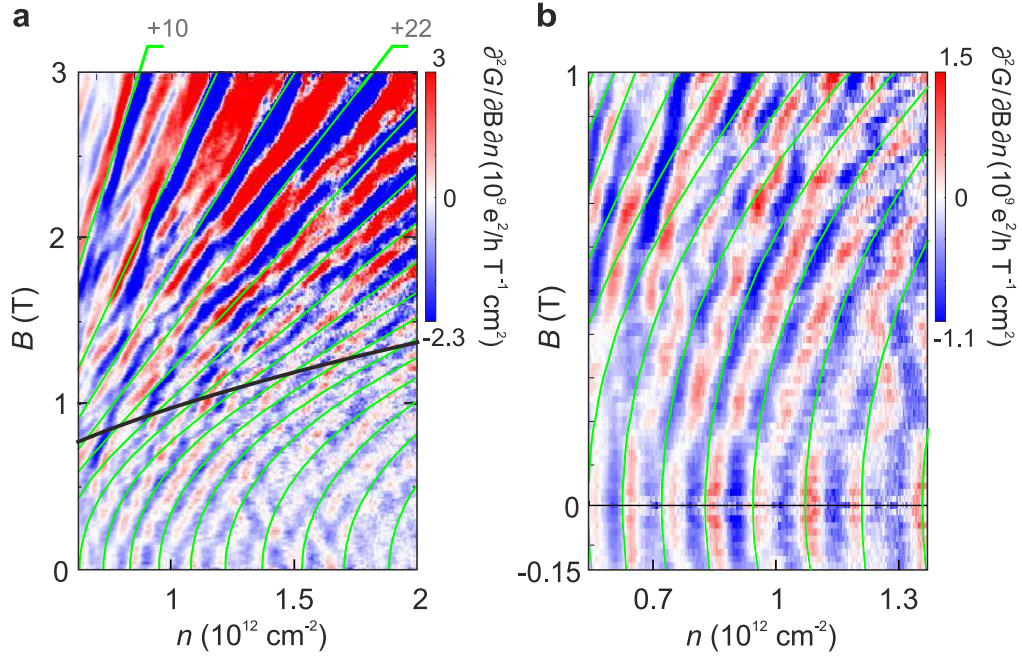


Figure 6.11: **Magnetic-field evolution of the size quantization at $T = 6$ K.** (a) Derivative plot of the transconductance as a function of magnetic field and charge carrier density from a different cool-down of the 230 nm-wide device measured at $T = 6$ K. The solid green lines indicate the theoretical expectations of the magnetic evolution of the size quantization. The thick black line indicates the crossover from confinement to a Landau quantization regime, also visible in panel a of Fig. 6.10. (b) Zoom-in of Panel a for small magnetic fields ($B < 1$ T).

is defined by electrostatics (soft-confinement) with the edges of the devices merely contributing to back-scattering processes. Therefore, the distribution of scattering centers can be considered uniformly distributed within the bulk (situation A in Fig. 6.12d). Under this assumption, the concentration of scattering points necessary to achieve low transmission coefficients ($c_0 \approx 0.5$), may obscure the ballistic transport since, as soon as the average distance between scattering points (mean free path l_e) is shorter than Fermi wavelength λ_F , transport enters the diffusive regime. In other words, in traditional III-V heterostructures, a fairly low transmission coefficient erodes the ballistic nature of transport. On the other side, the "carved" nature of the graphene devices, may allow the coexistence of a ballistic channel (defect-free zone at the center, away from the device's edges) with a highly dense region of scattering points located at the edges of the graphene devices (red region in Fig. 6.12d), thus allowing the coexistence of ballistic transport phenomena with an associated reduced transmission coefficient.

Moreover, both experimental and theoretical investigations in traditional 2DEGs, e.g. GaAs heterostructures, show very clear and pronounced quantization plateaus [28]. In these heterostructures, and besides the aforementioned structural differences of the material boundaries [e.g. soft edges compared to graphene's hard edges (Fig. 6.12d)],

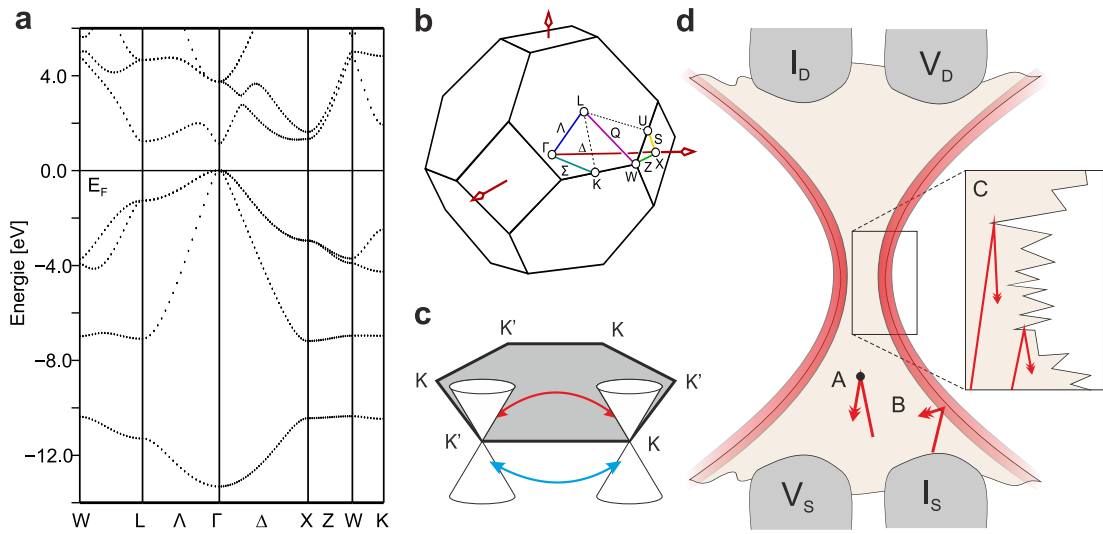


Figure 6.12: **Scattering mechanisms in graphene.** (a) Electronic band structures along lines of high symmetry for GaAs (reprinted from [27]). Transport in GaAs mostly happens through carriers around the Γ -point ($k = 0$). (b) First Brillouin zone of GaAs highlighting the lines of the diamond structure. (c) First Brillouin zone of graphene (gray shaded region) with the K and K' Dirac cones represented in two of the hexagon edges. Carriers responsible of transport do not have zero-momentum ($k \neq 0$). $K - K'$ inter-valley scattering processes allow shifts in momentum. (d) Schematic representation of the transport through a graphene quantum point contact. The scattering on a point defect in the bulk is represented in A. The scattering mechanism can also occur at the boundaries of the device (situation B). The scattering phenomena may also happen in the constricted area (situation C). In ballistic graphene devices, the region with a high concentration of scattering centers are the edges of the graphene device (region highlighted in red).

the charge carrier wavelength λ_F near the Γ point is very long and the lowest value of λ_F that is able to probe is limited by the square-relation of its dispersion relation (Fig. 6.12a). All in all, in traditional III-V 2DEGs the Fermi wavelength of the charge carriers cannot resolve disorder on the nanometer scale, like, for example, graphene's edge disorder. However, in graphene, the linear dispersion relation (Fig. 6.12c) allows the conducting charge carriers to probe disorder at a much shorter length scales, that together with the K - K' scattering possibilities (Fig. 6.12c) may substantially impacts transport characteristics (energy-dependent transmission coefficient).

The temperature dependence of the quantized conductance plateaus strongly confirms the divergences found between the magnetic evolution of the subbands at $T = 1.7$ K (Fig. 6.10) and $T = 6$ K (Fig. 6.11). Fig. 6.13 shows the temperature dependence of the back gate characteristics at both low and high carrier densities (Fig. 6.13a and b, respectively). We do not observe major differences between the low and high density

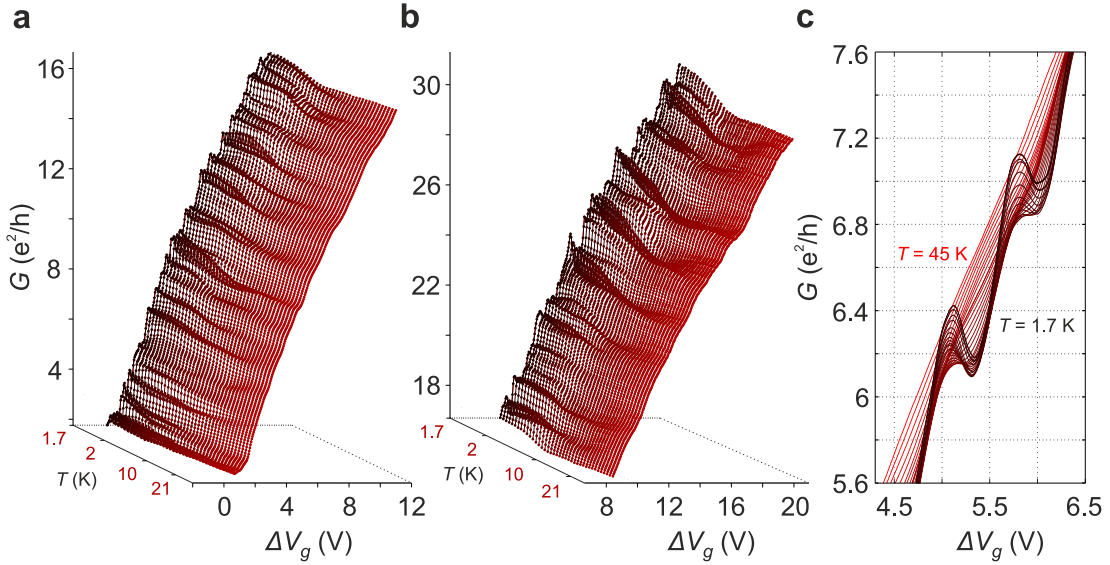


Figure 6.13: **Temperature dependence of the differential conductance.** (a) and (b) Differential conductance as a function of back-gate voltage and temperature at low (panel a) and high (panel b) carrier densities for the 230 nm-wide QPC. Measurements are recorded at temperatures from $T = 2$ K to $T = 24$ K in steps of 0.7 K. (c) Zoom-in of the temperature evolution of the shape of the steps in conductance.

regimes, with the interference structures (Fabry Perot-like oscillations) vanishing at lower temperatures ($T \approx 15$ K) and the quantized conductance plateaus surviving up to $T \approx 24$ K. Elevated temperatures appear thus, to enhance the observation of subbands in ballistic graphene nano-structures, in perfect agreement with the analysis of the evolution in B-field. Note that, the temperature dependence of the shape of the conductance plateaus in Fig. 6.13 c is heavily temperature-dependent and has a temperature behavior of the same order as the interference structures, further supporting that resonances and scattering play an important role in our structures and may obscure the observation of clear quantization plateaus.

We proceed with finite bias spectroscopy measurements to further support the confinement nature of the observed steps in conductance and extract the energy separation between successive subbands, i.e. subband spacing ΔE (Fig. 6.14, Fig. 6.15 and Fig. 6.16). Although, the plateaus in conductance do not lie at multiples of $\Delta G = 4e^2/h$, due to the aforementioned reduced transmission coefficient and/or lifting of the four-fold degeneracy (see Section 6.3), half conductance plateaus are certainly visible at high values of bias voltage V_b (Fig. 6.15b,c). The observation of these half-conductance plateaus (see also blue trace in Fig. 6.14c) undoubtedly confirms the confinement nature of the observed plateaus [29–31]. As depicted in Fig. 6.30b, plateaus at intermediate values of conductance are expected to emerge when the bias window eV_b is greater than the subband spacing ΔE ($eV_b > \Delta E$).

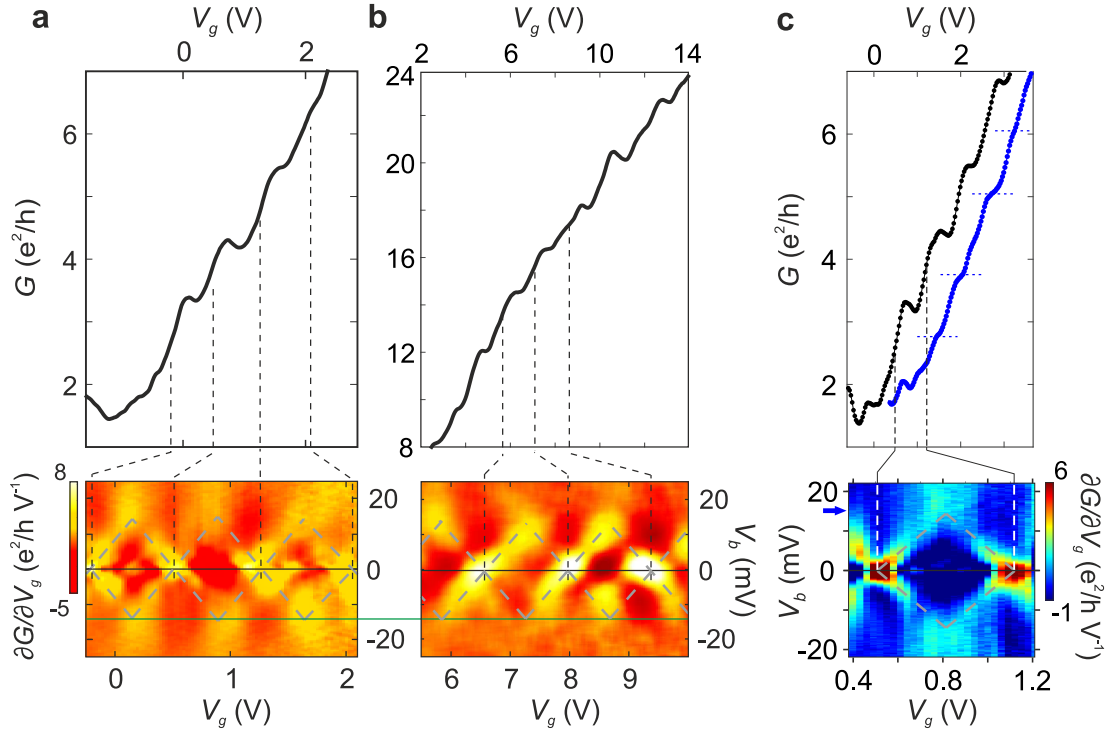


Figure 6.14: **Bias spectroscopy of the 230 nm-wide graphene constriction.** (a) Differential conductance G (upper panel) and differential transconductance $\partial G/\partial V_g$ (colored lower panel) as a function of back gate V_g and bias V_b voltages, measured at $B = 0$ T and $T = 6$ K. The differential conductance G (top panel) is measured at $V_b = 0$ V in the low- carrier density range. The vertical black dashed lines indicate the position of the subbands. The transconductance $\partial G/\partial V_g$ (bottom color-scaled panel) of the data shown in the upper panel, is measured as a function of an applied bias voltage V_b . The kinks are characterized by high values (yellow color) of transconductance. The diamond structures are highlighted by dashed gray diamonds. We extract an average subband spacing $\Delta E \approx 13.5 \pm 2$ meV (green line). (b) Same as panel (a) measured at high carrier densities. (c) Same as panel (a) for a second cool-down of the same device. The blue trace represents the differential conductance G measured at $V_b = 15$ mV (see blue arrow in lower colored panel). The horizontal blue dashed lines highlight the levels of conductance of the intermediate conductance steps, visible for energies above the subband spacing, e.g. $E \approx 15$ meV $>$ ΔE (blue conductance trace).

The Bias voltage spectroscopy measurements yields an estimate of the energy subband ΔE . We analyze six diamonds associated with conductance steps at the low- and high-conductance ranges (see Fig. 6.14). Extraction of the energy scale from the derivative of the differential conductance (color panels) yields $\Delta E \approx 13.5 \pm 2$ meV, leading to $v_F = 2W\Delta E/h \approx (1.5 \pm 0.2) \times 10^6$ m/s. This is a clear signature of a substantially renormalized Fermi velocity v_F in nano-structured graphene, that is in pretty

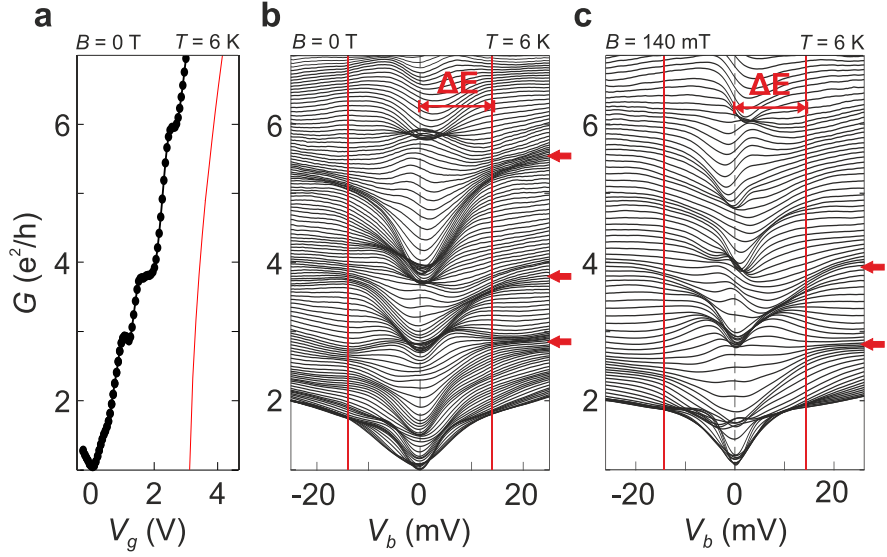


Figure 6.15: **Finite bias spectroscopy of the 230 nm-wide graphene QPC.** (a) Differential conductance G as a function of back-gate voltage, measured at $V_b = 0$ V, $B = 0$ T and $T = 6$ K. The red solid line shows the ballistic model of conductance, fitted at high carrier densities. (b) Differential conductance G as a function of source-drain voltage V_b . The traces are taken at fixed values of back-gate voltage V_g from -0.5 V (lower trace) to 3.0 V (upper trace) in steps of 30 mV. The dense regions correspond to steps in conductance. The intermediate steps in conductance at high bias voltage are marked by red arrows. The subband spacing $\Delta E \approx 13.5 \pm 3$ meV is marked by a vertical red line. (c) Differential conductance g as a function of source-drain voltage V_b measured at $B = 140$ mT. The intermediate kinks at high bias voltage are marked by red arrows. We extract an equal subband spacing as in panel b, $\Delta E \approx 13.5 \pm 3$ meV (vertical red line).

good agreement with previously reported Fermi velocity renormalization values [32, 33]. Variations in the data are due to temperature effects, potential variations and uncertainties in determining the exact extensions of the diamonds. All six extracted diamonds are taken from energy regions where size quantization signatures are clearly visible and reproducible - we are thus confident that the sample is in the quantum point contact regime for all six diamonds. Note that modifications of the gate-lever arm do not affect the bias spectroscopy data, since all energy scales are extracted from the bias voltage axis (V_b) which represents a direct energy-scale. The observed changes in v_F have been previously attributed to e-e interactions due to the assumed lack of disorder in the measured suspended graphene devices [32]. Although our devices show undeniable traces of ballistic transport, i.e. lack of disorder, we can not neglect electron-phonon coupling mechanisms as a source of v_F renormalization. Indeed, the disagreement between the geometrical and the data-extracted width (Fig. 6.6) has been treated throughout this section as a reduced transmission coefficient problem that may be pretty well related with electron-phonon interactions (Fig. 6.10 and Fig. 6.11).

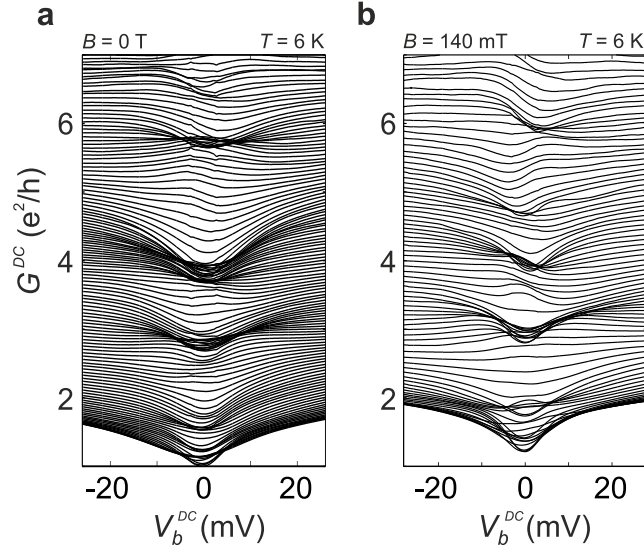


Figure 6.16: **Finite DC bias spectroscopy of the 230 nm-wide graphene QPC.** (a) DC bias spectroscopy of the same device as in Fig. 6.15. (b) Conductance G^{DC} as a function of DC source-drain voltage V_b^{DC} measured at $B = 140$ mT and $T = 6$ K, for the same device as in panel a.

We extract similar values of subband spacing ($\Delta E \approx 13.5 \pm 2$ and 13.5 ± 3 meV) in a second (Fig. 6.14c) and a third (Fig. 6.15) cool-down of the same device. The value of subband spacing is additionally confirmed at finite magnetic field (Fig. 6.15c). We note that, at $B = 140$ mT, the quantized subbands are still caused by geometric confinement rather than magnetic confinement (i.e., the quantum Hall regime).

To discard any spurious contribution from the AC measurement technique, the bias spectroscopy measurements have been repeated in a DC configuration, where the conductance $G = I/V = I_{DC}/V_{DC}$ is obtained from a symmetrically applied source-drain DC bias voltage V_{DC} . Although the resolution of the DC conductance (Fig. 6.16) is not sufficient to reveal the half-conductance plateaus, i.e. not suited for extracting the subband spacing ΔE , the conductance plateaus are still visible at identical values of conductance as in the AC configuration (Fig. 6.15).

In conclusion, we have demonstrated ballistic conductance of confined Dirac fermions in high-mobility graphene quantum point contacts sandwiched by hexagonal boron nitride. Away from the Dirac point, we observe a linear increase in conductance as a function of the Fermi wave-vector with a slope proportional to constriction width. More importantly, superimposed to the evolution of the conductance, we identified traces of conductance quantization. Magnetic field and bias spectroscopy measurements supports the four-fold degenerate nature of the electronic sub-bands as well as the presence of resonances and scattering events along the electronic path. The associated low transmission coefficient ($T < 1$) of the transport modes, disentangle the apparent disagreement between extracted and geometrical width within Landau-Büttiker framework. Moreover, the energy extraction from the bias spectroscopy measurements shows a renormalization of the Fermi velocity v_F , with consistent values (reproducible for successive cool-downs)

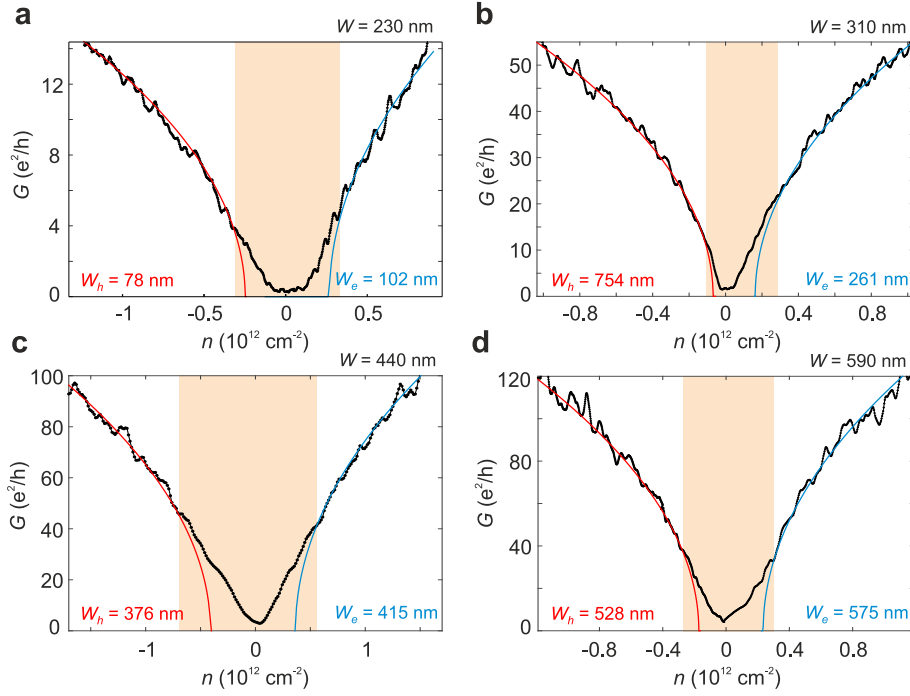


Figure 6.17: **Regime of ballistic conductance.** (a) Back-gate characteristic measured at $B = 0 T$ and $T = 1.5 K$ as a function of charge carrier density n for the 230 nm- (a), 310 nm- (b), 440 nm- (c) and 590 nm-wide (d) graphene QPCs. Shaded orange regions denote deviations from the Landau-Büttiker model $G \propto \sqrt{k_F}$ shown in red. The extracted widths for holes and electrons are marked in blue and red, respectively.

of up to $v_F \approx 1.5 \times 10^6$ m/s.

6.2 Effect of edge localized states in the transport behavior

As pointed out in previous section, the transport characteristic of graphene nano-devices follows a ballistic model of conductance only in the high-energy range. Even if, close to the charge neutrality point, the disagreement between model and data has been already introduced (Section 6.1), we just identified the problem without discussing the origin and implications of these findings. Moreover, although the disagreement between data and model was clearly visible for the 230 nm and the 310 nm devices (Fig. 6.5 and Fig. 6.8), the situation is common among all measured devices (see low energy range of the conductance traces in Fig. 6.6a and in Fig. 6.17). Note that, as introduced in previous chapter (Section 6.1), we will differentiate between width extracted from the conductance measurements and SEM extracted width throughout this section.

The deviation from the ideal Landau Büttiker model $G \propto \sqrt{n}$ (gray shaded region in Fig. 6.8 and orange shaded region in Fig. 6.5, Fig. 6.7 and Fig. 6.17) could have its origin on a non-constant, e.g energy-dependent, transmission coefficient and/or a

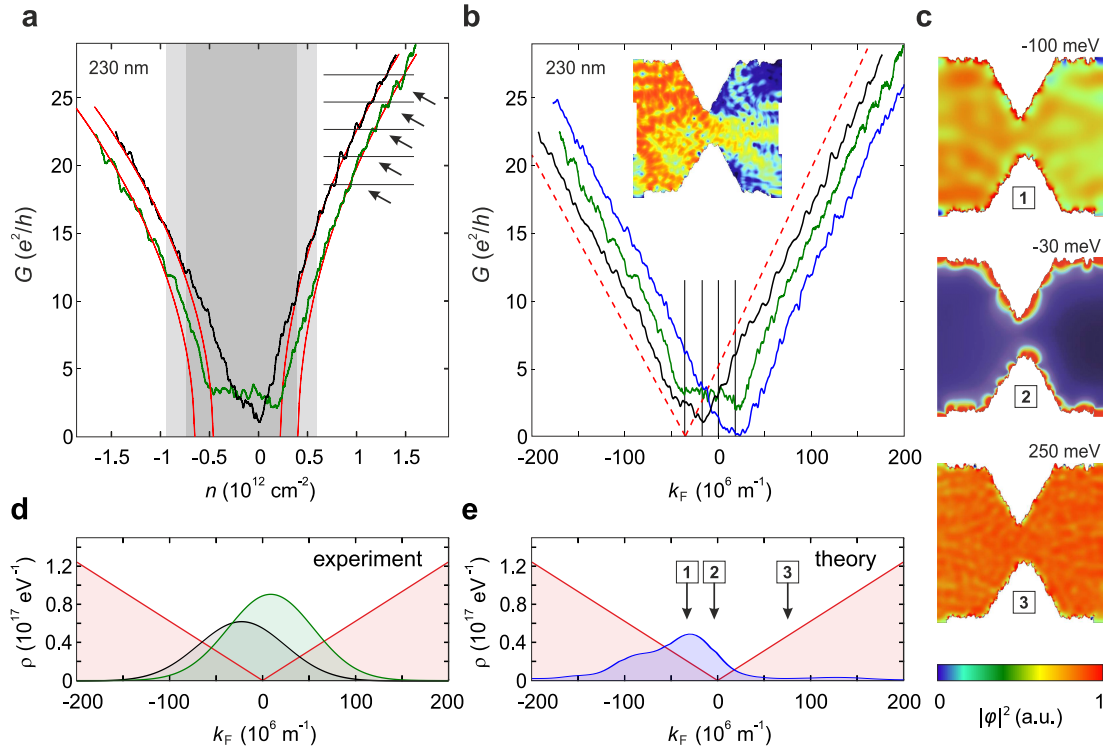


Figure 6.18: **Linear conductance through graphene quantum point contacts.** **a**, Conductance traces of two different cool-downs (black and green curve) of the 230 nm-wide quantum point contact as a function of charge carrier density. For the black (green) cool-downs, shaded gray (light gray) regions denote deviations from the ideal Landauer Büttiker model $G \propto \sqrt{n}$ shown in red. **b**, Experimental conductance trace as a function of k_F after correction for the density of trap states (black and green curves) and theoretical simulations of graphene quantum point contact (blue curve). Theoretical results are rescaled to experimental device size as determined from panel a. Ideal linear transmission is shown in red as guide to the eye. Curves are offset horizontally for clarity. **c**, Local density of states of graphene quantum point contact from tight-binding simulations, at three different energies (-100 meV, -30 meV and 250 meV; see also arrows in panel e). **d**, Graphene density of states extracted from experiment and **e** from simulation. Both experiment and theory find a substantial contribution from trap states around the Dirac point.

variation from the linear density of states of ideal bulk graphene. In Fig. 6.18, we show the conductance as function of n for two different cool-downs of the same graphene QPC of width ~ 230 nm. The gray shaded regions highlight the cool-down dependent low carrier density range of substantial deviation from $G \propto \sqrt{n}$. We note that the square-root relation between the Fermi wave vector k_F and the gate voltage V_g of Eq. 6.3 assumes constant gate coupling and the ideal linear density of states $\rho \propto |E|$ of Dirac fermions. Whereas we can neglect quantum capacitance effects of ideal graphene as

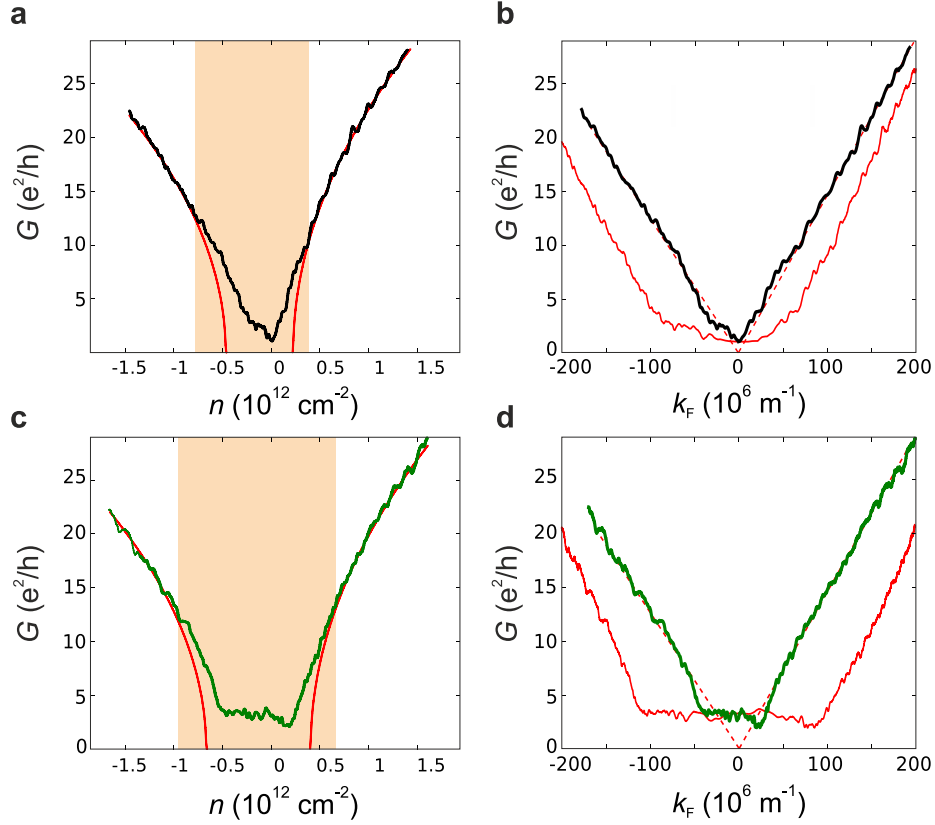


Figure 6.19: **Ballistic transport regime of the 230 nm-wide graphene constrictions.** (a) Low-bias four-terminal differential conductance G as a function of charge carrier density n for the 230 nm-wide graphene QPC. The red solid lines are fits to a simple capacitive coupling model [Eq. 6.3] at high carrier densities for the holes and electrons regime, respectively. Deviations appear in the gray-shaded region around the charge neutrality point. (b) Conductance G of panel (a) as a function of k_F using the ideal, linear density of states (red solid line), or including a finite density of trap states around the Dirac point (black solid line). The expected linear dependence of $G(k_F)$ on k_F is shown by red dashed line. (c) and (d) Same as (a) and (b) for a different cool-down of the same device. After exposing the sample to ambient conditions, the number of charge traps responsible for the flat area around the Dirac point increased significantly.

the origin of the divergences [34], localized states at the rough edges of our device are poorly described by the linear density of states of ideal bulk graphene [35]. While these states do not contribute to transport, they contribute to the charging characteristics of the back gate voltage. Consequently, the total charge carrier density n contains a contribution n_T of charge carriers in trap states, modifying the relation between n and k_F to:

$$\alpha \Delta V_g = n = k_F^2 \pi^{-1} + n_T (\Delta V_g). \quad (6.6)$$

Far away from the Dirac point $k_F^2 \gg \pi n_T$, the contribution due to trap states can well

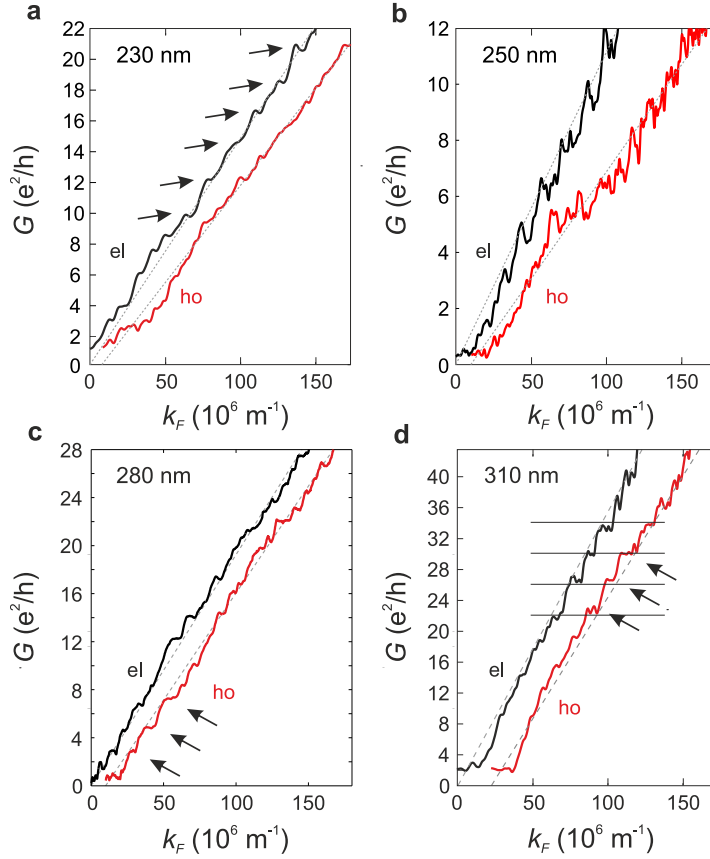


Figure 6.20: **Width-dependence of the kinks.** Four-terminal differential conductance G as a function of momentum k_F , for four different devices of widths 230 nm (a), 250 nm (b), 280 nm (c) and 310 nm (d). The transmission traces are shown in black (red) for electrons (holes) as a function of the rescaled k_F (see main text and Eq. 6.6). The arrows highlight the steps in conductance, with conductance jumps of about $T_0 \times 4e^2/h$. T_0 has been extracted from the overall transmission of the device, see Fig. 6.6. As an example, $T_0 \approx 0.95$ for the 310 nm-wide QPC. The traces are shifted horizontally for clarity.

be neglected, and we recover the expected square root relation. However, close to the Dirac point, $\alpha\Delta V_g$ will approach $n_T\Delta V_g$. To obtain a theoretical estimate of n_T , i.e. the number of trap states, we perform tight-binding simulations of the density of states of rough-edged devices. The calculated local density of states of a rough-edged constriction show strong clustering of trap states at the device edges (see Fig. 6.18c), which energetically lie close to the Dirac point (Fig. 6.18e). Note that, the observed deviation of G (Fig. 6.18a) opens up the opportunity to extract the density of trap states n_T from experimental conductance data (e.g. Fig. 6.18d), and thus a new pathway for device characterization. By using Eq. 6.3 and Eq. 6.6 we linearize $G(k_F)$ down to very low k_F values Fig. 6.18b in order to extract the trap state density n_T as function of energy $E = \pm\hbar v_F k_F$, where v_F is the Fermi velocity, or alternatively, as a function of k_F

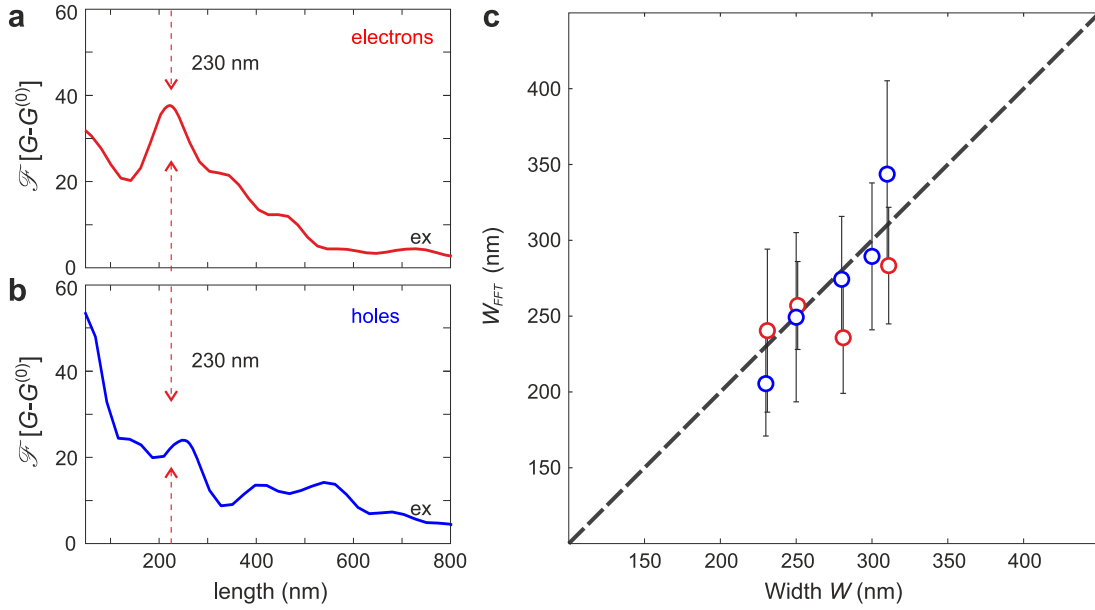


Figure 6.21: **Width dependence of the subband spacing.** (a) Fourier transform of the $G - G^{(0)}$ electron conductance through the 230 nm-wide graphene constriction, both for experiment (red trace, noted "ex") and theory (black trace, noted "th"). The first peak of the Fourier transform (marked by red arrows) is in agreement with the width W of the quantum point contact. (b) Same as (a) for the hole conductance. The size of the first peak is substantially reduced for both experiment and theory due to the presence of localized states that lead to additional scattering. (c) Comparison of the width extracted from the Fourier transform (W_{FFT}) of the conductance traces (see Fig. 6.20) with the geometric width W extracted from SEM images, for five different devices.

(Fig. 6.18d). We model the density of states of the device by a linear contribution from bulk graphene, and a number of localized trap states with a Gaussian distribution in eigenenergy around the Dirac point. In Fig. 6.18d we show $n_T(E)$ for the traces discussed in Fig. 6.18a. We note very good qualitative agreement between simulation and experiment (compare Fig. 6.18e and Fig. 6.18d). Quantitative correspondence would require a detailed analysis of the chemical composition of the device edges.

Interestingly, the trap state density indeed crucially depends on edge chemistry. The only difference between the green and black traces in Fig. 6.18a and Fig. 6.18b is that the device has been exposed to air for several days leading to a wider n -region of substantial deviation (compare light-gray and gray shaded regions in Fig. 6.18a). While the slope is the same between both cool-downs (i.e. extracted width) and the small features on the conductance trace are reproducible (see black arrows pointing to conductance steps visible in the conductance trace of both cool-downs in Fig. 6.18a), the number of trap states (i.e. region of deviation around the CNP) is significantly enhanced (compare also green and blue trace in Fig. 6.19) for the second cool-down. Using the extracted

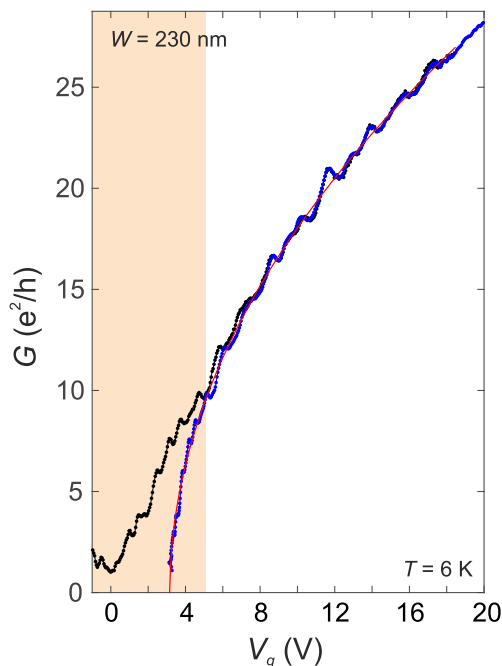


Figure 6.22: **Effect of the rescaling procedure on the back-gate characteristics.** Low-bias four-terminal differential conductance of the 230 nm-wide graphene QPC as a function of back-gate voltage before (black trace) and after (blue trace) applying the rescaling procedure to the charge carriers (Eq. 6.6). The ideal Landauer-Büttiker model of conductance is marked in red.

density of states, we can finally obtain a conductance as a linear function of k_F for the whole energy range (Fig. 6.18b and panels b and d of Fig. 6.19).

With the conductance traces G linearized as a function of k_F (Fig. 6.18b), we stress that our data agrees remarkably well with ballistic transport simulations through the device geometry (inset of Fig. 6.18b) using our modular Green's function approach [25] (see blue trace in Fig. 6.18b): we simulate the 4-probe constriction geometry of width W , taken from SEM images, scaled down by a factor of four to obtain a numerically feasible problem size. To remove residual effects from the ideal leads, we average over different lead widths $W \sim 60-80$ nm. To account for the etched edges in the devices, we include an edge roughness of $\Delta W/W = 20\%$ for the constriction. This comparatively large edge roughness (which is consistent with the systematic reduction of transmission through the constriction when using the average conductance) is probably due to microcracks at the edges of the device. Remarkably, theory and experiment show similar smoothed, irregular modulations (see Fig. 6.18b), instead of sharp size quantization steps [36]. Their origin lies in the perturbation of the quantization steps by the strong scattering at the rough edges of the device (see Section 6.1) and/or by interference effects induced by the geometry (the adiabatic condition will be treated in Section 6.3). We note that calculations with smaller edge disorder show a larger average conductance, yet very similar "kink" structures. Even though our simulation does not include the full

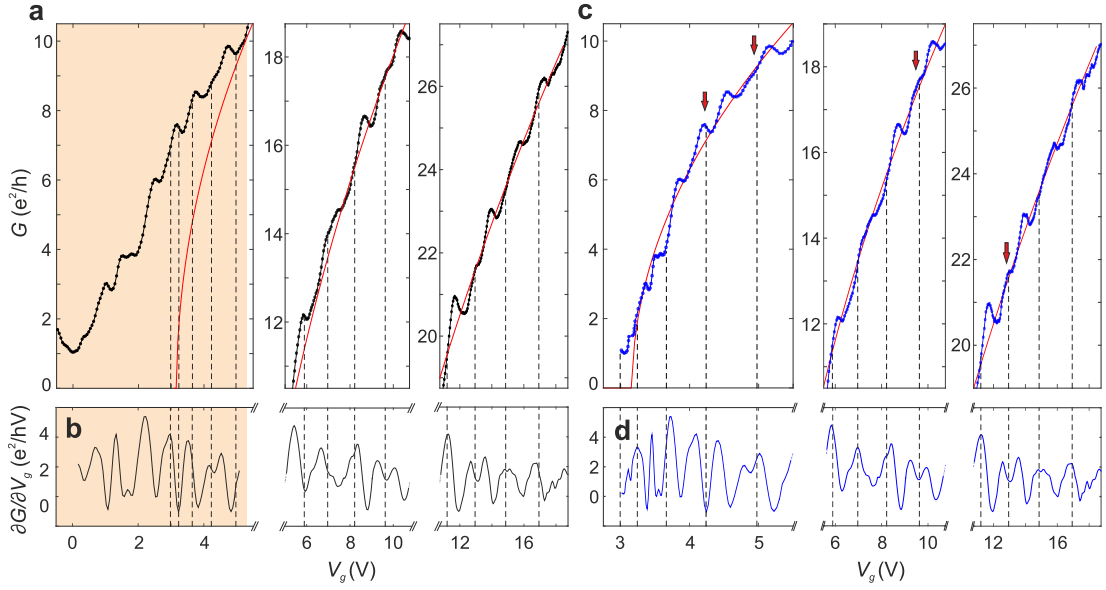


Figure 6.23: **Sub-band position as a proof of the charge carrier rescaling procedure.** (a) Low-bias four-terminal differential conductance G of the 230 nm-wide graphene constriction as a function of back-gate voltage V_g . The theoretical position of the subbands in the V_g -axis is indicated by vertical dashed lines. Close to the Dirac point (leftmost subpanel) measurements deviate from the ideal Landau model $G \propto \sqrt{k_F}$ shown in red (orange-shaded region). (b) Derivative plot $\partial G/\partial V_g$ of the conductance trace shown in panel (a). The correlation between the expected position of the subbands (vertical dashed lines) and measurements holds only at high carrier densities. (c) Same as (a) after rescaling of the charge carriers (Eq. 6.6). The vertical dashed lines indicate the theoretical position of the subbands, as in panel (a). The red arrows indicate the subbands with lifted degeneracy (see Section 6.3). (d) Derivative plot $\partial G/\partial V_g$ of the conductance trace in panel (c).

range of experimental sources of scattering such as bulk disorder, electron-electron, or electron-phonon coupling, the edge-disorder induced scattering alone is strong enough to reduce the visibility of size quantization features. By contrast, both experimental and theoretical investigations of, e.g., semiconducting GaAs heterostructures show very clear, pronounced quantization plateaus [37].

More importantly, once the conductance G is linearized as a function of momentum k_F (see Fig. 6.20), we can alternatively extract the width of the devices by studying the periodicity of the conductance steps as a function of k_F . By subtracting the zeroth-order Fourier component $\propto k_F$ (or $\propto \sqrt{n}$), the superimposed modulations/steps in the conductance $\delta G(k_F) = G - G^{(0)}$ provide direct information on the quantized conductance through the constriction. One key observation is that the Fourier transform of $\delta G(k_F)$ offers an alternative route towards the determination of the constriction width complementary to that from the mean conductance $G^{(0)}$. For example, the pronounced

peak of the first harmonic at 230 nm (red arrows in Fig. 6.21a,b) is consistent with the constriction width W derived from the SEM image. Interestingly, our simulation also correctly reproduces the experimental observation that the peak in the Fourier spectrum of $\delta G(k_F)$ is more pronounced on the electron side than on the hole side (Fig. 6.21a,b).

Performing such a Fourier analysis for several devices (Fig. 6.20) yields much closer agreement with the geometric width W (Fig. 6.21c) as compared with an estimate based only on the zeroth-order Fourier component G^0 (Fig. 6.6c). The analysis of the position of the conductance steps in the energy axis, or equivalently the Fourier spectroscopy of conductance modulations as a function of k_F thus allows to disentangle the reduced transmission due to scattering at the edges ($c_0 W$) from the effective width of the constriction.

As stated in previous Section 6.1, the observed steps in conductance are undeniably associated with conductance quantization. In the following, we will use the position of the individual quantization steps to corroborate the validity of our rescaling procedure (Eq. 6.6). As previously mentioned, the square root relation between back gate voltage and Fermi energy is modified by the presence of edge states (Fig. 6.22). Thus, the energy position of the sub-bands is expected to diverge accordingly.

In a first order approximation, the band structure of a graphene constriction of width W can be described as a collection of sub-bands originating from the quantization of the wave-vector perpendicular to the transport direction,

$$k_{\perp} = \pm |M + \alpha| \pi / W, \quad (6.7)$$

where $M = 0, \pm 1, \pm 2, \dots$ is an integer denoting the sub-band index, and $0 \leq |\alpha| < 0.5$ is a Maslov index related to the boundary conditions at the edges (for simplicity we use $\alpha = 0$, i.e. a zigzag ribbon). Within the energy range where the ballistic model (marked in red in Fig. 6.23) fits the conductance trace, the theoretical position of the subbands (marked by vertical black dashed lines) for a 230 nm-wide graphene constriction ($V_g^M = \pi M^2 / \alpha W^2$) are in excellent agreement with the jumps in conductance (see Fig. 6.23a). The agreement between model and data is also visible in the derivative of the differential conductance $\partial G / \partial V_g$ (Fig. 6.23b). However, at lower energies (shaded orange background in Fig. 6.23a,b), we find no reasonable match between model (Eq. 6.7) and data, although the magnetic evolution, the bias spectroscopy and the temperature dependence measurements presented in Section 6.1 confirmed the confinement nature of the observed jumps in conductance. Only after rescaling of the carrier density based on the effective density of states introduced in Eq. 6.7, we obtain a much more accurate correspondence between data and model, also for the lowest sub-bands (blue trace in Fig. 6.23c,d).

In this section we analyzed the effects of graphene edges and conclude that a straightforward linear density of states model is not directly applicable in ballistic nano-structured graphene devices. Instead, one needs to account for the additional charge carrier trap states that, close to the charge neutrality point, distorts this linear relation.

We determined the density of localized edge states n_T by the linearization of the conductance background and used the presence of quantization signatures (sub-bands

formation) to validate our model, thus offering a unique handle on edge physics in graphene devices.

6.3 Breaking of the four-fold degeneracy in ballistic graphene nano-structures

One of the major interest of graphene is that low-energy carriers are well described as 2D mass-less Dirac fermions. Besides the real-spin degree of freedom, the dispersion relation of graphene is characterized by two equivalent Dirac cones and hence by its four-fold degenerate Dirac bands. Although the breaking of these multiple degrees of freedom, manifested as further Hall plateaus outside the normal integer sequence, have been well studied at high magnetic fields [38], not much is known about the robustness of these symmetry states at zero Tesla. As reported in Section 6.1, the observation of electronic subbands in the transport characteristics of ballistic graphene constrictions opens the door to study, at zero Tesla, the robustness of this four-fold degenerate system.

In this section, we report on the degeneracy lifting of the electronic subbands in graphene 1D systems. The degeneracy of the energy subbands appears to be drastically modified by the amount of trap states at the edges. The effects are visible on the transport characteristics at low temperatures ($T = 2$ to 20 K, see Fig. 6.13) by comparing successive cool-downs of the same device (Fig. 6.25 and Fig. 6.26). As introduced in Section 6.2, the density of trap states n_T can be extracted at low energies by comparing the conductance trace G to the model $\propto \sqrt{n}$. We will show that the trap states density n_T not only influences the charging behavior (Section 6.2), and thus the conductance through the graphene constriction, but also modifies the electronic band structure.

In Section 6.1 we proved the 1D nature of the conductance steps visible in back gate characteristic of several devices (see Section 6.2, specially Fig. 6.20). The reduced transmission probability of the quantized modes was attributed to an uncontrolled scattering of the charge carriers at the rough edges. Thus, the quantized conductance plateaus appear blurred, even at low temperatures ($k_B T \ll \Delta E$, see Fig. 6.13). Here on, we introduce the detailed analysis of the position of the one-dimensional (1D) subbands and its associated transmission coefficient T for two graphene nanoribbons of similar width ($W \approx 230$ nm) but different shapes. The lifting of the four-fold degenerate subbands, visible in the back-gate characteristics of both devices, is confirmed by bias spectroscopy and magnetic field dependent measurements.

The two graphene constrictions discussed in this section have different shapes. The device shown in Fig. 6.24a and b, has a typical quantum point contact QPC geometry, whereas the device appearing in Fig. 6.24d and e shows a rectangular pattern of constant width, i.e a traditional nanoribbon shape. Both devices have been fabricated from the same hBN-graphene-hBN sandwich hetero-structure. Samples are contacted in a four-terminal configuration to avoid contributions from the metal-graphene interface resistance (Fig. 6.24). After rescaling of the trap states as introduced in Section 6.2,

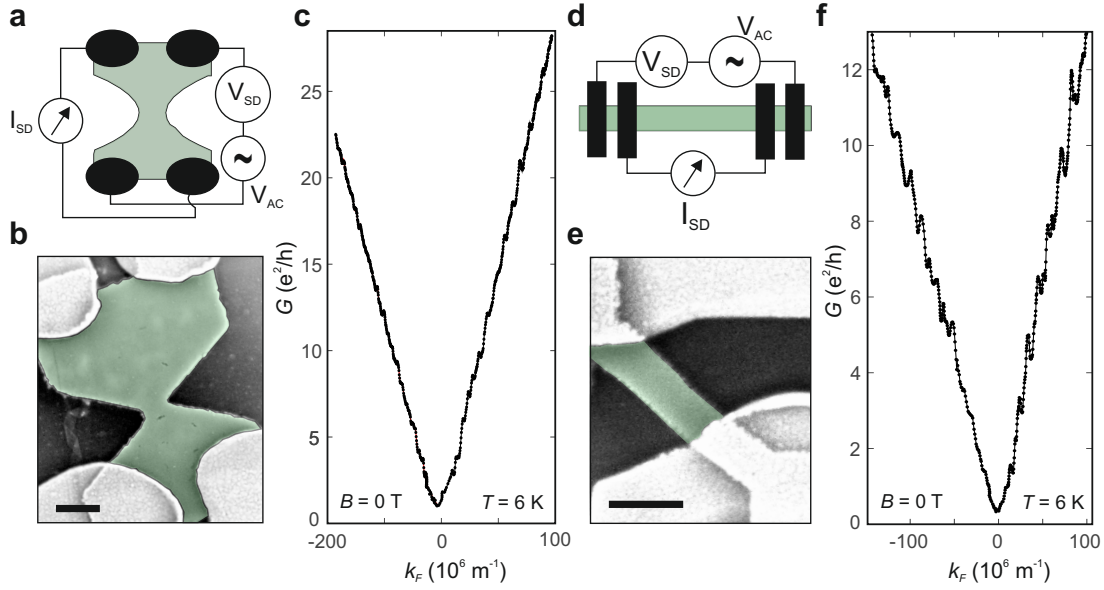


Figure 6.24: **Shape-dependent back-gate characteristics.** **a** and **d**, Schematic representation of the two different device geometries contacted in a four-probe configuration. The differential conductance $G = dI/dV = I_{SD}/V_{SD}$ is measured from an AC excitation voltage $V_{AC} = 250 \mu V$ on both samples. **b** and **e**, False colored Scanning Electron Microscope (SEM) images of the fabricated devices. The Au metal contacts appear in white, the top hBN layer in green and the SiO_2 substrate in gray. The scale bar is 500 nm. **c** and **f**, Low-bias differential conductance G as a function of k_F from the devices shown in panel **b** and **e**, respectively, after rescaling of the charge carriers (see Section 6.2).

the back-gate characteristics of both devices show robust and reproducible traces of confinement quantization equidistant in k_F (see the plateaus-like features in Fig. 6.24c and f). For the QPC device (Fig. 6.24a and b), the same conductance measurements are repeated after a second cool-down (red trace in Fig. 6.25a and b).

In transport measurements, the position of a subband is characterized by a sudden increase in conductance. Experimentally, we extract their position by derivating the conductance G in respect to the back-gate voltage V_g , $\partial G/\partial V_g$ (Fig. 6.23b and d), or alternatively $\partial G/\partial k_F$. The position of the subbands (maximum of $\partial G/\partial k_F$) are marked by black and red vertical dashed lines (for the first and second cool-down, respectively) in Fig. 6.26a, b, and by black and red circles in Fig. 6.26c. The extracted positions are in good agreement with the theoretical expectations (green vertical in Fig. 6.26b) for an ideal zigzag ($\alpha = 0$) graphene nanoribbon of the same with $W = 230$ nm (Eq. 6.7).

Surprisingly, besides the equidistant four-fold degenerate subbands (Fig. 6.10 and Fig. 6.11), we observe the presence of splitted subbands, marked by black arrows in Fig. 6.26a,b, for the conductance trace of the first cool-down (black trace). This degeneracy lifting phenomena is directly visible in the back-gate characteristic by the formation of half conductance plateaus (black arrows in (Fig. 6.26a and b). The re-

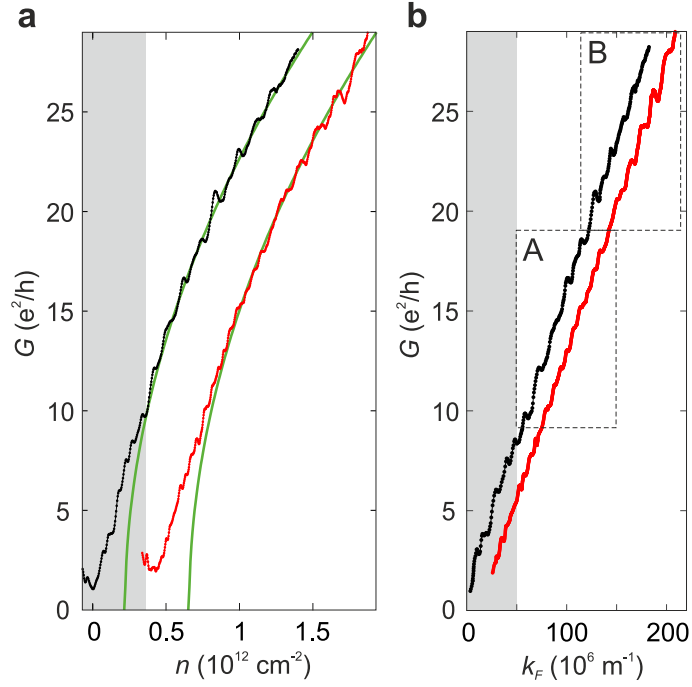


Figure 6.25: **Rescaling of the charge carriers and cool-down dependence.** (a) Conductance traces for two different cool-downs (black and red curves) of the QPC device shown in Fig. 6.24a and b, as a function of charge carrier density. For the first cool-down (black trace), the shaded gray region denote deviations from the ideal Landauer Büttiker model $G \propto \sqrt{n}$ shown in green. The second cool-down curve (red trace) is offset horizontally for clarity. (b) Experimental conductance traces shown in panel represented as a function of k_F , after rescaling by the trap states density n_T . The dashed regions A and B are analyzed in Fig. 6.26.

sulting two-fold degenerate subbands (empty circles in Fig. 6.26c) have therefore an associated conductance increase ΔG of roughly half the value of the original four-fold subbands (compare black filled circles with empty black ones in Fig. 6.26c). Moreover, the analysis of the second cool-down (red trace in Fig. 6.26), indicates the complete lifting of most of the 1D subbands (empty circles in Fig. 6.26c). The same situation is observed for the ribbon-shaped device (Fig. 6.24d-f), with hints of conductance plateaus (black arrows in Fig. 6.27) developing at the position of a theoretically expected subband (compare the position of the subbands marked by a black arrow, with the dashed red lines in Fig. 6.27a).

The splitting of the subbands can be associated to the local crystallographic orientation of the edges. To first a order approximation, the 1D energy subbands have each the following dispersion relation:

$$E_M(k_{\parallel}) = \pm \hbar v_F \sqrt{k_{\parallel}^2 + k_{\perp}^2} = \pm \hbar v_F \sqrt{k_{\parallel}^2 + (M + \alpha)^2 \pi^2 / W^2}, \quad (6.8)$$

as introduced previously (Eq. 6.7). For values $\alpha \neq 0$, every four-fold degenerate subband

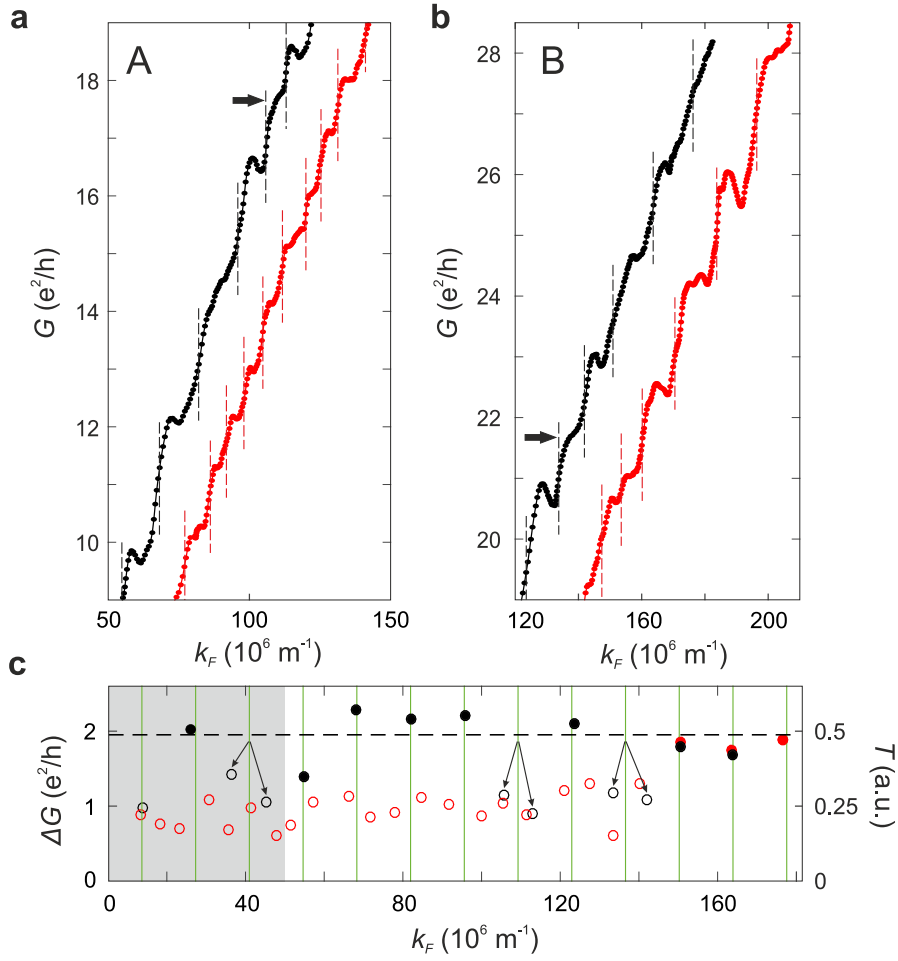


Figure 6.26: **Degeneracy lifting of the sub-bands.** (a) and (b) Conductance traces as a function of k_F inside the A and B dashed regions of Fig. 6.25a. The black arrows indicate the degeneracy broken subbands of the first cool-down (black trace). The position of the subbands in the k_F -axis are characterized by sudden increases of conductance (local maxima of $\partial G/\partial k_F$) and are indicated by horizontal dashed lines. (c) The colored circles mark the position of the subbands in the k_F axis (vertical dashed lines in panel a) with its associated step in conductance ΔG . The theoretical position of the subbands in the k_F -axis is indicated by vertical green lines. The filled and empty circles indicate the four-fold and two-fold degenerate subbands, respectively. The right Y-axis indicate the associated transmission coefficient T .

splits into two two-fold degenerate subbands. Fig. 6.28 illustrates the splitting process for an $\alpha = 0.15$. The conductance can be then expressed as:

$$G = 2 \frac{e^2}{h} M = 2 \frac{e^2}{h} \text{Int}\left(\frac{W k_F}{\pi}\right) \approx 2 \frac{e^2}{h} \frac{W k_{\perp}}{\pi}, \quad (6.9)$$

where $\text{Int}(x)$ represents the integer that is just smaller than x , k_F is the momentum

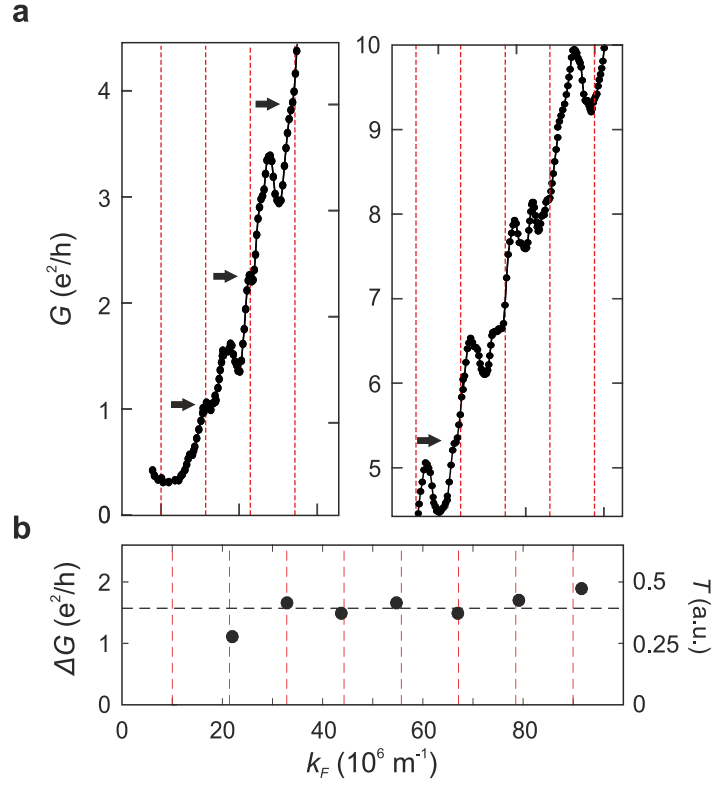


Figure 6.27: **Observation of degeneracy-broken subbands.** (a) Conductance G as a function of k_F for the 230 nm-wide graphene ribbon (Fig. 6.24e). The black arrows indicate the degeneracy-broken subbands. The theoretical position of the subbands (refer to Eq. 6.7) in V_g -axis is indicated by vertical dashed red lines, in panel a and b. (b) The black circles indicate the position in k_F of the energy subbands (local maximum of $\partial G/\partial k_F$). Their associated step in conductance ΔG is indicated in left-axis. The average conductance step ΔG_{avg} is marked by a horizontal black dashed line. The right Y-axis indicate the associated transmission coefficient T .

at the Fermi energy and k_{\perp} refer to the allowed transverse modes. The factor 2 corresponds to the spin degree of freedom. A visual representation of the subbands lifting process on the transport characteristics is shown in Fig. 6.28c, for $\alpha = 0.15$.

To support the confinement nature of the half conductance plateaus (refer to Fig. 6.14, Fig. 6.15 and Fig. 6.16) and thus prove the degeneracy lifting process, we study the transport characteristics as a function of bias voltage V_b . With finite bias spectroscopy measurements we can directly extract the subband spacing energy ΔE as well as the associated degeneracy-breaking energies $\Delta E'$ and $\Delta E''$ (Fig. 6.29 and Fig. 6.30). The differential conductance G of a third cool-down of the graphene QPC device as a function of bias and back-gate voltages (Fig. 6.29) shows an unexpected sequence of conductance plateaus at values $G \approx 1.7, 2.2, 3.1, 4.4$ and $5.6 e^2/h$. As already mentioned during Section 6.1, the confinement features are extremely cool-down dependent mostly for the

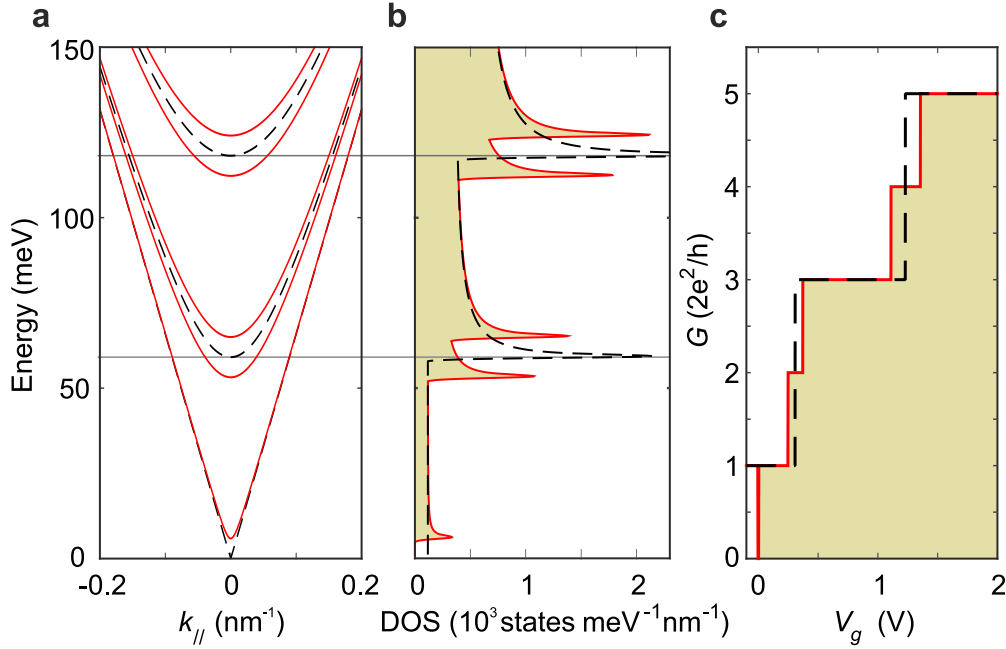


Figure 6.28: **Degeneracy lifting of the energy subbands.** (a) Calculated energy dispersion relation of a zigzag graphene ribbon ($\alpha=0$, black dashed lines) and a randomly oriented ribbon ($\alpha=0.15$, red solid lines). (b) Resulting density of states of the zigzag and randomly oriented graphene ribbons shown in panel a. Temperature is set to $T=3$ K. (c) Associated conductance G as a function of back-gate voltage V_g for the zigzag (black dashed line) and randomly oriented ribbon (red solid line), at $T=0$ K.

lower modes, i.e for energies close to the charge neutrality point (refer to Fig. 6.9), due to resonances and/or localization of the electron wave-functions. Indeed, the conductance plateaus (Fig. 6.29) do not lie at multiples of $G_0=4e^2/h$, since the transmission coefficient of the modes is heavily reduced ($T \approx 0.5$). Nonetheless, the trademark of conductance quantization is still recognized by the presence of intermediate conductance plateaus at higher V_b (blue trace in Fig. 6.29c). The lifting of the 1D subbands is clearly visible in the conductance as a function of V_b and in the line cut at $V_b = 0$ (red arrows in Fig. 6.29a and b, respectively). Even if the levels of conductance are not comparable with the values from the first and second cool-downs (Fig. 6.26), the half-conductance plateaus still emerge at the middle of two consecutive four-fold degenerate plateaus. The position of the subbands are extracted via $\partial G/\partial V_g$ and we distinguish between degenerate and lifted subbands by solid and dashed lines, respectively (Fig. 6.29b).

The differential transconductance $\partial G/\partial V_g$ of the data in Fig. 6.29a, allows the direct read-out of the energy bands. Panel d of Fig. 6.29 displays a diamond-like structure (highlighted by dashed white lines) that define the regions of high transconductance (white/yellow color) separating the zero- and high-bias plateaus, marked G_g and G_{il}/G_{iu} in Fig. 6.28c and Fig. 6.29a, respectively. Note that G_{il} and G_{iu} represent the value of conductance of the lower (G_{il}) and upper (G_{iu}) intermediate plateaus. The

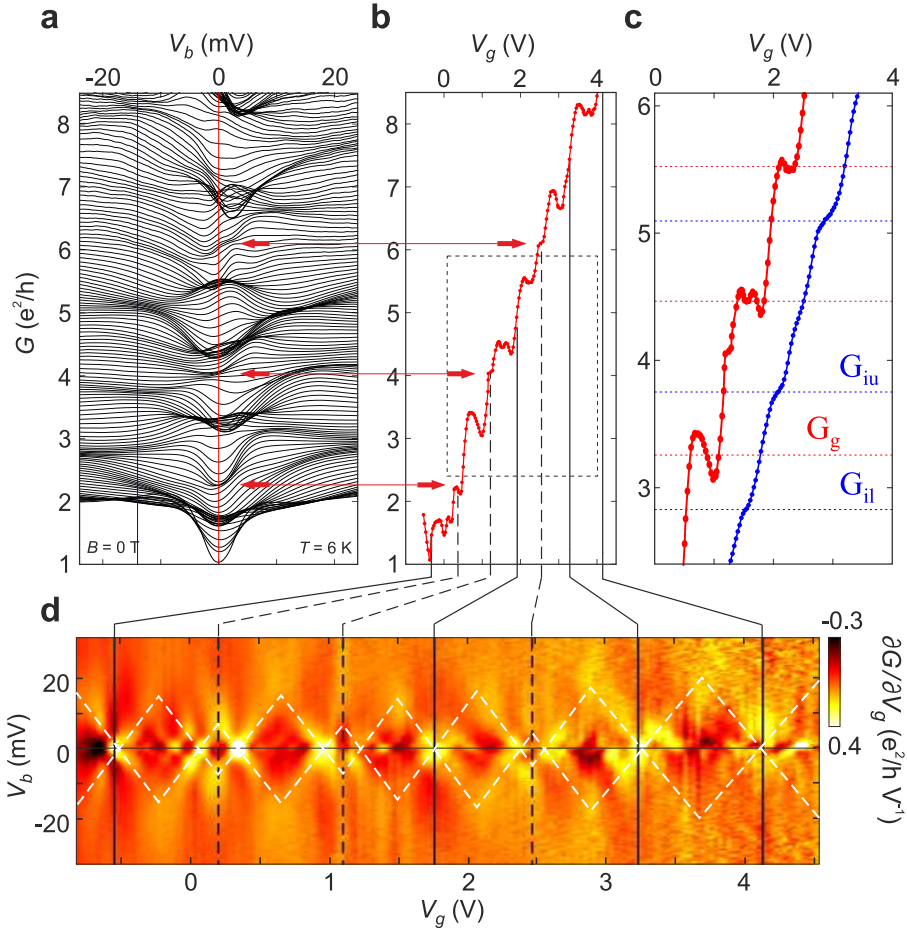


Figure 6.29: **Bias voltage spectroscopy of the degeneracy lifting.** (a) Conductance G as a function of source-drain voltage V_b measured at $B=0$ T and $T=6$ K. The traces are taken at fixed values of back-gate voltage V_g from -0.5 V to 4.6 V in steps of 30 mV. The red arrows (also shown in panel b) indicate the degeneracy-broken plateaus. (b) Back-gate trace at $V_b=0$ V. The vertical black solid (dashed) lines indicate the position in back-gate voltage of the degenerate (degeneracy-broken) sub-bands. (c) Close-up in the dashed box of panel b (red trace) and back-gate trace at $V_b=-14$ mV (blue trace). The dashed red and blue horizontal lines indicate the conductance value of the plateaus at $V_b=0$ V and -14 mV, respectively. (d) Transconductance $\partial G / \partial V_g$ of the data shown in panel a. The position of the sub-bands at zero bias voltage are marked by solid and dashed lines for four-fold and two-fold degenerate sub-bands, respectively.

high transconductance boundaries arise when the subbands align with the source-drain voltage V_b (Fig. 6.30b). Fig. 6.30 shows a high-resolution bias spectroscopy measurements of the two regions in Fig. 6.29d where the lifting of the subbands is visible. We extract the energies from the intersection of high transconductance lines (marked by * in Fig. 6.30a). In our case though, due to lifting of the subbands, we observe the

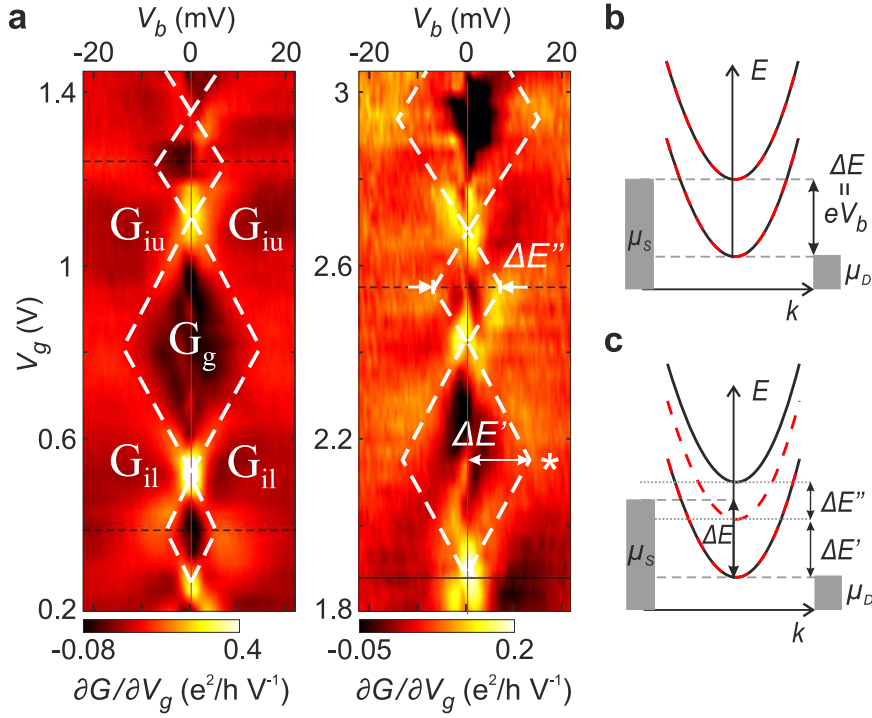


Figure 6.30: **Lifting of the four-fold degeneracy.** (a) Two-dimensional color plots of the differential transconductance $\partial G/\partial V_g$ highlighting the broken-degeneracy process. The intersection (indicated by *) of the high transconductance lines (marked by dashed white lines) allows the extraction of the subband spacing $\Delta E = \Delta E' + \Delta E''/2$. The position in V_g of the degenerate and broken subbands are marked by solid and dashed black lines, respectively. The conductance values G_0 , G_{IU} and G_{IL} are specified in Fig. 6.29c. (b) and (c) Schematic representations of the bias voltage spectroscopy when the source-drain electrochemical potential window ($\Delta E = \mu_S - \mu_D = eV_b$) equals the subband spacing (ΔE) for the degenerate (panel b) and the degeneracy-lifted situations (panel c).

development of a smaller diamond-like structure of energy $\Delta E''$ where otherwise high transconductance line was expected. That is, all solid black lines in Fig. 6.29b,d and Fig. 6.30a represent the position of four-fold degenerate subband and correspond to the intersect of adjoining diamonds. The dashed black lines denote two-fold degenerate subbands and intersect in the middle of small diamonds of energy $\Delta E''$. The subbands spacing can be then calculated as $\Delta E = \Delta E' + \Delta E''/2 \approx 13 \text{ meV} + 3 \text{ meV} \approx 16 \text{ meV}$. The schematic representation of the degenerate and lifted cases is shown in Fig. 6.30b and c, respectively.

The confinement nature of the conductance plateaus have been confirmed in Section 6.1 by following its transition from size quantization at zero Tesla to Landau quantization at high magnetic fields. The degeneracy lifting of the subbands is also expected to evolve as a function of magnetic field in order to recover the four-fold degeneracy

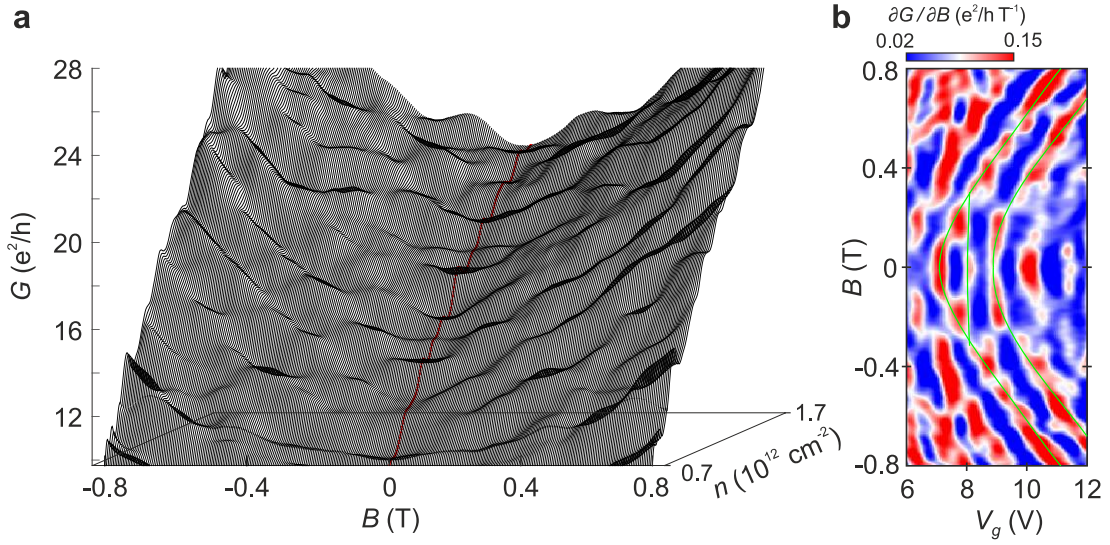


Figure 6.31: **Magnetic-field evolution of the size quantization at $T=6 \text{ K}$.** (a) Differential conductance G as a function of magnetic field B and charge carrier density n of the 230 nm-wide graphene QPC device. Conductance steps of reduced $\sim 1 e^2/h$ units of conductance are visible at $G \approx 18 e^2/h$ and $22 e^2/h$. (b) Derivative of the differential conductance $\partial G / \partial B$ as a function of magnetic field B and back gate voltage V_g , for the same device as in panel a.

inherent of bulk graphene [3, 4]. Fig. 6.31 shows the evolution of the sub-bands as a function of B-field. It is indeed expected to recover the four-fold degeneracy before entering the quantum Hall Effect QHE regime since the Hall plateaus follow the half-integer quantization sequence ($\nu = 2, 6, 10 e^2/h$) at relative values of magnetic field $B < 4T$ (see Fig. 6.10) The conductance increase ΔG associated to the sub-bands is generally $\sim 2 e^2/h$, in agreement with a four-fold degenerate sub-band with a transmission coefficient of $T \approx 0.5$. Moreover, conductance steps with a smaller conductance increase $\Delta G \approx 1 e^2/h$, are also visible at $G \approx 18 e^2/h$ and $22 e^2/h$. These lifted sub-bands merge with another plateau at $\sim 0.15 T$, forming four-fold degenerate sub-bands as expected at high magnetic fields.

Throughout this section, we introduce the lifting of the degeneracy in graphene nano-constrictions, highlighting the unexpected robustness of the valley degeneracy in graphene nano-structures. Findings are supported by bias and B-field dependent measurements. Even though the breaking of the four-fold degeneracy can be theoretically associated with the valley-degeneracy lifting due to a specific crystallographic orientation of the edges, no conclusive assumptions can be deduced to explain the observed mode-dependency of the lifting process.

References

1. Young, A. *et al.* Quantum interference and Klein tunnelling in graphene heterojunctions. *Nature Physics* **5**, 222 (2009).
2. Tworzydło, J. *et al.* Sub-Poissonian Shot Noise in Graphene. *Phys. Rev. Lett.* **96**, 246802 (2006).
3. Novoselov, K. S. *et al.* Two-dimensional gas of massless Dirac fermions in graphene. *Nature* **438**, 197–200 (2005).
4. Zhang, Y. *et al.* Experimental observation of the quantum Hall effect and Berry's phase in graphene. *Nature* **438**, 201–204 (2005).
5. Du, X. *et al.* Fractional quantum Hall effect and insulating phase of Dirac electrons in graphene. *Nature* **462**, 192–195 (2009).
6. Bolotin, K. I. *et al.* Observation of the fractional quantum Hall effect in graphene. *Nature* **462**, 196–199 (2009).
7. Novoselov, K. S. *et al.* Electric Field Effect in Atomically Thin Carbon Films. *Science* **306**, 666–669 (2004).
8. Dean, C. R. *et al.* Boron nitride substrates for high-quality graphene electronics. *Nature Nanotechnology* **5**, 722–722 (2010).
9. Wang, L. *et al.* One-Dimensional Electrical Contact to a Two-Dimensional Material. *Science* **342**, 614–617 (2013).
10. Lin, Y. *et al.* Electrical observation of subband formation in graphene nanoribbons. *Phys. Rev. B* **78**, 161409 (2008).
11. Tombros, N. *et al.* Quantized conductance of a suspended graphene nanoconstriction. *Nature Physics* **7**, 697–700 (2011).
12. Wang, X. *et al.* Graphene nanoribbons with smooth edges behave as quantum wires. *Nature Nanotechnology* **6**, 563–567 (2011).
13. Wang, L. *et al.* One-Dimensional Electrical Contact to a Two-Dimensional Material. *Science* **342**, 614–617 (2013).
14. Terrés, B. *et al.* Disorder induced Coulomb gaps in graphene constrictions with different aspect ratios. *Appl. Phys. Lett.* **98**, 032109 (2011).
15. Masubuchi, S. *et al.* Boundary Scattering in Ballistic Graphene. *Phys. Rev. Lett.* **109**, 036601 (2012).
16. Giesbers, A. J. M. *et al.* Scaling of the quantum Hall plateau-plateau transition in graphene. *Phys. Rev. B* **80**, 241411 (2009).
17. Yazyev, O. *et al.* Magnetic Correlations at Graphene Edges, Basis for Novel Spintronics Devices. *Phys. Rev. Lett.* **100**, 047209 (2008).
18. Rycerz, A. *et al.* Valley filter and valley valve in graphene. *Nature Physics* **3**, 172–175 (2007).
19. Wang, L. *et al.* Josephson effect in ballistic graphene. *Phys. Rev. B* **74**, 041401(R) (2006).

20. Yang, L. *et al.* Magnetic Edge-State Excitons in Zigzag Graphene Nanoribbons. *Phys. Rev. Lett.* **101**, 186401 (2008).
21. Yang, L. *et al.* Tunable symmetry breaking and helical edge transport in a graphene quantum spin Hall state. *Nature* **505**, 528 (2014).
22. Van Ostaay, J. *et al.* Dirac boundary condition at the reconstructed zigzag edge of graphene. *Phys. Rev. B* **84**, 195434 (2011).
23. Novoselov, K. S. *et al.* Room-Temperature Quantum Hall Effect in Graphene. *Science*, **315**, 5817, 1379 (2007).
24. Vera-Marun, I. J. *et al.* Quantum Hall transport as a probe of capacitance profile at graphene edges. *Appl. Phys. Lett.* **102**, 013106 (2013).
25. Libisch, F. *et al.* Coherent transport through graphene nanoribbons in the presence of edge disorder. *New Journal of Physics* **14**, 123006 (2012).
26. Nixon, J. *et al.* Conductance of quantum point contacts calculated using realistic potentials. *Superlattices and Microstructures* **9**, 2 (1991).
27. Rohlfing, M. *et al.* Quasiparticle band-structure calculations for C, Si, Ge, GaAs, and SiC using Gaussian-orbital basis sets. *Phys. Rev. B* **48**, 17791 (1993).
28. Van Wees, B. *et al.* Quantized conductance of point contacts in a two-dimensional electron gas. *Phys. Rev. Lett.* **60**, 848 (1988).
29. Kouwenhoven, L. *et al.* Nonlinear conductance of quantum point contacts. *Phys. Rev. B* **39**, 8040 (1989).
30. Patel, N. *et al.* Properties of a ballistic quasi-one-dimensional constriction in a parallel high magnetic field. *Phys. Rev. B* **44**, 10973 (1991).
31. Glazman, L. *et al.* Reflectionless quantum transport and fundamental ballistic-resistance steps in microscopic constrictions. *JETP Lett.* **48**, 4, 238 (1988).
32. Elias, D. C. *et al.* Dirac cones reshaped by interaction effects in suspended graphene. *Nature Physics* **8**, 172 (2012).
33. Hwang, C. *et al.* Fermi velocity engineering in graphene by substrate modification. *Scientific reports* **2**, 590 (2012).
34. Reiter, R. *et al.* Negative quantum capacitance in graphene nanoribbons with lateral gates. *Phys. Rev. B* **89**, 115406 (2014).
35. Bischoff, D. *et al.* Characterizing wave functions in graphene nanodevices: Electronic transport through ultrashort graphene constrictions on a boron nitride substrate. *Phys. Rev. B* **90**, 115405 (2014).
36. Mucciolo, E. R. *et al.* Conductance quantization and transport gaps in disordered graphene nanoribbons. *Phys. Rev. B* **79**, 075407 (2009).
37. Van Wees, B. J. *et al.* Quantized conductance of point contacts in a two-dimensional electron gas. *Phys. Rev. Lett.* **60**, 848 (1988).
38. Zhang, Y. *et al.* Landau-Level Splitting in Graphene in High Magnetic Fields. *Phys. Rev. Lett.* **96**, 136806 (2006).

7.1 Conclusion

This thesis presents a detailed study on the nature of disorder in graphene nanostructures, in order to uncover its mechanism and minimize its impact in the electronic transport properties. Section 4.1 introduced the electrical transport behavior of graphene constrictions to highlight the limitations induced by disorder. Transport has been shown to be mainly dominated by disorder rather than reflecting the density of states of a quasi-1D system. Section 4.2.1 focuses on characterizing bulk disorder via magnetically confined quantum dots arising within the bulk. This section revealed the strong contribution of electron-phonon interactions in the graphene- SiO_2 system.

Section 4.3.1 showed the impact of a random crystallographic orientation of the edges, i.e. edge disorder, by a Raman spectroscopy study of pristine graphene nanoribbons with highly oriented edges (Section 4.3.1). Results brought experimental evidences of crystal disorientation at the edges of traditional plasma etched ribbons. Regarding its electrical transport fingerprint, edge disorder and their associated localized states have been analyzed in detail in Section 4.4, where we introduced a method to minimize the contribution of the edge disorder. Results represent a valid experimental turnaround for realistic graphene nanodevices, that are applicable to any 2D-material.

In the meanwhile, in the quest for high-mobility graphene we follow the trend of encapsulating graphene in between hBN layers in order to minimize bulk disorder in our graphene nanostructures. Our fabrication method is based on a dry transfer technique allowing for high quality graphene devices (Section 5.1). First Hall bar devices show the broken symmetry of the Landau states under finite magnetic fields. For fields $B > 1T$ both the longitudinal and transversal conductances diverge as a function of magnetic field, which indicates the opening of a field induced gap enhanced by exchange interactions (Section 5.1).

This newly developed dry transfer method in combination with a four terminal configuration was used to investigate 1D ballistic phenomena in graphene quantum point

contacts (Section 6.1). Our devices show for the very first time robust and reproducible four-fold degenerate quantized conductance steps in graphene. Results point to valley degeneracy conservation in graphene 1D systems, which is of major importance for electronic application since it doubles the level of conductance associated to a single state. Further studies have revealed important information about the way in which disorder couples to the special symmetries of electrons in graphene, such as their ‘valley’ degree of freedom (also known as pseudospin) (Section 6.3).

7.2 Outlook

Having a deep understanding on the sources and mechanism of disorder is essential to work towards high quality graphene devices. This thesis focused mainly on the experimental turnarounds to solve the associated limitations to the disorder. The electrostatic gating proposed to overcome the edge-induced disorder and the dry-transfer technique to fabricate hBN-graphene-hBN devices demonstrated tangible advances in transport measurements. With the observation of ballistic and interference phenomena in hBN-graphene-hBN devices, an interesting field of experimental research is at reach. Transport experiments that rely on the principles of electron optics such as Veselago lenses, Klein-tunneling transistors or ballistic rectifiers opens new perspectives in both fundamental and industrial research, that go way beyond the current graphene fields of application.

8.1 Magnetically confined QDs

Additional to the Diamonds plots presented in Section 4.2.1, we measure the localized states of the first Landau level LL_{+1} shown in Fig. 4.14f. The four consecutive resonances start at $B \approx 3.5T$ and are visible up to $B \approx 9T$ (Fig. 8.2). The Diamond plot measurements show the characteristic diamond pattern (inset A, B, C and D in Fig. 8.2). All measurements, the magnetic evolution of the resonances and the corresponding diamond plots have been measured at $T = 2K$. We extract the charging energies directly from the extension of the diamonds in the V_{bias} axis (Fig. 8.2). We do not observe marked differences between the charging energies E_c evaluated at different

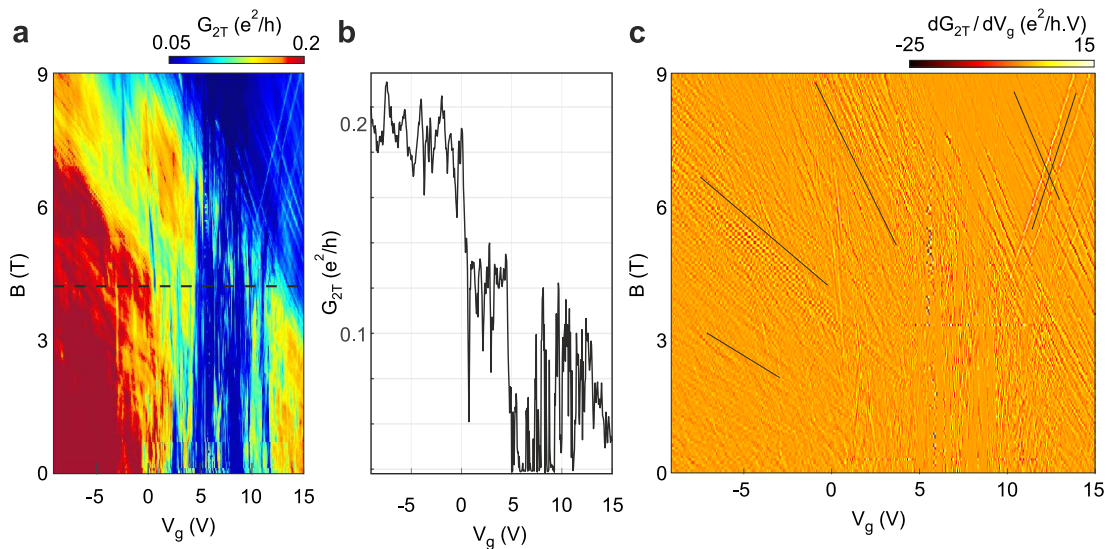


Figure 8.1: **Quantum Hall effect phase.** Magnetic evolution of the four charging events associated to a LL_{+1} . Bias spectroscopy measurements have been taken at $B = 5.6, 5, 4.6$ and $4.2T$, noted A, B, C and D, respectively. All measurements have been recorded at $T = 2K$.

$B(T)$	$\Delta_1(meV)$	$\Delta_2(meV)$	$\Delta_3(meV)$	$\Delta_4(meV)$
5.6	4.7	4.0	4.8	5.0
5	5.1	5.9	5.0	5.5
4.6	6.2	5.0	5.7	6.4
4.2	11.6	12.0	12.5	14.2

Table 8.1: Values of charging energy E_c as a function of B-field, extracted from the diamonds shown in Fig. 8.2. The magnetic field does not seem to modify the dimensions of the quantum dot, in agreement with Fig. 4.16.

values of magnetic field.

8.2 Temperature dependence of symmetry broken states.

In this appendix we show the temperature dependence of the R_{xx} minimum at $\nu = +3, +7, \text{ and } +11$. The Landau level quantization at that filling factors is not as well

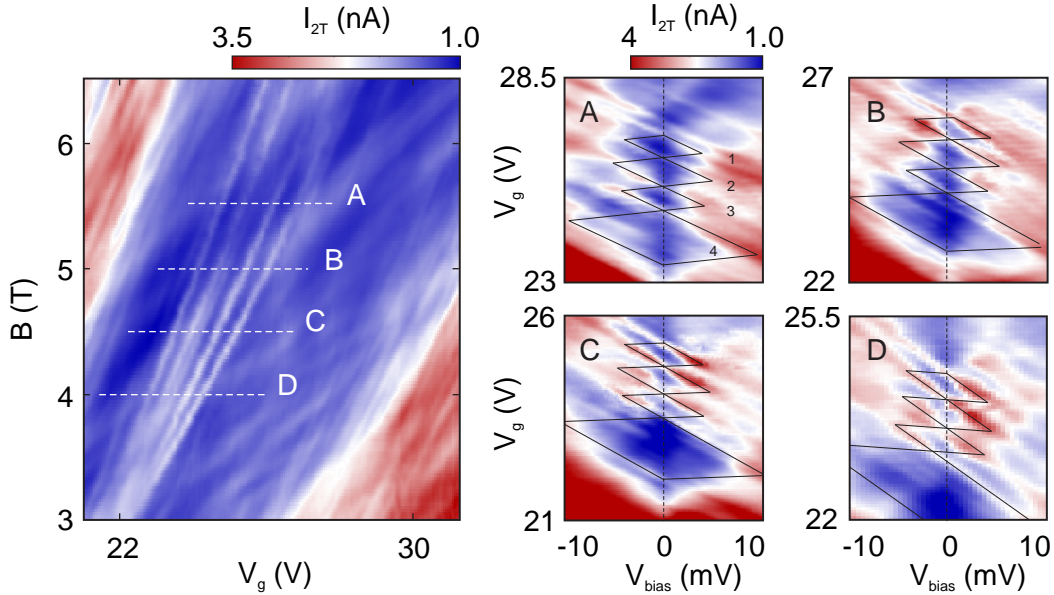


Figure 8.2: **Charging energies of magnetic QDs.** Magnetic evolution of the four charging events associated to a LL_{+1} . Bias spectroscopy measurements have been taken at $B = 5.6, 5, 4.6$ and $4.2T$, noted A, B, C and D, respectively. All measurements have been recorded at $T = 2K$.

resolved as for $\nu = 0, \pm 1, +8$, and $+12$ (Fig. 5.6). Nevertheless, we were able to extract their evolution as a function of temperature (Fig. 8.4).

The fact that the conductance plateaus at $\sigma_{xy} = +3, +7$, and $+11e^2/h$, and their associated minimum in σ_{xx} , are not so well develop (Fig. 5.5), may be linked to disorder. As introduced in Section 5.1 the lifting of the four-fold degenerate Landau levels is supposedly mediated by electron-electron interactions [1, 2]. It is then expected that small perturbations may disturb the fine interactions between charge carriers. In fact, the observation of symmetry broken states has been traditionally related to the quality of graphene samples [3]. It could be then the case that disorder around the energy ranges $E_{\nu=+3}$, $E_{\nu=+7}$ and $E_{\nu=+11}$ are stronger, thus hindering the observation of clear broken symmetry states. The results issued from Fig. 8.4 are also included in Tab. 5.1.

Fig. 8.5 shows the extracted localization lengths for the filling factors ν . We do not observe any pattern of ξ on the magnetic evolution. Moreover, although ξ denotes the typical extension of the electron wave-function and it is usually dependent on ξ , we

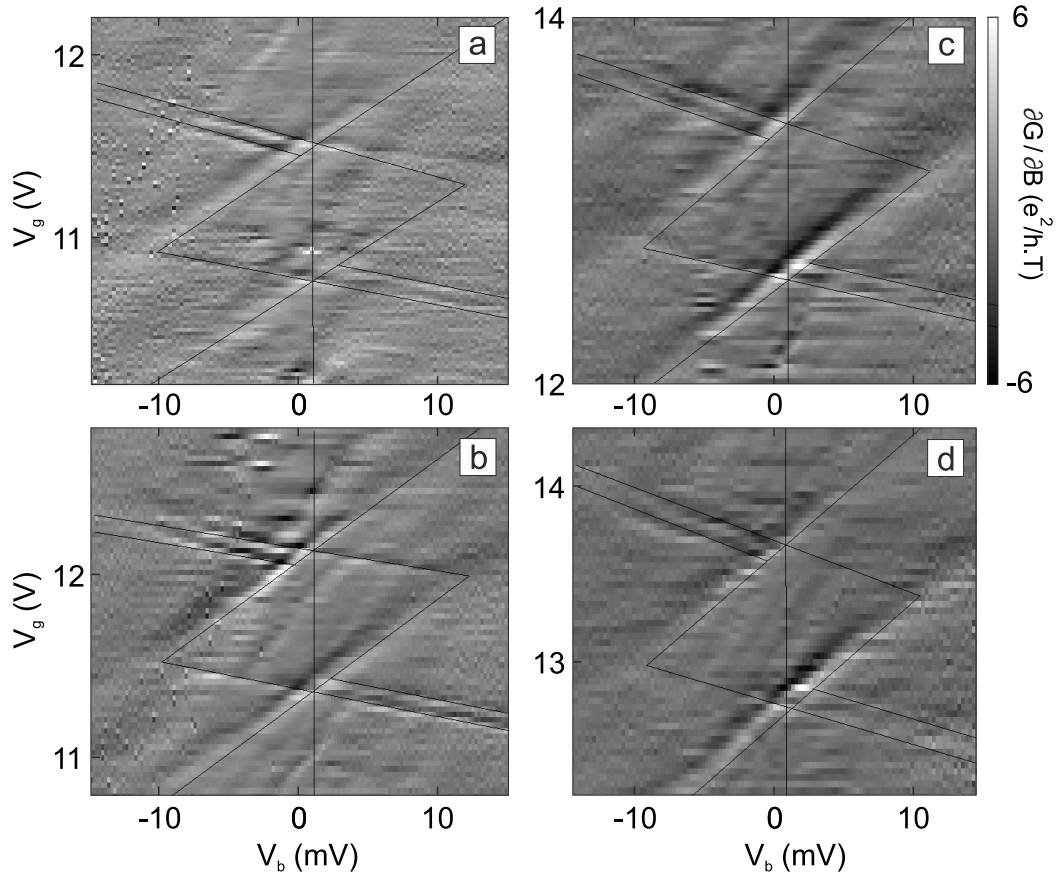


Figure 8.3: **Extraction of the energy-scales.** Extraction of the energy-scales from the high resolution measurements in Fig. 4.16a-d. The diamond is associated to the quantum phase $\nu = -2$, measured at $T = 15 \text{ mK}$ and $B = 6.1, 6.6, 7.7$ and 8 T (panels a, b, c and d, respectively).

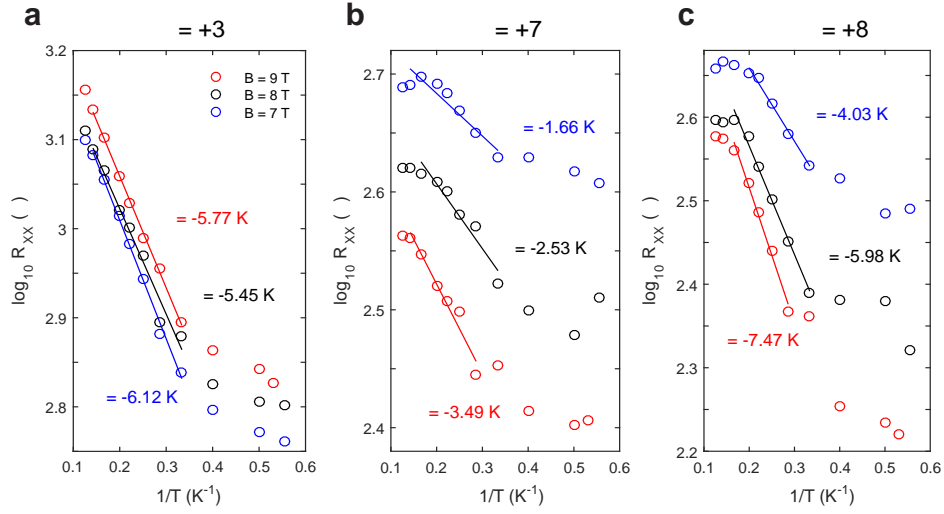


Figure 8.4: **Temperature dependence of symmetry broken states.** a - c Temperature dependence of the R_{xx} minimum at $\nu = +3, 7,$ and $+8,$ in the symmetry broken IQHE regime. Measurements are taken at $B = 7, 8$ and $9 T,$ represented in blue, black and red colors, respectively. The energy gaps Δ are extracted by linear fits to the data. Measurements are recorded at $T = 2 K.$

neither observe any dependence of ξ with $\nu.$ The absolute values of ξ lie nonetheless around $\sim 1 \mu m$ (See panel e of Fig. 5.8).

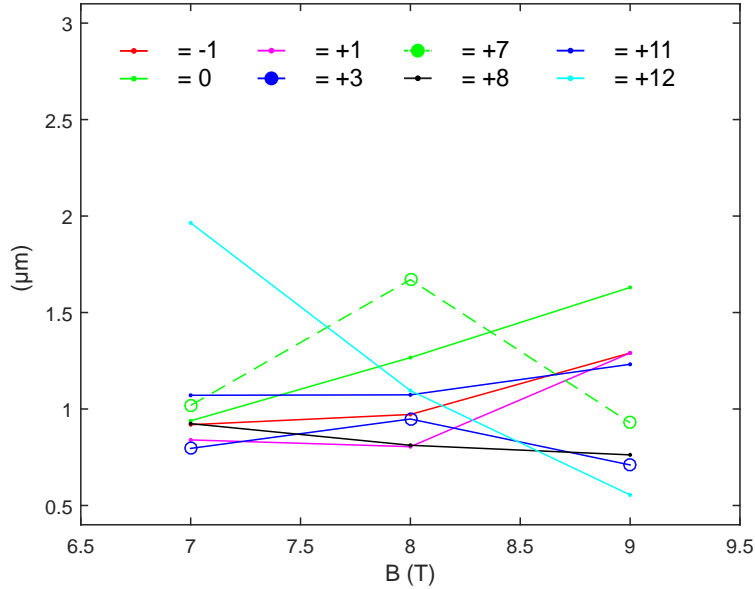


Figure 8.5: **Magnetic evolution of the localization length.** Extracted localization length ξ as a function of B-field, measured for all filling factors.

References

1. Yan, J. *et al.* Electric Field Effect Tuning of Electron-Phonon Coupling in Graphene. *Phys. Rev. Lett.* **98**, 166802 (2007).
2. Goerbig, M. O. Electronic properties of graphene in a strong magnetic field. *Review of Modern Physics* **83**, 112–123 (2010).
3. Young, A. F. *et al.* Spin and valley quantum Hall ferromagnetism in graphene. *Nature Physics* **8**, 550–556 (2012).

8.3 Process parameters

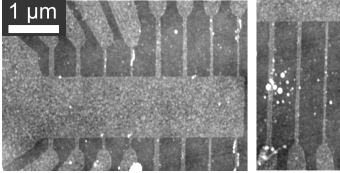
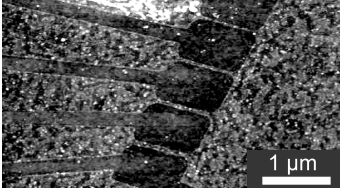
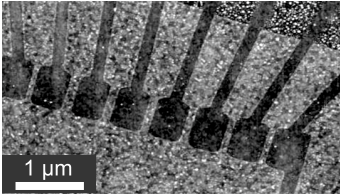
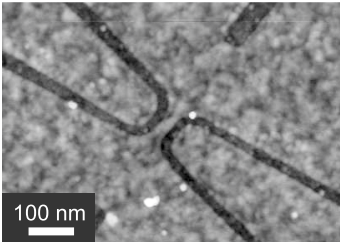
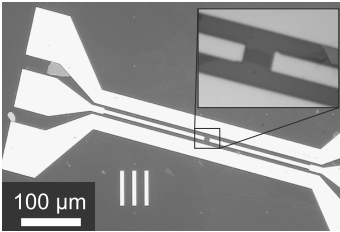
Process	Description of process steps
EBL markers on wafer	<p>1. Clean wafer: a) 5 min. acetone, 5 min. isopropanol b) Blow dry with N₂</p> <p>2. Coat with PMMA: a) Prebake wafer at 150 °C for 5 min. b) Spin-coat first layer: ARP 649.04 PMMA 200K, at 6000 rpm for 30 s, bake at 170 °C for 15 min. c) Spin-coat second layer: ARP 669.04 PMMA 600K, at 6000 rpm for 30 s, bake at 170 °C for 15 min.</p> <p>3. Ebeam exposure: Write marker scheme with a dose of 480 μC/cm², a beam current of 5 nA and a beam step size of 12.5 nm</p> <p>4. Development: 60 sec. AR-600-55 developer, 30 sec. isopropanol, blow dry with N₂</p>
Marker evaporation	<p>1. Plasma asher 10 s at 200W</p> <p>2. Metal evaporation 5 nm Cr at 0.1 nm/sec., 50 nm Au at 0.2 nm/sec.</p> <p>3. Lift off 15 min. in acetone until metal starts lifting, blow acetone with pipette and use ultra sonication (US) if necessary (up to maximum power)</p> <p>4. Clean sample a) 2 min. in acetone in US at maximum b) 2 min. in isopropanol in US at maximum c) Blow dry with N₂</p>
Dicing wafer	<p>1. Protection resist AZ-5214, 30 s at 4000 rpm. Bake for 3 min at 80°.</p> <p>2. Dicing Dice into 7x7 mm² dies (also called "chips")</p>
Preparing the glass stack for the transfer of exfoliated graphene, see Section 3.3	<p>1. Clean glass a) Put glass (0656.1 Carl Roth) for 2 min. in acetone in US at maximum power b) Blow dry with N₂</p> <p>2. Attach adhesive tape Attach adhesive tape (Pritt "Schluss mit Schere") in the middle of the glass, try to avoid bubbles</p> <p>3. Coat with co-polymer Spin-coat glass/tape stack with co-polymer (Elvacite 2550) for 30 sec. at 3000 rpm, bake at 110 °C for 5 min. (PMMA 950K can also be used)</p>
Preparing the PVA/PMMA stack for fabrication method in Section 3.2	<p>1. Clean Si wafer a) 5 min. acetone in US at maximum power, 2 min. in US at maximum power b) Blow dry with N₂</p> <p>2. Coat with PVA/PMMA a) Prebake wafer at 110 °C for 5 min. b) Spin-coat first layer: 4 % PVA (polyvinylalcohol), at 3000 rpm for 30 s, bake at 110 °C for 2 min. c) Spin-coat second layer: ARP 679.04 PMMA 950K, at 3000 rpm for 30 s, bake at 110 °C for 10 min.</p>

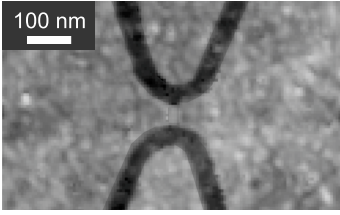
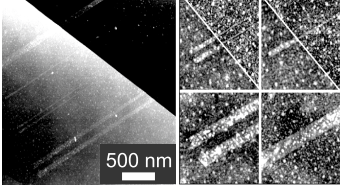
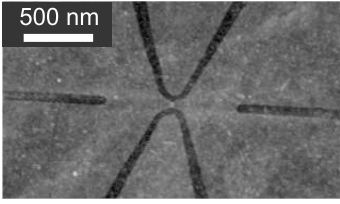
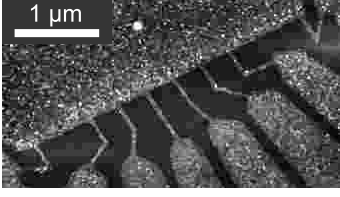
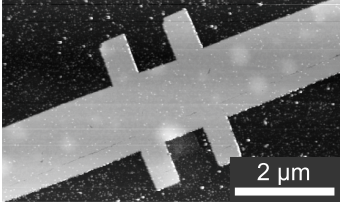
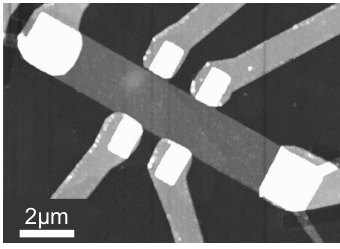
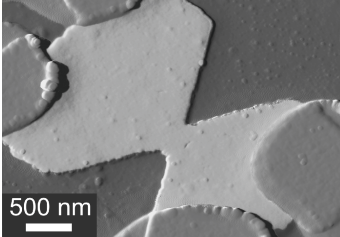
Process	Description of process steps
Depositing graphene/hBN on SiO_2 chip, PVA/PMMA-SiO_2 chip or glass stack	<p>1. Clean chips (only for Si^{++}/SiO_2)</p> <p>a) 5 min. in acetone in US at max. power b) 2 min in isopropanol in US at max. power c) 5 min plasma ashing at 600 W</p> <p>2. Exfoliation</p> <p>Exfoliate according to Section 3.1 right after plasma ashing (for Si^{++}/SiO_2) or spin-coating (for glass stacks, or PVA/PMMA-SiO_2 chips)</p> <p>3. Cleaning (only for SiO_2)</p> <p>a) 5 min. acetone, 2 min. isopropanol b) Blow dry with N_2</p>
Plasma etching of graphene on hBN	<p>1. Clean samples</p> <p>2 min. in acetone, 1 min. isopropanol, blow dry with N_2</p> <p>2. Coat with PMMA</p> <p>a) Prebake die at 170 °C for 5 min. b) Spin-coat ARP 679.04 PMMA 200K, at 6000 rpm for 30 s, bake at 170 °C for 15 min.</p> <p>3. Ebeam exposure</p> <p>Write etching mask with a dose of 300 $\mu C/cm^2$, a beam current of 100 pA and a beam step size of 1 nm</p> <p>4. Development</p> <p>60 sec. AR-600-55, 30 sec. isopropanol, blow dry with N_2</p> <p>5. Reactive ion etching (RIE1 Jülich)</p> <p>a) Without sample in chamber: O_2 flow 20 sscm, Ar flow rate 20 sscm, electrode power 300 W, pressure 0.025 mbar for 15 min. b) Without sample in chamber: O_2 flow 0 sscm, Ar flow rate 40 sscm, electrode power 100 W, pressure 0.025 mbar for 5 min. c) With sample in chamber: O_2 flow 8 sscm, Ar flow rate 32 sscm, electrode power 60 W, pressure 0.025 mbar for 8 sec.</p> <p>6. Clean samples</p> <p>15 min. acetone, 30 min. DMSO (at 60 °C), 15 min. acetone, 5 min. isopropanol, blow dry with N_2</p> <p>7. Anneal samples</p> <p>3 h at 450 °C at a pressure of 5×10^{-10} mbar (for further details refer to [1])</p>
Plasma etching graphene-hBN sandwiches <u>hardmask</u>	<p>1. Clean samples</p> <p>2 min. in acetone, 1 min. isopropanol, blow dry with N_2</p> <p>2. Coat with PMMA</p> <p>a) Pre-bake die at 170 °C for 5 min. b) Spin-coat ARP 679.04 PMMA 200K, at 6000 rpm for 30 s, bake at 170 °C for 15 min.</p> <p>3. Ebeam exposure</p> <p>Write etch mask with a dose of 300 $\mu C/cm^2$, a beam current of 1 nA and a beam step size of 5 nm</p> <p>4. Development</p> <p>60 sec. AR-600-55, 30 sec. isopropanol, blow dry with N_2</p> <p>5. Metal evaporation</p> <p>20 nm Cr at 0.1 nm/sec.</p> <p>6. Lift off</p> <p>15 min. in acetone until metal starts to lift, blow acetone with pipette until gold is removed</p>

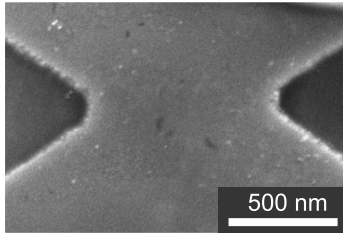
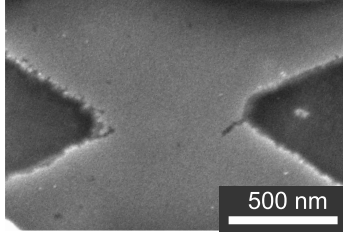
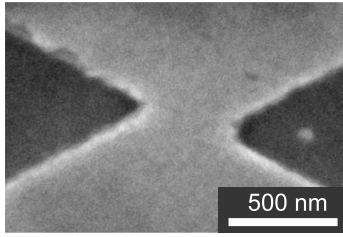
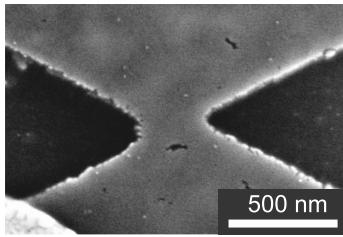
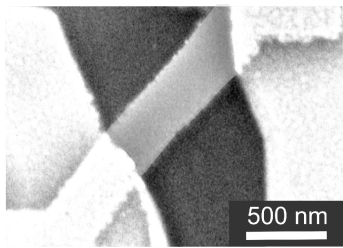
Process	Description of process steps
Plasma etching graphene-hBN sandwiches hardmask	<p>7. Clean samples 15 min. acetone, 30 min. DMSO (at 60 °C), 15 min. acetone, 5 min. isopropanol, blow dry with N₂</p> <p>8. Reactive ion etching (RIE Aachen) a) Without sample in chamber perform standard cleaning procedure b) With sample in chamber: 5 sccm Ar 20 sccm SF₆ at a pressure of 3 Pa and a power of 60 W</p> <p>9. Remove Cr etch mask a) Rinse 30 sec. in chrome etch (TMAH) b) Rinse 10 min. in water (pre-clean basin) and 15 min. in (pure basin)</p>
EBL contacts graphene (Jülich)	<p>1. Clean sample a) 2 min. acetone, 1 min. isopropanol b) blow dry with N₂</p> <p>2. Coat with PMMA a) Pre-bake sample at 170 °C for 5 min. b) Spin-coat first layer: ARP 649.04 PMMA 200K, at 6000 rpm for 30 s, bake at 170 °C for 15 min. c) Spin-coat second layer: ARP 669.04 PMMA 600K, at 6000 rpm for 30 s, bake at 170 °C for 15 min.</p> <p>3. Ebeam exposure a) Small contacts: dose 450 μC/cm², beam current 100 pA and beam step size 1 nm (50 μm around the sample) b) Medium contacts: dose of 400 μC/cm², a beam current of 5 nA and a beam step size of 12.5 nm (250 μm around the sample) c) Large contacts and bond pads: dose of 300 μC/cm², a beam current of 150 nA and a beam step size of 50 nm</p> <p>4. Development 60 sec. AR-600-55 developer, 30 sec. isopropanol, blow dry with N₂</p>
EBL contacts graphene (Aachen)	<p>1. Clean sample a) 2 min. acetone, 1 min. isopropanol b) Blow dry with N₂</p> <p>2. Coat with PMMA a) Pre-bake sample at 170 °C for 5 min. b) Spin-coat first layer: ARP 639.04 PMMA 50K, at 4000 rpm for 30 s, bake at 180 °C for 5 min. c) Spin-coat second layer: ARP 679.04 PMMA 950K, at 6000 rpm for 30 s, bake at 180 °C for 5 min.</p> <p>3. Ebeam exposure a) Small contacts: dose 100 μC/cm², beam step size 5.5 nm, beam current 15 pA, acceleration 10 kV, aperture 7.5 μm, writing field size 350 μm (50 μm around the sample) b) Large contacts and bond pads: dose 100 μC/cm², beam step size 60 nm, beam current 3.7 nA, acceleration 10 kV, aperture 120 μm, writing field size 2000 μm</p> <p>4. Development 75 sec. AR-600-55 developer, 10 sec. isopropanol, blow dry with N₂</p>
Contact evaporation	<p>1. Metal evaporation 5 nm Cr in 0.1 nm/sec., 50-100 nm Au in 0.2 nm/sec</p> <p>2. Lift off 15 min. in acetone until metal starts to lift, blow acetone with pipette until gold is removed</p> <p>3. Clean sample 2 min. in acetone, 1 min. in isopropanol, blow dry with N₂</p>

8.4 List of samples

The following table contains the SFM, SEM or optical images of the samples investigated within the time-frame of this thesis. The samples which do not appear in the thesis are referenced to the corresponding publication.

name	picture	device info	measurement
NT43		<ul style="list-style-type: none"> • Graphene 2T nanoribbons on SiO_2 • Etching: Ar/O_2 plasma (PMMA hard mask) • Contacts: Cr/Au 	<ul style="list-style-type: none"> • Aspect ratio dependence of the transport characteristics - See Section 4.1
NT01		<ul style="list-style-type: none"> • Graphene 2T nanoribbons on SiO_2 • Etching: Ar/O_2 plasma (PMMA hard mask) • Contacts: Cr/Au 	<ul style="list-style-type: none"> • Transport characterization of HF dipped graphene nanoribbons - See reference [2]
NT02 to NT04		<ul style="list-style-type: none"> • Graphene 2T nanoribbons on SiO_2 • Etching: Ar/O_2 plasma (PMMA hard mask) • Contacts: Cr/Au 	<ul style="list-style-type: none"> • Transport characterization of HF dipped graphene nanoribbons - See reference [2]
G30 to G38		<ul style="list-style-type: none"> • Side-gated 4T graphene nanoribbons on SiO_2 • Etching: Ar/O_2 plasma (PMMA hard mask) • Contacts: Cr/Au 	<ul style="list-style-type: none"> • Transport characterization and effect on the edges of HF dipped side-gated graphene nanoribbons - See reference [2]
RF1 to RF3		<ul style="list-style-type: none"> • Coplanar waveguides on SiO_2 • Etching: Ar/O_2 plasma (PMMA hard mask) • Contacts: Cr/Au 	<ul style="list-style-type: none"> • RF characterization (S-parameters) of graphene based HF coplanar waveguides - See reference [3]

name	picture	device info	measurement
WAG10		<ul style="list-style-type: none"> • Side-gated 4T graphene nanoribbons on SiO_2 • Etching: Ar/O_2 plasma etching using a PMMA hard mask • Contacts: Cr/Au 	<ul style="list-style-type: none"> • Bulk disorder characterization by probing magnetically confined QDs - See Section 4.2.1
WAE100		<ul style="list-style-type: none"> • Graphene 2T nanoribbons on SiO_2 and hBN • Etching: No etching • Contacts: No contacts 	<ul style="list-style-type: none"> • Raman spectroscopy of lithography-free graphene nanoribbons - See Section 4.3
WAG11		<ul style="list-style-type: none"> • Side-gated 4T graphene nanoribbons on SiO_2 • Etching: Ar/O_2 plasma (PMMA hard mask) • Contacts: Cr/Au 	<ul style="list-style-type: none"> • Reduction of edge disorder via electrostatic gating - See Section 4.4
NTA1 to NTA3		<ul style="list-style-type: none"> • Bi-layer graphene 2T nanoribbons on SiO_2 • Etching: Ar/O_2 plasma (PMMA hard mask) • Contacts: Cr/Au 	<ul style="list-style-type: none"> • Transport characterization of bi-layer graphene interconnects - See Section 4.5
CSC10		<ul style="list-style-type: none"> • hBN-graphene-hBN Hall bar on SiO_2 • Etching: $Ar-SF_6$ plasma (Cr hard mask) • Contacts: Cr/Au 	<ul style="list-style-type: none"> • Characterization of the electrical transport behavior of hBN-graphene-hBN devices - See Section 5.1
AD102		<ul style="list-style-type: none"> • hBN-graphene-hBN Hall bar on SiO_2 • Etching: $Ar-SF_6$ plasma (Cr hard mask) • Contacts: Cr/Au 	<ul style="list-style-type: none"> • Impact of thermal annealing on the electrical characteristics of hBN-graphene-hBN devices. • Spatial control of laser-induced doping profiles - See [4] and [5]
T1		<ul style="list-style-type: none"> • 4T hBN-graphene-hBN QPCs on SiO_2 • Etching: Ar/SF_6 plasma (Cr hard mask) • Contacts: Cr/Au 	<ul style="list-style-type: none"> • Observation of quantized conductance in ballistic graphene QPCs • Observation of degeneracy lifting in ballistic graphene nanoribbons - See Section 6.1

name	picture	device info	measurement
T1		<ul style="list-style-type: none"> • 4T hBN-graphene-hBN nanoribbons on SiO_2 • Etching: Ar/SF_6 plasma (Cr hard mask) • Contacts: Cr/Au 	<ul style="list-style-type: none"> • Observation of quantized conductance in ballistic graphene QPCs • Observation of degeneracy lifting in ballistic graphene nanoribbons - See Section 6.1
T1		<ul style="list-style-type: none"> • 4T hBN-graphene-hBN nanoribbons on SiO_2 • Etching: Ar/SF_6 plasma (Cr hard mask) • Contacts: Cr/Au 	<ul style="list-style-type: none"> • Observation of quantized conductance in ballistic graphene QPCs • Observation of degeneracy lifting in ballistic graphene nanoribbons - See Section 6.1
T1		<ul style="list-style-type: none"> • 4T hBN-graphene-hBN nanoribbons on SiO_2 • Etching: Ar/SF_6 plasma (Cr hard mask) • Contacts: Cr/Au 	<ul style="list-style-type: none"> • Observation of quantized conductance in ballistic graphene QPCs • Observation of degeneracy lifting in ballistic graphene nanoribbons - See Section 6.1
T1		<ul style="list-style-type: none"> • 4T hBN-graphene-hBN nanoribbons on SiO_2 • Etching: Ar/SF_6 plasma (Cr hard mask) • Contacts: Cr/Au 	<ul style="list-style-type: none"> • Observation of quantized conductance in ballistic graphene QPCs • Observation of degeneracy lifting in ballistic graphene nanoribbons - See Section 6.1
T2		<ul style="list-style-type: none"> • 4T hBN-graphene-hBN nanoribbons on SiO_2 • Etching: Ar/SF_6 plasma (Cr hard mask) • Contacts: Cr/Au 	<ul style="list-style-type: none"> • Shape-dependence of the ballistic transport • Observation of degeneracy lifting in ballistic graphene nanoribbons - Section 6.3

Publications

S. Somanchi, B. Terrés, J. Peiro, M. Staggenborg, K. Watanabe, T. Taniguchi, B. Beschoten and C. Stampfer, “*From diffusive to ballistic transport in etched graphene constrictions and nanoribbons*”, Ann. Phys. **529**, 1700082 (2017).

B. Terrés, L. A. Chizhova, F. Libisch, D. Joerger, A. Girschik, K. Watanabe, T. Taniguchi, S. V. Rotkin, J. Burgdörfer and C. Stampfer, “*Size quantization of Dirac fermions in graphene constrictions*”, Nature Communications **7**, 11528 (2016).

C. Neumann, L. Rizzi, S. Reichardt, B. Terrés, T. Khodkov, K. Watanabe, T. Taniguchi and C. Stampfer, “*Spatial control of laser-induced doping profiles in graphene on hexagonal boron nitride*”. ACS Appl. Mater. Interfaces **8** (14), pp 9377–9383 (2016).

C. Neumann, S. Reichardt, M. Drögeler, B. Terrés, K. Watanabe, T. Taniguchi, S. V. Rotkin and C. Stampfer, “*Low B Field Magneto-Phonon Resonances in Single-Layer and Bilayer Graphene*”, Nano Letters **15**, 1547 (2015).

B. Terrés, S. Reichardt, C. Neumann, K. Watanabe, T. Taniguchi and C. Stampfer, “*Raman spectroscopy on mechanically exfoliated pristine graphene ribbons*”, Physica Status Solidi B, DOI: 10.1002/pssb.201451398 (2014).

M. Drögeler, F. Volmer, M. Wolter, B. Terrés, K. Watanabe, T. Taniguchi, G. Güntherodt, C. Stampfer, and B. Beschoten, “*Nanosecond spin lifetimes in single- and few-layer graphene-hBN heterostructures at room temperature*”, Nano Lett. **14** (11), pp 6050–6055 (2014).

S. Engels, B. Terrés, F. Klein, S. Reichardt, M. Goldsche, S. Kuhlen, K. Watanabe, T. Taniguchi and C. Stampfer, “*Impact of thermal annealing on graphene devices encapsulated in hexagonal boron nitride*”, Physics Status Solidi B, DOI: 10.1002/pssb.201451384 (2014)

S. Engels, B. Terrés, A. Epping, T. Khodkov, K. Watanabe, T. Taniguchi, B. Beschoten

and C. Stampfer, “Limitations to carrier mobility and phase-coherent transport in bilayer graphene”, Phys. Rev. Lett. **113**, 126801 (2014).

J. Dauber, B. Terrés, C. Volk, S. Trellenkamp, and C. Stampfer, “Reducing disorder in graphene nanoribbons by chemical edge modification”, Appl. Phys. Lett. **104**, 083105 (2014).

R. Reiter, U. Derra, S. Birner, B. Terrés, F. Libisch, J. Burgdörfer, and C. Stampfer, “Negative quantum capacitance in graphene nanoribbons with lateral gates”, Phys. Rev. B **89**, 115406 (2014).

S. Engels, P. Weber, B. Terrés, J. Dauber, C. Meyer, C. Volk, S. Trellenkamp and C. Stampfer, “Fabrication of coupled graphene-nanotube quantum devices”, Nanotechnology **24**, 035204 (2013).

J. Dauber, B. Terrés, S. Trellenkamp and C. Stampfer, “Encapsulating graphene by ultra-thin alumina for reducing process contaminations”, Physica Status Solidi B **249**, 2526 (2012).

S. Fringes, C. Volk, C. Norda, B. Terrés, J. Dauber, S. Engels, S. Trellenkamp and C. Stampfer, “Electronic excited states in bilayer graphene double quantum dots”, Physica Status Solidi B **248**, 2684 (2011).

C. Volk, S. Fringes, B. Terrés, J. Dauber, S. Engels, and C. Stampfer, “Electronic excited states in bilayer graphene double quantum dots”, Nano. Lett. **11**, 3571 (2011).

C. Stampfer, S. Fringes, J. Güttinger, F. Molitor, C. Volk, B. Terrés, J. Dauber, S. Engels, S. Schnez, A. Jacobsen, S. Dröscher, T. Ihn and K. Ensslin, “Transport in Graphene Nanostructures”, Frontiers of Physics **6**, 271 (2011).

B. Terrés, C. Volk, S. Trellenkamp, and C. Stampfer, “Transport in kinked bi-layer graphene interconnects”, Proceedings of the 2011 6th IEEE International Conference on Nano/Micro Engineered and Molecular Systems.

B. Terrés, J. Dauber, C. Volk, S. Trellenkamp and C. Stampfer, “Disorder induced Coulomb gaps in graphene constrictions with different aspect ratios”, Appl. Phys. Lett. **98**, 032109 (2011).

List of Figures

2.1	Fig.01	8
2.2	Fig.02	13
2.3	Fig.03	14
2.4	Fig.04	15
2.5	Fig.05	16
2.6	Fig.06	18
2.7	Fig.07	19
2.8	Fig.08	20
2.9	Fig.09	22
2.10	Fig.10	23
2.11	Fig.11	24
3.1	Fig.12	30
3.2	Fig.13	31
3.3	Fig.14	32
3.4	Fig.15	33
3.5	Fig.16	34
3.6	Fig.17	35
3.7	Fig.18	36
3.8	Fig.19	37
3.9	Fig.20	38
4.1	Fig.21	42
4.2	Fig.22	43
4.3	Fig.23	45
4.4	Fig.24	46
4.5	Fig.25	47
4.6	Fig.26	48
4.7	Fig.27	49
4.8	Fig.28	54

4.9	Fig.29	55
4.10	Fig.30	57
4.11	Fig.31	58
4.12	Fig.32	59
4.13	Fig.33	60
4.14	Fig.34	61
4.15	Fig.35	64
4.16	Fig.36	65
4.17	Fig.37	71
4.18	Fig.38	72
4.19	Fig.39	74
4.20	Fig.40	76
4.21	Fig.41	81
4.22	Fig.42	83
4.23	Fig.43	84
4.24	Fig.44	85
4.25	Fig.45	86
4.26	Fig.46	87
4.27	Fig.47	88
4.28	Fig.48	89
4.29	Fig.49	92
4.30	Fig.50	93
4.31	Fig.51	95
4.32	Fig.52	96
4.33	Fig.53	97
4.34	Fig.54	98
4.35	Fig.55	99
4.36	Fig.56	100
4.37	Fig.57	101
4.38	Fig.58	102
4.39	Fig.59	103
4.40	Fig.60	105
4.41	Fig.61	106
4.42	Fig.62	107
4.43	Fig.63	108
4.44	Fig.64	112
4.45	Fig.65	113
4.46	Fig.66	114
4.47	Fig.67	115
4.48	Fig.68	116
4.49	Fig.69	117
5.1	Fig.70	122
5.2	Fig.71	123
5.3	Fig.72	124
5.4	Fig.73	125

5.5	Fig.74	126
5.6	Fig.75	127
5.7	Fig.76	129
5.8	Fig.77	130
6.1	Fig.78	136
6.2	Fig.79	137
6.3	Fig.80	138
6.4	Fig.81	139
6.5	Fig.82	141
6.6	Fig.83	142
6.7	Fig.84	143
6.8	Fig.85	144
6.9	Fig.86	145
6.10	Fig.87	146
6.11	Fig.88	147
6.12	Fig.89	148
6.13	Fig.90	149
6.14	Fig.91	150
6.15	Fig.92	151
6.16	Fig.93	152
6.17	Fig.94	153
6.18	Fig.95	154
6.19	Fig.96	155
6.20	Fig.97	156
6.21	Fig.98	157
6.22	Fig.99	158
6.23	Fig.100	159
6.24	Fig.101	162
6.25	Fig.102	163
6.26	Fig.103	164
6.27	Fig.104	165
6.28	Fig.105	166
6.29	Fig.106	167
6.30	Fig.107	168
6.31	Fig.108	169
8.1	Fig.119	175
8.2	Fig.120	176
8.3	Fig.121	177
8.4	Fig.122	178
8.5	Fig.123	178

Acknowledgements

With the end of this thesis comes the time to thank all the people who were contributing, in some way or another, to the work that I have been developing during these last years. I thank Prof. Dr. Christoph Stampfer for bringing the chance to do research on advanced and cutting-edge research topics like graphene and providing the adequate research environment to do so. Prof. Dr. Markus Morgenstern for being open to discussions on quantum Hall effect and co-examining this thesis. Prof. Dr. Slava V. Rotkin for the lively discussions on the physics behind the data and his support and good ideas on its interpretation. Prof. Dr. Fabian Hassler for help in correcting chapter 5 of the thesis and being open to discussions. Matthias Goldsche for his support on the metallization process. Special thanks go to Uwe Wichmann for his help with electronics and measurements systems. I also would like to thank my former Master and Bachelor students Nick Brogart, Ulrike Derra, Danny Jörger, Sebastian Thiesing and special thank to Jan Dauber who contributed a great deal to this thesis. Stephan Engels for the clean room transfer sessions and the lively discussions on our work. Christian Volk, Christoph Neumann, Regine Ockelmann, Martin Ollers, Matthias Goldsche, Michael Schmitz, Shaham Jafarpisheh, André Müller, Sammy Pissinger, Frank Vollmer, Sowmya Somanchi, Sven Reichardt, Gerard Verbiest, Alexander Epping, Christopher Franzen and all other members of the group for the nice working atmosphere and help with any kind of problems. Special thanks go to Julian Peiro for his samples and important contribution to our last publication and David de la Peña for trying to teach me quantum physics. I would also like to thank Giovanni Viola for his Sunday coffee at university and his lively discussions. and Luca Banszerus for correcting my rather poor translation to the abstract in German. I do not forget to thank Alexander Georgi and Christian Saunus for the great times in the football field. A very special mention goes to Stefan Trelenkamp and the rest of the clean room staff in Julich Forschungszentrum for helping during the fabricating of the graphene devices. Big thanks go to Jorg Schirra and Sascha Mohr who worked countless nights and during weekends to ensure helium supply. Thanks to my friends outside the physikszentrum, David, Carlos, Rosa, Irune, Antonio, Johanna, Yara, Santi and Gonzalo for sharing my free-time outside the lab. Especially, I would like to thank my parents for the wise advices and support throughout my entire life. Without them, I would not have finished my studies. Finally, with all my fondness,

my most special thankfulness to Doro for all her understanding and help even when I could not spend with her all the time I would had wanted. Thank you!

Curriculum Vitae

Persönliche Angaben

GEBURTSDATUM: 01. Februar 1980, Barcelona, Spanien
NATIONALITÄT: Spanisch
ANSCHRIFT: Werastraße 48, 70190 Stuttgart
TELEFON: +49 176 25777850
E-MAIL: bernat.terres@gmail.com
PROFIL: www.researchgate.net/profile/Bernat_Terres

Beruflicher Werdegang

- 10/08 - 07/09 | Praktikum bei der **SINEUROP Nanotech GmbH**, Stuttgart.
- Herstellung und Messung von elektromagnetischen Abschirmmaterialien basierend auf Kohlenstoffnanoröhrchen (CNT).
 - Entwurf, Simulation und Auswertung von einem Hochfrequenzapparat für die Messung der elektromagnetischen Abschirmeffizienz von planaren Materialien.
 - Wachstum von CNTs mittels chemischer Gasphasenabscheidung (CVD) auf Wolframdrähten zur Herstellung von Röntgen Kathoden.
- 09/06 - 07/07 | Mitarbeiter bei der **KNOSOS S.L. (Amper Group)**, Barcelona (Spanien).
- Projektbeschreibung für Kunden im Bereich der GPS-Position, Radiokommunikation (GPRS, TETRA, TETRAPOL), Systemintegration und Mobilitätssysteme.
 - Projektentwicklung und -ausarbeitung der technischen Spezifikation für die Bereitstellung eines Wi-Fi Mesh-Netzwerks für die Stadt Barcelona.

- 02/08 - 06/08 | Mitarbeiter in der **Fraunhofer Technologie-Entwicklungsgruppe (TEG)**, Stuttgart.
- Entwurf, Simulation und Auswertung von CNT-basierten transparenten AM-FM Antennen auf Glasoberflächen.
 - Entwicklung und Anwendung von CNT-basierten Verbundmaterialien (elektromagnetische Abschirmung und elektronischer Schaltungen).
- 07/06 - 09/06 | Praktikum bei der **CISC Semiconductor Design+Consulting GmbH**, Klagenfurt (Österreich).
- Entwurf, Simulation (Elektromagnetische Hochfrequenzsoftware SONNET) und Auswertung von UHF RFID Antennen.
 - Systemprogrammierung des UHF RFID Lesegeräts.
- 02/00 - 10/04 | Mitarbeiter bei der **TEGÜE s.c.p**, Barcelona (Spanien).

Akademischer Werdegang

- 05/15 - 09/15 | Deutsch für den Beruf (Stufe B2). **Berlitz**, Sprachschule Stuttgart.
- 09/09 - 12/14 | Promotionsstudium an dem II. Physikalischen Institut A der **RWTH Aachen** und Peter-Grundberg-Institut 9 des **Forschungszentrums Jülich (JARA-FIT Initiative)**.
Doktorarbeit: "Ballistic transport in graphene nanostructures".
Betreuer: Prof. Dr. Christoph STAMPFER.
- 07/07 - 09/08 | Diplomarbeit am **Max Planck Institut** für Festkörperphysik (MPI-FKF), Stuttgart. Abteilung: Prof. Dr. Klaus von KLITZING.
Thema: "Transparent Conductive Coatings based on Carbon Nanotubes".
Betreuer: Prof. Dr. Siegmund ROTH.
Abschluss: mit Auszeichnung.
- 09/98 - 06/07 | Studium der Elektrotechnik (Diplom Ingenieur für Elektrotechnik) an der **Universitat Politècnica de Catalunya (UPC)**, Barcelona, (Spanien).
- 09/85 - 06/98 | **Lycée Français de Barcelone (LFB)**, Französische Schule in Barcelona (Spanien). Baccalauréat scientifique (Abitur).

Sprachkenntnisse

KATALANISCH	Muttersprache
SPANISCH	Muttersprache
FRANZÖSISCH	Verhandlungssicher
ENGLISCH	Verhandlungssicher
DEUTSCH	Verhandlungssicher

EDV-Kenntnisse

BETRIEBS-SYSTEME	Windows OS, Unix OS (Ubuntu), DOS
CAD ENTWURF	Tanner L-edit, AutoCAD
SIMULATION	ADS (Agilent), Sonnet, KWANT, Nextnano, Comsol
PROG. SPRACHE	Matlab, LabView, C, C++, Java, VHDL, Assembler
WEITERE	CorelDraw, Photoshop, MS Office, Latex

Ehrenamt

AUGUST 2002 “European Summer University” (**AEGEE Europa**) in Blagoevgrad, Bulgarien (Sprachkurse, gemeinsame Aktivitäten mit Studenten aus ganz Europa).

HOBBYS Snowboard, Fußball, Automechanik, Kochen für und mit Freunden.